

**INTERACTION OF CHARGED
FLUID
WITH THE ASTROPHYSICAL
BLACK HOLES**

**Thesis for the degree of
Doctor of Philosophy (Science)
of
Jadavpur University
2000**

BANIBRATA MUKHOPADHYAY

Satyendranath Bose National Centre for Basic Sciences
Block-JD, Sector-III, Salt Lake, Calcutta - 700 098
India

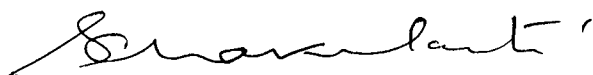
**INTERACTION OF CHARGED
FLUID
WITH THE ASTROPHYSICAL
BLACK HOLES**

**Thesis submitted for the
Doctor of Philosophy (Science)
degree of the
Jadavpur University**

BANIBRATA MUKHOPADHYAY
Satyendranath Bose National Centre for Basic Sciences
Block-JD, Sector-III, Salt Lake, Calcutta-700098
India

CERTIFICATE FROM THE SUPERVISOR

This is to certify that the thesis entitled “**INTERACTION OF CHARGED FLUID WITH THE ASTROPHYSICAL BLACK HOLES**” submitted by Sri Banibrata Mukhopadhyay who got his name registered on 24th August, 1998 for the award of Ph.D. (Science) degree of Jadavpur University, absolutely based upon his own work under the Supervision of Prof. Sandip K. Chakrabarti and that neither this thesis nor any part of it has been submitted for any degree/diploma or any other academic award any where before.



PROFESSOR SANDIP K. CHAKRABARTI

S.N.Bose National Centre for Basic Sciences

Block-JD, Sector-III, Calcutta-700098, India

27th September, 2000

Prof; Sandip K. Chakrabarti

Associate Professor

S. N. Bose National Centre
FOR BASIC SCIENCES

JD Block; Salt Lake, Calcutta-97

I DEDICATE MY THESIS AND PH.D. DEGREE
TO

MY SCHOOL TEACHER

MR. KUMAR KRISHNA CHOUDHURY,

MY 'DIDIBHAI' LABANI

AND 'ALL OF MY FRIENDS'

ACKNOWLEDGMENT

I would first like to express my sincerest gratitude to my supervisor Professor Sandip K. Chakrabarti. I am grateful to him for his guidance which helped me to carry out my thesis work. His valuable suggestions and teaching have helped me to learn a lot. In all over my Ph.D. research period he has supported me continuously which helped to finish my thesis smoothly. I can never forget all the days which I have spent with him during my Ph.D. work.

I would like to thank all the academic and non-academic staff of 'S.N.Bose National Centre for Basic Sciences' where I have carried out my thesis work. It would not be possible for me to carry out the research work without the help of my colleagues in my Centre. I would like to thank all our Astrophysics Group members, students and members of other groups and Post-M.Sc. students in my Centre.

I express my special thanks to my senior Kaushik Ghosh of 'Saha Institute of Nuclear Physics, Calcutta' and my friend Sudip Bhattacharyya of 'Indian Institute of Science, Bangalore' for academic discussion and mental support in different times of my Ph.D. period. I would also like to thank Anuj Nandi for reading the manuscript of the thesis carefully.

Finally I would like to thank my all 'Friends', 'Relatives' and 'Family Members' for continuous encouragement during my Ph.D. period.

CONTENTS

SUMMARY AND PLAN OF THE THESIS	1
PART-I NUCLEOSYNTHESIS AROUND BLACK HOLES ...	3
1 <i>INTRODUCTION</i>	4
1.1 What is Nucleosynthesis?	4
1.2 Primordial Nucleosynthesis	4
1.3 Chemical Evolution of the Galaxy	7
1.4 Chemical Evolution of the Star	10
1.5 Description of Major Nuclear Processes and Reaction Rate Equations	13
1.6 Brief idea about Nucleosynthesis around Black Hole	18
2 <i>EVOLUTION OF ACCRETION DISK MODELS</i>	22
2.1 Bondi Flow	22
2.2 Thin Accretion Disk	25
2.3 Thick Accretion Disk	29
2.4 Modern Accretion Disk	30
2.4.1 Shock Formation and Corresponding Conditions	33
2.4.2 Outflows from the Accretion Disk	35
2.5 Basic Properties of the Advective Disk and Motivation of Nucleosynthesis Work	36
2.6 Basic Equations of the Problem	43
3 <i>NUCLEOSYNTHESIS IN ACCRETION FLOWS</i>	48
3.1 Typical Solutions of Accretion Flows	50
3.1.1 Selection of Models	55
3.1.2 Selection of the Reaction Network	58
3.2 Results	62
3.2.1 Nucleosynthesis in Moderately Hot Flows	64
3.2.2 Nucleosynthesis in Hot Flows	81
3.2.3 Nucleosynthesis in Cooler Flows	92
3.3 Formation of Neutron Disk and Neutron Torus	93
3.4 Nucleosynthesis Induced Instability?	101

<i>4 IMPLICATIONS OF THE NUCLEOSYNTHESIS IN THE ACCRETION DISK</i>	104
<i>REFERENCES-I</i>	109
PART-II BEHAVIOUR OF FERMIONIC PARTICLES AROUND BLACK HOLES	116
<i>1 INTRODUCTION</i>	117
1.1 Spinor Analysis	119
1.2 Dirac Equation and its Separation	124
1.2.1 Basis Vectors of Newman-Penrose formalism in terms of Kerr Geometry	125
1.2.2 Separation of Dirac Equation into Radial and Angular parts	126
<i>2 SOLUTION</i>	129
2.1 Solution of Angular Dirac Equation	129
2.2 Solution of Radial Dirac Equation	131
2.3 Examples of Solutions	138
<i>3 CONCLUSIONS</i>	144
<i>REFERENCES-II</i>	147
THE LIST OF PUBLICATIONS	149
THE RE-PRINT OF PUBLICATIONS	152

Summary and Plan of the Thesis

We study the interaction of charged matter with an Astrophysical black hole. We look into two types of interactions. In one case, the bulk charged fluid is considered to fall onto the black hole due to the strong gravitational effect. During the infall of the matter nuclear reactions take place among various species contained in the infalling fluid. We study this nucleosynthesis thoroughly around stellar mass black holes which presumably form through the supernova explosion. We watch the behaviour of the bulk matter during its infall onto the black hole without concentrating on the behaviour of individual element. Of course during the infall of the matter, abundance of different isotopes are changed. We see that the energy release due to nuclear reactions sometimes dominates over the viscous energy of the flow; in those cases disk may be unstable. In some of the cases enormous neutron is produced around black hole and forming neutron torus. We check thoroughly all these phenomena systematically. This is the main part of the thesis.

Apart from this rather macroscopic aspect of the black hole astrophysics, we study interaction of individual particles specifically Fermionic particles with a black hole. Although we can develop ways to obtain the solution for any half-integral spin particles, here we consider the simplest case where the spin of the particle is chosen to be only half (e.g., electrons, neutrinos etc.). To find the nature of the interaction, we need to solve the Dirac equation in a curved space-time. Although we can choose the black hole having any mass, to get the significant interaction we choose only those black holes which were presumably produced in the early Universe as a result of the perturbation in the homogeneous background density field. These are called

primordial black hole. They have mass of the order of 10^{18} gm and clearly, they cannot be formed by supernova explosion. All the mini black holes with mass $M \lesssim 10^{15}$ gm can radiate their energy in a time less than the age of the Universe. Only the primordial black holes with mass $M \gtrsim 10^{15}$ gm could exist today.

So the thesis is divided into two parts. In the first and the major part, we study nucleosynthesis around black holes. In section 1, we present an introduction on nucleosynthesis. In §2, we give an idea of evolution of accretion disk model. In §3, we describe the nucleosynthesis in accretion disk. Finally in §4, we present some implications of nucleosynthesis around black holes.

The part two is comparatively brief. Here, in section 1, we give an introduction about the interaction of spin-half particles with black hole. In §2, we show some solutions of the Dirac equation. Finally in §3, we draw some concluding remarks.

PART-I

NUCLEOSYNTHESIS AROUND BLACK HOLES

1 Introduction

Here we introduce briefly the subject *nucleosynthesis* and its connection with astrophysical system. First of all we will define the term nucleosynthesis then will discuss about the origin and evolution of the nuclear elements in the Universe. To describe this evolution we plan to discuss about primordial nucleosynthesis, chemical evolution of the galaxy and the star in brief way step by step. Finally we give a brief idea about nucleosynthesis in accretion disk.

1.1 What is Nucleosynthesis?

Nucleosynthesis is a way in which a system of one set of nuclei transforms to another set in a given thermodynamical condition. Commonly, this refers to the ‘Primordial Nucleosynthesis’ of matter in the early universe. However, nucleosynthesis is present in stars, in boundary layers of neutron stars and in accreting matter around compact objects like black hole. In short, nucleosynthesis can take place in any hot dense medium where entropy is high.

1.2 Primordial Nucleosynthesis

In the very early universe, particle physics is the most dominant physics. Main confrontation between the theoretical ideas about the early Universe and observations comes in the epoch since nucleosynthesis started. One of the first predictions which comes from the particle physics and cosmology was constraint on the number of light ($\leq 10\text{MeV}$) neutrino flavours, N_ν by the Big Bang nucleosynthesis. This limit happens to be $N_\nu \leq 3$. When the cosmological limit was first proposed, the particle physics limits on this quantity ran into thousands. Thus the cosmological statement of small

numbers seemed very risky. Because of particle theory alone did not limit N_ν , a cosmological constraint is extremely important. It is therefore of great relief that this cosmological prediction was finally tested to be correct in the laboratory by collider experiments. From the pioneering work of Peebles (1966) and Wagoner, Fowler & Hoyle (1967) that the lightest elements like D , ${}^3\text{He}$, ${}^4\text{He}$ and ${}^7\text{Li}$ should be synthesized during the earliest epochs of the Universe evolution. According to Sciama (during the first CERN-ESO meeting held in Geneva in November, 1983) ‘Early nucleosynthesis is a triumph for the Big-Bang theory’ (Audouze 1989). Below, the primordial abundance determination of D , ${}^3\text{He}$, ${}^4\text{He}$ and ${}^7\text{Li}$ are discussed shortly.

The quark-hadron transition can produce variation in the ratio n/p in the early Universe and that the mixture of such variable n/p ratios can fit D , ${}^3\text{He}$, ${}^4\text{He}$ abundances (Schramm 1989; Applegate, Hogan & Scherrer 1987). Also the large variation of n/p seems to inevitably over produce ${}^7\text{Li}$. After Big-Bang, during the first few seconds nuclear abundances are in statistical equilibrium but the corresponding abundance of any nucleus above neutron and proton (which are formed by quark-hadron phase transition) is very low because of high entropy per baryon. It can be mentioned here that in accretion disk the entropy is also very high. When kT falls to 0.3 Mev, the equilibrium mass fraction of ${}^4\text{He}$ reaches about 0.15 (for $n/p \sim 0.2$) but the equilibrium condition is no longer applicable after this. Nuclear reactions become too slow, partly from Coulomb barriers and partly because of low (still near-equilibrium) abundances of lighter nuclei D , ${}^3\text{He}$ and ${}^4\text{He}$. Only when the D/p ratio (depending on the balance between $p - n$ captures and photo-dissociation) has built up to a value of order 10^{-5} at $kT \sim 0.1$ MeV, do nuclear reactions effectively build up to ${}^4\text{He}$, which then uses up virtually all the neutrons remaining from

freeze-out and subsequent decay. After the formation of ${}^4\text{He}$, traces of lighter elements survive because nuclear reactions are frozen out by low density and temperature before their destruction is complete and still smaller traces of ${}^7\text{Li}$ and ${}^7\text{Be}$ are formed. The series of reactions which take place in primordial nucleosynthesis are given as: $p(n, \gamma)D$, $D(D, n){}^3\text{He}$, $D(D, p)T$, ${}^3\text{He}(D, p){}^4\text{He}$, $T(D, n){}^4\text{He}$, ${}^3\text{He}(\alpha, \gamma){}^7\text{Be}$, $T(\alpha, \gamma){}^7\text{Li}$, ${}^7\text{Be}(n, p){}^7\text{Li}$, ${}^7\text{Li}(p, \alpha){}^4\text{He}$, $T(\gamma, \gamma){}^3\text{He}$ (with $\tau_{1/2}=12.2$ Yr.), ${}^7\text{Be}(\gamma, \gamma){}^7\text{Li}$ (by K-capture after recombination). Few of these reactions take place in accretion disk also but with different reaction rates because these rates depend on density and temperature. The nuclear reactions in accretion disk are described in §3.2.

All deuterium in the Universe are originated from Big-Bang nucleosynthesis because thermonuclear reactions in stars only cause net destruction of D and it is vastly more abundant than other light nuclei like ${}^6\text{Li}$ or ${}^9\text{Be}$ that are basically result of spallation reactions (Pagel 1997). The first evidence for primordial deuterium abundance was obtained in the early 1970s from the studies of the solar wind, planetary atmospheres and the interstellar medium. These studies give an average ${}^3\text{He}/{}^4\text{He} \sim 4.1 \times 10^{-4}$. With $He/H \sim 0.1$ for the Sun, this is equivalent to ${}^3\text{He}/H \sim 4.1 \times 10^{-5}$. Black (1971) and Geiss & Reeves (1972) computed proto solar ${}^3\text{He}$ abundance present in the wind from the primitive Sun and attributed the excess in the present day solar wind to proto-solar deuterium which was burnt to ${}^3\text{He}$ during Solar evolution. The proto-solar deuterium abundance is thus about 2.6×10^{-5} which is in fair agreement with observation. Bania et al. (1987) have analysed the abundance of ${}^3\text{He}$ with improved determination technique avoiding various sources of systematic errors. Although the range of possible interstellar ${}^3\text{He}/H$ abundance is somewhat reduced with respect to the one reported by Rood et al. (1984) there are

still very large variations of the ${}^3\text{He}$ abundance as $1.2 \times 10^{-5} \leq {}^3\text{He}/H \leq 1.5 \times 10^{-4}$.

${}^4\text{He}$ has been thoroughly observed in metal poor galaxies (Lequeux et al. 1979; Kunth & Sargent 1983; Pagel et al. 1986). From Kunth (1986) and Shields (1986) abundance of ${}^4\text{He} = 0.24 \pm 0.01$. Audouze (1989) concluded the abundance of ${}^4\text{He}$ to be 0.235 ± 0.012 . Also by the Voyager measurement of He/H at the surface of Uranus, abundance of ${}^4\text{He} = 0.262 \pm 0.048$ (Audouze 1989). It might be noted that variable n/p seems to also have high values for ${}^4\text{He}$. In particular, any realistic spectrum of quark-hadron parameters rather than a single, fine-tuned value not only over-produces Li but also ${}^4\text{He}$.

The abundance determination of ${}^7\text{Li}$ concerning the old population II stars performed by Spite & Spite (1982) and Audouze (1989) such as $\text{Li}/H \sim 10^{-10}$ in such stars have been confirmed by two further independent analysis. One was performed by Hobbs & Duncan (1987) and another was by Rebolo, Molaro & Beckman (1988). As was noted by Audouze (1989), the difference of behaviour of the Li/H and O/H abundance ratio with respect to Fe/H for instance constitutes a very important argument in favour of a low primordial abundance of ${}^7\text{Li}$ so that ${}^7\text{Li}/H$ is roughly 2×10^{-10} .

1.3 Chemical Evolution of the Galaxy

From the discovery of microwave background, it is assumed that the Universe was originated from a hot big-bang (Peebles 1966; Schramm & Wagoner 1977). From detailed nucleosynthesis calculation based on hot big-bang model it is shown that no heavier element than ${}^9\text{Be}$ could be synthesized primordially with an abundance more than 10^{-14} by mass fraction. But in today's Universe there are appreciable amounts

of elements heavier than helium. Out of these elements 2% of the visible mass are believed to have been synthesized in stars or starlike objects. Cosmic gas fragmentation into huge gas clouds forming galaxies and further fragmentation of which possibly led the formation of stars. Stars evolve on timescales ranging from several millions to tens of billions of years, synthesize elements in their central parts and emit the processed elements into the interstellar medium at various stages. The interstellar medium is thus enriched with heavy elements and the stars formed thereafter are born with a higher metallicity. This cycle should go on until all gas in the interstellar medium is exhausted. Thus the chemical evolution of galaxies involves understanding the spatial distribution and temporal evolution of various elements in the galaxies by taking into account the process of star formation, distribution of stars according to their masses and chemical compositions and the final yields of various elements and any detectable remnants of the parent stars.

Ideas of modern astrophysics and astrochemistry were originated from Maghnad Saha (Saha 1920, 1921). By the middle of the 1950s it became clear that elements in the galaxies and stars could not have been synthesized in the hot big-bang. The metallicity of the interstellar medium should increase monotonically with time through the evolution of stars. So from the measure of metallicity, age can be obtained. Studies of stellar structure combined with the spectral colour and luminosity distributions of stars yielded the first frequency distribution of stars according to their masses which is called the initial mass function. In 1959, Schmidt (1959) suggested an empirical expression relating star formation with local density of gas in the interstellar medium. Van den Bergh (1962) and Schmidt (1963) found frequency distributions of Sun type stars according to their metallicity that did not agree with the calculated one which

was done from a simple model of chemical evolution. This discrepancy i.e., significant underabundance of metal-poor stars is known as G-dwarf problem.

The first solution of G-dwarf problem was suggested by Truran & Cameron (1971) in which they assumed a prompt initial enrichment of models with a non-zero initial metallicity ($Z_0 \neq 0$). Larson (1972) suggested the infall model which assumes an inflow of metal-free gas from the halo and the rate of inflow proportional to the local star formation rate. Lynden-Bell (1975) considered the inflow together with a non-zero initial metallicity. Tinsley (1975) and Ostriker & Thuan (1975) proposed collapse models where the rate of inflow of gas was assumed to have metallicity proportional to the metallicity of disk and to compensate for star formation rate. These models were constructed from Larson's (1973) own model of star formation or disk formation.

The increasing interaction of the chemical evolution of the disk with that of the pre-existing halo was revealed in the pioneering measurements of the abundance of various heavy elements. These showed widely varying Fe/H relation (Clegg 1977). There are no depletion in the O/H ratio with respect to the Fe/H ratio which is the case for new stars. Thus, the differential evolution is suggested in the various elements with time. At least three phases of the Galactic evolution were identified in terms of three different metallicity dependent populations of stars. In the cases of thin young disk, the abundance of most elements changes proportional to Fe/H . On the other hand, in thick disk cases, significant changes in trends of various elements relative to iron are noticed. The α -rich and neutron-rich heavy elements are produced essentially independent of initial iron abundance through supernova explosions of the short-lived massive stars, which do not contribute a significant amount of iron. The bulk of iron is produced by relatively long-lived progenitors of the type Ia supernova

explosions. The abundances of C , N , Mg , Al , Ca , Sr , Ba and a few other elements again change their abundance ratios beyond Fe/H ratio.

The change of the observational numbers with time invalidates most of the theoretical analysis based on the previous results of observations. For example G-dwarf metallicity distributions which were used before 1989 differ greatly from those given by Pagel (Beckman & Pagel 1989). The gas distribution differs by few factors depending on whose distribution is used. The assumed variation of yields could be different in various models.

1.4 Chemical Evolution of the Star

Star possesses a self-gravitating mechanism in which the temperature is adjusted so that the outflow of energy through the star is balanced by nuclear energy generation except at catastrophic phases. The temperature required to give this adjustment depends on the particular nuclear fuel available. Hydrogen requires a lower temperature than helium; helium requires a lower temperature than carbon and so on. At iron this increasing of temperature sequence stops because the energy generation by the fusion process ends here. In initial stage, when hydrogen is present, the temperature is adjusted to hydrogen as fuel which is comparatively low. If hydrogen is exhausted as stellar evolution proceeds, the temperature rises until helium becomes the principal fuel. When all the helium nuclei are exhausted, the temperature rises further until the next nuclear fuel comes into operation and so on. This automatic temperature rise is brought about in each case by the conversion of gravitational energy into thermal energy. Since the penetration of Coulomb barrier occurs more readily as the temperature rises, it can be anticipated that the sequence will be the one in which

reactions take place between nuclei with greater and greater nuclear charges. As it becomes possible to penetrate larger and larger barriers the nuclei will evolve towards configuration of greater and greater stability, so that heavier and heavier nuclei will be synthesized until iron is reached. Thus there must be a progressive conversion of light nuclei into heavier ones as the temperature rises (Burbidge et al. 1957).

The temperature of star is not constant everywhere. As the central temperature is maximum, corresponding nuclear evolution is most advanced there. On the other hand on the surface, this evolution is least as temperature is minimum. Thus the composition of star can not be expected to be uniform throughout. A stellar explosion does not accordingly lead to the ejection of material of one definite composition but instead a whole range of compositions may be expected. Also there are mixing of central material outward and outer material inward. Material ejected from one star may subsequently become condensed in another star. So the elements of the star are evolving by all these series of processes.

Now we briefly describe several processes through which elements are synthesized. Hydrogen burning is responsible for the majority of the energy production in the stars. By the *CNO* cycle and *pp*-chain helium is synthesized from hydrogen. The helium burning process is responsible for the synthesis of carbon from helium and by further α -particle addition for the production of ^{16}O , ^{20}Ne . With the addition of α -particle successively to ^{20}Ne , the nuclei ^{24}Mg , ^{28}Si , ^{32}S , ^{36}Ar , ^{40}Ca and may be ^{44}Ca , ^{48}Ti are produced. Under condition of high temperature and density, the isotopes of vanadium, chromium, manganese, iron, cobalt and nickel are synthesized. This process is called equilibrium process (Hoyle 1946, 1954). Also neutron captures are taking place in stars whose time-scale is very long ranging from 100 years to 10^5

years. This synthesis is responsible for the production of the majority of the isotopes in the range $23 \leq A \leq 46$ excluding those synthesized predominantly by the α -process and for a considerable proportion of the isotopes in the range $63 \leq A \leq 209$. There is another type of neutron capture process which has very short time-scale like 0.01 – 10sec. This is called the rapid-capture process or, simply, the ‘r-process’. In this process isotopes in the range $70 \leq A \leq 209$ are produced. Through this process some light elements like ${}^{36}\text{S}$, ${}^{46}\text{Ca}$, ${}^{48}\text{Ca}$, perhaps ${}^{47}\text{Ti}$, ${}^{49}\text{Ti}$ and ${}^{50}\text{Ti}$ are produced. In stars, as in an accretion disk, few proton-capture process or emission of n by γ -ray absorption take place. By this process proton rich isotopes are produced but with low abundances compared with the nearly normal and neutron-rich isotopes. There is another process called ‘x-process’ which is responsible for the synthesis of deuterium, lithium, beryllium and boron. x-process is collectively more than one process but characteristic of all of these produced elements is that they are very unstable at the temperature of the stellar interior, so that it appears probable that they have been produced in regions of low density and temperature. The typical abundances of few of the isotopes which are synthesized in a young star (may be Sun) are given as: $p = 7.425 \times 10^{-1}$, $D = 2.948 \times 10^{-5}$, ${}^3\text{He} = 2.538 \times 10^{-5}$, ${}^4\text{He} = 2.380 \times 10^{-1}$, ${}^7\text{Li} = 1.055 \times 10^{-8}$, ${}^{11}\text{B} = 5.765 \times 10^{-9}$, ${}^{16}\text{O} = 8.779 \times 10^{-3}$, ${}^{24}\text{Mg} = 5.562 \times 10^{-4}$ etc. When we study nucleosynthesis in accretion disk in later Sections, this type of abundance of different isotopes are chosen as the initial abundance since matter is supplied to the disk from the nearby star or companion stars.

In §1.5 we will describe more about few of the major nuclear processes mentioned above. In later Sections we will see that in the disk main reactions are proton-capture, rapid-proton capture, sometimes neutron capture processes, dissociation of

the elements etc.

1.5 Description of Major Nuclear Processes and Reaction Rate Equations

Here we will discuss briefly about different nuclear reactions which may come in this thesis in different places. We mainly will concentrate on the discussion of pp chains, CNO cycle, proton capture and rp process, α process, photo-dissociation (Chakrabarti et al. 1987).

(a) pp chain:

By this process protons can be converted into helium nuclei via different reactions. If only protons are present the reactions proceed through the so-called ppI chain following the set of reactions as $p(p, \gamma)D$, $D(p, \gamma)^3He$, $^3He(^3He, 2p)^4He$. After production of 4He , 7Be is produced by $^4He(^3He, \gamma)^7Be$. Depending upon the fate of 7Be , two series of reactions may follow and are called the $ppII$ and $ppIII$ chains. They are respectively as, $^4He(^3He, \gamma)^7Be$, $^7Be(e^-, \nu)^7Li$, $^7Li(p, \alpha)^4He$ and $^4He(^3He, \gamma)^7Be$, $^7Be(p, \gamma)^8B$, $^8B(e^-, \nu)^8Be$, $^8Be(\gamma, \alpha)^4He$. The pp chain is effective for the temperature range as $T_9 \sim 0.01 - 0.2$ (T_9 is the temperature in unit of 10^9K). As the hydrogen burning time scale by pp chain reactions is of the order 10^{18} sec so the conversion to helium from hydrogen through pp chain reaction is possible not only if the temperature (T_9) is in between 0.01 and 0.2 but also if the residence time of the system is very large.

(b) CNO cycle:

If the matter of the system consisted only of hydrogen and helium, then only the reactions of pp chain would be responsible for hydrogen depletion, but usually there are traces of heavy elements. In the presence of some carbon (which may be produced

via triple-alpha reaction, i.e., ${}^4\text{He}(\alpha, \gamma){}^8\text{Be}(\alpha, \gamma){}^{12}\text{C}$), nitrogen and oxygen nuclei, the hydrogen to helium conversion is more efficient. This is called as *CNO* cycle which operates as ${}^{12}\text{C}(p, \gamma){}^{13}\text{N}(e^+, \nu){}^{13}\text{C}(p, \gamma){}^{14}\text{N}(p, \gamma){}^{15}\text{O}(e^+, \nu){}^{15}\text{N}(p, \alpha){}^{12}\text{C}$. For these reactions the operating temperature can be as low as $T_9 \sim 0.02$. At low temperature the *CNO* cycle is limited by the proton capture rate of ${}^{14}\text{N}$. When $T_9 \gtrsim 0.3$, the proton capture on ${}^{13}\text{N}$ completes with positron decay and the *CNO* cycle changes into a hot *CNO* cycle (*HCNO* cycle). The basic reactions of hot *CNO* cycle are ${}^{12}\text{C}(p, \gamma){}^{13}\text{N}(p, \gamma){}^{14}\text{O}(e^+, \nu){}^{14}\text{N}(p, \gamma){}^{15}\text{O}(e^+, \nu){}^{15}\text{N}(p, \alpha){}^{12}\text{C}$. The *HCNO* cycle operates in the temperature range as $0.5 \gtrsim T_9 \gtrsim 0.3$. So the temperature (T_9) range of *CNO* cycle is $0.02 - 0.5$.

When the initial abundance of ${}^{16}\text{O}$ is considerable (may be same as Sun), it dumps ${}^{14}\text{N}$ into *CNO* cycle in the following way: ${}^{16}\text{O}(p, \gamma){}^{17}\text{F}(e^+, \nu){}^{17}\text{O}(p, \alpha){}^{14}\text{N}$. This process continues until ${}^{16}\text{O}$ depletion is balanced by the reaction ${}^{15}\text{N}(p, \gamma){}^{16}\text{N}$. This can increase the flow of *CNO* or *HCNO* by increasing *CNO* seeds. When $T_9 > 0.1$, ${}^{17}\text{O}$ can change in the following way: ${}^{17}\text{O}(p, \gamma){}^{18}\text{F}(p, \alpha){}^{15}\text{O}$, again producing *CNO* seeds.

(c) Rapid proton capture and proton capture process:

In the case of proton-rich environment, when temperature $T_9 \sim 0.5$, for a given neutron number nuclei will keep capturing protons until the positron decay dominates proton capture. This process is known as rapid proton capture process or in short *rp* process. In the high temperature region *rp* process is favoured over *CNO* cycle. Also in temperature lower than $0.5 \times 10^9\text{K}$ elements like ${}^{18}\text{O}$, ${}^{15}\text{N}$, ${}^6\text{Li}$, ${}^7\text{Li}$ etc. capture proton and hydrogen burning takes place. These are called proton capture reaction. By these reactions isotopes convert as: ${}^{18}\text{O}(p, \alpha){}^{15}\text{N}(p, \alpha){}^{12}\text{C}$, ${}^6\text{Li}(p, {}^3\text{He}){}^4\text{He}$, ${}^7\text{Li}(p, \alpha){}^4\text{He}$, ${}^{11}\text{B}(p, \gamma){}^3{}^4\text{He}$, ${}^{17}\text{O}(p, \alpha){}^{14}\text{N}$ etc.

(d) α processes:

The triple α reaction is also important for $T_9 \gtrsim 0.1$. It will produce *CNO* seeds for pure hydrogen burning. It also process light elements into heavy elements. In sufficiently hot environment helium can be significantly processed by the triple α (3α) reaction. By the burning process of carbon, neon, oxygen etc. free particles like p , n and α s are provided which are useful to mediate further nucleosynthesis. Following 3α reaction, helium burning can go into ‘alpha process’. In the presence of large quantity of helium, the alpha capture reactions produce heavy elements whose atomic weight is multiple of 4, i.e., $^{12}\text{C}(\alpha, \gamma)^{16}\text{O}(\alpha, \gamma)^{20}\text{Ne}(\alpha, \gamma)^{24}\text{Mg}(\alpha, \gamma)^{28}\text{Si}(\alpha, \gamma)^{32}\text{S}(\alpha, \gamma)^{36}\text{Ar}(\alpha, \gamma)$ etc. upto ^{56}Ni . Beyond ^{56}Ni , the mean binding energy per nucleon decreases for these $Z = 2n$, $A \doteq 4n$ nuclei. Here Z and A are atomic number and mass number respectively, n is a positive integer. Alpha elements beyond ^{40}Ca are beta (e^+) unstable. Thus ^{56}Ni finally becomes ^{56}Fe by capturing two electrons.

(e) Photodissociation:

When temperature $T_9 \gtrsim 0.8$ few elements like D , ^3He start to dissociate to produce their daughter elements. By this process elements are hit by photons and break up with the absorption of the energy from the system, because total mass in the left hand side of the reaction is less than that of the right hand side. This is called photo-dissociation of the elements. The corresponding reactions are like, $D(\gamma, n)p$, $^3\text{He}(\gamma, p)D$ etc. Also at even higher temperature, $T_9 \sim 5 - 15$, the heavier nuclei like ^4He can be dissociated. Photodissociation of ^{56}Ni may be represented schematically as $^{56}\text{Ni}(\gamma, \alpha)13^4\text{He}$. The Q -value for this reaction is 87.85MeV. By the photo-dissociation of ^{56}Fe to α ($Q = 124.4\text{MeV}$) and that to p and n ($Q = 28.3\text{MeV}$) huge amount of the energy can be absorbed from the system. The reactions are $^{56}\text{Fe}(\gamma, 4n)13^4\text{He}$ and

${}^4\text{He}(\gamma, 2n)2p$.

Now we give the idea about how the nucleosynthesis problem in a system can be solved, where different nuclear reactions take place. Due to the interactions among different isotopes nuclear energy is released which depends on corresponding reaction rate which is dependent on temperature of the system. As an example, for two body reaction, total reaction rate per unit volume can be written as (Clayton 1983),

$$r_{12} = \frac{N_1 N_2 \lambda_{12}}{(1 + \delta_{12})} \quad (\text{I.1})$$

where, λ_{12} is the reaction rate per pair of particles. N_1 and N_2 are number density of the interacting isotopes as,

$$N_i = \frac{\rho N_A Y_i}{A_i}. \quad (\text{I.2})$$

Here, Y_i = abundance of i th isotope, A_i = atomic mass number of i th isotope, N_A = Avogadro Number = 6.023×10^{23} and ρ = density of the matter.

Now we will briefly talk about the reaction rate equation to have an idea about how the abundance of isotopes are changed:

Here as an example we consider a simplistic nuclear network with only three reactions and three isotopes. Although in our final calculation we will use 255 isotopes and corresponding set of reactions.

We choose the isotopes in the network as p , D and ${}^4\text{He}$. The nuclear reactions are considered out of those three isotopes as $p(p, \gamma)D$ (fusion of protons), $D(\gamma, n)p$ (deuterium dissociation) and ${}^4\text{He}(\gamma, D)D$ (helium dissociation). The corresponding rate equations are

$$\frac{dY_p}{dt} = -\lambda_{pp}Y_p + \frac{1}{2}\lambda_d Y_D \quad (\text{I.3})$$

$$\frac{dY_D}{dt} = -\lambda_D Y_D + \frac{1}{2}\lambda_{He} Y_{He} + 2\lambda_{pp} Y_p \quad (\text{I.4})$$

$$\frac{dY_{He}}{dt} = -\lambda_{He}Y_{He}. \quad (\text{I.5})$$

Here we consider the corresponding backward reactions rate are negligibly small compared to the forward one. From those equations we can write

$$\frac{d}{dt} \begin{pmatrix} Y_p \\ Y_D \\ Y_{He} \end{pmatrix} = \begin{pmatrix} -\lambda_{pp} & \frac{1}{2}\lambda_d & 0 \\ 2\lambda_{pp} & -\lambda_d & \frac{\lambda_{He}}{2} \\ 0 & 0 & -\lambda_{He} \end{pmatrix}, \quad (\text{I.6})$$

which is of the form

$$\frac{d}{dt}V = \Lambda V. \quad (\text{I.7})$$

Here 3 components of the vector V are Y_p , Y_D and Y_{He} (actually Y_{4He}) and Λ is the 3×3 matrix. The solution consists of finding three eigenvectors of Λ , defined as (Clayton 1983)

$$\Lambda V_1 = \lambda_1 V_1, \quad \Lambda V_2 = \lambda_2 V_2, \quad \Lambda V_3 = \lambda_3 V_3 \quad (\text{I.8})$$

where, λ_1 , λ_2 and λ_3 are 3 eigenvalues of Λ . From Eqn. (I.7) it follows that if $V(t)$ is expressed as a linear combination of the eigenvectors with exponential time dependence as (Clayton 1983)

$$V(t) = ae^{\lambda_1 t}V_1 + be^{\lambda_2 t}V_2 + ce^{\lambda_3 t}V_3, \quad (\text{I.9})$$

where a, b, c are constant coefficients, then Eqn. (I.7) is exactly satisfied. This is correct only if individual nuclear lifetimes are constant. This condition can not be strictly met if there is a gradual depletion of p and possibilities of changes in temperature.

From the elementary theory, it is known that the solution for eigenvalues as in Eqn. (I.8) can be obtained only if the eigenvalues themselves are such that the determinant of the matrix $(\Lambda - \lambda\mathbf{I})$ vanishes. The secular equation is given as

$$\begin{vmatrix} -(\lambda_{pp} + \lambda) & \frac{1}{2}\lambda_d & 0 \\ 2\lambda_{pp} & -(\lambda_d + \lambda) & \frac{\lambda_{He}}{2} \\ 0 & 0 & -(\lambda_{He} + \lambda) \end{vmatrix} = 0. \quad (\text{I.10})$$

Solving this equation we can find out eigenvalue λ s and eigenvector V s as

$$\lambda_1 = 0, \quad V_1 = \begin{pmatrix} \frac{\lambda_d}{\sqrt{\lambda_d^2 + 4\lambda_{pp}^2}} \\ \frac{2\lambda_{pp}}{\sqrt{\lambda_d^2 + 4\lambda_{pp}^2}} \\ 0 \end{pmatrix} \quad (\text{I.11a})$$

$$\lambda_2 = -\lambda_{He}, \quad V_2 = \frac{1}{\sqrt{\lambda_d^2 + 4(\lambda_{pp} - \lambda_{He})^2 + 16(\lambda_{He} - \lambda_d - \lambda_{pp})^2}} \begin{pmatrix} \lambda_d \\ 2(\lambda_{pp} - \lambda_{He}) \\ 4(\lambda_{He} - \lambda_d - \lambda_{pp}) \end{pmatrix} \quad (\text{I.11b})$$

$$\lambda_3 = -(\lambda_{pp} + \lambda_d), \quad V_3 = \frac{2}{\sqrt{5}} \begin{pmatrix} -1/2 \\ 1 \\ 0 \end{pmatrix} \quad \text{or if } \lambda_{He} = 0, \quad V_3 = \begin{pmatrix} -1/3 \\ 2/3 \\ 2/3 \end{pmatrix}. \quad (\text{I.11c})$$

The eigenvalue $\lambda_1 = 0$ corresponds to the fact that abundances in this ratio do not change in time. This is the equilibrium abundance. By putting these solution of V s and λ s into Eqn. (I.9) we get the exact solution of abundance of different isotopes (Clayton 1983).

In general, if we choose n number of isotopes in the network then corresponding matrix Λ will be of $n \times n$ dimension and vectors V will be of n dimensional column matrix. Following the same method described above, solving the rate equations, abundance of different isotopes can be found for any time.

1.6 Brief idea about Nucleosynthesis around Black Hole

Before going into the detail discussion of nucleosynthesis in accretion disk let us present a brief outline about accretion disk and nucleosynthesis in it. When matter falls through the accretion disk towards a black hole, nuclear reactions can occur. Naturally, due to these reactions, abundance of several species may change and nuclear energy may be released in a large scale.

What is an accretion disk? Usually when matter falls, it comes with some angular

momentum and falls towards a black hole in a spiral path. As a result, a matter distribution is formed around black hole which is called ‘Accretion Disk’. The rate of falling of the matter is called the ‘Accretion rate’ which depends mainly on viscosity, density and angular momentum of the in-falling matter. Since a black hole could not be seen, one can only be sure about the existence of a black hole by observing the different phenomena inside the accretion disk. Nuclear reactions i.e., the nucleosynthesis is one of such phenomena. The interaction within the in-falling matter, out of which the accretion disk around the black hole is formed, gives rise to various nuclear reactions. From the discussion of §1.4, we know in a star significant nuclear fusion takes place, mainly due to the presence of hydrogen (proton) as $3p(p, 2e^+)^4He$, $p(p, e^+)D$. Sometimes proton capture reactions such as, ${}^7Li(p, \alpha)^4He$ also take place. In all the cases total mass of the left hand side is greater than that of right hand side, so energy is released (exothermic reaction) by these reactions. In the case of a star, the temperature is low and pp -chain and CNO cycle are possible. For comparatively low temperature, the pp -chain is active but in the case of high temperature CNO cycle is more prominent in burning protons as we discussed in §1.4. Basically, through these processes hydrogen (proton) is converted into helium and huge amount of nuclear energy is released. The number of carbon, nitrogen and oxygen nuclei in the case of CNO cycle remain conserved. These behave as catalysts. Their presence just enhance the rate of the reactions i.e., the conversion rate to helium from proton i.e., the evolution of nuclear energy. Apart from the hydrogen burning, a few of the other reactions are also outlined in the last Section.

Unlike the stellar case, where the central temperature is of the order of $10^7 K$ and the density is around 10^{-1} gm/cc, in the case of black hole accretion disk the

temperature is high (of the order of $10^9 K$) and even though the density is low (of the order of 10^{-4} gm/cc for stellar mass black hole accretion disk and much lower for black holes located at the galactic centers) enough. Although the density of the disk is low compared to that of star but on their spiral path the matter is heated up. The temperature of the matter becomes so high that after the Big-Bang nucleosynthesis the most favourable temperature to allow significant nucleosynthesis is attained in disks. Also corresponding entropy of the infalling matter in the disk is very high as sometimes of the order $10^{16} - 10^{18}$ erg/K. All these motivate us to study the nucleosynthesis in the accretion disk. On their path, the matter may achieve favourable temperature for proton capture and rapid-proton capture (rp-process) reactions. Due to these reactions nuclear energy is released in the disk (exothermic reaction). Sometimes this nuclear energy may dominate over the energy released due to the viscous processes inside the disk. As matter falls, the potential energy is converted to the kinetic energy and then to thermal energy i.e.,

$$\text{Potential Energy} \rightarrow \text{Kinetic Energy} \rightarrow \text{Thermal Energy.}$$

Consequently, as matter comes close towards the black hole, the temperature increases. In this high temperature region helium, deuterium may start to burn through photo-dissociation process. At high accretion rates, a large number of photon is produced inside the matter, as a result of Compton cooling, the matter cools down due to transfer of energy from the hot matter to the cold photon. On the other hand, for low accretion rate, matter does not get sufficient photon to cool down by inverse Compton effect. So at low accretion rate near black hole, temperature is high and the photo-dissociation is more effective than the case of high accretion rate. With photo-dissociation, huge amount of energy is absorbed from the disk. Higher the

temperature of the disk, higher will be the absorption rate of energy. This process is continued till the photo-dissociation is complete.

In the case of some accretion disks, where viscosity arises mainly due to the magnetic coupling and the accretion rate is low; the neutrons, after being produced by the dissociation of deuterium nuclei, do not accrete rapidly. They are charge neutral and are not coupled by magnetic viscosity. But all the other elements (ion, proton etc.) will fall towards the black hole under the influence of magnetic viscosity. Here as the radius of the disk decreases neutron abundance in each radius increases and at a certain point abundance gets maximum value i.e., the peak attains, then again up to black hole horizon abundance decreases monotonically. Although the process was started with zero abundance of neutron, at the end, with steady condition, prevailing the neutron abundance could be as high as 10% at the peak. Thus a 'Neutron Torus' is formed in the disk. Neutrons of this torus interact with freshly accreted matter and enhance neutron rich isotopes.

2 Evolution of Accretion Disk Models

Before going into details of nucleosynthesis in accretion disk we would like to discuss the evolution of the disk models. We describe how the basic equations of the disk are improved with improved understanding of the accretion process. Here we choose the units of distance, time and velocity to be $2GM/c^2$, $2GM/c^3$ and c , respectively where, G is the gravitational constant, M is the mass of the central object and c is the velocity of light.

2.1 Bondi Flow

The process by which the matter is being captured by the gravitational object is called accretion. When matter with angular momentum falls into the central gravitating object a disk like structure called accretion disk is formed around the compact object as was explained in earlier Section. In 1952, Bondi (1952) studied the spherical accretion where matter falls without any angular momentum. This is known as Bondi Flow. Before we understand the spherical accretion solution onto a black hole it is easier to discuss the flow on a Newtonian star.

The steady-state radial momentum equation of motion of this infalling matter is given by

$$\vartheta \frac{d\vartheta}{dr} + \frac{1}{\rho} \frac{d\rho}{dr} + \frac{1}{r^2} = 0, \quad (\text{I.12})$$

where, ϑ is radial speed, ρ is the density, P is the isotropic pressure, r is the radial coordinate of the infalling matter.

The equation of continuity can be written as,

$$\frac{1}{r^2} \frac{d}{dr} (\rho \vartheta r^2) = 0. \quad (\text{I.13})$$

We are considering adiabatic flow with equation of state $P = K\rho^\gamma$, where γ is chosen constant called adiabatic index, K is measuring the entropy of the flow. Considering all these informations and integrating above energy momentum equation we get

$$E = \frac{1}{2}\vartheta^2 + na^2 - \frac{1}{r} = \text{Constant}, \quad n = \frac{1}{\gamma - 1} \quad (\text{I.14})$$

The mass flux is obtained as

$$\dot{M} = \rho\vartheta r^2 \quad (\text{I.15})$$

which is basically baryon number conservation equation.

Now using $\rho = \left(\frac{a^2}{\gamma K}\right)^n$, Eqn. (I.15) becomes

$$\dot{\mathcal{M}} = a^{2n}\vartheta r^2. \quad (\text{I.16})$$

Then $\dot{\mathcal{M}} = \dot{M}\gamma^n K^n$ is conserved in the flow. Chakrabarti (1990b) refers this quantity as the ‘accretion rate’ and later (Chakrabarti 1996a) ‘entropy accretion rate’. From Eqn. (I.14) and (I.15) we get (Chakrabarti 1990b)

$$\frac{d\vartheta}{dr} = \frac{\frac{1}{r^2} - \frac{2a^2}{r}}{\frac{a^2}{\vartheta} - \vartheta} = \frac{N}{D} \quad (\text{I.17})$$

From the sonic point condition we get $\vartheta_c = a_c$, $r_c = \frac{1}{2a_c^2}$.

Here, subscript c is referred as critical point. r_c is called sonic point since no disturbance created within this radius can cross this radius (also known as the sound horizon) and escape to a large distance. This is analogous to the event horizon of a black hole since no electromagnetic disturbance can escape outside that horizon.

The relativistic equations governing the flow around a black hole are very complicated. However, if one chooses the central black hole to be the Schwarzschild type (zero angular momentum) and uses Paczyński-Wiita pseudo-potential concept

(Paczynski & Wiita 1980) the form of basic radial momentum equation same as that of the Newtonian star, except that the gravitational potential term is replaced by $-\frac{1}{2(r-1)}$. If one chooses this potential in Newtonian equation, the geometry around a Schwarzschild black hole is mimicked. The results in exact black hole geometry and using this potential become similar with very minor difference.

The origin of the analytical form of the potential can be understood as follows: If we calculate the Keplerian angular momentum in Schwarzschild geometry we get (Shapiro & Teukolsky 1983)

$$\lambda_K^2 = \frac{r^3}{2(r-1)^2}. \quad (\text{I.18})$$

However, using the potential mentioned above, one can calculate the centrifugal force which balances gravity from:

$$\frac{\lambda_K^2(PW)}{r^3} = \frac{1}{2(r-1)^2}. \quad (\text{I.19})$$

Where (PW) indicates Keplerian angular momentum obtained using the potential above. We note that both the angular momentum distributions are identical.

Using this potential, the energy equation can be written for black hole accretion as

$$E = \frac{1}{2}\vartheta^2 + na^2 - \frac{1}{2(r-1)} = \text{Constant}. \quad (\text{I.20})$$

The mass flux equation is same as Eqn. (I.15). Now from Eqn. (I.20) and (I.15) we get

$$\frac{d\vartheta}{dr} = \frac{\frac{1}{2(r-1)^2} - \frac{2a^2}{r}}{\frac{a^2}{\vartheta} - \vartheta} = \frac{N}{D}. \quad (\text{I.21})$$

For the sonic point condition we get

$$\vartheta_c = a_c \text{ and } r_c = 1 + \frac{1}{8a_c^2} + \sqrt{\frac{1}{4a_c^2} + \frac{1}{64a_c^4}} \text{ (Chakrabarti 1990b).}$$

This r_c is the sonic location. If a_c is allowed to infinity, the sonic point stays at the horizon, namely at $r = 1$ as in the case of Schwarzschild geometry. Other properties are similar to the Bondi solution in Newtonian geometry.

2.2 Thin Accretion Disk

So far only spherical accretion flows have been discussed. In those cases the infall velocity is very high so the density is very low for a given accretion rate. When the flow has some angular momentum the inflow velocity becomes smaller and density is much higher. In this case the infall time becomes higher and viscosity has time to dissipate angular momentum and energy except very close to the black hole. As matter loses angular momentum, it sinks deeper into the potential well and radiates more efficiently. The actual efficiency depends on viscosity and cooling process inside the disk.

In the case of a binary system, when one of the components is compact, the companion is stripped of its matter due to the tidal effect. The matter with angular momentum falls towards the central body as the angular momentum is removed by viscosity. The flow encircling the compact object forms a quasi-spherical structure around it, preferably in the orbital plane. This quasi-stationary structure is commonly known as accretion disk. Although it contains very little matter compared to the binary components but it is the most important ingredient of an accreting binary system from the observational point of view.

In the case of active galaxies and quasars, matter may be supplied to the central black hole very intermittently and the angular momentum of the supplied matter is not necessarily Keplerian. This is because the matter may be originated from the wind

of star clusters. Also the loosing of the angular momentum may be the result of the collision with other winds. So the flow is expected to be of low angular momentum, quasi-spherical and mostly advective.

In the case of thin disk the half-thickness of the disk $h(r) \ll r$. The heat generated by the viscous stress is radiated in the vertical direction so that the disk becomes cool as $kT \ll GMm_p/r$ in contrary to the case of a spherical accretion where $kT \sim GMm_p/r$. This means the disks are non-adiabatic. Here M is the mass of the black hole and m_p is the mass of the proton, k is the Boltzmann constant. So the thin disk is non-adiabatic. The vertical velocity is negligible compared to the radial and azimuthal velocity. As the accretion rate is assumed to be much lower compared to the Eddington rate and pressure is neglected, specific angular momentum distribution is Keplerian. The surface density of the disk Σ at radius r can be written as,

$$\Sigma = \int_{-h(r)}^{h(r)} \rho dz, \quad (\text{I.22})$$

where, ρ is the density at the equatorial plane. Now, by replacing the integral of products by the products of averages (Matsumoto et al. 1984),

$$\Sigma = 2h(r)\rho. \quad (\text{I.23})$$

For the Keplerian disk, the stress tensor is

$$W_{r\phi} = \eta r \frac{d\Omega}{dr} = -\frac{3}{2}\eta\Omega \quad (\text{I.24})$$

where, Keplerian angular velocity $\Omega^2 = \frac{GM}{r^3}$ and η is the coefficient of dynamic viscosity.

Let f_ϕ is the viscous stress exerted in the ϕ direction by the fluid element at r on the neighbouring element at $r + dr$. This viscous stress is related to the stress tensor

as $f_\phi = -W_{r\phi}$ and

$$f_\phi = -W_{r\phi} = \frac{3}{2}\eta\Omega = \frac{3}{2}\eta \left(\frac{GM}{r^3}\right)^{1/2}. \quad (\text{I.25})$$

To get the steady-state disk solution we need to solve the four sets of equations given below simultaneously (Chakrabarti 1996b). Also the law of viscosity must be specified which should transport angular momentum outwards allowing to fall the matter in.

The governing equations for a steady flow are:

(a) Rest mass conservation:

As the flow approaches compact object it is compressed and the density is increased. We assume baryons are conserved; then integrating the continuity equation we get

$$\dot{M} = 2\pi r \Sigma \vartheta = \text{Constant}. \quad (\text{I.26})$$

(b) Angular momentum conservation:

Because angular momentum distribution is Keplerian, infalling of the matter inside indicates the transportation of angular momentum outwards. This requires significant viscosity in the disk. The torque applied by the viscous stress is given by

$$\mathcal{G} = f_\phi(2\pi r \cdot 2h(r))r = \dot{M}(GM)^{1/2}(r^{1/2} - r_0^{1/2}) \quad (\text{I.27})$$

where, r_0 is the inner edge of the disk which is assumed at the marginally stable orbit.

(c) Equation governing the energy conservation:

The viscous heat generated as

$$Q^+ \sim \frac{W_{r\phi}^2}{\eta} = -\frac{f_\phi W_{r\phi}}{\eta}. \quad (\text{I.28a})$$

The flux is obtained as

$$F(r) = h(r)Q^+ = \frac{3\dot{M}GM}{4\pi r^3} \left(1 - \left(\frac{r_0}{r}\right)^{1/2}\right). \quad (\text{I.28b})$$

The luminosity of the disk is

$$L = \int_{r_0}^{\infty} 2F \cdot 2\pi r dr = \frac{1}{2} \frac{GM\dot{M}}{r_0}. \quad (\text{I.28c})$$

So the luminosity is exactly half the potential energy of the matter at the inner edge of the disk. This is because of the Keplerian distribution of the matter.

If there is no loss of energy, the rotational velocity can be obtained at the inner edge of the disk as

$$\frac{1}{2} v_{\phi K}^2 = \frac{GM}{2r} \quad (\text{I.28d})$$

because of the choice of angular momentum distribution. So half of the energy must come out of the disk whatever be the physical viscosity.

(d) Vertical momentum balance:

As mentioned earlier the component of vertical velocity is negligible compared to other components (radial and azimuthal). The vertical momentum balance equation in this case becomes:

$$\frac{1}{\rho} \frac{dP}{dz} = -\frac{GM}{r^2} \frac{z}{r}. \quad (\text{I.29a})$$

Letting, $\Delta P \sim P$ and $\Delta z \sim h(r)$, we get $h(r) \sim \frac{a_s}{\Omega}$. Thus,

$$\frac{h(r)}{r} \sim \frac{a_s}{v_{\phi}}, \quad (\text{I.29b})$$

where a_s is adiabatic sound speed. Since we choose $h(r) \ll r$ (thin disk condition), the azimuthal flow is supersonic. In the case of viscous flow the viscous stress can be written as

$$f_{\phi} = -W_{r\phi} \sim P = \text{total pressure on the matter.}$$

So in general $f_{\phi} = \alpha P$ with $\alpha < 1$. This is the α disk prescription of Shakura & Sunyaev (1973).

The standard accretion disk model is useful to explain the observations in binary systems and active galaxies (Pringle 1981; Shapiro & Teukolsky 1983; Frank et al. 1992). As in this model the advective term is not accounted correctly the disk is terminated at the marginally stable orbit and the inner boundary condition is not made to satisfy correctly.

2.3 Thick Accretion Disk

Here, the accretion rate is considered high ($\dot{M} \gg \dot{M}_{Edd}$). The pressure is incorporated to find the dynamical structure of the disk and determination of the thermodynamical quantities inside the disk. The presence of radiation pressure makes the disk geometrically thick ($h(r) \sim r$). After incorporating the radiation pressure term the radial Euler's equation becomes,

$$\vartheta \frac{d\vartheta}{dr} + \frac{1}{\rho} \frac{dP}{dr} - \frac{\lambda^2}{r^3} + F(r) = 0 \quad (\text{I.30})$$

where, $F(r)$ is the gravitational force and λ is the specific angular momentum. Ignoring the advective term $\vartheta \frac{d\vartheta}{dr}$ we get (Chakrabarti 1996b)

$$\lambda \propto \left(r^3 F(r) + \frac{r^3}{\rho} \frac{dP}{dr} \right). \quad (\text{I.31})$$

Here, the angular momentum is higher (lower) than that of Keplerian distribution if pressure gradient term is positive (negative). The term is significant when $\frac{GM}{r} \sim \frac{P}{\rho} \sim a^2$, where a is sound speed. Maraschi et al. (1976) first studied quantitatively the effect of radiation pressure on angular momentum distribution. Paczyński and his collaborators (Paczyński & Bisnovatyi-Kogan 1981; Paczyński & Muchotrzeb 1982) included the advection and pressure effects in the transonic accretion disks but they did not perform any systematic study. Global solutions for thick accretion disk were

only possible when advection term was dropped. Some full general relativistic exact solution for thick accretion disk are done by Chakrabarti (1985).

In the case of thick accretion disk, the force acting on blob of matter inside it are described as: the gravitational force acts radially inwards and the centrifugal force acts in a direction normal to the angular momentum vector outwards. The net force is acted along the effective gravity. To maintain hydrostatic equilibrium a force of equal magnitude due to the pressure gradient must act opposite to this direction.

2.4 Modern Accretion Disk

Observation of Cyg X-1 in the early seventies appears to indicate that it emits X-rays in two states (Agrawal 1972; Tananbaum 1972). Inner optically thin region is thought to emit hard X-rays and the outer optically thick flow is thought to emit soft X-rays (Thorne & Price 1975). Ichimaru (1977) showed that the advection is important close to the black hole and obtained a new optically thin solution which includes heating, cooling and advection. Ichimaru found that depending on outer boundary the solution can go over to the optically thick and thin branch. However, there was no global solution. In case of inviscid adiabatic flow an example of global solution was provided (Fukue 1987) where study of shocks similar to that in solar winds and galactic jets was made.

In the so called 'Slim-Disk' model (Abramowicz 1988) using local solutions instabilities near the inner edge of the disk are removed with the addition of advective term. This was done in optically thick limit. Chakrabarti (1990a,b) first obtained satisfactory global solution of the governing equation in the optically thick or thin limit including advection, viscosity, heating and cooling in the limit of isothermality

condition. Here single temperature disk models of which are Keplerian far away were considered.

The accretion onto central black holes in binary systems and in active galaxies and quasars the angular momentum of the flow need not be Keplerian everywhere. In the binary system, matter could be accreted both through the winds as sub-Keplerian flow and through the Keplerian flow. In the case of low mass X-ray binary (LMXB) systems where the winds may absent, the sub-Keplerian matter could still be produced from Keplerian flow close to the black hole. In an active galaxy, the same situation may prevail although in these cases matter is accreted solely from the winds of the stars, very far away which has very little angular momentum. The sub-Keplerian flow whether it originates from Keplerian disk or not will have significant velocity, since the centrifugal pressure is not sufficient to overcome gravity. The sub-Keplerian flow first accretes quasi-spherically with infall time-scale similar to the free-fall time-scale as $t_{infall} \sim r/v_{ff} \sim r^{3/2}$ until the specific angular momentum of the flow becomes comparable to the local Keplerian angular momentum i.e., $\lambda^2(r) \sim \lambda_K^2(r)$. At this point, $r \sim \lambda^2(r)$, the flow may be virtually stopped by the centrifugal barrier and a standing shock may form. After that flow continues, it attains supersonic speed and falls into the black hole.

Now we will study the transonic flows in a realistic astrophysical system. We choose the equation of motion in equatorial plane of the central object but the flow is in hydrostatic equilibrium in the transverse direction. We assume a thin, rotating, adiabatic accretion or wind flow near a compact object. The matter flows through the disk in a spiral path. Since matter is assumed to move in equatorial plane in vertical equilibrium, the position coordinate is expressed in terms of single cartesian-

like coordinate x in place of r to describe the motion of the incoming flow. The basic equations of the flows as follows (Chakrabarti 1989):

(a) The energy conservation equation can be written as

$$E = \frac{\vartheta^2}{2} + na^2 + \frac{\lambda^2}{2x^2} - \frac{1}{2(x-1)}. \quad (\text{I.32})$$

As previous, we use the Paczyński-Wiita pseudo-potential concept.

(b) The mass flux conservation equation (apart from the geometric factor) is given by

$$\dot{M} = \vartheta \rho x h(x). \quad (\text{I.33})$$

$h(x)$ is half thickness of the disk defined as $h(x) = ax^{1/2}(x-1)$ exactly same as defined earlier but here we use coordinate x in place of r .

As usual we write the mass conservation equation in terms of ϑ , x and a as

$$\dot{M} = \vartheta a^q x^{3/2}(x-1), \quad q = 2n + 1. \quad (\text{I.34})$$

This $\dot{M}(\propto \dot{M}K^n)$ is called entropy accretion rate which may not be constant at the shock location due to generation of entropy.

As in a Bondi flow, doing sonic point analysis, we get

$$\vartheta_c^2 = \nu a_c^2, \quad \text{where } \nu = \frac{2}{\gamma + 1} \quad \text{and} \quad a_c^2 = \frac{2(x_c - 1)(\lambda_K^2 - \lambda^2)}{\nu x_c^2(5x_c - 3)}. \quad (\text{I.35})$$

The energy of the flow E with angular momentum λ passing through critical point x_c is given by,

$$E = \frac{\lambda^2}{2x_c^2} \left[1 - \frac{(4n+4)(x_c-1)}{(5x_c-3)} \right] + \frac{(n+1)x_c}{(x_c-1)(5x_c-3)} - \frac{1}{2(x_c-1)}. \quad (\text{I.36})$$

So we can conclude that there can be more than one critical points for particular energy and angular momentum.

From Eqn. (I.35) as a_c^2 is always greater than zero, the angular momentum at the critical point must be less than the Keplerian value. Although we started with three conserved quantities namely E , $\dot{\mathcal{M}}$ and λ , not all of them can be specified independently if the flow is transonic. This is because as we have three unknowns $\vartheta(x)$, $a(x)$ and x_c we need three equations to solve them uniquely. Together with the two transonic conditions as Eqn. (I.35) we need only one quantity: either energy or accretion rate. Thus as in the case of Bondi flow, $\dot{\mathcal{M}} = \dot{\mathcal{M}}(E, \lambda)$. In other words, the parameters for a stationary transonic solution lie on a hypersurface (Chakrabarti 1990b):

$$\mathcal{F}(E, \dot{\mathcal{M}}, \lambda) = 0. \quad (\text{I.37})$$

It can be concluded that, if a compact object is brought in the middle of a cloud of certain specific energy, then a stationary transonic solution joining infinity to the compact object selects the amount of matter which is going to accrete. Thus the accretion rate is the eigenvalue of the problem. If matter, other than eigenvalue, is pushed towards the compact object using external force, then the resulting flow will be non-stationary till it reaches another equilibrium configuration if it exists corresponding to the new force field.

2.4.1 Shock Formation and Corresponding Conditions

At the shock (Chakrabarti 1989), the flow jumps from supersonic to subsonic branch. In the case of black hole accretion this is possible if flow passes through two critical points one on each side of shock location x_s . A shock is characterised by four quantities: shock location x_s , possible jumps in two independent velocities ϑ , a and entropy

K i.e.,

$$x = x_s \quad (\text{I.38a})$$

$$\Delta a = a_+(x_s) - a_-(x_s) \quad (\text{I.38b})$$

$$\Delta \vartheta = \vartheta_+(x_s) - \vartheta_-(x_s) \quad (\text{I.38c})$$

$$\Delta K = K_+ - K_- \quad (\text{I.38d})$$

The subscript “ $-$ ” and “ $+$ ” denote quantities before and after the shock respectively. At the shock the conserved quantities are (Chakrabarti 1989, 1990b),

$$\dot{M}_+ = \dot{M}_- \quad (\text{I.39a})$$

$$\bar{P}_+ + \bar{\rho}_+ \vartheta_+^2 = \bar{P}_- + \bar{\rho}_- \vartheta_-^2. \quad (\text{I.39b})$$

Eqn. (I.39a-b) provides two constraints on these four quantities (Eqn. (I.38a-d)). \bar{P} and $\bar{\rho}$ denote averaged pressure and density respectively.

We can think of three distinct types of shock corresponding to three extreme physical situations: Rankine-Hugoniot shock ($E_+ = E_-$), isentropic compression waves ($\dot{M}_+ = \dot{M}_-$) and isothermal shock ($a_+ = a_-$) (Chakrabarti 1990b).

In case of Rankine-Hugoniot shock energy is not radiated through the surface of the flow i.e., radiative cooling mechanism is extremely inefficient. The postshock temperature is higher. For this type of shock, $E_+ = E_-$, $T_+ > T_-$ and $s_+ > s_-$ ($\dot{M}_+ > \dot{M}_-$), where s is the entropy of the flow.

In case of isentropic compression waves, entropy does not change in the flow but some energy is lost at the discontinuity. The amount of entropy generated at the shock is comparable to the entropy radiated away. For this type of shock, $s_+ = s_-$, $E_+ < E_-$ and $T_+ > T_-$.

In the case of isothermal shock radiative cooling is very efficient. Some energy and entropy are lost from the surface of the flow at the shock location to keep the postshock temperature equal to its preshock value. For this type of shock, $T_+ = T_-$, $E_+ < E_-$ and $s_+ < s_-$.

2.4.2 Outflows from the Accretion Disk

It is believed that from the center of active galaxies cosmic radio jets are originated. Even in so called ‘micro-quasars’ such as GRS 1915+105 which are believed to have stellar mass black holes (Mirabel & Rodriguez 1994) the outflows are common. Also collimated outflows in SS433 are well known now (Margon 1984). Here, our approach to discuss the mass outflow rate is same as Chakrabarti (1999) and Das & Chakrabarti (1999). Close to the black hole, where infall time-scale $x/v(x)$ is short compared to the viscous time-scale (unless $\alpha \geq 1$) in the region of last few to couple of ten Schwarzschild radius angular momentum remains roughly constant. Constant angular momentum flow introduces large centrifugal force which forms a dense region around a black hole. This centrifugal pressure supported boundary layer of the black hole is called CENBOL. As black hole does not has any hard surface, it is the effective surface layer of the black hole. Chakrabarti (1999) suggested one simple method to compute the outflow rate assuming that the inflow and outflow are both conical. We are assuming for the sake of argument that our system is made up of the infalling gas, the dense boundary layer of the compact object and the outflowing wind. The sub-Keplerian hot and dense quasi-spherical region forms either due to centrifugal barrier or due to pair plasma pressure or due to pre-heating effects. The incoming matter compressed and heated above (the heating is due to the geometric compression at the CENBOL) comes out from the disk at the CENBOL. If the flow is compressed and

heated at the centrifugal barrier around a black hole it would also radiate enough to keep the flow isothermal. Thus following Chakrabarti (1999) we can give a simple expression for ratio of mass outflow rate and mass inflow rate assuming the flow is extremely collimated. If R is the compression ratio, Θ_{in} is the solid angle subtended by the inflow and Θ_{out} is the solid angle subtended by the outflowing cone one obtains mass outflow rate as

$$R_{\dot{m}} = \frac{\dot{M}_{out}}{\dot{M}_{in}} = \frac{\Theta_{in}}{\Theta_{out}} \frac{R}{4} \left[\frac{R^2}{R-1} \right]^{3/2} \exp \left[\frac{3}{2} - \frac{R^2}{R-1} \right], \quad (I.40)$$

apart from the geometric factor. The expression is independent of location of the sonic point and the size of the shock. This is because Newtonian potential is used throughout the calculation. As we choose only low luminosity then outflow rate is independent of accretion rate. For high luminous flow, Comptonization will cool down the dense region and corresponding mass loss will be negligible. When fully general relativistic calculations are made these dependency will appear explicitly. Exact and detailed computations using both the transonic inflow and outflow are in Das (1998) and Das & Chakrabarti (1999), they computed self-consistently the compression ratio R .

2.5 Basic Properties of the Advective Disk and Motivation of Nucleosynthesis Work

Angular momentum in accretion disks around black holes must deviate from a Keplerian distribution, since the presence of ion, radiation or inertial pressure gradient forces become as significant as the gravitational and centrifugal forces (Chakrabarti 1996a,b; and references therein). The inertial pressure close to a black hole is high, because, on the horizon, the inflow velocity must be equal to the velocity of light.

For causality, the velocity of sound must be less than the velocity of light. In fact, in the extreme equation of state of $P = \frac{c^2}{3}\rho$ (where c is the velocity of light and P and ρ are the isotropic pressure and mass density respectively), the sound speed is only $c/\sqrt{3}$. Thus, the flow must pass through a sonic point and becomes supersonic before entering into the horizon. A flow which must pass through a sonic point must also be sub-Keplerian (Chakrabarti 1996b and references therein), and this causes the deviation. If the accretion rate is low, the flow cools down only by inefficient bremsstrahlung and Comptonization processes, unless the magnetic field is very high (Shvartsman 1971; Rees 1984; Bisnovatyi-Kogan 1998). This hot flow can undergo significant nucleosynthesis depending on the inflow parameters. Earlier, in the context of thick accretion disks calculations of changes in composition inside an accretion disk were carried out (Chakrabarti et al. 1987; Hogan & Applegate 1987; Arai & Hashimoto 1992; Hashimoto et al. 1993), but the disk models used were not completely self-consistent, in that neither the radial motion, nor the cooling and heating processes were included fully self-consistently. Secondly, only high accretion rates were used. As a result, the viscosity parameter required for a significant nuclear burning was extremely low ($\alpha_{vis} < 10^{-4}$). Here, we do the computation after including the radial velocity in the disk and the heating and cooling processes. We largely follow the solutions of Chakrabarti (1996a) to obtain the thermodynamic conditions along a flow. The results presented here are reported in Mukhopadhyay (1998), Chakrabarti & Mukhopadhyay (1999), Mukhopadhyay (1999) and Mukhopadhyay & Chakrabarti (2000).

Close to a black hole horizon, the viscous time-scale is so large compared to the infall time-scale that the specific angular momentum λ of matter remains almost con-

stant and sub-Keplerian independent of viscosity (Chakrabarti 1996a,b; Chakrabarti 1989). Because of this, as matter accretes, the centrifugal force λ^2/x^3 increases much faster compared to the gravitational force GM/x^2 (where G and M are the gravitational constant and the mass of the black hole respectively, λ and x are the dimensionless angular momentum and the radial distance from the black hole). As a result, close to the black hole (at $x \sim \lambda^2/GM$) matter may even virtually stop to form standing shocks (Chakrabarti 1989). Whether Shock is formed or not, as the flow slows down, the kinetic energy of matter is converted into thermal energy in the region where the centrifugal force dominates. Hard X-rays and γ -rays are expected from here (Chakrabarti & Titarchuk 1995). In this centrifugal pressure supported hot ‘boundary layer’ (CENBOL) of the black hole (Chakrabarti et al. 1996) we find that for low accretion rates, ${}^4\text{He}$ of the infalling matter is completely photo-dissociated and no ${}^7\text{Li}$ could be produced. In this region, about ten to twelve percent of matter is found to be made up of pure neutron for the low accretion hot cases. These neutrons should not accrete very fast because of very low magnetic viscosity associated with neutral particles (Rees et al. 1982) while protons are dragged towards the central black hole along with the field lines. Of course, both the neutrons and protons would have ‘normal’ ionic viscosity, and some slow accretion of protons (including those produced after neutron decay) would still be possible. If the ionic viscosity is less compared to magnetic viscosity neutron disk and torus may form. In contrast to neutron stars, the *neutron disks* which we find are not dense. Nevertheless, they can participate in the formation of neutron rich isotopes and some amount of deuterium. They can be eventually dispersed into the galaxy through jets and outflows, which come out from CENBOL (Chakrabarti 1999; Das & Chakrabarti 1999), thereby

possibly of influencing the metallicity of the galaxy.

On the equatorial plane, where the viscosity is the highest, a Keplerian disk deviates to become sub-Keplerian *very close* to the black hole (Chakrabarti & Titarchuk 1995; Wiita 1982). Away from the equatorial plane, viscosity is lower and the flow deviates from a Keplerian disk farther out. This is because the angular momentum transport is achieved by viscous stresses. Weaker the viscosity, longer is the distance through which angular momentum goes to match with a Keplerian disk. When the viscosity of the disk is decreased on the whole, the Keplerian disk recedes from the black hole forming quiescence states when the objects become very faint in X-rays (Ebisawa et al. 1996). Soft photons from the Keplerian disk are intercepted by this sub-Keplerian boundary layer (CENBOL) and photons are energized through the Compton scattering process. For higher Keplerian rates, electrons and protons cool down completely and the black hole is in a *soft state* (Tanaka & Lewin 1995). Here, bulk motion Comptonization produces the power-law tail of slope $\alpha \sim 1.5$ (Chakrabarti & Titarchuk 1995; Titarchuk et al. 1997). For lower Keplerian rates, the Compton cooling is incomplete and the temperature of the boundary layer remains close to the virial value,

$$T_p \sim \frac{1}{2k} m_p c^2 \frac{x_g}{x} = 5.2 \times 10^{11} \left(\frac{10}{x/x_g} \right) \text{ K.} \quad (\text{I.41})$$

In this case, bremsstrahlung is also important and the black hole is said to be in a *hard state* with energy spectral index α ($F_\nu \sim \nu^{-\alpha}$, where ν is the frequency of the photon) close to 0.5. In Eqn. (I.41), m_p is the mass of the proton, $x_g = 2GM/c^2$ is the Schwarzschild radius of the black hole. In this low Keplerian rate, electrons are cooler typically by a factor of $(m_p/m_e)^{1/2}$ unless the magnetic field is very high.

Present high energy observations seem to support the apparently intriguing as-

pects of black hole accretion mentioned above. For instance, the constancy of (separate) spectral slopes in soft and hard states has been observed by many people (Ebisawa et al. 1994; Miyamoto et al. 1991; Ramos et al. 1997; Grove et al. 1998; Vargas et al. 1997). ASCA observations of Cygnus X-1 seem to indicate that the inner edge of the Keplerian component is located at around $15x_g$ (instead of $3x_g$) (Gilfanov et al. 1997). HST FOS observations of the black hole candidate A0620-00 in quiescent state seem to have very faint Keplerian features (McClintock et al. 1995) indicating the Keplerian component to be farther out at low accretion rates. Bulk motion Comptonization close to the horizon has been considered to be a possible cause of the power-law tail in very soft states (Crary et al. 1996; Ling et al. 1997; Cui et al. 1997). However, some alternative modes may not be ruled out to explain some of these features.

This observed and predicted dichotomy of states of black hole spectra motivated us to investigate the nuclear reactions thoroughly for both the states. We use 255 nuclear elements in the thermo-nuclear network starting from neutron, proton, deuterium etc. till ^{72}Ge and the nuclear reaction rates valid for high temperatures. We assume that accretion on the galactic black hole is taking place from a disk where matter is supplied from a normal main sequence star. That is, we choose the abundance of the injected matter to be that of the sun. In reality initial abundance may be chosen from some older stars or G/K type stars. Of course, when the disk temperature is very high, the result is nearly independent of the initial composition.

Following Chakrabarti (1997) and Chakrabarti (1998c), in Fig. I.1 we show one cartoon picture of accretion and winds in the advective region around a compact object. The region is intercepted by photons.

Centrifugally and Thermally driven outflows

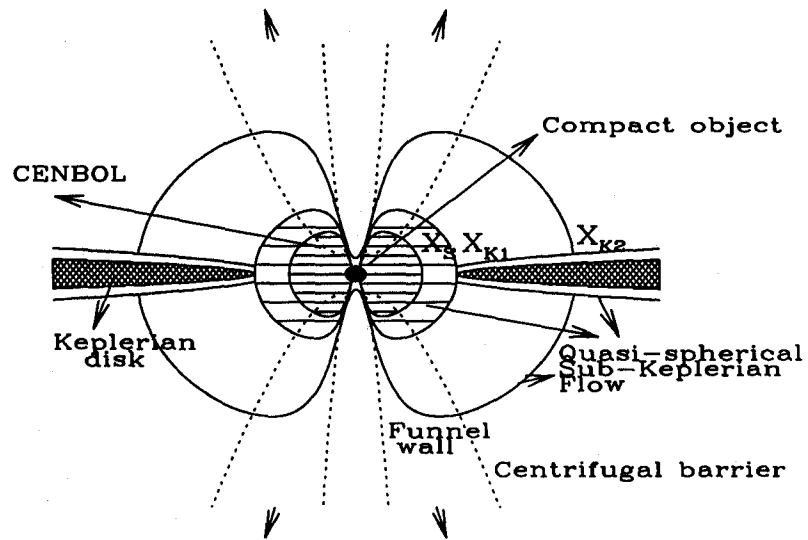


Fig. I.1. Cartoon diagram of accretion flows, winds in Quasi-spherical sub-Keplerian flow around compact object. The centrifugal pressure supported boundary layer CENBOL and funnel wall for outflows are shown in the picture.

As the hot matter approaches a black hole, photons originated by the bremsstrahlung process, as well as those intercepted from the Keplerian disk, start to photo-dissociate deuterium and helium in the advective region if they achieve their required temperature. There also proton-capture reactions take place. If the initial temperature, when matter deviates from Keplerian to sub-Keplerian region is comparatively low then dissociation does not take place initially, only proton-capture reactions start. As matter approaches towards the black hole its temperature increases and attends the favourable temperature to start the dissociation reactions. Mainly dissociation of three elements take place. First deuterium starts to burn then with the increase of temperature dissociation of ${}^3\text{He}$ starts. At much higher temperature ${}^4\text{He}$ comes into the game and starts to burn. There are two challenging issues at this stage which we address first: (a) Thermodynamic quantities such as density and temperature inside a disk are computed using a *thin disk* approximation, i.e., the vertical height $h(x)$ at a radial distance x very small compared to x ($h(x) \ll x$), and assuming the flow to be instantaneously in vertical equilibrium. However, at a low rate, it is easy to show that the disk is optically thin in the vertical direction $\int_0^{h(x)} \rho \sigma dh < 1$ (σ is the Thomson scattering cross-section). However, soft photons from the Keplerian disk enter radially and $\int_1^{x_s} \rho \sigma dx > 1$, generally. In fact, this latter possibility changes the soft photons of a few KeV from a Keplerian disk to energies up to $\sim 1\text{MeV}$ by repeated Compton scattering (Sunyaev & Titarchuk 1980; Chakrabarti & Titarchuk 1995) while keeping the photon number constant. The spectrum of the resultant photons emitted to distant observers becomes a power law $F_\nu \sim \nu^{-\alpha}$ instead of a blackbody, where $\alpha \sim 0.5$ for hard state and $\alpha \sim 1.5$ for soft states of a black hole. (b) Now that the spectrum is not a blackbody, strictly speaking, the computation of

photo-disintegration rate that is standard in the literature (which utilizes a Planckian spectrum) cannot be followed. Fortunately, this may not pose a major problem. As we shall show in §3.3, the standard photo-disintegration rate yields a lower limit of the actual rate that takes place in the presence of power-law photon spectra. Thus, usage of the correct rate obtainable from a power-law spectrum would, if anything, strengthen our assertion about the photo-disintegration around a black hole. After photo-disintegration by these hard photons, all that are left are protons and neutrons. The exact location where the dissociation actually starts may depend on the detailed photon spectrum, i.e., optical depth of this boundary layer and the electron temperature (Mukhopadhyay 1998; Mukhopadhyay 1999; Chakrabarti & Mukhopadhyay 1999; Mukhopadhyay & Chakrabarti 2000).

2.6 Basic Equations of the Problem

We use well understood model of the accretion flow close to the black hole in sub-Keplerian region of the disk. To treat with more generalized flow we consider viscous flow with angular momentum which may be varied with location. The energy is dissipated in the disk due to presence of viscosity and nuclear burning. We solve the following equations (Chakrabarti 1996a,b) to obtain the thermodynamic quantities:

(a) The radial momentum equation:

$$v \frac{dv}{dx} + \frac{1}{\rho} \frac{dP}{dx} + \frac{\lambda_{Kep}^2 - \lambda^2}{x^3} = 0. \quad (\text{I.42a})$$

This is nothing but Euler's equation. First term is advective term which actually gives the information of kinetic energy of the infalling matter. Second term is arised due to pressure acting on the volume element by the matter itself. Last one is the

combination of gravitational and centrifugal force terms.

(b) The continuity equation:

$$\frac{d}{dx}(\Sigma x \vartheta) = 0, \quad (\text{I.42b})$$

here, $\Sigma = h(x)\rho$ is the vertically integrated density. It is assumed that the flow parameters are unchanged in the vertical direction.

(c) The azimuthal momentum equation:

$$\vartheta \frac{d\lambda(x)}{dx} - \frac{1}{\Sigma x} \frac{d}{dx}(x^2 W_{x\phi}) = 0, \quad (\text{I.42c})$$

$W_{x\phi}$ is the azimuthal pressure which is basically viscous stress in this case.

(d) The entropy equation:

$$\begin{aligned} \Sigma v T \frac{ds}{dx} &= \frac{h(x)\vartheta}{\Gamma_3 - 1} \left(\frac{dp}{dx} - \Gamma_1 \frac{p}{\rho} \right) = Q_{mag}^+ + Q_{nuc}^+ + Q_{vis}^+ - Q^- \\ &= Q^+ - g(x, \dot{m})Q^+ = f(\alpha, x, \dot{m})Q^+. \end{aligned} \quad (\text{I.42d})$$

Since the fluid is considered as viscous, energy is being dissipated in the flow. Here, Q^+ and Q^- are the viscous heat gained and lost by the flow where for simplicity Q^- is chosen proportional to Q^+ with proportionality constant $g(\alpha, x, \dot{m}) = 1 - f(\alpha, x, \dot{m})$, where $f(\alpha, x, \dot{m})$ is the cooling factor and \dot{m} is the mass accretion rate in unit of the Eddington rate. Here, we have included the possibility of magnetic heating Q_{mag}^+ (due to stochastic fields; Shvartsman 1971; Shapiro 1973; Bisnovatyi-Kogan 1998) and nuclear energy release Q_{nuc}^+ as well (Taam & Fryxell 1985) while the cooling is provided by bremsstrahlung, Comptonization, endothermic nuclear reactions and neutrino emissions. A strong magnetic heating might equalize ion and electron temperatures (Bisnovatyi-Kogan 1998) but this would not affect our conclusions. On the

right hand side, we wrote Q^+ collectively proportional to the cooling term for simplicity (purely on dimensional grounds). We use the standard definitions of Γ (Cox & Giuli 1968),

$$\Gamma_3 = 1 + \frac{\Gamma_1 - \beta}{4 - 3\beta}, \quad (\text{I.43a})$$

$$\Gamma_1 = \beta + \frac{(4 - 3\beta)^2(\gamma - 1)}{\beta + 12(\gamma - 1)(1 - \beta)} \quad (\text{I.43b})$$

and $\beta(x)$ is the ratio of gas pressure to total pressure as,

$$\beta(x) = \frac{\rho k T / \mu m_p}{\rho k T / \mu m_p + \bar{a} T^4 / 3 + B(x)^2 / 4\pi}. \quad (\text{I.44})$$

Here, \bar{a} is the Stefan constant, k is the Boltzmann constant, m_p is the mass of the proton, μ is the mean molecular weight. Using the above definitions, Eqn. (I.42d) becomes,

$$\frac{4 - 3\beta}{\Gamma_1 - \beta} \left[\frac{1}{T} \frac{dT}{dx} - \frac{1}{\beta} \frac{d\beta}{dx} - \frac{\Gamma_3 - 1}{\rho} \frac{d\rho}{dx} \right] = f(\alpha, x, \dot{m}) \frac{Q^+}{\vartheta P h(x)} = \frac{f \alpha x}{v} \frac{d\Omega}{dx}. \quad (\text{I.42e})$$

Here, we shall concentrate on solutions with constant β . We will keep β constant throughout the particular cases. Actually, we study in detail only the special cases, $\beta \sim 0$ and $\beta \sim 1$, so we shall liberally use $\Gamma_1 = \frac{4}{3} = \Gamma_3$ and $\Gamma_1 = \gamma = \Gamma_3$ respectively. The condition $\beta \sim 0$ implies the radiation dominated flow i.e., relativistic flows of matter. We note here that unlike *self-gravitating* stars where $\beta = 0$ causes instability, here this is not a problem. Although close to the black hole flows must be relativistic whatever be its initial velocity (i.e., β must be $\frac{4}{3}$) and very far away from the black hole flows need not be relativistic (so β need not be $\frac{4}{3}$) but here we have considered β constant throughout the particular cases. Similarly, we shall consider the cases for $f(\alpha, x, \dot{m}) = \text{constant}$, though as is clear, $f \sim 0$ in the Keplerian disk region and probably much greater than 0 near the black hole depending on the efficiency

of cooling (governed by \dot{m} , for instance). We use the Paczyński-Wiita potential (Paczyński & Wiita 1980) to describe the black hole geometry. $W_{x\phi}$ is the vertically integrated viscous stress as mentioned above, $h(x) \sim ax^{1/2}(x-1)$ is the half-thickness of the disk at radial distance x (both measured in unit of $2GM/c^2$) obtained from vertical equilibrium assumption (Chakrabarti 1989), where a is the sound speed ($a^2 = \gamma P/\rho$), $\lambda(x)$ is the specific angular momentum, ϑ is the radial velocity, s is the entropy density of the flow. The constant α above is the Shakura-Sunyaev (1973) viscosity parameter used to express stress tensor in terms of the total pressure Π due to radial motion ($\Pi = W + \Sigma\vartheta^2$, where W and Σ are the integrated pressure and density respectively (Chakrabarti & Molteni 1995) in the viscous flows. With this choice, $W_{x\phi}$ keeps the specific angular momentum continuous across of the shock. Here we will use MIXed Shear Stress (MISStress) prescription (Chakrabarti 1996a,b). The stress tensor can be written in two ways. On the one hand it can be defined as $W_{x\phi}(1) = -\alpha\Pi$. On the other hand, it can be defined as $W_{x\phi}(2) = \eta x \frac{d\Omega}{dx}$. Again the expression of heat generation is defined as $Q^+ = W_{x\phi}^2/\eta$. In this expression if we use only $W_{x\phi}(1)$, no information of actual shear is introduced. If only $W_{x\phi}(2)$ is used, the equations become difficult to solve. So we use in heating expression, the combination of both $W_{x\phi}(1)$ and $W_{x\phi}(2)$. So the viscous heat generation can be written as

$$Q^+ = \frac{\alpha(W + \Sigma v^2)\lambda}{x^{3/2}(x-1)}. \quad (\text{I.45})$$

From the continuity equation (Eqn. (I.42b)), we find the mass accretion rate to be given by

$$\dot{M} = 2\pi\rho h(x)\vartheta x, \quad (\text{I.46})$$

here, 2π is the geometric factor.

From the azimuthal momentum Eqn. (I.42c),

$$\lambda - \lambda_{in} = \alpha \frac{x}{\vartheta} a^2 \left(\frac{2}{3\gamma - 1} + M^2 \right), \quad (\text{I.47})$$

where, $M = \vartheta/a$ is the Mach number of the flow and λ_{in} is the specific angular momentum at the inner edge of the flow, i.e., at the horizon.

For a complete run, we supply the basic parameters, namely, the location of the sonic point through which the flow must pass just outside the horizon x_{in} , the specific angular momentum at the inner edge of the flow λ_{in} , the polytropic index γ , the ratio f of advected heat flux $Q^+ - Q^-$ to heat generation rate Q^+ , the viscosity parameter α and the accretion rate \dot{m} . The derived quantities are: x_K where the Keplerian flow deviates to become sub-Keplerian, the ion temperature T_p , the flow density ρ , the radial velocity v and the azimuthal momentum λ of the entire flow from x_K to the horizon. Temperature of the ions obtained from above equations is further corrected using a cooling factor F_{Comp} obtained from the results of radiative transfer of Chakrabarti & Titarchuk (1995). Electrons cool due to Comptonization, but they cause the ion cooling also since ions and electrons are coupled by Coulomb interaction. F_{Comp} , chosen here to be constant in the advective region, is the ratio of the ion temperature computed from radiation-hydrodynamic (Chakrabarti & Titarchuk 1995) and hydrodynamic (Chakrabarti 1996a) considerations. In this way at each radius we can have the information of disk parameters.

3 Nucleosynthesis in Accretion Flows

Here, we mainly study nucleosynthesis in disks where the photo-dissociation may or may not be complete and other reactions may be important, and show that depending on the accretion parameters, abundances of new isotopes may become abnormal around a black hole in accretion flows. Thus, observation of these isotopes may give a possible indication of black holes at the galactic center or in a binary system.

Earlier, Chakrabarti (1986) and Chakrabarti et al. (1987) initiated discussions of nucleosynthesis in sub-Keplerian disks around black holes and concluded that for very low viscosity (α parameter less than around 10^{-4}) and high accretion rates (typically, ten times the Eddington rate) there could be significant nucleosynthesis in thick disks. Radiation-pressure-supported thick accretion flows are cooler and significant nucleosynthesis was not possible unless the residence time of matter inside the accretion disk was made sufficiently high by reducing viscosity. The conclusions of this work were later verified by Arai & Hashimoto (1992) and Hashimoto et al. (1993).

However, the theory of accretion flows which contains a centrifugal-pressure-supported hotter and denser region in the inner part of the accretion disk has been developed more recently (Chakrabarti 1990c; Chakrabarti 1996a). The improvement in the theoretical understanding can be appreciated by comparing the numerical simulation results done in the eighties (Hawley et al. 1984, 1985) and in the nineties (Molteni et al. 1994; Molteni et al. 1996; Ryu et al. 1997). Whereas in the eighties the matching of theory and numerical simulations was poor, the matching of the results obtained recently is close to perfect. It is realized that in a large region of the parameter space, especially for lower accretion rates, the deviated flow would be hot

and a significant nuclear reaction is possible without taking resort to very low viscosity. Because of high viscosity residence time of the infalling matter may short but due to very high temperature ($\sim 10^{10}\text{K}$) significant nuclear reactions mainly dissociation of elements take place.

We arrive at a number of the important conclusions: (a) Significant nucleosynthesis is possible in the accretion flows. Whereas most of the matter of modified composition enters inside the black hole, a fraction may go out through the winds and will contaminate the surroundings in due course. The metallicity of the galaxies may also be influenced. (b) In some parameter regions, nuclear energy release or absorption may be of same order or greater than the energy release or absorption due to viscous effect of the disk. Generation or absorption of energy due to exothermic and endothermic nuclear reactions could seriously affect the stability of a disk. (c) Hot matter is unable to produce Lithium (${}^7\text{Li}$) or Deuterium (D) since when the flow is hot, photo-dissociation (photons partially locally generated and the rest supplied by the nearby Keplerian disk (Shakura & Sunyaev 1973) when the region is optically thin) is enough to dissociate all the elements completely into proton and neutron. Even when photo-dissociation is turned off (low opacity cases or when the system is fundamentally photon-starved) Li was not found to be produced very much. (d) Most significantly, we show that one does not require a very low viscosity for nucleosynthesis in contrary to the conclusions of the earlier works in thick accretion disk (Chakrabarti et al. 1987).

We already have presented in §2.6 the basic equations which govern accretion flows around a compact object. Since we are interested to study the nucleosynthesis around black hole only we will find the solution of the equation for general compact

objects by imposing boundary condition for black hole. In §3.1 we present a set of solutions of these equations which would be used for nucleosynthesis work. First of all we compute pure thermodynamic quantities. Then on this background (knowing velocity, density, sound speed, viscous energy etc. at each radius) when matter falls we compute the energy due to nuclear reactions to check whether it is comparable or not with viscous energy in the disk. When nucleosynthesis is insignificant with respect to the viscous dissipation, we compute thermodynamic quantities ignoring nuclear energy generation/absorption, otherwise we include it. We divide all the disks into three categories: ultra-hot, moderately hot, and cold. We present the results of nucleosynthesis for these cases separately. We find that in ultra-hot cases, the matter is completely photo-dissociated. In moderately hot cases, proton-capture processes along with dissociation of deuterium and ${}^3\text{He}$ are the major processes. In the cold cases, no significant nuclear reactions go on, only the proton capture reactions of very small order take place. Then we discuss the stability properties of the accretion disks in presence of nucleosynthesis and conclude that only the very inner edge of the flow is affected. In those unstable cases, in the inner edge of the disk nuclear energy becomes comparable with viscous energy to affect the disk but the outer region is still unaffected and the disk is stable. Nucleosynthesis may affect the metallicities of the galaxies as well as Li abundance in companions in black hole binaries.

3.1 Typical Solutions of Accretion Flows

In our work below, we choose a Schwarzschild black hole i.e., the black hole is non-rotating and space-time is spherically symmetric. We also choose the CGS unit when we find it convenient to do so. The nucleosynthesis work is done using CGS unit and

the energy release rates are in that unit as well. The location where the flow deviates from a Keplerian disk will depend on the cooling and heating processes (which depend on viscosity). Several solutions of the governing equations (see Eqn. I.42(a-e)) are given in Chakrabarti (1996a). By and large, we follow this paper to compute thermodynamical parameters along a flow. Due to computational constraints, we include energy generation due to nuclear reactions (Q_{nuc}) only when it is necessary (namely, when $|Q_{\text{nuc}}|$ is comparable to energy generation due to viscous effects as mentioned above) and we do not consider energy generation due to magnetic dissipation (due to reconnection effects, for instance). In Fig. I.2, we show a series of solutions which we employ to study nucleosynthesis processes. We plot the ratio λ/λ_K (Here, λ and λ_K are the specific angular momentum of the disk and the Keplerian angular momentum respectively) as a function of the logarithmic radial distance. The coefficient of the viscosity parameters are marked on each curve. The other parameters of the solution are in TABLE I.2. These solutions are obtained with constant $f = 1 - Q^-/Q^+$ and Q^+ includes only the viscous heating. In presence of significant nucleosynthesis, the solutions are obtained by choosing $f = 1 - Q^-/(Q^+ + Q_{\text{nuc}})$, where Q_{nuc} is the net energy generation or absorption due to exothermic and endothermic reactions. The motivation for choosing the particular cases are mentioned in the next section. At $x = x_K$, the ratio $\lambda/\lambda_K = 1$ and therefore x_K represents the transition region where the flow deviates from a Keplerian disk. First, note that when other parameters (basically, specific angular momentum and the location of the inner sonic point) remain roughly the same, x_K changes inversely with viscosity parameter α_{Π} (Chakrabarti 1996a). (The only exception is the curve marked with 0.01. This is because, it is drawn for $\gamma = 5/3$; all other curves are for $\gamma = 4/3$). From the figure it is clear that as the

viscosity parameter decreases, residence time of the matter in the disk increases, size of the sub-Keplerian region of the disk increases i.e., sub-Keplerian matter takes more time to match with Keplerian region. If one assumes, as Chakrabarti & Titarchuk (1995) and Chakrabarti (1997) did, that the alpha viscosity parameter *decreases* with vertical height, then it is clear from the general behaviour of Fig. I.2 that x_K would go up with height. The disk will then look like a sandwich with higher viscosity Keplerian matter flowing along the equatorial plane. As the viscosity changes, the sub-Keplerian and Keplerian flows redistribute (Chakrabarti & Molteni 1995) and the inner edge of the Keplerian component also recedes or advances. This fact that the inner edge of the disk should move in and out when the black hole goes into soft or hard state (as observed by, e.g., Gilfanov et al. 1997; Zhang et al. 1997) is thus naturally established from this disk solution.

In Chakrabarti (1990b) and Chakrabarti (1996a), it was pointed out that in a large region of the parameter space, especially for intermediate viscosities, centrifugal-pressure-supported shocks would be present in the hot, accretion flows. In these cases a shock-free solution passing through the outer sonic point was present. However, this branch is not selected by the flow and the flow passes through the higher entropy solution through shock and the inner sonic point instead. This assertion has been repeatedly verified independently by both theoretically (Yang & Kafatos 1995; Nobuta & Hanawa 1994; Lu & Yuan 1997; Lu et al. 1997) and numerical simulations (with independent codes, Chakrabarti & Molteni 1993; Sponholz & Molteni 1994; Ryu et al. 1995; Molteni et al. 1996 and references therein). When the shock forms, the temperature of the flow suddenly rises and the flow slows down considerably, raising the residence time of matter significantly. This effect of shock-induced nucleosynthesis

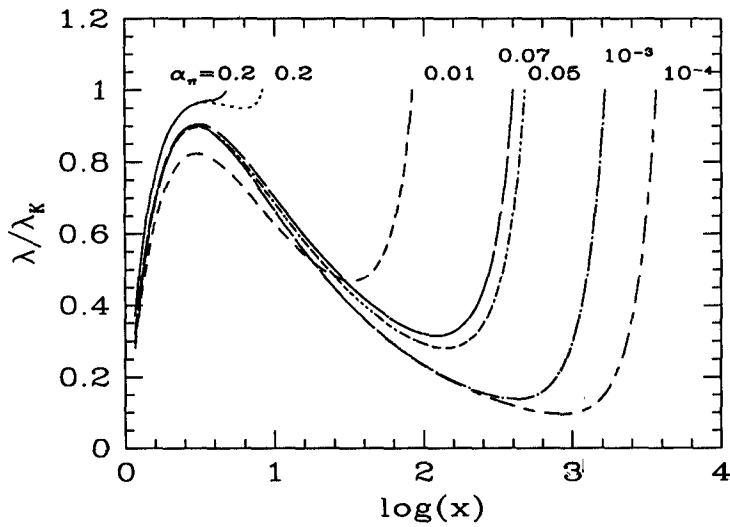


Fig. I.2. Variation of λ/λ_K with logarithmic radial distance for a few solutions which are employed to study nucleosynthesis. The viscosity parameter α_Π is marked on each curve. $x = x_K$ where $\lambda/\lambda_K = 1$, represents the location where the flow deviates from a Keplerian disk. Note that except for the dashed curve marked 0.01 (which is for $\gamma = 5/3$, and the rest are for $\gamma = 4/3$), x_K generally rises with decreasing α_Π . Thus, high viscosity flows must deviate from the Keplerian disk closer to the black hole.

is also studied in the next sub-section and, for comparison, the changes in composition in the shock-free branch were also computed, although it is understood that the shock-free branch is unstable. Our emphasis is not on shocks per se, but on the centrifugal-pressure-dominated region where the accreting matter slows down. When the shock does not form, the rise in temperature is more gradual. We generally follow the results of Chakrabarti & Titarchuk (1995) and Chakrabarti (1997) to compute the temperature of the Comptonized flow in the sub-Keplerian region which may or may not have shocks. Basically we borrow the mean factor $F_{\text{Compt}} \lesssim 1$ by which the temperature of the flow at a given radius x ($< x_K$) is reduced due to Comptonization process from the value dictated by the single-temperature hydrodynamic equations. This factor is typically $1/30 \sim 0.03$ for very low ($\lesssim 0.1$) mass accretion rate of the *Keplerian component* (which supplies the soft photons for the Comptonization) and around $1/100 \sim 0.01$ or less for higher Keplerian accretion rates. In presence of magnetic fields, some dissipation is present due to reconnections. Its expression is $Q_{\text{mag}} = \frac{3B^2}{16\pi x\rho}v$ (Shvartsman 1971; Shapiro 1973). We do not assume this heating here.

The list of major nuclear reactions such as *pp* chain, *CNO* cycle, proton capture, alpha (α) processes, photo-dissociation etc. which may take place inside a disk are given in §1.5. Due to the hotter nature of the sub-Keplerian disks, especially when the accretion rate is low and Compton cooling is negligible, the major process of hydrogen burning is some proton capture process (which operates at $T \gtrsim 0.5 \times 10^9\text{K}$) and mostly (p, α) reactions as opposed to the *pp* chain (which operates at much lower temperature $T \sim 0.01 - 0.2 \times 10^9\text{K}$) and *CNO* cycle (which operates at $T \sim 0.02 - 0.5 \times 10^9\text{K}$) as was pointed out earlier.

Typically, accretion onto a stellar-mass black hole takes place from a binary companion which could be a main sequence star. In a supermassive black hole at a galactic center, matter is presumably supplied by a number of nearby stars. Because it is difficult to establish the initial composition of the inflow, we generally take the solar abundance as the abundance of the Keplerian disk. Furthermore, the Keplerian disk being cooler, and the residence time inside it being insignificant compared to the hydrogen burning time-scale, we assume that for $x \gtrsim x_K$, the composition of the gas remains the same as that of the companion star, namely, Sun. Thus our computation starts only from the time when matter is launched from the Keplerian disk. Occasionally, for comparison, we run the models with an initial abundance same as the output of big-bang nucleosynthesis (hereafter referred to as ‘big-bang abundance’). These cases are particularly relevant for nucleosynthesis around proto-galactic cores and the early phase of star formations. We have also tested our code with an initial abundance same as the composition of late-type stars since in certain cases they are believed to be companions of galactic black hole candidates (Martin et al. 1992, 1994; Filippenko et al. 1995; Harlaftis et al. 1996).

3.1.1 Selection of Models

In selecting models for which the nucleosynthesis should be studied, the following considerations were made. According to Chakrabarti & Titarchuk (1995) and Chakrabarti (1997), there are two essential components of a disk. One is Keplerian (of rate \dot{m}_d) and the other is sub-Keplerian halo (of rate \dot{m}_h). For $\dot{m}_d \lesssim 0.1$ and $\dot{m}_h \lesssim 1$, the black hole remains in hard states. A lower Keplerian accretion rate *generally* implies a lower viscosity and a larger x_K ($x_K \sim 30 - 1000$; see, Chakrabarti 1996a and Chakrabarti 1997). Lower the Keplerian rate means low rate of matter

coming into the disk. As the matter supply rate is low, energy momentum transfer rate is low which signifies lower value of viscosity parameters. In this parameter range the protons remain hot, typically, $T_p \sim 1 - 10 \times 10^9 \text{K}$ or so. This is because the efficiency of emission is lower ($f = 1 - Q^-/Q^+ \sim 0.1$, where, Q^+ and Q^- are the height-integrated heat generation and heat loss rates [$\text{ergs cm}^{-2} \text{sec}^{-1}$] respectively. Also, according to Rees (1984), it is argued that if $\dot{m}/\alpha^2 \lesssim 1$ the bremsstrahlung cooling and inverse-Compton cooling are indeed inefficient. So the estimation of \dot{m}/α^2 is a good indication of the cooling efficiency of the hot flow, because high \dot{m}/α^2 means high rate of supply of matter as well as photon from Keplerian disk and therefore high rate of cooling.). Thus, we study a group of cases (Group A) where the net accretion rate $\dot{m} \sim 1.0$ and the viscosity parameter $\alpha \sim 0.001 - 0.1$. The Comptonization factor $F_{\text{Compt}} \sim 0.03$, i.e., the cooling due to Comptonization reduces the mean temperature roughly by a factor of around 30, which is quite reasonable. Here, although the density of the gas is low, the temperature is high enough to cause significant nuclear reactions in the disk. These belongs to moderately hot case.

When the net accretion rate is very low ($\dot{m} \lesssim 0.01$) such as in a quiescence state of an X-ray novae, the dearth of soft photon keeps the temperature of the sub-Keplerian flow to a very high value and a high Comptonization factor $F_{\text{Compt}} \sim 0.1$ could be used (Group B). Here significant nuclear reaction takes place, even though the density of matter is very low. Basically, the entire amount of matter is photo-dissociated into protons and neutrons in this case even when opacity is very low. This belongs to ultra hot case. It is noted that the number density of photon is much higher than that of deuterium, helium etc. so, lower accretion rate (lower rate of transfer of soft photon from Keplerian to sub-Keplerian region) does not make any significant influence on

dissociation.

In the event where the inflow consist of both the Keplerian (accretion rate \dot{m}_d) and sub-Keplerian (accretion rate \dot{m}_h) matter as the modern theory predicts, there would be situations where the *net* accretion rate is high, say $\dot{m} = \dot{m}_d + \dot{m}_h \sim 1 - 5$, and yet the gas temperature is very high ($T > 10^9$). This happens when viscosity is low to convert sub-Keplerian inflow into a Keplerian disk. Here, most of the inflow is in the sub-Keplerian component and very little ($\dot{m}_d \sim 0.01$) matter is in the Keplerian flow. Dearth of soft photon keeps the disk hot, while the density of reactants is still high enough to have profuse nuclear reactions. The simple criteria for the cooling efficiency as pointed was out in previous page (that $\dot{m}/\alpha^2 > 1$ would cool the disk, see Rees 1984) will not hold since the radiation source (Keplerian disk) is different from the cooling body (sub-Keplerian disk). Although the accretion rate is high enough most part of the matter is not coming from the Keplerian region so due to the lower Keplerian rate soft photons are not profuse enough to cool down the disk.

One could envisage yet another set of cases (Group C), where the accretion rate is very high ($\dot{m} \sim 10 - 100$), and the soft photons are so profuse that the sub-Keplerian region of the disks becomes very cold. In this case, typically, viscosity is very high, 0.2 ; x_K becomes low ($x_K \sim 3 - 10$). The efficiency of cooling is very high ($Q^+ \approx Q^-$, i.e., $f \approx 0$) almost same as that in Keplerian disk. The Comptonization factor is low, $F_{\text{Compt}} \lesssim 0.01$, the black hole is in a soft state. There is no significant nuclear reaction in these cases. A small amount of nuclear energy is generated through the proton capture reactions which is much lower order of magnitude than viscous energy release. So in this case we can safely neglect the nuclear energy release in the disk. In the proto-galactic phase when the supply of matter is *very* high, while the viscosity

may be so low (say, 10^{-4}) that the entire amount is not accreted, one can have an ultra-cold accretion flow with $F_{\text{Compt}} \sim 10^{-3}$. In this case also not much nuclear reaction goes on.

The above simulations have been carried out with polytropic index $\gamma = 4/3$. In reality, the polytropic index could be in between $4/3$ and $5/3$. If $\gamma < 1.5$ then shocks would form as in some of the above cases. However, for $\gamma > 1.5$, standing shocks would not form (Chakrabarti 1996a). We have included two illustrative examples of shock-free case with $\gamma = 5/3$ which is very hot and we have presented the result in Group B. In these cases, the Keplerian component is far away and the intercepted soft photons are very few. The disk is very hot so that almost all the elements are photo-dissociated into neutron and proton. Finally the disk consists of neutron and proton only. This may be called *Neutron Disk*.

3.1.2 Selection of the Reaction Network

In selecting the reaction network we kept in mind the fact that hotter flows may produce heavier elements through triple- α and proton and α capture processes. Similarly, due to photo-dissociation, significant neutrons may be produced. Thus, we consider a sufficient number of isotopes on either side of the stability line. The network thus contains neutron, proton, till ${}^{72}\text{Ge}$ – altogether 255 nuclear species. The network of coupled non-linear differential equation is linearized and evolved in time along the solution of Chakrabarti (1996a) obtained from a given set of initial parameters of the flow. This well proven method is widely used in the literature (see Arnett & Truran 1969; Woosley et al. 1973). Below in TABLE I.1 we give the list of all nuclear species we consider here and their abundance.

TABLE I.1

n	p	${}^4\text{He}$	D	T
0.0	7.425×10^{-1}	2.380×10^{-1}	2.948×10^{-5}	0.0
${}^4\text{H}$	${}^3\text{He}$	${}^6\text{He}$	${}^6\text{Li}$	${}^7\text{Li}$
0.0	2.538×10^{-5}	0.0	7.337×10^{-10}	1.055×10^{-8}
${}^8\text{Li}$	${}^7\text{Be}$	${}^8\text{Be}$	${}^9\text{Be}$	${}^{10}\text{Be}$
0.0	0.0	0.0	1.916×10^{-10}	0.0
${}^{11}\text{Be}$	${}^8\text{B}$	${}^9\text{B}$	${}^{10}\text{B}$	${}^{11}\text{B}$
0.0	0.0	0.0	1.310×10^{-9}	5.765×10^{-9}
${}^{12}\text{B}$	${}^{11}\text{C}$	${}^{12}\text{C}$	${}^{13}\text{C}$	${}^{14}\text{C}$
0.0	0.0	3.931×10^{-3}	4.755×10^{-5}	0.0
${}^{13}\text{N}$	${}^{14}\text{N}$	${}^{15}\text{N}$	${}^{14}\text{O}$	${}^{15}\text{O}$
0.0	9.439×10^{-4}	3.718×10^{-6}	0.0	0.0
${}^{16}\text{O}$	${}^{17}\text{O}$	${}^{18}\text{O}$	${}^{17}\text{F}$	${}^{18}\text{F}$
8.779×10^{-3}	3.545×10^{-6}	2.014×10^{-5}	0.0	0.0
${}^{19}\text{F}$	${}^{20}\text{F}$	${}^{21}\text{F}$	${}^{19}\text{Ne}$	${}^{20}\text{Ne}$
4.372×10^{-7}	0.0	0.0	0.0	1.774×10^{-3}
${}^{21}\text{Ne}$	${}^{22}\text{Ne}$	${}^{23}\text{Ne}$	${}^{20}\text{Na}$	${}^{21}\text{Na}$
4.534×10^{-6}	1.429×10^{-4}	0.0	0.0	0.0
${}^{22}\text{Na}$	${}^{23}\text{Na}$	${}^{24}\text{Na}$	${}^{21}\text{Mg}$	${}^{22}\text{Mg}$
0.0	3.578×10^{-5}	0.0	0.0	0.0
${}^{23}\text{Mg}$	${}^{24}\text{Mg}$	${}^{25}\text{Mg}$	${}^{26}\text{Mg}$	${}^{27}\text{Mg}$
0.0	5.562×10^{-4}	7.302×10^{-5}	8.375×10^{-5}	0.0
${}^{28}\text{Mg}$	${}^{23}\text{Al}$	${}^{24}\text{Al}$	${}^{25}\text{Al}$	${}^{26}\text{Al}$
0.0	0.0	0.0	0.0	0.0
${}^{27}\text{Al}$	${}^{28}\text{Al}$	${}^{29}\text{Al}$	${}^{30}\text{Al}$	${}^{25}\text{Si}$
6.257×10^{-5}	0.0	0.0	0.0	0.0
${}^{26}\text{Si}$	${}^{27}\text{Si}$	${}^{28}\text{Si}$	${}^{29}\text{Si}$	${}^{30}\text{Si}$
0.0	0.0	7.047×10^{-4}	3.697×10^{-5}	2.538×10^{-5}
${}^{31}\text{Si}$	${}^{32}\text{Si}$	${}^{28}\text{P}$	${}^{29}\text{P}$	${}^{30}\text{P}$
0.0	0.0	0.0	0.0	0.0
${}^{31}\text{P}$	${}^{32}\text{P}$	${}^{33}\text{P}$	${}^{34}\text{P}$	${}^{29}\text{S}$
8.801×10^{-6}	0.0	0.0	0.0	0.0
${}^{30}\text{S}$	${}^{31}\text{S}$	${}^{32}\text{S}$	${}^{33}\text{S}$	${}^{34}\text{S}$
0.0	0.0	4.271×10^{-4}	3.477×10^{-6}	2.014×10^{-5}

^{35}S	^{36}S	^{37}S	^{32}Cl	^{33}Cl
0.0	8.648×10^{-8}	0.0	0.0	0.0
^{34}Cl	^{35}Cl	^{36}Cl	^{37}Cl	^{38}Cl
0.0	3.793×10^{-6}	0.0	1.282×10^{-6}	0.0
^{39}Cl	^{40}Cl	^{33}Ar	^{34}Ar	^{35}Ar
0.0	0.0	0.0	0.0	0.0
^{36}Ar	^{37}Ar	^{38}Ar	^{39}Ar	^{40}Ar
8.609×10^{-5}	0.0	1.701×10^{-5}	0.0	6.005×10^{-10}
^{41}Ar	^{42}Ar	^{36}K	^{37}K	^{38}K
0.0	0.0	0.0	0.0	0.0
^{39}K	^{40}K	^{41}K	^{42}K	^{43}K
3.743×10^{-6}	4.804×10^{-10}	2.839×10^{-7}	0.0	0.0
^{44}K	^{45}K	^{37}Ca	^{38}Ca	^{39}Ca
0.0	0.0	0.0	0.0	0.0
^{40}Ca	^{41}Ca	^{42}Ca	^{43}Ca	^{44}Ca
6.464×10^{-5}	0.0	4.528×10^{-7}	9.684×10^{-8}	1.533×10^{-6}
^{45}Ca	^{46}Ca	^{47}Ca	^{48}Ca	^{49}Ca
0.0	2.687×10^{-9}	0.0	1.493×10^{-7}	0.0
^{40}Sc	^{41}Sc	^{42}Sc	^{43}Sc	^{44}Sc
0.0	0.0	0.0	0.0	0.0
^{45}Sc	^{46}Sc	^{47}Sc	^{48}Sc	^{49}Sc
4.152×10^{-8}	0.0	0.0	0.0	0.0
^{50}Sc	^{42}Ti	^{43}Ti	^{44}Ti	^{45}Ti
0.0	0.0	0.0	0.0	0.0
^{46}Ti	^{47}Ti	^{48}Ti	^{49}Ti	^{50}Ti
2.473×10^{-7}	2.283×10^{-7}	2.318×10^{-6}	1.738×10^{-7}	1.706×10^{-7}
^{51}Ti	^{52}Ti	^{46}V	^{47}V	^{48}V
0.0	0.0	0.0	0.0	0.0
^{49}V	^{50}V	^{51}V	^{52}V	^{53}V
0.0	1.010×10^{-9}	4.093×10^{-7}	0.0	0.0
^{54}V	^{48}Cr	^{49}Cr	^{50}Cr	^{51}Cr
0.0	0.0	0.0	7.957×10^{-7}	0.0
^{52}Cr	^{53}Cr	^{54}Cr	^{55}Cr	^{56}Cr
1.589×10^{-5}	1.851×10^{-6}	4.658×10^{-7}	0.0	0.0

^{50}Mn	^{51}Mn	^{52}Mn	^{53}Mn	^{54}Mn
0.0	0.0	0.0	0.0	0.0
^{55}Mn	^{56}Mn	^{57}Mn	^{58}Mn	^{52}Fe
1.427×10^{-5}	0.0	0.0	0.0	0.0
^{53}Fe	^{54}Fe	^{55}Fe	^{56}Fe	^{57}Fe
0.0	7.695×10^{-5}	0.0	1.262×10^{-3}	3.018×10^{-5}
^{58}Fe	^{59}Fe	^{60}Fe	^{61}Fe	^{54}Co
4.132×10^{-6}	0.0	0.0	0.0	0.0
^{55}Co	^{56}Co	^{57}Co	^{58}Co	^{59}Co
0.0	0.0	0.0	0.0	3.623×10^{-6}
^{60}Co	^{61}Co	^{62}Co	^{63}Co	^{56}Ni
0.0	0.0	0.0	0.0	0.0
^{57}Ni	^{58}Ni	^{59}Ni	^{60}Ni	^{61}Ni
0.0	5.335×10^{-5}	0.0	2.112×10^{-5}	9.275×10^{-7}
^{62}Ni	^{63}Ni	^{64}Ni	^{65}Ni	^{66}Ni
2.995×10^{-6}	0.0	7.844×10^{-7}	0.0	0.0
^{58}Cu	^{59}Cu	^{60}Cu	^{61}Cu	^{62}Cu
0.0	0.0	0.0	0.0	0.0
^{63}Cu	^{64}Cu	^{65}Cu	^{66}Cu	^{67}Cu
6.122×10^{-7}	0.0	2.803×10^{-7}	0.0	0.0
^{68}Cu	^{59}Zn	^{60}Zn	^{61}Zn	^{62}Zn
0.0	0.0	0.0	0.0	0.0
^{63}Zn	^{64}Zn	^{65}Zn	^{66}Zn	^{67}Zn
0.0	1.069×10^{-6}	0.0	6.342×10^{-7}	9.456×10^{-8}
^{68}Zn	^{69}Zn	^{70}Zn	^{71}Zn	^{62}Ga
4.343×10^{-7}	0.0	1.492×10^{-8}	0.0	0.0
^{63}Ga	^{64}Ga	^{65}Ga	^{66}Ga	^{67}Ga
0.0	0.0	0.0	0.0	0.0
^{68}Ga	^{69}Ga	^{70}Ga	^{71}Ga	^{72}Ga
0.0	4.275×10^{-8}	0.0	2.926×10^{-8}	0.0
^{73}Ga	^{64}Ge	^{65}Ge	^{66}Ge	^{67}Ge
0.0	0.0	0.0	0.0	0.0
^{68}Ge	^{69}Ge	^{70}Ge	^{71}Ge	^{72}Ge
0.0	0.0	4.624×10^{-8}	0.0	6.348×10^{-8}

The reaction rates were taken from Fowler et al. (1975) including updates by Harris et al. (1983). Other relevant references from where rates have been updated are: Thielemann (1980); Wallace & Woosley (1981); Wagoner et al. (1967); Fuller et al. (1980, 1982). For details of the procedure of adopting reaction rates, see, Chakrabarti et al. (1987) and Jin et al. (1989). The solar abundance which was used as the initial composition of the inflow was taken from Anders & Ebihara (1982).

Thielemann (1980) has given a formula to express different nuclear reaction rates in terms of an exponential function. It depends on temperature in the unit of 10^9 (T_9) and seven constant coefficients (c_i s) as

$$\langle \sigma v \rangle_i = r_i = \exp(g_i) \quad (I.48)$$

where, $g_i = c_i^1 + c_i^2/T_9 + c_i^3/T_9^{(1/3)} + c_i^4 T_9^{(1/3)} + c_i^5 T_9 + c_i^6 T_9^{(5/3)} + c_i^7 \log(T_9)$, i indicates corresponding reaction about which we are interested. For different reactions the constant coefficients c_i s will be different.

3.2 Results

In this section, we present a few major results of our simulations using different parameter groups as described in §3.1.1. For a complete solution of the sub-Keplerian disks (Chakrabarti 1996a) we need to provide (a) the mass of the black hole M , (b) the viscosity parameter α_{Π} , (c) the cooling efficiency factor f , (d) the Comptonization factor F_{Compt} , (e) the net accretion rate of the flow \dot{m} , (f) the inner sonic point location x_{in} through which the flow must pass and finally, (g) the specific angular momentum λ_{in} at the inner sonic point.

The following table gives the cases we discuss here. The Π -stress viscosity parameter α_{Π} , the location of the inner sonic point x_{in} and the value of the specific

angular momentum at that point λ_{in} are free parameters. The net accretion rate \dot{m} , the Comptonization factor F_{Compt} and the cooling efficiency f are related quantities (Chakrabarti & Titarchuk 1995; Chakrabarti 1997). For extremely inefficient cooling, $f \sim 1.0$, and for extremely efficient cooling, $f = 0$ or even negative. The derived quantities, such as the value of maximum temperature T_9^{max} of the flow (in unit of 10^9K), density of matter (in CGS unit) at T_9^{max} , x_K , the locations from where the Keplerian disk on the equatorial plane becomes sub-Keplerian are also provided in the table. In the rightmost column, we present whether the inner edge of the disk is stable (S) or unstable (U) in the presence of the nucleosynthesis in accretion flow. Three groups are separated as the parameters are clearly from three distinct regimes.

TABLE I.2

Model	M/M_{\odot}	γ	x_{in}	λ_{in}	α_{II}	\dot{m}	f	F_{Compt}	x_K	T_9^{max}	ρ_{max}	S/U
A.1	10	4/3	2.7945	1.65	0.001	1	0.1	0.03	1655.7	5.7	6.2×10^{-7}	S
A.2	10	4/3	2.9115	1.6	0.07	1	0.1	0.03	401.0	4.7	4.9×10^{-7}	S
A.3	10^6	4/3	2.9115	1.6	0.07	1	0.1	0.03	401.0	4.7	4.9×10^{-12}	U
B.1	10	4/3	2.8695	1.6	0.05	0.01	0.5	0.1	481.4	16.5	3.9×10^{-9}	S
B.2	10	4/3	2.8695	1.6	0.05	4	0.5	0.1	481.4	16.5	1.6×10^{-8}	U
B.3	10	5/3	2.4	1.5	0.01	0.001	0.5	0.1	84.4	47	3.3×10^{-10}	S
B.4	10	5/3	2.35	1.55	0.01	0.001	0.6	0.1	85.1	37	2.9×10^{-10}	S
B.5	10	4/3	2.795	1.65	0.2	0.01	0.2	0.1	8.4	13	1.1×10^{-8}	S
B.6	10	4/3	2.7	1.65	0.2	0.01	0.1	0.1	4.2	11	1.1×10^{-8}	S
C.1	10	4/3	2.795	1.65	0.2	100	0.0	0.01	4.8	0.8	1.1×10^{-4}	S
C.2	10^6	4/3	2.795	1.65	10^{-4}	100	0.0	0.001	3657.9	0.2	6.2×10^{-10}	S

The basis of our three groupings are clear from the TABLE I.2. Very low $\dot{m}/\alpha_{\text{II}}^2$ in Group B makes the cooling efficiency to be very small. Thus we choose a relatively large $f \sim 0.1 - 0.5$. For the case B.2, we see that $\dot{m}/\alpha_{\text{II}}^2 \gg 1$ but still we consider it as very hot case and keep in Group B. This is because, though the accretion rate

for B.2 case is chosen high but this is due to high rate of halo i.e., \dot{m}_h is very high but \dot{m}_d is low. As the Keplerian rate is still low the supply of soft photon is very low. Thus, in all the cases of Group B the cooling due to Comptonization is very low ($F_{\text{Compt}} \sim 0.1$). Therefore the disks could be ultra-hot. Intermediate $\dot{m}/\alpha_{\text{ff}}^2$ in Group A means that the efficiency of cooling is intermediate, $f \sim 0.1$ and the Compton cooling of the sub-Keplerian region is average: $F_{\text{Compt}} \sim 0.03$. The sub-Keplerian disk in this case is neither too hot nor too cold. Extremely high $\dot{m}/\alpha_{\text{ff}}^2$ causes a strong cooling in Group C. Thus, we choose $f = 0$ and a very efficient Compton cooling, $F_{\text{Compt}} \sim 0.01 - 0.001$. As a result, the disk is also very cold. Now, we present our numerical simulation results in these cases.

3.2.1 Nucleosynthesis in Moderately Hot Flows

Case A.1: In this case, the termination of the Keplerian component in the weakly viscous flow takes place at $x = 1655.7$. The soft photons intercepted by the sub-Keplerian region reduce the temperature of this region but not by a large factor. The net accretion rate $\dot{m} = 1$ is the sum of (very low) Keplerian component and the sub-Keplerian component. Using computations of Chakrabarti & Titarchuk (1995) and Chakrabarti (1997) for $\dot{m}_d \sim 0.1$ and $\dot{m}_h \sim 0.9$, we find that the electron temperature T_e is around 60keV, i.e., $T_9 \sim 0.6$ (T_9 is the temperature in unit of 10^9K) and the ion temperature is around $T_9 = 2.5$. This fixes the Comptonization factor to about $F_{\text{Compt}} = 0.03$. This factor is used to reduce the temperature distribution of solutions of Chakrabarti (1996a) (which does not explicitly use Comptonization) to temperature distribution *with* Comptonization. The ion temperature (in T_9) and density (in unit of $10^{-10} \text{ gm cm}^{-3}$ to bring in the same plot) distribution computed in this manner are shown in Fig. I.3a. Figure I.3b gives the velocity distribution (velocity is

measured in unit of 10^{10} cm sec $^{-1}$). Note the sudden rise in temperature and slowing down of matter close to the centrifugal barrier at $x \sim 30$. Figure I.3c shows the changes in composition as matter is accreted onto the black hole. Only those species with abundance $Y_i \gtrsim 10^{-4}$ have been shown for clarity. Also, compositions closer to the black hole are shown, as variations farther out are negligible. Most of the burning of species takes place below $x = 10$. A significant amount of the neutron (with a final abundance of $Y_n \sim 10^{-3}$) is produced by the photo-dissociation process. Note that closer to the black hole, ^{12}C , ^{16}O , ^{24}Mg and ^{28}Si are all destroyed completely, even though at around $x = 5$ or so, the abundance of some of them went up first before going down. Among the new species which are formed closer to the black hole are ^{30}Si , ^{46}Ti , ^{50}Cr . The final abundance of ^{20}Ne is significantly higher than the initial value. This was not dissociated as the residence time in hotter region was insufficient. Thus a significant metallicity could be supplied by winds from the centrifugal barrier.

Figure I.3d shows the energy release and absorption due to exothermic and endothermic nuclear reactions (Q_{nuc}) that are taking place inside the disk (solid). Superposed on it are the energy generation rate Q^+ (long dashed curve) due to viscous process and the energy loss rate Q^- in the sub-Keplerian flows. For comparison, we also plot the hypothetical energy generation and loss rates (short dashed curves marked as Q_{Kep}^+ and Q_{Kep}^- respectively) if the disk had purely Keplerian angular momentum distribution even in the sub-Keplerian regime. All these quantities are in unit of 3×10^6 and they represent height-integrated energy release rate (ergs cm $^{-2}$ sec $^{-1}$). Note that these Q s are in logarithmic scale (if $Q < 0$, $-\log(|Q|)$ is plotted). As matter leaves the Keplerian flow, the proton capture (p, α) processes (such as $^{18}\text{O}(p, \alpha)^{15}\text{N}$, $^{15}\text{N}(p, \alpha)^{12}\text{C}$, $^6\text{Li}(p, \alpha)^3\text{He}$, $^7\text{Li}(p, \alpha)^4\text{He}$, $^{11}\text{B}(p, \gamma)3\alpha$, $^{17}\text{O}(p, \alpha)^{14}\text{N}$, etc.)

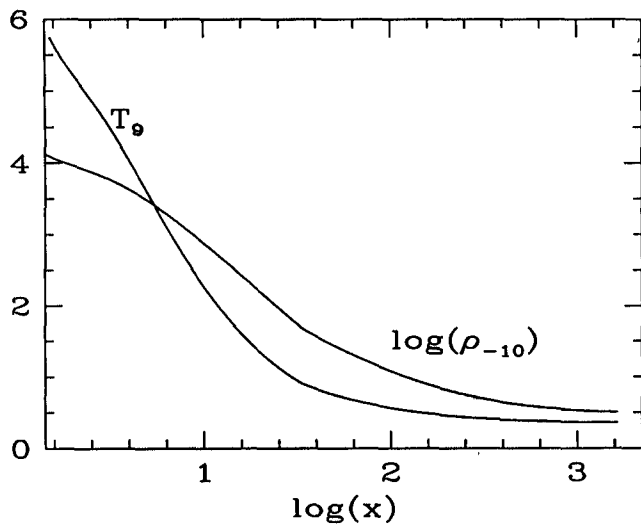


Fig. I.3a

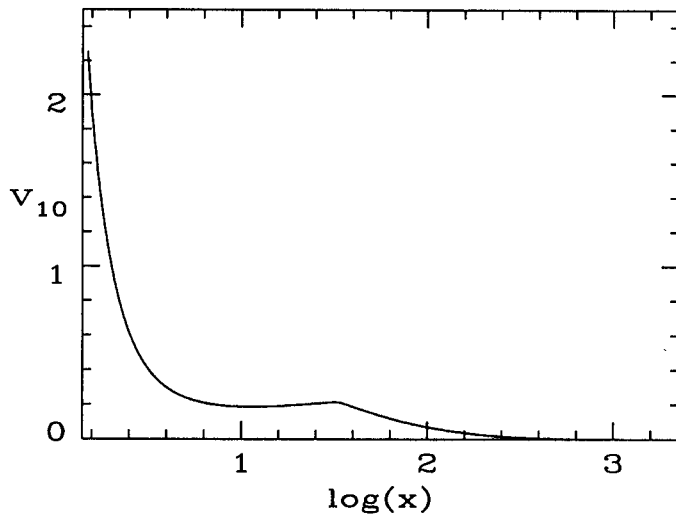


Fig. I.3b

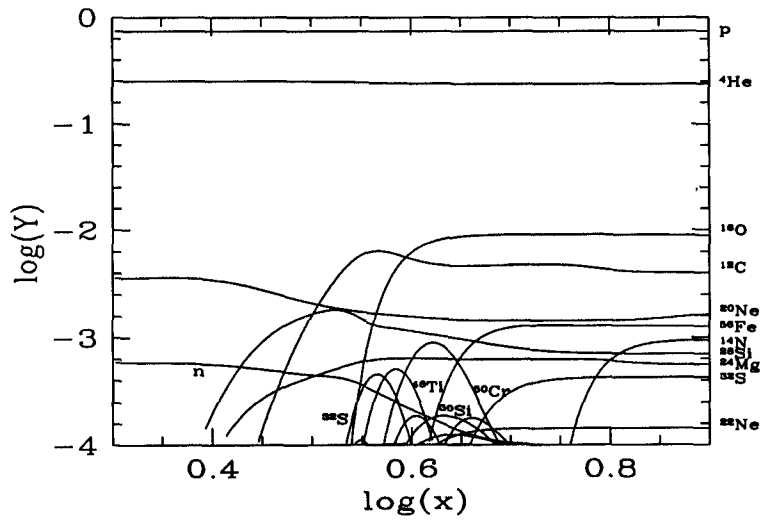


Fig. I.3c

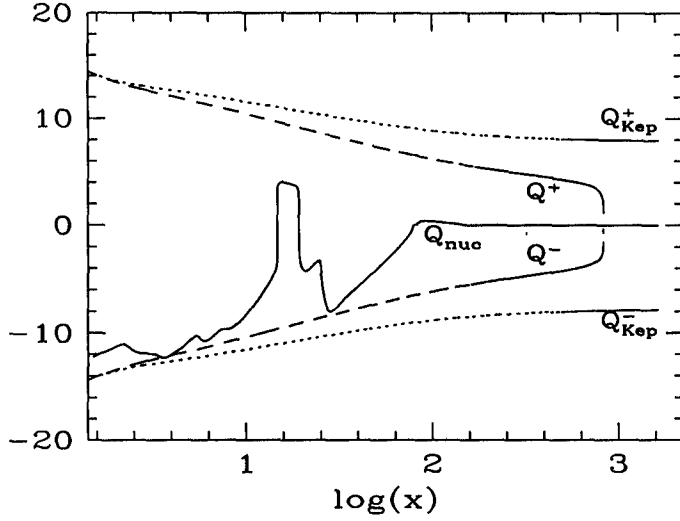


Fig. I.3d

Fig. I.3. Variation of (a) ion temperature (T_9) and density (ρ_{-10}), (b) radial velocity v_{10} , (c) matter abundance Y_i in logarithmic scale and (d) various forms of height-integrated specific energy release and absorption rates (in $\text{ergs cm}^{-2} \text{sec}^{-1}$) when the model parameters are $M = 10M_\odot$, $\dot{m} = 1.0$, $\alpha_\Pi = 0.001$ as functions of logarithmic radial distance (x in unit of Schwarzschild radius). Q is in logarithmic scale. See text and TABLE I.2 for other parameters of Case A.1 which is considered here. The centrifugal barrier slows down and heats up matter where a significant change in abundance takes place ($\Delta Y_i \sim 10^{-3}$).

burn hydrogen and release energy to the disk (since the temperature of the disk is very high, pp chains or CNO cycles are not the dominant processes for the energy release as described in §1.5 and §1.6). At around $x = 40$, the deuterium starts burning ($D(\gamma, n)p$) and the endothermic reaction causes the nuclear energy release to become ‘negative’, i.e., a huge amount of energy is absorbed from the disk. At the completion of the deuterium burning (at around $x = 20$) the energy release tends to go back to the positive value to the level dictated by the original proton capture processes. Excessive temperature at around $x = 5$ breaks ${}^3\text{He}$ down into deuterium (${}^3\text{He}(\gamma, p)D$, $D(\gamma, n)p$). Another major endothermic reaction which is dominant in this region is ${}^{17}\text{O}(\gamma, n){}^{16}\text{O}$. These reactions absorb a significant amount of energy from the flow. Note that in few regions the nuclear energy release or absorption is of the same order as the energy release due to viscous process. This energy was incorporated in computing thermodynamic quantities following these steps:

- (a) Compute thermodynamic quantities without nuclear energy
- (b) Run nucleosynthesis code and compute Q_{nuc}
- (c) Fit Q_{nuc} using piecewise analytical functions and include this into the definition of f ,

$$f = 1 - \frac{Q^-}{Q^+ + Q_{\text{nuc}}} \quad (\text{I.49})$$

- (d) Do sonic point analysis once more using this extra heating/cooling term and compute thermodynamic quantities.
- (e) Repeat from step (b) till the results converge. In this present case, there is virtually no difference in the solutions and the solution appears to be completely stable under nucleosynthesis.

Case A.2: Here we choose the same net accretion rate, but with a larger viscosity. As a result, the Keplerian component moves closer. The Comptonization is still not very effective, and the flow is moderately hot as above with $F_{\text{Compt}} = 0.03$. The flow deviates from a very hot (sufficient to cause the flow to pass through the outer sonic point) Keplerian disk at $x_K = 401.0$, then after passing through an outer sonic point at $x = 50$ and through a shock at $x_S = 15$, the flow enters into the black hole through the inner sonic point at $x = 2.9115$. We show the results both for the shock-free branch (i.e., the one which passes through only the outer sonic point before plunging into the black hole, dotted curves) and the shocked branch of the solution (solid curves). Figure I.4a shows the comparison of the temperatures and densities (scaled in the same way as in Fig. I.3a). The temperature and density jump sharply at the shock. Figure I.4b shows the comparison of the radial velocities. The velocity sharply drops at the shock. Both of these effects hasten the nuclear burning in the case which includes the shock. Figure I.4c shows the comparison of the abundances of only those species whose abundances reached a value of at least 10^{-4} . The difference between the shocked and the shock-free cases is that in the shock case similar burning takes place farther away from the black hole because of much higher temperature in the post-shock region.

The nature of the (height integrated) nuclear energy release is very similar to Case A.1 as the major reactions which take place inside the disk are basically same, except that the exact locations where any particular reaction takes place are different since they are temperature sensitive. In Fig. I.4d, we show all the energy release/absorption components for the shocked flow (solid curve). For comparison, we include the nuclear energy curve of the shock-free branch (very long dashed curve). Note that in the

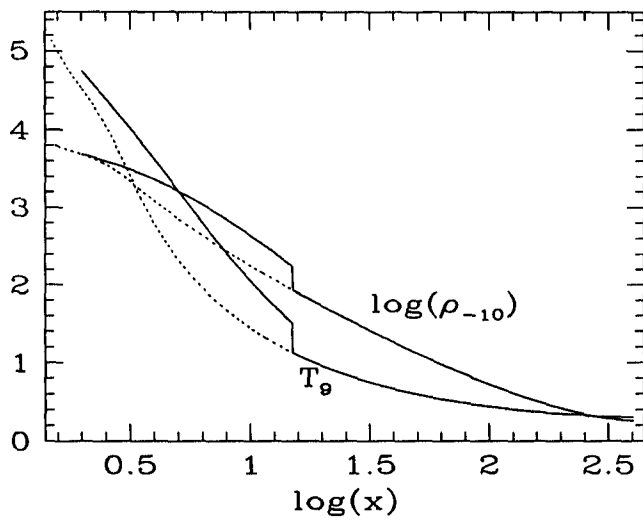


Fig. I.4a

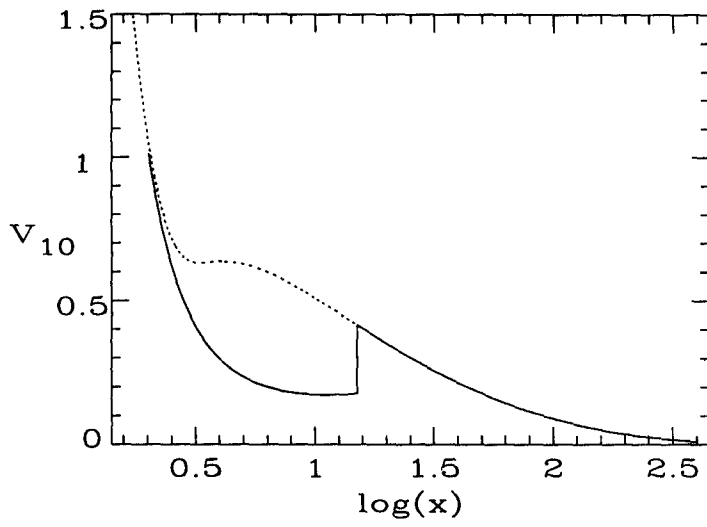


Fig. I.4b

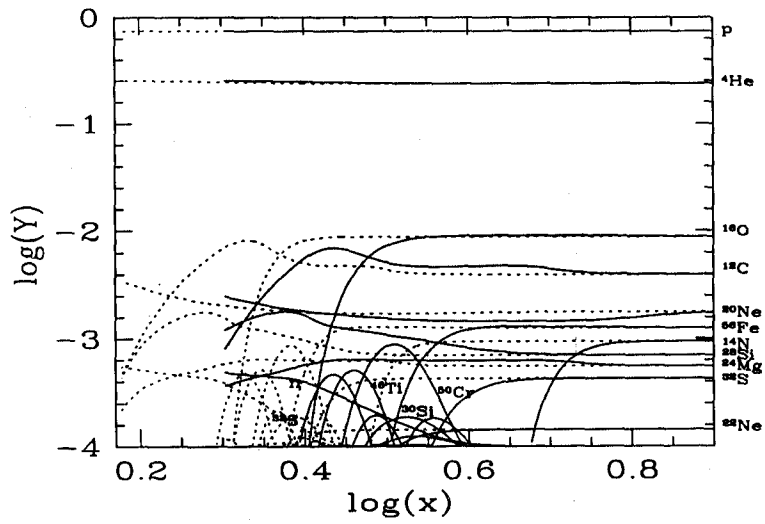


Fig. I.4c

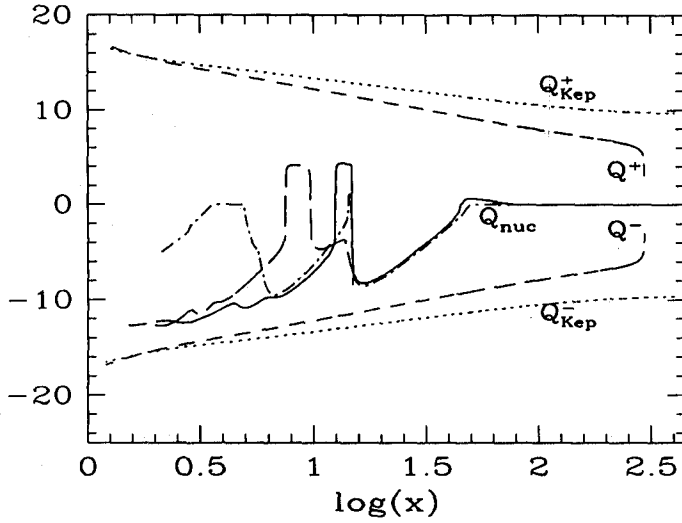


Fig. I.4d

Fig. I.4.: Variation of (a) ion temperature (T_9) and density (ρ_{-10}), (b) radial velocity v_{10} , (c) matter abundance Y_i in logarithmic scale and (d) various forms of specific energy release and absorption rates when the model parameters are $M = 10M_\odot$, $\dot{m} = 1.0$, $\alpha_\Pi = 0.07$ as functions of logarithmic radial distance (x in unit of Schwarzschild radius). See text and TABLE I.2 for other parameters of Case A.2 which is considered here. Solutions in the stable branch with shock are solid curves and those without the shock are dotted in (a-c). Curves in (d) are described in the text. At the shock, temperature and density rise significantly and cause a significant change in abundance even farther out. Shock-induced winds may cause substantial contamination of the galactic composition when parameters are chosen from these regions.

post-shock region, hotter and denser flow of the shocked-branch causes a particular nuclear reaction to take place farther away from a black hole when compared with the behaviour in the shock-free branch as is also reflected in the composition variation in Fig. I.4c. The viscous energy generation (Q^+) and the loss of energy (Q^-) from the disk (long dashed) are shown. As before, these quantities, if the inner part had Keplerian distribution, are also plotted (short dashed). When big-bang abundance is chosen to be the initial abundance, the net composition does not change very much, but the dominating reactions themselves are somewhat different because the initial compositions are different. The dot-dashed curve shows the nuclear energy release/absorption in the shocked flow when big-bang abundance is chosen. All these quantities are, as before, in unit of 3×10^6 and they represent height integrated energy release rate ($\text{ergs cm}^{-2} \text{sec}^{-1}$). For instance, in place of proton capture reactions for computations with solar abundance, the fusion of deuterium into ${}^4\text{He}$ plays a dominant role via the following reactions: $D(D, n){}^3\text{He}$, $D(p, \gamma){}^3\text{He}$, $D(D, p)T$, ${}^3\text{He}(D, p){}^4\text{He}$. This is because no heavy elements were present to begin with and proton capture processes involving heavy elements such as were prevalent in the solar abundance case cannot take place here. Endothermic reactions at around $x \sim 20 - 40$ are dominated by deuterium dissociation as before. However, after the complete destruction of deuterium, the exothermic reaction is momentarily dominated by neutron capture processes (due to the same neutrons which are produced earlier via $D(\gamma, n)p$) such as ${}^3\text{He}(n, p)T$ which produces the spike at around $x = 14.5$. Following this, ${}^3\text{He}$ and T are destroyed as in the solar abundance case (i.e., ${}^3\text{He}(\gamma, p)D$, $D(\gamma, n)p$, $T(\gamma, n)D$) and reaches the minimum in the energy release curve at around $x = 6$. The tendency of going back to the exothermic region is stopped due to the photo-dissociation of ${}^4\text{He}$ via ${}^4\text{He}(\gamma, p)T$

and ${}^4\text{He}(\gamma, n){}^3\text{He}$. At the end of the big-bang abundance calculation, a significant amount of neutron is produced. The disk was found to be perfectly stable under nuclear reactions.

Case A.3: This case is exactly same as A.2 except that the mass of the black hole is chosen to be $10^6 M_{\odot}$. The temperature and velocity variations are similar to the above case. Because the accretion rate (in non-dimensional units) is the same, the density (which goes as \dot{m}/r^2v) is lower by a factor of 10^{-5} . Tenuous plasma should change its composition significantly only at higher temperatures than in the previous case. However, the increase in residence time by a factor of around 10^5 causes the nuclear burning to take place farther out even at a lower temperature. This is exactly what is seen. Figure I.5a shows the comparison (without including nuclear energy) of the composition of matter when the flow has a shock (solid curves) and when the flow is shock-free (short dashed curve). We recall that the shock-free flow is in reality not stable. It is kept only for comparison purposes. Note that unlike earlier cases, a longer residence time also causes to burn all the ${}^{20}\text{Ne}$ that was generated from ${}^{16}\text{O}$.

In Fig. I.5b, we show a comparison of various height-integrated energy release and absorption curves as in Fig. I.4d (in $\text{ergs cm}^{-2} \text{sec}^{-1}$). The nuclear energy remains negligibly small till around $x = 100$. After that the endothermic reactions dominate. This is due to the dissociation of D , ${}^3\text{He}$ and ${}^7\text{Li}$ and also of ${}^{12}\text{C}$, ${}^{16}\text{O}$, ${}^{20}\text{Ne}$ etc., all of which produce ${}^4\text{He}$. The solid curve is for the branch with a shock and the very long dashed curve is for the shock-free branch. A small amount of neutron is produced ($Y_n \sim 10^{-3}$) primarily due to the dissociation of D . These considerations are valid for solar abundance as the initial composition. In the case of big-bang abundance (dash-dotted curve), similar reactions take place but no elements heavier than ${}^7\text{Li}$

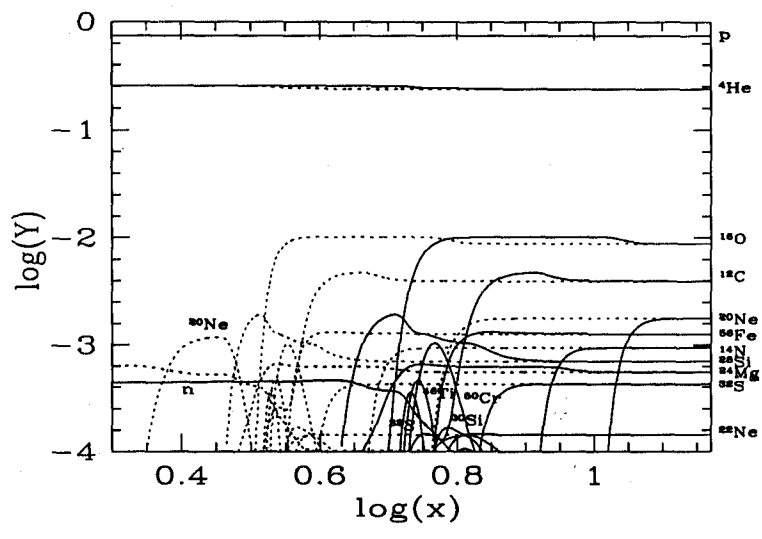


Fig. 1.5a

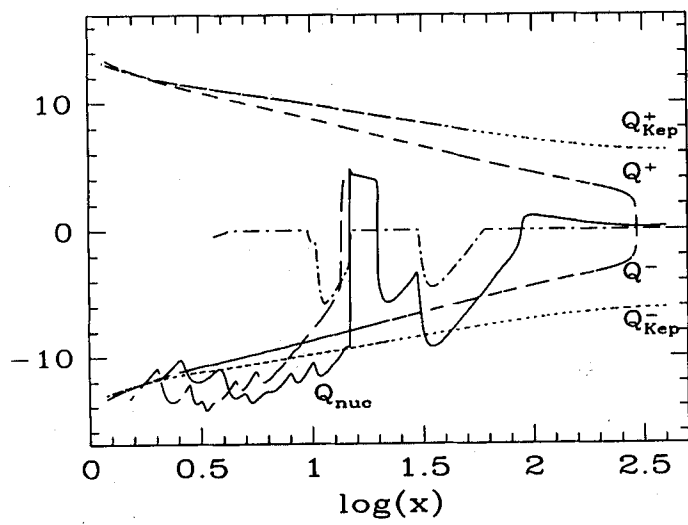


Fig. I.5b

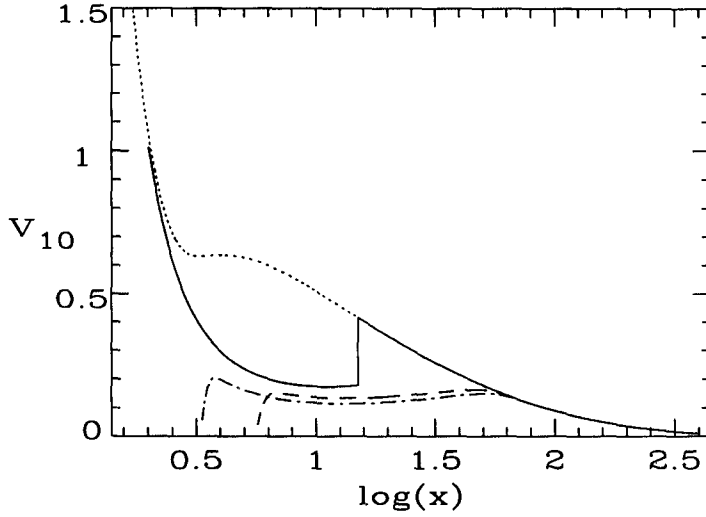


Fig. I.5c

Fig. I.5.: Variation of (a) matter abundance Y_i in logarithmic scale, (b) various forms of height-integrated specific energy release and absorption rates and (c) velocity (in unit of 10^{10}cm s^{-1}) when the model parameters are $M = 10^6 M_\odot$, $\dot{m} = 1.0$, $\alpha_\Pi = 0.07$ as functions of logarithmic radial distance (x in unit of Schwarzschild radius). See text and TABLE I.2 for other parameters of Case A.3. In (a) solutions in the stable branch with shock are solid curves and those without the shock are short dashed. Curves in (b) are described in the text. Basic conclusions are as in the previous case. In (c), dot-dashed curve and dashed curve are drawn when nuclear energy is taken into account.

are involved. The three successive dips are due to dissociation of D , ${}^3\text{He}$ and ${}^4\text{He}$ respectively.

Below $x = 10$, $|Q_{\text{nuc}}|$ is larger compared to Q^+ by 3-4 orders of magnitude. This is because of the superposition of a large number of photo-dissociation effects. We expect that in this case the disk would be unstable. This is exactly what we see. In Fig. I.5c, we show the effects of nuclear reactions more clearly. The dotted curve and the solid curve are, as in Fig. I.4b, the variation of velocity for the solution without and with shock, respectively. The dot-dashed curve represents velocity variation without shock when nuclear reaction is included. The dashed curve is the corresponding solution when nucleosynthesis of the shocked branch is included. Both branches are unstable since the steady flow is subsonic at the inner edge. In these cases, the flow is expected to pass through the inner sonic point in a time-dependent manner and some sort of quasi-periodic oscillations cannot be ruled out.

3.2.2 Nucleosynthesis in Hot Flows

Case B.1: This case is chosen with such a set of parameters that a standing shock forms at $x_s = 13.9$. A very low accretion rate is chosen so that the Compton cooling is negligible and the flow remains very hot (Comptonization factor $F_{\text{Compt}} = 0.1$). We show the results both for the shock-free branch (short dashed) and the shocked branch (solid) of the solution. Figure I.6a shows the comparison of the temperatures and densities (in unit of 10^{-20} gm cm $^{-3}$ to bring in the same plot). Figure I.6b shows the comparison of the radial velocities. This behaviour is similar to that shown in Case A.2. Because the temperature is suitable for photo-dissociation, we chose a very small set of species in the network (only 21 species up to ${}^{11}\text{B}$ are chosen). Figure I.6c shows the comparison of the abundances of proton (p), ${}^4\text{He}$ and neutron (n). In the

absence of the shock, the breaking up of ${}^4\text{He}$ into n and p takes place much closer to the black hole, while the shock hastens it due to higher temperature and density. Although initially the flow starts with $Y_p = 0.7425$ and $Y_{{}^4\text{He}} = 0.2380$, at the end of the simulation, only proton ($Y_p \sim 0.8786$) and neutron ($Y_n \sim 0.1214$) remain and the rest of the species become insignificant.

Figure I.6d shows the comparison of the height-integrated nuclear energy release and absorption (units are as Fig. I.3d). As the flow leaves the Keplerian disk at $x_K = 481.4$, the deuterium and ${}^9\text{Be}$ are burnt instantaneously at the cost of some energy from the disk. At the end of deuterium burning at around $x = 200$, the rp and proton capture processes (mainly via ${}^{11}\text{B}(p, \gamma){}^3\text{He}$ which releases significant energy) and neutron capture (${}^3\text{He}(n, p)\text{T}$) take place, but further in, ${}^3\text{He}$ (via ${}^3\text{He}(\gamma, p)\text{D}$) first and ${}^4\text{He}$ (mainly via ${}^4\text{He}(\gamma, n){}^3\text{He}$ and ${}^4\text{He}(\gamma, p)\text{T}$, $\text{T}(\gamma, n)\text{D}$) subsequently, are rapidly dissociated. As soon as the entire helium is burnt out, the energy release/absorption becomes negligible. This is because there is nothing left other than free protons and neutrons and hence no more reactions take place and no energy is released or absorbed. The solid curve is for the branch with a shock and the very long dashed curve is for the shock-free branch. Inclusion of an opacity factor (which reduces photo-dissociation) shifts the burning towards the black hole. The disk is found to be completely stable even in presence of nucleosynthesis.

Case B.2: As discussed in §3.1.1, in extreme hard states, a black hole may accrete very little matter in the Keplerian component and very large amount of matter in the sub-Keplerian component. To simulate this we used B.1 parameters, but $\dot{m} = 4$. The resulting solution is found to be unstable when shocks are present. In Fig. I.6b, we superimposed velocity variation without nuclear energy (same as with nuclear energy

as far as Case B.1 is concerned) and with nuclear energy. The dash-dotted curve next to the un-shocked branch and dashed curve next to the shocked branch show the resulting deviation. While the branch without shock still remains stable, the other branch is distinctly unstable as the steady-state solution is sub-sonic at the inner edge. The only solution available must be non-steady with oscillations near the sonic point.

Case B.3: In this case, accretion rate is chosen to be even smaller ($\dot{m} = 0.001$) and the polytropic index is chosen to be $5/3$. The maximum temperature reaches $T_9^{\max} = 47$. After leaving the Keplerian flow, the temperature and velocity of the flow monotonically increase. Because of excessive temperature, D and 3He are photo-dissociated immediately after the flow leaves the Keplerian disk at $x_K = 84.4$. At around $x = 30$, all 4He is photo-dissociated exactly as in Case B.1. Subsequently, the flow contains only protons and neutrons and there is no more energy release from the nuclear reactions. This behaviour is clearly seen in Fig. I.7. The notations are the same as in the previous run. This ultra-hot case is found to be stable since the energy release took place far away from the black hole where the matter was moving slowly and therefore the rate (Q_{nuc}) was not high compared to that due to viscous dissipation (units are as Fig. I.3d).

Case B.4: This is another case where the accretion rate is chosen small as 0.001 and polytropic index is chosen as $5/3$ as in previous case. Apart from these, because of small viscosity (0.01), the disk is so hot that the sub-Keplerian flow deviates from a Keplerian disk farther away at $x = 85.1$. Similar to case B.3, here 4He dissociates completely at a distance of around $x = 25$ where the density and temperature are $\rho = 2.29 \times 10^{-11} \text{ gm cm}^{-3}$ and $T = 6.3 \times 10^9 \text{ K}$. As the nuclear energy curve is similar

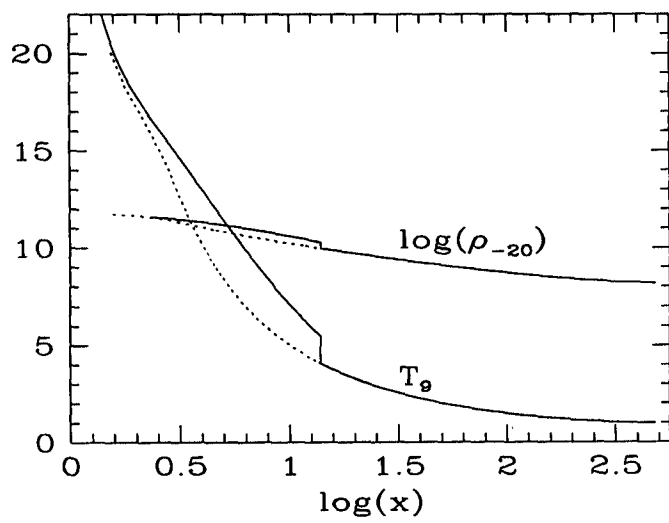


Fig. I.6a

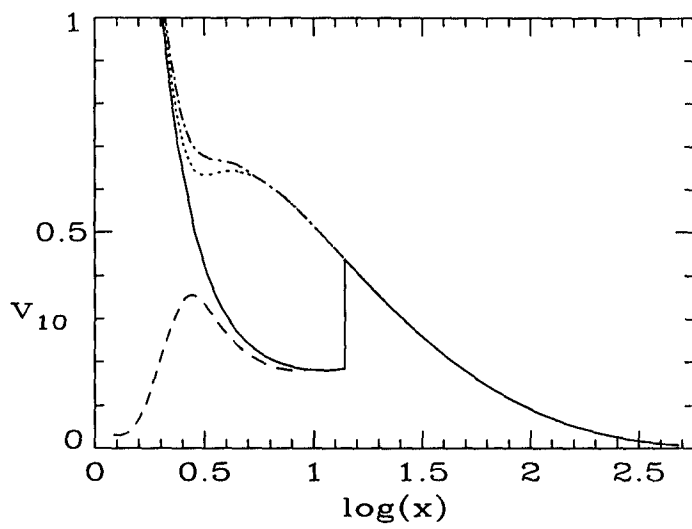


Fig. I.6b

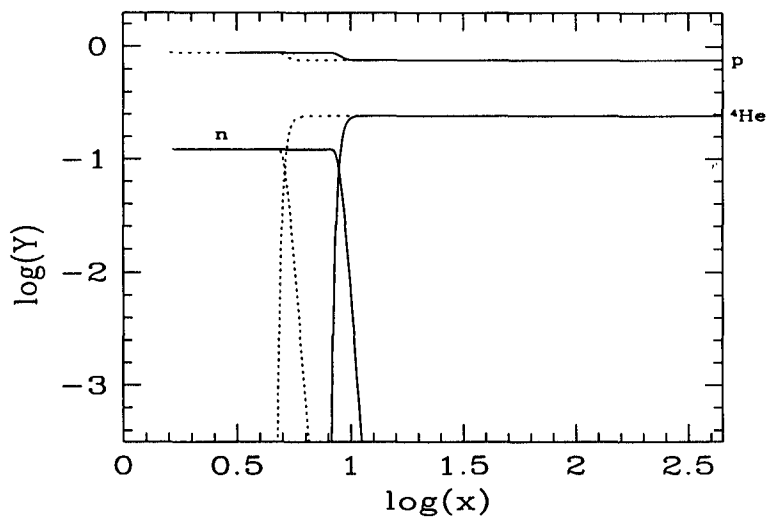


Fig. I.6c

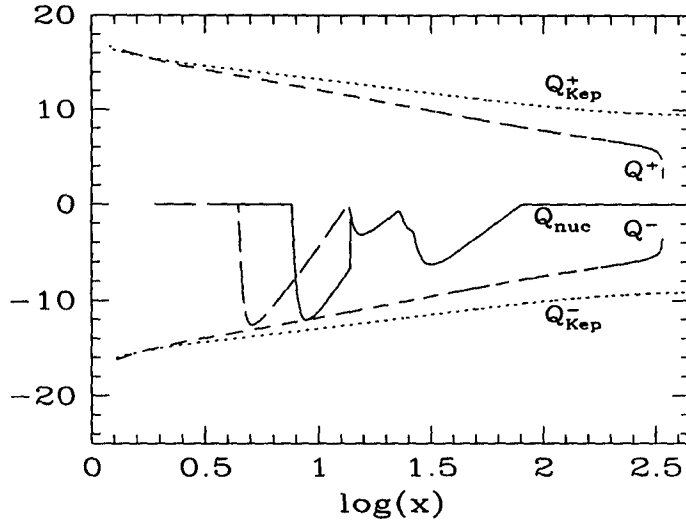


Fig. I.6d

Fig. I.6. Variation of (a) ion temperature (T_9) and density (ρ_{-20}), (b) radial velocity v_{10} , (c) matter abundance Y_i in logarithmic scale and (d) various forms of height-integrated specific energy release and absorption rates when the model parameters are $M = 10M_\odot$, $\dot{m} = 0.01$, $\alpha_\Pi = 0.05$ as functions of logarithmic radial distance (x in unit of Schwarzschild radius). See text and TABLE I.2 for other parameters of Case B.1 which is considered here. Solutions in the stable branch with shock are solid curves and those without the shock are short dashed in (a-c). Curves in (d) are described in the text. The ultra-hot temperature of the flow photo-dissociates ${}^4\text{He}$ into protons and neutrons. The shocked branch (which is stable) causes such dissociation farther out from the black hole than the unstable shock-free branch. In (b), dot-dashed curve and dashed curve are drawn when nuclear energy is taken into account and $\dot{m} = 4$ is chosen (Case B.2).

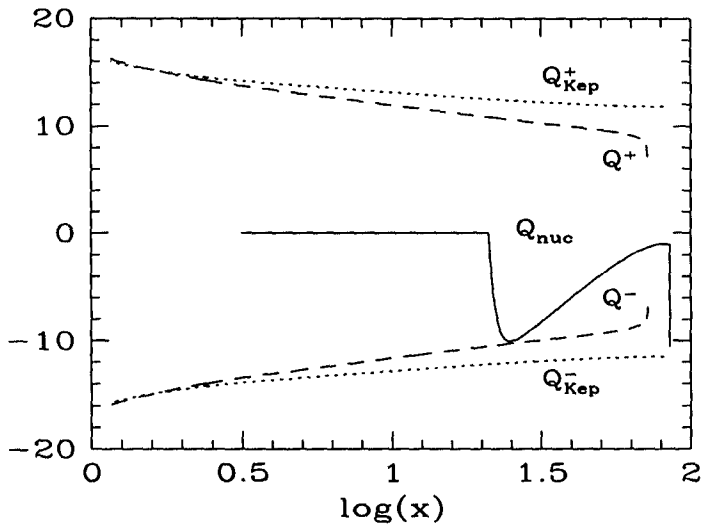


Fig. I.7. Specific nuclear energy rate variation curve (solid) for a $\gamma = 5/3$, ultra-hot case ($T_9^{\max} = 44$) as functions of logarithmic radial distance (x in unit of Schwarzschild radius). The entire initial abundance is photo-dissociated at $x \gtrsim 30$. The viscous energy generation curve (Q^+) and absorption curve (Q^-) [both long dashed] are presented for comparison. Q_{Kep}^{\pm} (dotted) curves are the specific energy generation and absorption rates provided the inner disks were Keplerian. Q s are in unit of $\text{ergs cm}^{-2} \text{sec}^{-1}$. See TABLE I.2 for parameters of Case B.3.

to the case B.3, Fig. I.7 (except the locations where different burnings take place), we do not show it again. Maximum temperature attained in this case is $T^{\max} = 37 \times 10^9$ K. Both the neutron and proton are enhanced for $x \lesssim 25$. This disk is consisting a large amount of neutron although initially we started with zero abundance of it.

Case B.5: In this case, the net accretion rate is low ($\dot{m} = 0.01$) but viscosity is high and the efficiency of emission is intermediate ($f = 0.2$). That means that the temperature of the flow is high ($F_{\text{Compt}} = 0.1$, maximum temperature $T_9^{\max} = 13$). Matter deviates from a Keplerian disk at around $x_K = 8.4$. Assuming that the high viscosity is due to stochastic magnetic field, protons would be drifted towards the black hole due to magnetic viscosity, but the neutrons will not be drifted (Rees et al. 1982). They will generally circle around the black hole till they decay. This principle has been used to do the simulation in this case. The modified composition in one sweep is allowed to interact with freshly accreting matter with the understanding that the accumulated neutrons do not drift radially. After few iterations or sweeps the steady distribution of the composition is achieved. Figure I.8a shows the neutron distribution in the sub-Keplerian region. The formation of a ‘neutron torus’ is very apparent in this result. In fact, the formation of a neutron disk is very generic in all the hot accretion flows as also seen in Cases B.1-B.3 (details are given in later §3.3). The nuclear reactions leading to the neutron torus formation are exactly same as previous cases and are not described here. However, we wish to present the energy release curve in Fig. I.8b, only to impress the fact that the degree of absorption of nuclear energy from a given annulus of the disk is generally correlated with the amount of neutrons deposited in that annulus. This is because no significant reactions other than photo-dissociation are taking place in the disk.

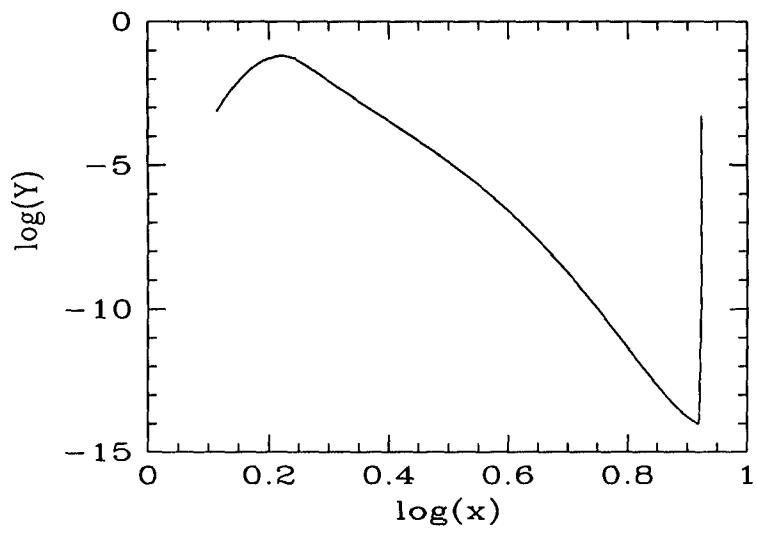


Fig. I.8a

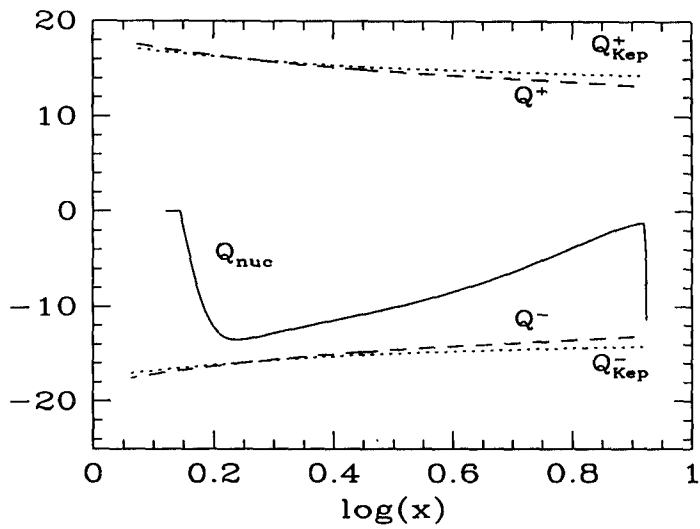


Fig. I.8b

Fig. I.8. Formation of a *neutron torus* in a hot inflow. (a) Neutron abundance (b) Various height-integrated specific energy release and absorption rates as a function of the logarithmic radial distance (x in unit of Schwarzschild radius, units same as in Fig. I.3d). Note the correlation of the neutron abundance with the degree of nuclear energy absorption. This is due to the endothermic nature of the photo-dissociation. See, TABLE I.2 for parameters of Case B.4.

Case B.6: This is another case where the viscosity is due to the stochastic magnetic lines. We choose again a very high viscosity ($\alpha = 0.2$) in the sub-Keplerian regime. The cooling is chosen marginally inefficient. It is not as inefficient as other ultra-hot cases but still is not as efficient as in a Keplerian disk: $Q^- \sim 0.9Q^+$ which is same as that in intermediate hot cases (Cases A). Although in this case residence time is small but as the cooling time-scale is larger than the infall time-scale the disk is hot enough to make it one of the ultra-hot case. The specific angular momentum at the inner edge is, $\lambda_{in} = 1.65$ (in unit of $2GM/c$). The flow deviates from a Keplerian disk at 4.2 Schwarzschild radii. It is to be noted that Q^- includes *all possible* types of cooling, such as bremsstrahlung, Comptonization as well as cooling due to neutrino emissions. We assume that the flow is magnetized so that only ions have larger viscosity. Here also the neutron torus is formed in the disk. As the features are same as the case B.5 we do not show the figures.

3.2.3 Nucleosynthesis in Cooler Flows

Case C.1: Here we choose a high-viscosity flow with a very high accretion rate. Matter deviates from the Keplerian disk very close to the black hole, $x_K = 4.8$. The flow in the centrifugal barrier is cooler (maximum temperature $T_9^{\max} = 0.8$). Figure I.9a shows the variation of the temperature and density (in unit of 10^{-5} gm cm $^{-3}$ to bring in the same plot) of the flow. Figure I.9b shows the velocity variation. Clearly, high viscosity removes the centrifugal barrier completely and matter falls in almost freely. Due to very short residence time, no significant change in the composition takes place. Only a small amount of proton capture (mainly due to $^{11}\text{B}(p, \gamma)^{12}\text{C}$, $^{16}\text{O}(p, \alpha)^{13}\text{N}$, $^{15}\text{N}(p, \alpha)^{12}\text{C}$, $^{18}\text{O}(p, \alpha)^{15}\text{N}$, $^{19}\text{F}(p, \alpha)^{16}\text{O}$) takes place. A small amount of deuterium dissociation also takes place, but it does not change the energetics significantly. Figure

I.9c shows the height-integrated energy release curves (units are same as in Case A.1). Since the contribution due to nuclear reactions (Q_{nuc}) is very much smaller than the viscous energy release, the flow is not found to be unstable in this case.

Case C.2: This is a test case for the proto-galactic accretion flow. In the early phase of galaxy formation, the supply of matter is high, and the temperature of the flow is very low. The viscosity may or may not be very high, but we choose very low (presumably, radiative) viscosity ($\alpha = 10^{-4}$). The motivation is to use similar parameters as were used by Jin et al. (1989) while studying the nucleosynthesis in thick accretion disks. The central mass $M = 10^6 M_{\odot}$, the maximum temperature is, $T_9^{\text{max}} \sim 0.2$ and the Comptonization factor $F_{\text{Compt}} = 0.001$. The temperature variation is similar to Fig. I.3a when scaled down by a factor of 30 (basically by the ratio of the F_{Compt} values). The velocity variation is similar to Fig. I.3b and is not repeated here. Due to the low temperature, there is no significant change in the nuclear abundance. Note that since thick accretion disks are rotation dominated, the residence time was very long in the simulation of Chakrabarti et al. (1987) and there *was* significant change in composition even at lower temperatures. But in this case the flow radial velocity is very high and the residence time is shorter. The nuclear energy release is negligible throughout and is not shown.

3.3 Formation of Neutron Disk and Neutron Torus

To produce neutron disk and torus we start with a relativistic flow (polytropic index $\gamma = 4/3$) with the low accretion rate. We use the mass of the central black hole to be $M = 10M_{\odot}$ throughout. We choose a very high viscosity and the corresponding α parameter (Shakura & Sunyaev 1973) is 0.2 in the sub-Keplerian regime. Due

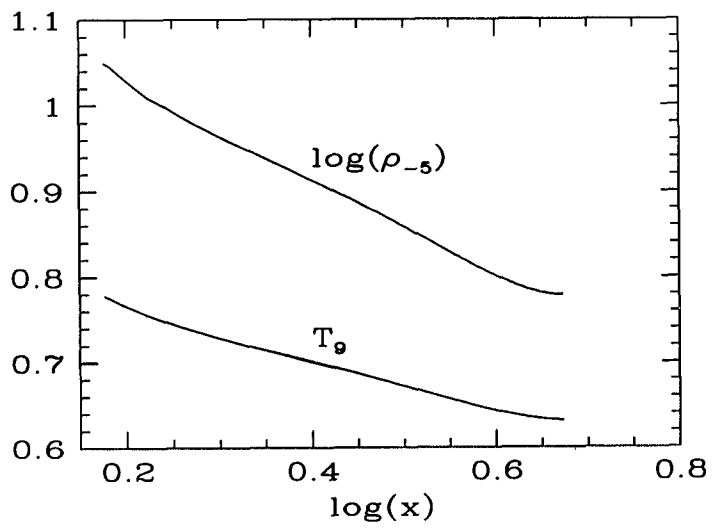


Fig. I.9a

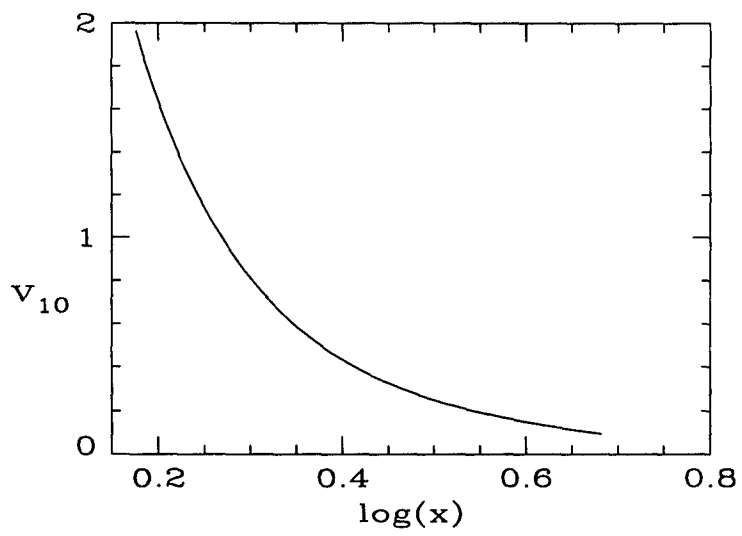


Fig. I.9b

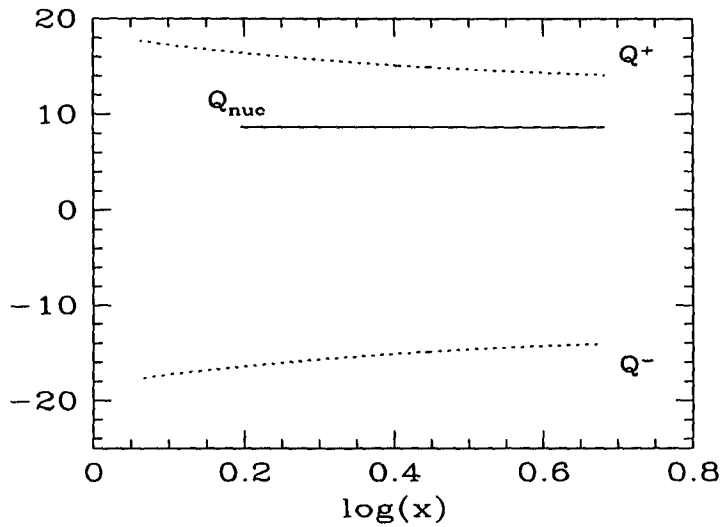


Fig. I.9c

Fig. I.9. Variation of (a) ion temperature (T_9) and density (ρ_{-5}) (b) radial velocity v_{10} , and (c) various forms of specific energy release and absorption rates (units same as in Fig. I.3d) when the model parameters are $M = 100M_\odot$, $\dot{m} = 10$, $\alpha_{\text{II}} = 0.2$ as functions of logarithmic radial distance (x in unit of Schwarzschild radius). See text and TABLE I.2 for other parameters of case C.1, considered here. Not much nucleosynthesis takes place in this case.

to poor supply of the soft photons from Keplerian disk, the Comptonization in the boundary layer is not complete; we assume a standard value of Comptonization factor (Chakrabarti & Titarchuk 1995) in this regime: $F_{Comp} \sim 0.1$, i.e., ions (in the radiation-hydrodynamic solution) are one-tenth as hot as obtained from the hydrodynamic solutions. (For high accretion rate, $\dot{m} \gtrsim 0.3$, $F_{Comp} \sim 0.001$ and ions and electrons both cool to a few KeV ($\sim 10^7$ K)). In the parameter regions for all cases of Case B as mentioned in §3.2.2 either neutron disk or torus may form. Here we will discuss these formations in detail. For the case B.5 the typical density and temperature near the marginally stable orbit at $x = 3$ are $8.5 \times 10^{-8} \text{ gm cm}^{-3}$ and $7.5 \times 10^9 \text{ K}$ respectively where the thermonuclear depletion rates $N_i \langle \sigma v \rangle$ for the $D(\gamma, p)n$, ${}^4\text{He}(\gamma, D)D$ and ${}^4\text{He}(\alpha, p){}^7\text{Li}$ reactions are given by $1.6 \times 10^{14} \text{ gm}^{-1} \text{ s}^{-1}$, $4 \times 10^{-3} \text{ gm}^{-1} \text{ s}^{-1}$ and $1.9 \times 10^{-12} \text{ gm}^{-1} \text{ s}^{-1}$ respectively. Here, N_i is the number density of the reactant elements (say for i th isotope) given as Eqn. (I.2), σ is the reaction cross-section, v is the Maxwellian average velocity of the reactants and $\langle \sigma v \rangle$ is the reaction rate. At these rates, the time-scale of these reactions are given by, $4 \times 10^5 \text{ sec}$, $5 \times 10^{11} \text{ sec}$ and $4 \times 10^{20} \text{ sec}$ respectively indicating that the deuterium burning is the fastest of the reactions. In fact, it would take about a second to burn initial deuterium with $Y_D = 10^{-5}$. The ${}^7\text{Li}$ does not form at all because the ${}^4\text{He}$ dissociates to D much faster.

The above depletion rates have been computed assuming Planckian photon distribution corresponding to ion temperature T_p . The wavelength λ_{Planck} at which the brightness is highest at $T = T_p$ is shown in Fig. I.10 in the dashed curve (in unit of 10^{-11} cm). Also shown is the average wavelength of the photon $\lambda_{Compton}$ (solid curve) obtained from the spectrum $F_\nu \sim \nu^{-\alpha}$. The average has been performed over

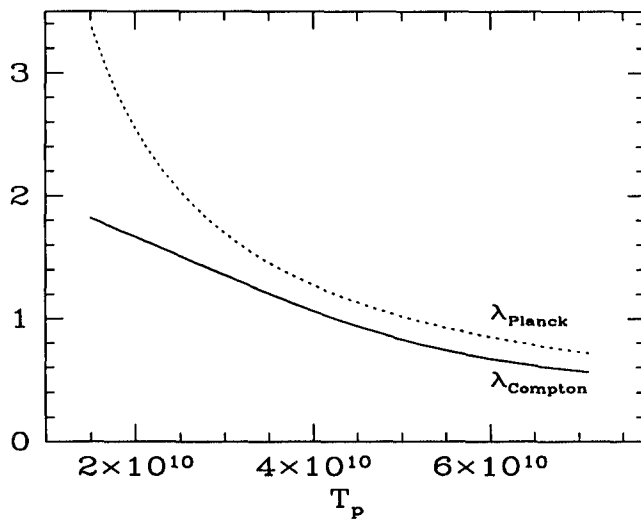


Fig. I.10. Comparison of wavelength λ_{Planck} at peak blackbody intensity (dotted) with the mean (taken between 2 and 50KeV) wavelength of the Comptonized power law spectrum (solid) of the emitted X-rays. Wavelengths are measured in unit of 10^{-11} cm.

the region 2 to 50KeV of the photon energy in which the hard component is usually observed,

$$\langle F_\nu \rangle = \frac{\int_{\nu_{min}}^{\nu_{max}} F_\nu d\nu}{\int_{\nu_{min}}^{\nu_{max}} d\nu} = \nu_{Compton}^{-\alpha} \quad (I.50)$$

where, ν_{min} and ν_{max} are computed from 2 and 50KeV respectively. The average becomes a function of the energy spectral index α ($F_\nu \propto \nu^{-\alpha}$), which in turn depends on the ion and electron temperatures of the medium. We follow Chakrabarti & Titarchuk (1995) to compute these relations. We note that $\lambda_{Compton}$ is *lower* compared to λ_{Planck} for all ion temperatures we are interested in. Thus, the disintegration rates and other reaction rates with Planckian distribution that we employed in all of our computations are clearly a lower limit. Our assertion of the formation of a neutron disk and torus and other elements should be strengthened when Comptonization is included.

Figure I.11a shows the result of the numerical simulation for the disk model mentioned above. Logarithmic abundance of neutron Y_n is plotted against the logarithmic distance from the black hole. First simulation produced the dash-dotted curve for the neutron distribution, forming a miniature neutron torus. As fresh matter is added to the existing neutron disk, neutron abundance is increased as neutrons do not fall in rapidly. Thus the simulation is repeated several times in order to achieve a converging steady pattern of the neutron disk as was described in §3.2.2. Although fresh neutrons are deposited, the stability of the distribution is achieved through neutron decay and neutron capture reactions. Results after every ten iterations are plotted. The equilibrium neutron torus remains around the black hole indefinitely. The neutron abundance is clearly very significant (more than ten per cent!).

There are another two cases (B.3 & B.4) to have large neutron abundance where

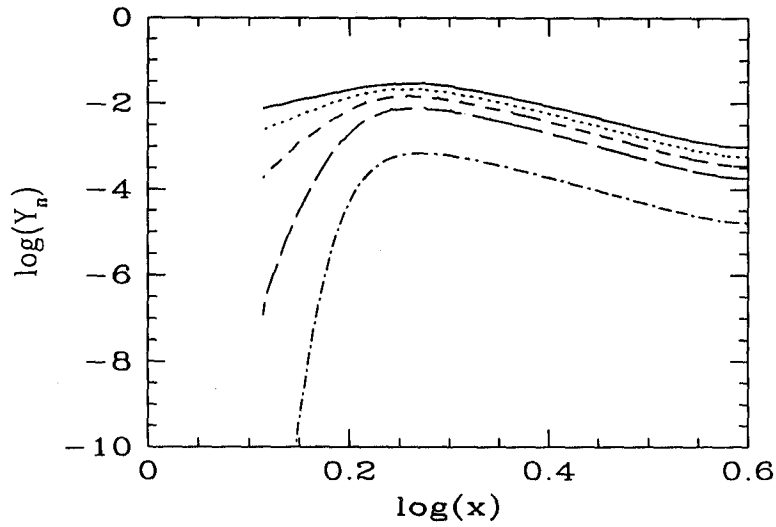


Fig. I.11a. Formation of a steady *neutron torus* in a hot inflow. Intermediate iteration results (from bottom to top: 1st, 11th, 21st, 31st and 41st iterations respectively) of the logarithmic neutron abundance Y_n in the flow as a function of the logarithmic radial distance (x in unit of Schwarzschild radius) are shown.

the accretion rate is smaller ($\dot{m} = 0.001$), the viscosity is so small ($\alpha = 0.01$) and the disk is so hot that the sub-Keplerian flow deviates from a Keplerian disk farther away. The polytropic index is that of a mono-atomic (ionized) hot gas, $\gamma = 5/3$. The Compton cooling factor is as above since it is independent of the accretion rates as long as the rate is low (Sunyaev & Titarchuk 1980; Chakrabarti & Titarchuk 1995). The cooling is assumed to be very inefficient because of lower density.

In Fig. I.11b, we show the logarithmic abundances of proton (p), helium (4He) and neutron (n) as functions of the logarithmic distance from the black hole. From the figure existence of a neutron disk (disk consisting of neutron mainly) is very apparent. The neutron disk also remains stable despite of neutron decay, since new matter moves in to maintain equilibrium.

3.4 Nucleosynthesis Induced Instability?

Chakrabarti et al. (1987), while studying nucleosynthesis in cooler, mainly rotating disks, suggested that as long as the nuclear energy release is smaller than the gravitational energy release, the disk would be stable. Here, we find that this suggestion is valid in presence of the advective term also. Indeed, even when momentarily the nuclear energy release or absorption is as high as the gravitational energy release (through viscous dissipation), the disk may be stable. For instance, in Case A.1 (Fig. I.3d) at around $x = 4$ these rates are similar. Yet the velocity, temperature and density distributions (Fig. I.3a-b) remain unchanged. In Case A.3, Q_{nuc} is several magnitudes greater than viscous energy release Q^+ and the thermodynamic quantities are indeed disturbed to the extent that the flow with same injected quantities (with the same density, velocity and their gradients) at the outer edge does not become

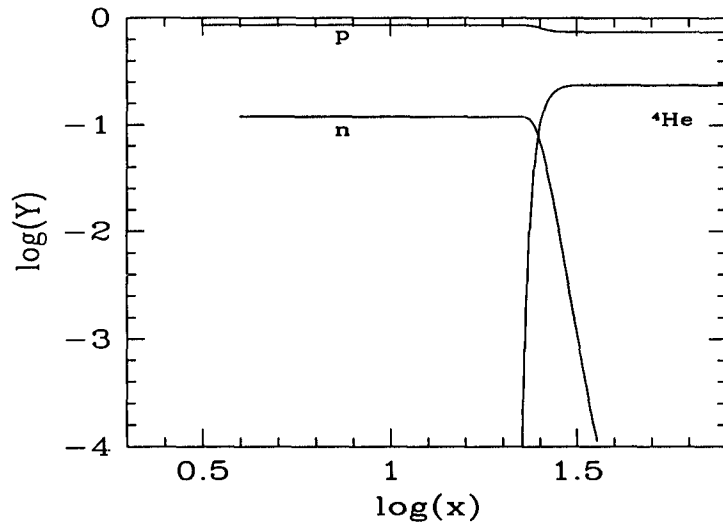


Fig. I.11b. Variation of matter abundance Y_i in logarithmic scale in a hot flow around a galactic black hole. Entire ${}^4\text{He}$ is photo-dissociated at around $x = 30x_g$ and the steady neutron disk is produced for $x < 30$ which is not accreted.

supersonic at the inner edge. In these cases, the flow must be unsteady in an effort to search for the ‘right’ sonic point to enter into the black hole. On the other hand, ultra-hot cases like B.2 show deviation in non-shocked solution while the shocked solution is unstable.

The general behaviour suggests that the present model of accretion disks is more stable under nuclear reactions compared to the earlier, predominantly rotating model. Here, the radial velocity (v) spreads energy release or absorption radially to a distance $v\tau_D(\rho, T) = vN_D/\dot{N}_D$ cm, where, N_D is the number density of, say, Deuterium and \dot{N}_D is its depletion rate. For a free fall, $v \sim x^{-1/2}$, while for most nuclear reactions, $\tau_D(\rho, T) \sim x^n$, with $n \gg 1$ (since reaction rates are strongly dependent on density and temperature). Thus, Q_{nuc} for the destruction of a given element spreads out farther away from the black hole, but steepens closer to it. Large dQ_{nuc}/dx causes instability since the derivatives such as dv/dx at the inner regions (including the sonic point) become imaginary.

4 Implications of the Nucleosynthesis in the Accretion Disk

So far, we explored the possibility of nuclear reactions in inner regions of the accretion flows. Because of high radial motion and ion pressure, matter deviates from a Keplerian disk close to the black hole. The temperature in this region is controlled by the efficiencies of bremsstrahlung and Comptonization processes (Chakrabarti & Titarchuk 1995; Chakrabarti 1997) and possible heating by magnetic fields (Shapiro 1973): for a higher Keplerian rate and higher viscosity, the inner edge of the Keplerian component comes closer to the black hole and the sub-Keplerian region becomes cooler (Chakrabarti & Titarchuk 1995). The nucleosynthesis in this soft state of the black hole is quite negligible. However, as the viscosity is decreased to around 0.05 or less, the inner edge of the Keplerian component moves away and the Compton cooling becomes less efficient due to the paucity of the soft photons. The sub-Keplerian region, though cooler by a factor of about $F_{\text{Compt}} = 0.01$ to 0.03 from that of the value obtained through purely hydrodynamical calculations of Chakrabarti (1996a), is still high enough to cause significant nuclear reactions to modify compositions. The composition changes very close to the black hole, especially in the centrifugal-pressure-supported denser region, where matter is hotter and slower.

The degree of change in compositions which takes place in the Group A and B calculations, is very interesting and its importance must not be underestimated. Since the centrifugal-pressure-supported region can be treated as an effective surface of the black hole which may generate winds and outflows in the same way as the stellar surface (Chakrabarti 1998a,b,c; Das & Chakrabarti 1999), one could envisage that the winds produced in this region would carry away a modified composition and

contaminate the atmosphere of the surrounding stars and the galaxy in general.

One could estimate the contamination of the galactic metallicity due to nuclear reactions. For instance, in Case A.1, ^{12}C , ^{16}O , ^{20}Ne , ^{30}Si , ^{44}Ca and ^{52}Cr are found to be over-abundant in some regions of the disk. Assume that, on an average, all the N stellar black holes are of equal mass M and have a non-dimensional accretion rate of around $\dot{m} \sim 1$ ($\dot{m} = \dot{M}/\dot{M}_{\text{Edd}}$). Let ΔY_i (few times 10^{-3}) be the typical change in composition of this matter during the run and let f_w be the fraction of the incoming flow that goes out as winds and outflows (could be from ten percent to more than a hundred percent when disk evacuation occurs, see Das & Chakrabarti, 1999), then in the lifetime of a galaxy (say, 10^{10} yrs), the total ‘change’ in abundance of a particular species deposited in the surroundings by all the stellar black holes is given by:

$$\langle \Delta Y_i \rangle_{\text{small}} \cong 10^{-7} \left(\frac{\dot{m}}{1} \right) \left(\frac{N}{10^6} \right) \left(\frac{\Delta Y_i}{10^{-3}} \right) \left(\frac{f_w}{0.1} \right) \left(\frac{M}{10 M_\odot} \right) \left(\frac{T_{\text{gal}}}{10^{10}} \text{Yr} \right) \left(\frac{M_{\text{gal}}}{10^{11} M_\odot} \right)^{-1}. \quad (\text{I.51})$$

The subscript ‘small’ is used here to represent the contribution from small black holes. We also assume a conservative estimation that there are 10^6 such stellar black holes in a galaxy, the mass of the host galaxy is around $10^{11} M_\odot$ and the lifetime of the galaxy during which such reactions are going on is about 10^{10} Yrs. We also assume that $\Delta Y_i \sim 10^{-3}$ and a fraction of ten percent of matter is blown off as winds. The resulting $\langle \Delta Y_i \rangle \sim 10^{-7}$ may not be very significant if one considers averaging over the whole galaxy. However, for a lighter galaxy $\langle \Delta Y_i \rangle$ could be much higher. For example, for $M_{\text{gal}} = 10^9 M_\odot$, $\langle \Delta Y_i \rangle \sim 10^{-5}$. This would significantly change the average abundances of ^{30}Si , ^{44}Ca and ^{52}Cr . On the other hand, if one concentrates on the region of the outflows only, the change in abundance is the same as in the disk, and should be detectable (e.g., through line emissions). One such observation of stronger iron-line emission was reported for SS433 (Lamb et al. 1983; see also

Arnould & Takahashi 1999, for a recent discussion on galactic contaminations).

When we consider a case like A.3, we find that ^{12}C , ^{16}O , ^{20}Ne , and ^{28}Si are increased by about 10^{-3} in some regions. In this case, the average change of abundance due to accretion onto the massive black hole situated at the galactic centre would be,

$$\langle \Delta Y_i \rangle_{\text{big}} \cong \text{few} \times 10^{-8} \left(\frac{\dot{m}}{1}\right) \left(\frac{\Delta Y_i}{10^{-3}}\right) \left(\frac{f_w}{0.1}\right) \left(\frac{M}{10^6 M_\odot}\right) \left(\frac{T_{\text{gal}}}{10^{10}} Yr\right) \left(\frac{M_{\text{gal}}}{10^{11} M_\odot}\right)^{-1}. \quad (\text{I.52})$$

Here, we have put ‘big’ as the subscript to indicate the contribution from the massive black hole. Even for a lighter galaxy, e.g., of mass $M_{\text{gal}} = 10^9 M_\odot$, $\Delta Y_i = 10^{-6}$ which may not be significant. If one considers only the regions of outflows, contamination may not be negligible.

A few related questions have been asked lately: Can lithium be produced in black hole accretion? We believe not. The spallation reactions (Jin 1990; Yi & Narayan 1997) may produce such elements assuming that a helium beam hits a helium target in a disk. Using a full network, rather than only He-He reaction, we find that the hotter disks where spallation would have been important also photo-dissociate (particularly due to the presence of photons from the Keplerian disk) helium to deuterium and then to proton and neutron before any significant lithium could be produced. Even when photo-dissociation is very low (when the Keplerian disk is far away, for instance), or when late-type stellar composition is taken as the initial composition, we find that the ^7Li production is insignificant, particularly if one considers more massive black holes ($M \sim 10^8 M_\odot$).

Recently, it has been reported by several authors (Martin et al. 1992; 1994; Fillipenko et al. 1995; Harlaftis et al. 1996) that a high abundance of Li is observed in late type stars which are also companions of black hole and neutron star candidates. This is indeed surprising since the theory of stellar evolution predicts that these

stars should have at least a factor of ten lower Li abundance. These workers have suggested that this excess Li could be produced in the hot accretion disks. However, in Mukhopadhyay (1998, 1999), Chakrabarti & Mukhopadhyay (1999) as well as in our Cases A and B computations we showed that Li is not likely to be produced in accretion disks. Indeed, we ran several cases with a mass fraction of He as high as 0.5 to 0.98, but we are still unable to produce Li with a mass fraction more than 10^{-10} . Recent work of Guessoum & Kazanas (1999) agrees with our conclusion that profuse neutrons would be produced in the disk. They farther suggested that these energetic neutrons can produce adequate Li through spallation reactions with the C , N , and O that is present in the atmosphere of these stars. For instance, in Cases B.1 and B.3 we see that neutrons could have an abundance ~ 0.1 in the disk. Since the production rate is similar to what Guessoum & Kazanas (1999) found, Li should also be produced on stellar surface at a similar rate.

What would be the neutrino flux on earth if nucleosynthesis does take place? The energy release by neutrinos (the pair neutrino process, the photoneutrino process and the plasma neutrino process) can be calculated using the prescription of Beaudet et al. (1967), (see also Itoh et al. 1996) provided the pairs are in equilibrium with the radiation field. However, in the case of accretion disks, the situation is significantly different from that inside a star (where matter is in static equilibrium). Because of rapid infall, matter density is much lower and the infall time-scale could be much shorter compared to the time-scale of various neutrino processes, especially the pair and photo-neutrino processes. As a result, the pair density need not attain equilibrium. One important thing in this context is the opacity (τ_{pair}) of the pair process. Following treatments of Colpi et al. (1984) we find that $\tau_{\text{pair}} < 1$ for all our cases, and

therefore pair process is expected to be negligible (for Case B.2, τ_{pair} is the highest [0.9]). Park (1990a,b), while studying pair creation processes in spherical accretion, shows that even in the most favourable condition, the ratio of positron (n_+) and ion (n_i) is no more than 0.05. A simple analysis suggests that neutrino production rate is many orders of magnitude smaller compared to what the equilibrium solutions of Beaudet et al. (1967) and Itoh et al. (1996) would predict. Thus, we can safely ignore the neutrino luminosity.

When the nuclear energy release or absorption is comparable to the gravitational energy release through viscous processes, we find that the disk is still stable. Stability seems to depend on how steeply the energy is released or absorbed in the disk. This in turn depends on $\tau_D v$, the distance traversed inside the disk by the element contributing the highest change of energy before depleting significantly. Thus, an ultra-hot case (Group B) can be stable even though a hot (Group A) case can be unstable as we explicitly showed by including nuclear energy release. In these ‘unstable’ cases, we find that the steady flow does not satisfy the inner boundary condition and becomes subsonic close to the horizon. This implies that in these cases the flow must become non-steady, constantly searching for the supersonic branch to enter into the black hole. This can induce oscillations as have been found elsewhere (Ryu et al. 1997). In such cases, one is required to do time dependent simulations (e.g., Molteni et al. 1994, 1996) including nuclear reactions.

REFERENCES-I

- Abramowicz M., 1988, *ApJ* 332, 646
- Agrawal S.K. et al., 1972, *Astrophys. & Space Sc.* 18, 408
- Anders E., Ebihara M., 1982, *Geochim. Cosmochim. Acta* 46, 2363
- Applegate J., Hogan C., Scherrer R., 1987, *Phys. Rev. D* 35, 115
- Arai K., Hashimoto M., 1992, *A&A* 254, 191
- Arnett W.D., Truran J., 1969, *ApJ* 157, 339
- Arnould M., Takahashi K., 1999, *Rep. Prog. Phys.* 62, 395
- Audouze J., 1989, *Proc. Yamada Conference*, Hayakawa S., Sato K. (eds.), Editions Universal Academy Press: Japan, 19
- Bania T.M., Rood R.T., Wilson T.L., 1987, *ApJ* 323, 30
- Beaudet G., Petrosian V., Salpeter E.E., 1967, *ApJ* 150, 979
- Beckman J.E., Pagel B.E.J., 1989, *Evolutionary Phenomena in Galaxies*, Cambridge University Press: Cambridge, 201
- Bisnovatyi-Kogan G., 1998, *Observational Evidence for Black Holes in the Universe*, Chakrabarti S.K. (ed.), Kluwer Academic Publishers: Dordrecht, 1
- Black D.C., 1971, *Nature Phys. Sci.* 234, 148
- Bondi H., 1952, *MNRAS* 112, 195
- Burbidge E.M., Burbidge G.R., Fowler W.A., Hoyle F., 1957, *Rev. Mod. Phys.* 29, 547
- Chakrabarti S.K., 1985, *ApJ* 288, 1
- Chakrabarti S.K., 1986, *Accretion Processes in Astrophysics*, Audouze J., Tran Thanh Van, J. (eds.), Editions Frontières: Paris, 155

- Chakrabarti S.K., 1989, ApJ 347, 365
- Chakrabarti S.K., 1990a, MNRAS 243, 610
- Chakrabarti S.K., 1990b, Theory of Transonic Astrophysical Flows, World Scientific: Singapore
- Chakrabarti S.K., 1990c, MNRAS 283, 325
- Chakrabarti S.K., 1996a, ApJ 464, 623
- Chakrabarti S.K., 1996b, Phys. Rep. 266, 229
- Chakrabarti S.K., 1997, ApJ 484, 313
- Chakrabarti S.K., 1998a, Ind. J. Phys. 72(B), 183
- Chakrabarti S.K., 1998b, Observational Evidence for Black Holes in the Universe, Chakrabarti S.K. (ed.), Kluwer Academic Publishers: Dordrecht, 19
- Chakrabarti S.K., 1998c, Ind. J. Phys. 72(B), 565
- Chakrabarti S.K., 1999, A&A 351, 185
- Chakrabarti S.K., Jin L., Arnett W.D., 1987, ApJ 313, 674
- Chakrabarti S.K., Molteni D., 1993, ApJ 417, 671
- Chakrabarti S.K., Molteni D., 1995, MNRAS 272, 80
- Chakrabarti S.K., Mukhopadhyay B., 1999, A&A 344, 105
- Chakrabarti S.K., Titarchuk L., 1995, ApJ 455, 623
- Chakrabarti S.K., Titarchuk L.G., Kazanas D., Ebisawa K., 1996, A&AS 120, 163
- Clayton D.D., 1983, Principles of Stellar Evolution and Nucleosynthesis, The University of Chicago Press: Chicago
- Clegg R., 1977, MNRAS 181, 1
- Colpi M., Maraschi L., Treves A., 1984, ApJ 280, 319
- Cox J.P., Giuli R.T., 1968, Principles of Stellar Structure, Gordon & Breach: New

York

- Crary D.J., Kouveliotou C., van Paradijs J. et al., 1996, ApJL 462, 71
- Cui W., Zhang S.N., Focke W., Swank J.H., 1997, ApJ 484, 383
- Das T.K., 1998, *Observational Evidence for Black Holes in the Universe*, Chakrabarti S.K. (ed.), Kluwer Academic Publishers: Dordrecht, 113
- Das T.K., Chakrabarti S.K., 1999, *Class. Quantum Grav.* 16, 3879
- Ebisawa K., Ogawa M., Aoki T. et al., 1994, PASJ 46, 375
- Ebisawa K., Titarchuk L., Chakrabarti S.K., 1996, PASJ 48, 59
- Filippenko A.V., Matheson T., Barth A.J., 1995, ApJ 455, L139
- Fowler W.A., Caughlan G.R., Zimmerman B.A., 1975, ARA&A 13, 69
- Frank J., King A.R., Raine D.J., 1992, *Accretion Power in Astrophysics* (2d ed.), Cambridge University Press: Cambridge
- Fukue J., 1987, PASJ 39, 309
- Fuller G.M., Fowler W.A., Newmann M.J., 1980, ApJS 42, 447
- Fuller G.M., Fowler W.A., Newmann M.J., 1982, ApJS 48, 279
- Geiss J., Reeves H., 1972, A&A 18, 126
- Gilfanov M., Churazov E., Sunyaev R.A., 1997, *Accretion Disks – New Aspects*, Meyer-Hofmeister E., Spruit H. (eds.), Springer: Heidelberg
- Grove J.E., Johnson W.N., Kroeger R.A. et al., 1998, ApJ 500, 899
- Guessoum N., Kazanas D., 1999, ApJ 512, 332
- Harlaftis E.T., Horne K., Filippenko, A.V., 1996, PASP 168, 762
- Harris M.J., Fowler W.A., Caughlan G.R., Zimmerman, B.A., 1983, ARA&A 21, 165
- Hashimoto M., Eriguchi Y., Arai K., Müller E., 1993, A&A 268, 131

Hawley J., Smarr L.L., Wilson J.R., 1984, ApJ 277, 296
Hawley J., Smarr L.L., Wilson J.R., 1985, ApJS 55, 211
Hobbs L.W., Duncan D.K., 1987, ApJ 317, 787
Hogan C.J., Applegate J.H., 1987, Nature 390, 236
Hoyle F., 1946, MNRAS 106, 343
Hoyle F., 1954, ApJSS 1, 121
Ichimaru S., 1977, ApJ 208, 701
Itoh N., Hayashi H., Nishikawa A., Kohyama Y., 1996, ApJS 102, 411
Jin L., 1990, ApJ 356, 501
Jin L., Arnett W.D., Chakrabarti S.K., 1989, ApJ 336, 572
Kunth D., 1986, PASP 98, 984
Kunth D., Sargent W., 1983, ApJ 273, 81
Lamb R.C., Ling J.C., Mahoney W.A. et al., 1983, Nature 305, 37
Larson R.B., 1972, Nature 236, 21
Larson R.B., 1973, MNRAS 161, 133
Lequeux J., Peimbert M., Rayo J.F., Serrano A., Torres-Peimbert S., 1979, A&A
80, 155
Ling J., Wheaton W.A., Wallyn P. et al., 1997, ApJ 484, 375
Lu J.F., Yu K.N., Yuan F., Young E.C.M., 1997, A&A 321, 665
Lu J.F., Yuan F., 1997, PASJ 49, 525
Lynden-Bell D., 1975, Vistas Astron. 19, 299
Maraschi L., Reina C., Treves A., 1976, ApJ 206, 295
Margon B., 1984, ARA&A 22, 507
Martin E.L., Rebolo R., Casares J., Charles P.A., 1992, Nature 358, 129

- Martin E.L., Rebolo R., Casares J., Charles P.A., 1994, ApJ 791, 435
- Matsumoto R., Kato S., Fukue J., Okazaki A.T., 1984, PASJ 36, 71
- McClintock J., Horne K., Remillard R.A., 1995, ApJ 442, 358
- Mirabel I.F., Rodriguez L.F., 1994, Nature 371, 46
- Miyamoto S., Kimura K., Kitamoto S., Dotani T., Ebisawa K., 1991, ApJ 383, 784
- Molteni D., Lanzafame G., Chakrabarti S.K., 1994, ApJ 425, 161
- Molteni D., Ryu D., Chakrabarti S.K., 1996, ApJ 470, 460
- Mukhopadhyay B., 1998, *Observational Evidence for Black Holes in the Universe*, Chakrabarti S.K. (ed.), Kluwer Academic Publishers: Dordrecht, 105
- Mukhopadhyay B., 1999, Ind. J. Phys. 73B, 917
- Mukhopadhyay B., Chakrabarti S.K., 2000, A&A 353, 1029
- Nobuta K., Hanawa T., 1994, PASJ 46, 257
- Ostriker J.P., Thuan T.X., 1975, ApJ 202, 353
- Paczyński B., Bisnovaty-Kogan G., 1981, Acta Astron. 31, 283
- Paczyński B., Muchotrzeb B., 1982, Acta Astron. 31, 1
- Paczyński B., Wiita P.J., 1980, A&A 88, 23
- Pagel B.E.J., 1997, *Nucleosynthesis and Chemical Evolution of Galaxies*, Cambridge University Press: Cambridge
- Pagel B.E.J., Terlevich R., Melnick J., 1986, PASP 98, 1005
- Park M., 1990a, ApJ 354, 64
- Park M., 1990b, ApJ 354, 83
- Peebles P., 1966, Phys. Rev. Lett. 16, 410
- Pringle J., 1981, ARA&A 19, 137

- Ramos E., Kafatos M., Fruscione A. et al., 1997, ApJ 482, 167
- Rebolo R., Molaro P., Beckman J., 1988, A&A 192, 192
- Rees, M.J., 1984, ARA&A 22, 471
- Rees M.J., Begelman M.C., Blandford R.D., Phinney E.S., 1982, Nature 295, 17
- Rood R.T., Bania T.M., Wilsa T.L., 1984, ApJ 280, 629
- Ryu D., Brown J.G.L., Ostriker J.P., Loeb A., 1995, ApJ 452, 364
- Ryu D., Chakrabarti S.K., Molteni D., 1997, ApJ 474, 378
- Saha M.N., 1920, Philos. Mag. Ser. VI 40, 159
- Saha M.N., 1921, Proc. R. Soc. London Ser. A 99, 135
- Schmidt M., 1959, ApJ 129, 243
- Schmidt M., 1963, ApJ 137, 758
- Schramm D., 1989, Proc. Yamada Conference, Hayakawa S., Sato K. (eds.), Editions University Academi Press: Japan, 33
- Schramm D., Wagoner R., 1977, Annu. Rev. Nucl. Part. Sci. 27, 37
- Shakura N.I., Sunyaev R.A., 1973, A&A 24, 337
- Shapiro S.L., 1973, ApJ 180, 531
- Shapiro S.L., Teukolsky S.A., 1983, Black Holes, White Dwarf and Neutron Stars, Wiley: New York
- Shields G.A., 1986, PASP 98, 1072
- Shvartsman V.F., 1971, Sov. Astron. A.J. 15, 377
- Spite F., Spite M., 1982, A&A 115, 357
- Sponholz H., Molteni D., 1994, MNRAS 271, 233
- Sunyaev R.A., Titarchuk L.G., 1980, A&A 86, 121
- Taam R.E., Fryxell B.A., 1985, ApJ 294, 303

Tanaka Y., Lewin W.H.G., 1995, X Ray Binaries, Lewin W.H.G., van Paradijs J., van den Heuvel E.P.J. (eds.), Cambridge University Press: England, 126

Tananbaum H. et al., 1972, ApJL 177, 5

Thielemann F.-K., 1980, Ph.D. Thesis, Max Planck Institut, Munich and Technische Hochschule: Darmstadt

Thorne K.S., Price R.H., 1975, ApJL 195, 101

Tinsley B.M., 1975, ApJ 197, 159

Titarchuk L., Mastichiadis A., Kylafis N., 1997, ApJ 487, 834

Truran J., Cameron A., 1971, Astrophys. Space Sci. 14, 179

Van den Bergh S., 1962, Astron. J. 67, 486

Vargas M., Goldwurm A., Laurent P. et al., 1997, ApJL 476, 23

Wagoner R., Fowler W.A., Hoyle F., 1967, ApJ 148, 3

Wallace R.K., Woosley S.E., 1981, ApJS 231, 26

Wiita P.J., 1982, Comm. Astrophys. 6, 251

Woosley S.E., Arnett W.D., Clayton D.D., 1973, ApJS 231, 26

Yang R., Kafatos M., 1995, A&A 295, 238

Yi I., Narayan R., 1997, ApJ 486, 38

Zhang S.N., Ebisawa K., Sunyaev R., et al., 1997, ApJ 479, 381

PART-II

BEHAVIOUR OF FERMIONIC PARTICLES AROUND BLACK HOLES

1 Introduction

Here we study the interaction of particles having half-integral spin (which may or may not have charge) with a black hole. We are familiar with Dirac equation in flat space by which we can investigate the behaviour of half-integral spin particle. With the introduction of general relativistic effects, the form of the Dirac equation is modified. For different background geometry like Kerr, Schwarzschild etc., the form of the Dirac equation and the corresponding solution will be expected to be different. In 1972, Teukolsky wrote down the Dirac equation in Kerr geometry (Teukolsky 1972). Chandrasekhar (1976) separated it into radial and angular parts in 1976. Later Chakrabarti (1984) solved the angular equation. In 1999, Mukhopadhyay & Chakrabarti (1999) have solved the radial Dirac equation in Schwarzschild geometry in a spatially complete manner. Here we will discuss these developments systematically and present some solutions. These work also can be done for charged black holes (Page 1976; Mukhopadhyay 2000).

After writing the Dirac equation in curved space-time particularly in Kerr geometry using Newman-Penrose formalism (Chandrasekhar 1983) it was modified and generalised. From the same equation of Teukolsky (1972), Dirac equation for Schwarzschild metric (Weinberg 1972), where the central black hole is static can be studied just by putting the angular momentum parameter a of the black hole to zero. Following the separation of Dirac equation by Chandrasekhar (1976) solution of angular part was done by Chakrabarti (1984). Mukhopadhyay (1999), Mukhopadhyay & Chakrabarti (1999, 2000), Mukhopadhyay (2000) and Chakrabarti & Mukhopadhyay (2000) have solved radial part of the Dirac equation. Also Jin (1998) has studied the scattering phenomena of spin-half particle from Schwarzschild black hole. Following

those approaches here we shall introduce the spatially complete solution of radial Dirac equation. Combined with the solution of the angular equation mentioned before, complete solution of Dirac equation can be obtained. Far away from the black hole the modified Dirac equation for Kerr and Schwarzschild geometry (Weinberg 1972; Chandrasekhar 1983) and the interaction of particles with space-time reduce into that of the flat space.

One of the most important solutions of Einstein's equation is that of the spacetime around and inside an isolated black hole. The spacetime at a large distance is flat and Minkowskian where usual quantum mechanics is applicable, while the spacetime closer to the singularity is so curved that no satisfactory quantum field theory could be developed as yet. An intermediate situation arises when a weak perturbation (due to, say, gravitational, electromagnetic or Dirac waves) originating from infinity impinges on a black hole, interacting with it. The resulting wave is partially transmitted into the black hole through the horizon and partially scatters off to infinity. In the linearized ('test field') approximation this problem has been attacked in the past by several authors (Teukolsky 1972, 1973; Chandrasekhar 1976, 1983). The master equations of Teukolsky (1972) which govern these linear perturbations for integral spin (e.g., gravitational and electromagnetic) fields were solved numerically by Press & Teukolsky (1973) and Teukolsky & Press (1974). Particularly interesting is the fact that whereas gravitational and electromagnetic radiations were found to be amplified in some range of incoming frequencies, Chandrasekhar (1983) predicted that no such amplifications should take place for Dirac waves because of the very nature of the potential experienced by the incoming fields. However, these later conclusions were drawn by Chandrasekhar using asymptotic solutions. Mukhopadhyay & Chakrabarti

(2000) and Chakrabarti & Mukhopadhyay (2000) have revisited this important problem not in asymptotic way but in a spatially complete manner to study the nature of the radial wave functions as a function of the Kerr parameter, rest mass and frequency of incoming particle.

Here we will first indicate how Dirac equation in curved space-time can be written using Newman-Penrose formalism (Chandrasekhar 1983). Newman-Penrose formalism is one of the tetrad formalisms where null basis are chosen instead of orthonormal basis. To fulfill the understanding of Dirac equation in this formalism we also need to know the ‘Spinor Analysis’ (Chandrasekhar 1983).

1.1 Spinor Analysis

In Minkowski space we consider a point x^i ($i = 0, 1, 2, 3$) on a null ray whose norm is defined as

$$(x^0)^2 - (x^1)^2 - (x^2)^2 - (x^3)^2 = 0. \quad (\text{II.1})$$

Now, we consider two complex numbers ξ^0 and ξ^1 , and their complex conjugate numbers $\bar{\xi}^{0'}$ and $\bar{\xi}^{1'}$ in terms of which each point can be written as,

$$x^0 = \frac{1}{\sqrt{2}}(\xi^0 \bar{\xi}^{0'} + \xi^1 \bar{\xi}^{1'}) \quad (\text{II.2a})$$

$$x^1 = \frac{1}{\sqrt{2}}(\xi^0 \bar{\xi}^{1'} + \xi^1 \bar{\xi}^{0'}) \quad (\text{II.2b})$$

$$x^2 = -\frac{i}{\sqrt{2}}(\xi^0 \bar{\xi}^{1'} - \xi^1 \bar{\xi}^{0'}) \quad (\text{II.2c})$$

$$x^3 = \frac{1}{\sqrt{2}}(\xi^0 \bar{\xi}^{0'} - \xi^1 \bar{\xi}^{1'}). \quad (\text{II.2d})$$

Conversely, we can write,

$$\xi^0 \bar{\xi}^{0'} = \frac{1}{\sqrt{2}}(x^0 + x^3) \quad (\text{II.3a})$$

$$\xi^0 \bar{\xi}^{1'} = \frac{1}{\sqrt{2}}(x^1 + ix^2) \quad (\text{II.3b})$$

$$\xi^1 \bar{\xi}^{0'} = \frac{1}{\sqrt{2}}(x^1 - ix^2) \quad (\text{II.3c})$$

$$\xi^1 \bar{\xi}^{1'} = \frac{1}{\sqrt{2}}(x^0 - x^3). \quad (\text{II.3d})$$

Let,

$$\xi_*^A = \alpha^A_B \xi^B, \quad (\text{II.4a})$$

$$\bar{\xi}_*^{A'} = \bar{\alpha}_{B'}^{A'} \bar{\xi}^{B'} \quad (\text{II.4b})$$

where, $(A, B, A', B' = 0, 1)$, are the linear transformations in complex two-dimensional spaces. The transformation of x^i is defined as,

$$x_*^i = \beta_j^i x^j. \quad (\text{II.5})$$

Now, using Eqns. (II.2) and (II.3) we can write,

$$\begin{aligned} x_*^0 &= \frac{1}{\sqrt{2}}(\alpha_0^0 \xi^0 + \alpha_1^0 \xi^1)(\bar{\alpha}_{0'}^{0'} \bar{\xi}^{0'} + \bar{\alpha}_{1'}^{0'} \bar{\xi}^{1'}) + \frac{1}{\sqrt{2}}(\alpha_0^1 \xi^0 + \alpha_1^1 \xi^1)(\bar{\alpha}_{0'}^{1'} \bar{\xi}^{0'} + \bar{\alpha}_{1'}^{1'} \bar{\xi}^{1'}) \\ &= \frac{1}{2}(\alpha_0^0 \bar{\alpha}_{0'}^{0'} + \alpha_0^1 \bar{\alpha}_{1'}^{0'})(x^0 + x^3) + \frac{1}{2}(\alpha_1^0 \bar{\alpha}_{1'}^{0'} + \alpha_1^1 \bar{\alpha}_{1'}^{1'})(x^0 - x^3) \\ &\quad + \frac{1}{2}(\alpha_0^0 \bar{\alpha}_{1'}^{0'} + \alpha_0^1 \bar{\alpha}_{1'}^{1'})(x^1 + ix^2) + \frac{1}{2}(\alpha_1^0 \bar{\alpha}_{0'}^{0'} + \alpha_1^1 \bar{\alpha}_{0'}^{1'})(x^1 - ix^2). \end{aligned} \quad (\text{II.6})$$

Similarly, we can write down the relations between x_*^1 , x_*^2 and x_*^3 with α 's and x 's.

Therefore, keeping in mind Eqn. (II.5) we can write,

$$\beta_0^0 + \beta_3^0 = \alpha_0^0 \bar{\alpha}_{0'}^{0'} + \alpha_0^1 \bar{\alpha}_{1'}^{0'},$$

$$\beta_0^0 - \beta_3^0 = \alpha_1^0 \bar{\alpha}_{1'}^{0'} + \alpha_1^1 \bar{\alpha}_{1'}^{1'},$$

$$\beta_1^0 - i\beta_2^0 = \alpha_0^0 \bar{\alpha}_{1'}^{0'} + \alpha_0^1 \bar{\alpha}_{1'}^{1'},$$

$$\beta_1^0 + i\beta_2^0 = \alpha_1^0 \bar{\alpha}_{0'}^{0'} + \alpha_1^1 \bar{\alpha}_{0'}^{1'}.$$

Now, imposing the condition that the transformation Eqn. (II.5) is Lorentzian we can write,

$$(\beta_0^0)^2 - (\beta_1^0)^2 - (\beta_2^0)^2 - (\beta_3^0)^2 = 1.$$

So,

$$\left\| \begin{array}{cc} \alpha_0^0 \bar{\alpha}_{0'}^{0'} + \alpha_0^1 \bar{\alpha}_{0'}^{1'} & \alpha_0^0 \bar{\alpha}_{1'}^{0'} + \alpha_0^1 \bar{\alpha}_{1'}^{1'} \\ \alpha_1^0 \bar{\alpha}_{0'}^{0'} + \alpha_1^1 \bar{\alpha}_{0'}^{1'} & \alpha_1^0 \bar{\alpha}_{1'}^{0'} + \alpha_1^1 \bar{\alpha}_{1'}^{1'} \end{array} \right\| = 1. \quad (\text{II.7})$$

This gives,

$$\left\| \begin{array}{cc} \alpha_0^0 & \alpha_1^0 \\ \alpha_0^1 & \alpha_1^1 \end{array} \right\| \left\| \begin{array}{cc} \bar{\alpha}_{0'}^{0'} & \bar{\alpha}_{1'}^{0'} \\ \bar{\alpha}_{0'}^{1'} & \bar{\alpha}_{1'}^{1'} \end{array} \right\| = \Delta \bar{\Delta} = 1. \quad (\text{II.8})$$

Now we consider $\Delta = \bar{\Delta} = 1$, so individually each transformation of ξ is Lorentzian. So we can conclude if the transformation Eqn. (II.5) is Lorentzian, the necessary condition is, the transformation Eqn. (II.4) is also Lorentzian.

Now we define spinors $\xi^A, \eta^{A'}$ of rank one as $\xi_*^A = \alpha_B^A \xi^B$ and $\eta_*^{A'} = \bar{\alpha}_{B'}^{A'} \eta^{B'}$, ($A, A', B, B' = 0$), where $\|\alpha_B^A\| = \|\bar{\alpha}_{B'}^{A'}\| = 1$. Since ξ^A and $\eta^{A'}$ are two spinors of same class,

$$\left\| \begin{array}{cc} \xi^0 & \xi^1 \\ \eta^0 & \eta^1 \end{array} \right\| = \xi^0 \eta^1 - \xi^1 \eta^0 \quad (\text{II.9})$$

which is invariant under unimodular transformation, i.e.,

$$\epsilon_{AB} \xi^A \eta^B \rightarrow \text{invariant} \quad (\text{II.10})$$

where, ϵ_{AB} is Levi-Civita symbol. Here as in the case of tensor analysis ϵ_{AB} and $\epsilon_{A'B'}$ are used to lower the spinor indices as, $\xi_A = \xi^C \epsilon_{CA}$.

Now, using above information the representation of position vector x^i can be written as

$$x^i \leftrightarrow \left| \begin{array}{cc} \xi^0 \bar{\xi}^{0'} & \xi^0 \bar{\xi}^{1'} \\ \xi^1 \bar{\xi}^{0'} & \xi^1 \bar{\xi}^{1'} \end{array} \right| = \frac{1}{\sqrt{2}} \left| \begin{array}{cc} x^0 + x^3 & x^1 + ix^2 \\ x^1 - ix^2 & x^0 - x^3 \end{array} \right|. \quad (\text{II.11})$$

Generally any vector X^i can be written in terms of spinor of rank two as,

$$X^i \leftrightarrow \begin{vmatrix} \xi^{00'} & \xi^{01'} \\ \xi^{10'} & \xi^{11'} \end{vmatrix} = \frac{1}{\sqrt{2}} \begin{vmatrix} X^0 + X^3 & X^1 + iX^2 \\ X^1 - iX^2 & X^0 - X^3 \end{vmatrix} = X^{AB'}. \quad (\text{II.12})$$

So a 4-vector is associated with a hermitian matrix such that,

$$\begin{aligned} (X^0)^2 - (X^1)^2 - (X^2)^2 - (X^3)^2 &= (X^0 + X^3)(X^0 - X^3) - (X^1 + iX^2)(X^1 - iX^2) \\ &= 2(\xi^{00'}\xi^{11'} - \xi^{01'}\xi^{10'}) = (\xi^{00'}\xi_{00'} + \xi_{11'}\xi^{11'} + \xi_{10'}\xi^{10'} + \xi^{01'}\xi_{01'}) = X_{AB'}X^{AB'}. \end{aligned}$$

From the definition of norm, we can write it in two different representations:

$$g_{ij}X^iX^j = \epsilon_{AC}\epsilon_{B'D'}X^{AB'}X^{CD'}. \quad (\text{II.13})$$

Therefore, we can transform $X^i \leftrightarrow X^{AB'}$ as (Chandrasekhar 1983),

$$X^i = \sigma_{AB'}^i X^{AB'} \quad (\text{II.14a})$$

$$X^{AB'} = \sigma_i^{AB'} X^i \quad (\text{II.14b})$$

where, $\sigma_i^{AB'}$ and $\sigma_{AB'}^i$ are nothing but Pauli matrices and their conjugate matrices with a factor $\frac{1}{\sqrt{2}}$.

A curved space-time is locally Minkowskian. At each point of space-time an orthonormal Dyad basis can be set up as $\zeta_{(a)}^A$ and $\zeta_{(a')}^{A'}$ ($a, a' = 0, 1$ and $A, A' = 0, 1$) for spinors.

We define, $\zeta_{(0)}^A = o^A$ and $\zeta_{(1)}^A = l^A$. The condition of orthonormality is $\epsilon_{AB}o^Al^B = o^0l^1 - o^1l^0 = o_Bl^B = -o^Al_A = 1$.

Also it is clear that, $\epsilon^{(a)(b)}\zeta_{(a)}^A\zeta_{(b)}^B = \epsilon^{AB}$. Then the null vectors are defined as $l^i \leftrightarrow o^A\bar{o}^{B'}$, $m^i \leftrightarrow o^A\bar{l}^{B'}$, $\bar{m}^i \leftrightarrow l^A\bar{o}^{B'}$, $n^i \leftrightarrow l^A\bar{l}^{B'}$.

Here, vectors obey relations of null tetrads such as,

$l^in_i = 1, m^i\bar{m}_i = -1$ and all other products give zero.

In this way using dyad basis we can set up four null vectors which are basis of Newman-Penrose formalism. Using Eqn. (II.14) we can write the basis explicitly as

$$l^i = \sigma_{AB'}^i \zeta_{(0)}^A \bar{\zeta}_{(0')}^{B'} = \sigma_{AB'}^i o^A \bar{o}^{B'}, \quad (\text{II.15a})$$

$$m^i = \sigma_{AB'}^i \zeta_{(0)}^A \bar{\zeta}_{(1')}^{B'} = \sigma_{AB'}^i o^A \bar{l}^{B'}, \quad (\text{II.15b})$$

$$\bar{m}^i = \sigma_{AB'}^i \zeta_{(1)}^A \bar{\zeta}_{(0')}^{B'} = \sigma_{AB'}^i l^A \bar{o}^{B'}, \quad (\text{II.15c})$$

$$n^i = \sigma_{AB'}^i \zeta_{(1)}^A \bar{\zeta}_{(1')}^{B'} = \sigma_{AB'}^i l^A \bar{l}^{B'}. \quad (\text{II.15d})$$

Thus, in Newman-Penrose formalism the Pauli matrices change their forms as (Chandrasekhar 1983),

$$\sigma_{AB'}^i = \frac{1}{\sqrt{2}} \begin{vmatrix} l^i & m^i \\ \bar{m}^i & n^i \end{vmatrix} \quad (\text{II.16a})$$

$$\sigma_i^{AB'} = \frac{1}{\sqrt{2}} \begin{vmatrix} n_i & -\bar{m}_i \\ -m_i & l_i \end{vmatrix}. \quad (\text{II.16b})$$

Therefore in this basis, the directional derivatives can be written as,

$$D = l^i \partial_i, \quad \underline{\Delta} = n^i \partial_i, \quad \delta = m^i \partial_i \quad \text{and} \quad \delta^* = \bar{m}^i \partial_i.$$

Thus, the spinor equivalents of Newman-Penrose formalism are

$$\partial_{00'} = D, \quad \partial_{11'} = \underline{\Delta}, \quad \partial_{01'} = \delta, \quad \partial_{10'} = \delta^*.$$

Due to the reason, as explained earlier $\nabla_i \leftrightarrow \nabla_{AB'}$, so we can write,

$$\nabla_i X_j = X_{j;i} \leftrightarrow \nabla_{AB'} X_{CD'} = X_{CD';AB'},$$

therefore,

$$X_{CD';AB'} = \sigma_{CD'}^j \sigma_{AB'}^i X_{j;i}. \quad (\text{II.17})$$

For covariant derivatives spin coefficients Γ are introduced. In the Newman-Penrose formalism these different coefficients are assigned in terms of special symbols which are given in TABLE II.1 below (Chandrasekhar 1983):

TABLE II.1

$\Gamma_{(a)(b)(c)(d')}$			
$(a)(b)$	00	01 or 10	11
$(c)(d')$			
00'	κ	ε	π
10'	ρ	α	λ
01'	σ	β	μ
11'	τ	γ	ν

1.2 Dirac Equation and its Separation

Before going into discussion, we should mention about the unit of the system. Here we have chosen throughout $h = c = G = 1$, where h = Plank constant, c = speed of light and G = gravitational constant.

The Dirac equation in flat space using Newman-Penrose formalism can be written as,

$$\sigma_{AB'}^i \partial_i P^A + i\mu_* \bar{Q}_{B'} = 0 \quad (\text{II.18a})$$

$$\sigma_{AB'}^i \partial_i Q^A + i\mu_* \bar{P}_{B'} = 0. \quad (\text{II.18b})$$

Here, P^A and $\bar{Q}^{A'}$ are the pair of spinors. $\mu_*/\sqrt{2}$ is the mass of the particles and $\sigma_{AB'}^i$ is nothing but Pauli matrix, because $1/\sqrt{2}$ factors are canceled in the equation.

In curved space time Dirac equation reduces to

$$\sigma_{AB'}^i P_{;i}^A + i\mu_* \bar{Q}^{C'} \epsilon_{C'B'} = 0, \quad (\text{II.19a})$$

$$\sigma_{AB'}^i Q_{;i}^A + i\mu_* \bar{P}^{C'} \epsilon_{C'B'} = 0, \quad (\text{II.19b})$$

where, $\sigma_{AB'}^i$ is same as defined in Eqn. (II.16a).

Now, consider $B' = 0$, then Eqn. (II.19a) reduces to

$$\sigma_{00'}^i P_{;i}^0 + \sigma_{10'}^i P_{;i}^1 - i\mu_* \bar{Q}^{1'} = 0$$

or,

$$(\partial_{00'}P^0 + \Gamma_{b00'}^0P^b) + (\partial_{10'}P^1 + \Gamma_{b10'}^1P^b) - i\mu_*\bar{Q}^{1'} = 0.$$

Therefore,

$$(D + \Gamma_{1000'} - \Gamma_{0010'})P^0 + (\delta^* + \Gamma_{1100'} - \Gamma_{0110'})P^1 - i\mu_*\bar{Q}^{1'} = 0. \quad (\text{II.20})$$

Similarly, choosing $B' = 1$, we can get another similar type of equation and then we can get corresponding conjugate equation of both by interchanging P and Q . Now choosing,

$$F_1 = P^0, F_2 = P^1, G_1 = \bar{Q}^{1'}, G_2 = -\bar{Q}^{0'}$$

and replacing various spin coefficients by their named symbols given in TABLE II.1 we get the the Dirac equation in Newman-Penrose formalism in its reduced form as (Chandrasekhar 1983; Mukhopadhyay 1999),

$$(D + \varepsilon - \rho)F_1 + (\delta^* + \pi - \alpha)F_2 = i\mu_*G_1, \quad (\text{II.21a})$$

$$(\underline{\Delta} + \mu - \gamma)F_2 + (\delta + \beta - \tau)F_1 = i\mu_*G_2, \quad (\text{II.21b})$$

$$(D + \varepsilon^* - \rho^*)G_2 - (\delta + \pi^* - \alpha^*)G_1 = i\mu_*F_2, \quad (\text{II.21c})$$

$$(\underline{\Delta} + \mu^* - \gamma^*)G_1 - (\delta^* + \beta^* - \tau^*)G_2 = i\mu_*F_1. \quad (\text{II.21d})$$

1.2.1 Basis Vectors of Newman-Penrose formalism in terms of Kerr Geometry

The contravariant form of Kerr metric is given as (Chandrasekhar 1983),

$$g^{ij} = \begin{pmatrix} \Sigma^2/\rho^2\Delta & 0 & 0 & 2aMr/\rho^2\Delta \\ 0 & -\Delta/\rho^2 & 0 & 0 \\ 0 & 0 & -1/\rho^2 & 0 \\ 2aMr/\rho^2\Delta & 0 & 0 & -(\Delta - a^2\sin^2\theta)/\rho^2\Delta\sin^2\theta \end{pmatrix} \quad (\text{II.22})$$

where, a is specific angular momentum of the black hole, M is the mass of the black hole, $\rho^2 = r^2 + a^2 \cos^2 \theta$ (should not be confused with the spin coefficient $\Gamma_{(0)(0)(1)(0')} = \rho$), $\Sigma^2 = (r^2 + a^2)^2 - a^2 \Delta \sin^2 \theta$, $\Delta = r^2 + a^2 - 2Mr$.

In Kerr geometry, the tangent vectors of null geodesics are: $\frac{dt}{d\tau} = \frac{(r^2+a^2)}{\Delta} E$, $\frac{dr}{d\tau} = \pm E$, $\frac{d\theta}{d\tau} = 0$, $\frac{d\phi}{d\tau} = \frac{a}{\Delta} E$, where τ is the proper time (not to be confused with spin coefficient $\Gamma_{(0)(0)(1)(1')} = \tau$). Here E is energy of the particle (Chandrasekhar 1983).

Now, the basis of Newman-Penrose formalism can be written in Kerr geometry as (in tetrad form) (Chandrasekhar 1983)

$$l_i = \frac{1}{\Delta}(\Delta, -\rho^2, 0, -a\Delta \sin^2 \theta), \quad (\text{II.23a})$$

$$n_i = \frac{1}{2\rho^2}(\Delta, \rho^2, 0, -a\Delta \sin^2 \theta), \quad (\text{II.23b})$$

$$m_i = \frac{1}{\bar{\rho}\sqrt{2}}[i a \sin \theta, 0, -\rho^2, -i(r^2 + a^2) \sin \theta], \quad (\text{II.23c})$$

$$l^i = \frac{1}{\Delta}(r^2 + a^2, \Delta, 0, a), \quad (\text{II.23d})$$

$$n^i = \frac{1}{2\rho^2}(r^2 + a^2, -\Delta, 0, a), \quad (\text{II.23e})$$

$$m^i = \frac{1}{\bar{\rho}\sqrt{2}}(i a \sin \theta, 0, 1, i \operatorname{cosec} \theta), \quad (\text{II.23f})$$

\bar{m}_i and \bar{m}^i are nothing but complex conjugates of m_i and m^i respectively and $\bar{\rho} = r + i a \cos \theta$.

1.2.2 Separation of Dirac Equation into Radial and Angular parts

It is clear that the basis vectors basically become derivative operators when these are applied as tangent vectors to the function $e^{i(\sigma t + m\phi)}$. Here, σ is the frequency of the particle (not to be confused with spin coefficient $\Gamma_{(0)(0)(0)(1')} = \sigma$) and m is the azimuthal quantum number (Chakrabarti 1983).

Therefore, we can write,

$$\vec{l} = D = \mathcal{D}_0, \quad \vec{n} = \underline{\Delta} = -\frac{\Delta}{2\rho^2}\mathcal{D}_0^\dagger, \quad \vec{m} = \delta = \frac{1}{\bar{\rho}\sqrt{2}}\mathcal{L}_0^\dagger, \quad \vec{\bar{m}} = \delta^* = \frac{1}{\bar{\rho}^*\sqrt{2}}\mathcal{L}_0,$$

where,

$$\mathcal{D}_n = \partial_r + \frac{iK}{\Delta} + 2n\frac{r-M}{\Delta}, \quad (\text{II.24a})$$

$$\mathcal{D}_n^\dagger = \partial_r - \frac{iK}{\Delta} + 2n\frac{r-M}{\Delta}, \quad (\text{II.24b})$$

$$\mathcal{L}_n = \partial_\theta + Q + n\cot\theta \quad (\text{II.25a})$$

$$\mathcal{L}_n^\dagger = \partial_\theta - Q + n\cot\theta. \quad (\text{II.25b})$$

$K = (r^2 + a^2)\sigma + am$, $Q = a\sigma\sin\theta + m\text{cosec}\theta$ (Chandrasekhar 1983; Chakrabarti & Mukhopadhyay 2000).

The spin coefficients can be written as a combination of basis vectors in Newman-Penrose formalism which are now expressed in terms of elements of different components of Kerr metric. So we are combining those different components of basis vectors in a suitable manner and get the spin coefficients as,

$$\kappa = \sigma = \lambda = \nu = \varepsilon = 0, \quad (\text{II.26a})$$

$$\text{and } \tilde{\rho} = -\frac{1}{\bar{\rho}^*}, \quad \beta = \frac{\cot\theta}{\bar{\rho}2\sqrt{2}}, \quad \pi = \frac{iasin\theta}{(\bar{\rho}^*)^2\sqrt{2}},$$

$$\tau = -\frac{iasin\theta}{\rho^2\sqrt{2}}, \quad \mu = -\frac{\Delta}{2\rho^2\bar{\rho}^*}, \quad \gamma = \mu + \frac{r-M}{2\rho^2}, \quad \alpha = \pi - \beta^*. \quad (\text{II.26b})$$

Using the above definitions and results and choosing $f_1 = \bar{\rho}^*F_1$, $g_2 = \bar{\rho}G_2$, $f_2 = F_2$, $g_1 = G_1$ the Dirac equation is reduced to

$$\mathcal{D}_0f_1 + 2^{-1/2}\mathcal{L}_{1/2}f_2 = (i\mu_*r + a\mu_*\cos\theta)g_1, \quad (\text{II.27a})$$

$$\Delta\mathcal{D}_{1/2}^\dagger f_2 - 2^{1/2}\mathcal{L}_{1/2}^\dagger f_1 = -2(i\mu_*r + a\mu_*\cos\theta)g_2, \quad (\text{II.27b})$$

$$\mathcal{D}_0g_2 - 2^{-1/2}\mathcal{L}_{1/2}^\dagger g_1 = (i\mu_*r - a\mu_*\cos\theta)f_2, \quad (\text{II.27c})$$

$$\Delta \mathcal{D}_{1/2}^\dagger g_1 + 2^{1/2} \mathcal{L}_{1/2} g_2 = -2(i\mu_* r - a\mu_* \cos\theta) f_1. \quad (\text{II.27d})$$

Now we will separate the Dirac equation into radial and angular parts by choosing,

$$f_1(r, \theta) = R_{-1/2}(r) S_{-1/2}(\theta), \quad f_2(r, \theta) = R_{1/2}(r) S_{1/2}(\theta),$$

$$g_1(r, \theta) = R_{1/2}(r) S_{-1/2}(\theta), \quad g_2(r, \theta) = R_{-1/2}(r) S_{1/2}(\theta).$$

Replacing these f_i and g_i ($i = 1, 2$) into Eqn. (II.27) and using separation constant λ we get (Chandrasekhar 1976),

$$\mathcal{L}_{\frac{1}{2}} S_{+\frac{1}{2}} = -(\lambda - am_p \cos\theta) S_{-\frac{1}{2}} \quad (\text{II.28a})$$

$$\mathcal{L}_{\frac{1}{2}}^\dagger S_{-\frac{1}{2}} = +(\lambda + am_p \cos\theta) S_{+\frac{1}{2}} \quad (\text{II.28b})$$

$$\Delta^{\frac{1}{2}} \mathcal{D}_0 R_{-\frac{1}{2}} = (\lambda + im_p r) \Delta^{\frac{1}{2}} R_{+\frac{1}{2}}, \quad (\text{II.29a})$$

$$\Delta^{\frac{1}{2}} \mathcal{D}_0^\dagger \Delta^{\frac{1}{2}} R_{+\frac{1}{2}} = (\lambda - im_p r) R_{-\frac{1}{2}}, \quad (\text{II.29b})$$

where, m_p is the mass of the particle which is nothing but $2^{1/2}\mu_*$. Also, $2^{1/2}R_{-1/2}$ is redefined as $R_{-1/2}$.

Eqns. (II.28) and (II.29) are the angular and radial Dirac equation respectively in coupled form with the separation constant λ (Chandrasekhar 1983).

2 Solution

2.1 Solution of Angular Dirac Equation

Decoupling Eqn. (II.28) we obtain the eigenvalue equation for spin- $\frac{1}{2}$ particles as

$$\left[\mathcal{L}_{\frac{1}{2}} \mathcal{L}_{\frac{1}{2}}^\dagger + \frac{am_p \sin \theta}{\lambda + am_p \cos \theta} \mathcal{L}_{\frac{1}{2}}^\dagger + (\lambda^2 - a^2 m_p^2 \cos^2 \theta) \right] S_{-\frac{1}{2}} = 0. \quad (\text{II.30})$$

Similarly, one can obtain decoupled equation for spin- $+\frac{1}{2}$ particles. Here, the separation constant λ is considered to be the eigenvalue of the equation. The exact solutions of this equation for λ and $S_{-\frac{1}{2}}$ are possible in terms of orbital angular momentum quantum number l and the spin of the particle s when the parameter $\rho_1 = \frac{m_p}{\sigma} = 1$. When the angular momentum of the black hole is zero i.e., Schwarzschild case, the equation is reduced to such a form that its solution is nothing but standard spherical harmonics such as (Newman & Penrose 1966; Goldberg et al. 1967),

$$S_{-1/2}(\theta)e^{im\phi} = {}_{-1/2}Y_{lm}(\theta, \phi). \quad (\text{II.31})$$

The eigenvalue i.e., the separation constant can be solved as,

$$\lambda^2 = (l + 1/2)^2. \quad (\text{II.32})$$

Similarly, for spin- $+\frac{1}{2}$ particle one can solve $S_{+1/2}$ as

$$S_{+1/2}(\theta)e^{im\phi} = {}_{+1/2}Y_{lm}(\theta, \phi), \quad (\text{II.33})$$

with same eigenvalue λ .

For any non-integral $|s|$, solutions are (Newman & Penrose 1966; Goldberg et al. 1967)

$$S_{\pm s}(\theta)e^{im\phi} = {}_{\pm s}Y_{lm}(\theta, \phi), \quad (\text{II.34})$$

$$\lambda^2 = (l + |s|)(l - |s| + 1). \quad (\text{II.35})$$

In the case of Kerr geometry, when $a \neq 0$ the equation can be solved by perturbative procedure (Chakrabarti 1984) with perturbative parameter $a\sigma$. The solution for $\rho_1 = m_p/\sigma = 1$ and $s = \pm \frac{1}{2}$ is (Chakrabarti 1984)

$$\lambda^2 = \left(l + \frac{1}{2}\right)^2 + a\sigma(p + 2m) + a^2\sigma^2 \left[1 - \frac{y^2}{2(l+1) + a\sigma x}\right], \quad (\text{II.36})$$

$$\frac{1}{2}S_{lm} = \frac{1}{2}Y_{lm} + \frac{a\sigma y}{2(l+1) + a\sigma x} \frac{1}{2}Y_{l+1m} \quad (\text{II.37a})$$

$$-\frac{1}{2}S_{lm} = -\frac{1}{2}Y_{lm} - \frac{a\sigma y}{2(l+1) + a\sigma x} -\frac{1}{2}Y_{l+1m} \quad (\text{II.37b})$$

where,

$$p = F(l, l); \quad x = F(l+1, l+1); \quad y = F(l, l+1) \quad (\text{II.38})$$

and

$$F(l_1, l_2) = [(2l_2 + 1)/(2l_1 + 1)]^{\frac{1}{2}} \langle l_2 1 m 0 | l_1 m \rangle \langle l_2 1 \frac{1}{2} 0 | l_1 \frac{1}{2} \rangle \\ + (-1)^{l_2-l} \rho_1 \sqrt{2} \langle l_2 1 -\frac{1}{2} 1 | l_1 \frac{1}{2} \rangle. \quad (\text{II.39})$$

with $\langle \dots | \dots \rangle$ are the usual Clebsh-Gordon coefficients.

If $\rho_1 \neq 1$ then exact solution is not possible. In those cases the analytical expression of eigenvalue and angular wave-function are found as infinite series and not in a compact form as the case of $\rho_1 = 1$.

From the general convergence of series expansions one can truncate the infinite series upto certain order for particular values of l , s and m . For $l = \frac{1}{2}$, $s = -\frac{1}{2}$ and $m = -\frac{1}{2}$, up to third order in $a\sigma$, one obtains (Chakrabarti 1984),

$$\lambda^2 = \left(l + \frac{1}{2}\right)^2 + a\sigma f_1(l, m) + (a\sigma)^2 f_2(l, m) + (a\sigma)^3 f_3(l, m), \quad (\text{II.40})$$

$$-\frac{1}{2}S_{\frac{1}{2}-\frac{1}{2}} = -\sin\theta - \left(\sin^3\frac{\theta}{2} - \sin\theta\cos\frac{\theta}{2}\right) \left[\frac{2}{3}a\sigma(1 + \rho_1) + \frac{4}{15}(a\sigma)^2(1 - \rho_1^2)\right]$$

$$+\frac{2}{5}(a\sigma)^2(1-\rho_1^2)\left[\sin^5\frac{\theta}{2}-6\sin^2\frac{\theta}{2}\cos^3\frac{\theta}{2}+3\sin\frac{\theta}{2}\cos^4\frac{\theta}{2}\right]. \quad (\text{II.41})$$

Here, f_1, f_2, f_3 are functions of l and m . The accuracy of eigenvalue and eigenfunction decreases as $a\sigma \rightarrow 1$.

2.2 Solution of Radial Dirac Equation

In the radial equation, independent variable r is extended from 0 to ∞ . For mathematical simplicity we change the independent variable r to r_* as

$$r_* = r + \frac{2Mr_+ + am/\sigma}{r_+ - r_-} \log\left(\frac{r}{r_+} - 1\right) - \frac{2Mr_- + am/\sigma}{r_+ - r_-} \log\left(\frac{r}{r_-} - 1\right) \quad (\text{II.42})$$

(for $r > r_+$), here in new r_* co-ordinate system horizon r_+ is shifted to $-\infty$ unless $\sigma \leq -\frac{am}{2Mr_+}$ (Chandrasekhar 1983), so the region is extended from $-\infty$ to ∞ . We also choose $R_{-\frac{1}{2}} = P_{-\frac{1}{2}}$, $\Delta^{\frac{1}{2}}R_{+\frac{1}{2}} = P_{+\frac{1}{2}}$. Then we are defining

$$(\lambda \pm im_p r) = \exp(\pm i\theta)\sqrt{(\lambda^2 + m_p^2 r^2)}$$

and

$$P_{+\frac{1}{2}} = \psi_{+\frac{1}{2}} \exp\left[-\frac{1}{2}i \tan^{-1}\left(\frac{m_p r}{\lambda}\right)\right],$$

$$P_{-\frac{1}{2}} = \psi_{-\frac{1}{2}} \exp\left[+\frac{1}{2}i \tan^{-1}\left(\frac{m_p r}{\lambda}\right)\right].$$

Finally choosing,

$$Z_{\pm} = \psi_{+\frac{1}{2}} \pm \psi_{-\frac{1}{2}}$$

and combining the differential Eqns. (II.29a-b) we get (Chandrasekhar 1983; Mukhopadhyay & Chakrabarti 2000),

$$\left(\frac{d}{d\hat{r}_*} - W\right) Z_+ = i\sigma Z_-, \quad (\text{II.43a})$$

and

$$\left(\frac{d}{d\hat{r}_*} + W\right) Z_- = i\sigma Z_+, \quad (\text{II.43b})$$

where,

$$\hat{r}_* = r_* + \frac{1}{2\sigma} \tan^{-1} \left(\frac{m_p r}{\lambda} \right)$$

and

$$W = \frac{\Delta^{\frac{1}{2}} (\lambda^2 + m_p^2 r^2)^{3/2}}{\omega^2 (\lambda^2 + m_p^2 r^2) + \lambda m_p \Delta / 2\sigma}, \quad (\text{II.44})$$

where, $\omega^2 = \frac{K}{\sigma}$.

Now decoupling Eqns. (II.43a-b) we get,

$$\left(\frac{d^2}{d\hat{r}_*^2} + \sigma^2\right) Z_{\pm} = V_{\pm} Z_{\pm}. \quad (\text{II.45})$$

where,

$$V_{\pm} = W^2 \pm \frac{dW}{d\hat{r}_*} \quad (\text{II.46})$$

and \hat{r}_* is extended from $-\infty$ (horizon) to $+\infty$.

The Eqn. (II.45) is nothing but one dimensional Schrödinger equation (Davydov 1976) with potentials proportional to V_{\pm} and the energy of the particle proportional to σ^2 (since the system is dimensionless) in Cartesian co-ordinate system. Now we will describe about corresponding solution (Mukhopadhyay & Chakrabarti 1998; Mukhopadhyay & Chakrabarti 1999; Mukhopadhyay 1999; Mukhopadhyay 2000; Mukhopadhyay & Chakrabarti 2000; Chakrabarti & Mukhopadhyay 2000).

Like transformation from r to r_* as is described previously, by transformation of the variable from r to \hat{r}_* the horizon is shifted from $r = r_+$ to $\hat{r}_* = -\infty$ unless $\sigma \leq \sigma_s = -am/2Mr_+$ (Eqn. II.42). If $\sigma \leq \sigma_s$, super-radiation is expected for particles with integral spins but not for those with half-integral spin (Chandrasekhar 1983). Thus, we concentrate on the region where, $\sigma > \sigma_s$.

The choice of parameters is generally made in such a way that there is a significant interaction between the particle and the black hole, i.e., when the Compton wavelength of the incoming wave is of the same order as the outer horizon of the Kerr black hole. Similarly, the frequency of the incoming particle (or wave) should be of the same order as inverse of light crossing time of the radius of the black hole. These yield (Mukhopadhyay & Chakrabarti 1999),

$$m_p \sim \sigma \sim [M + \sqrt{(M^2 - a^2)}]^{-1}. \quad (\text{II.47})$$

Thus, we need to deal with quantum (primordial) black holes to get ‘interesting’ results. The physical mass of those black holes of the order of 10^{18} gm, obviously, which do not form through supernova explosions. These black holes might be formed in early Universe as a result of the perturbation in the homogeneous background density field (Shapiro & Teukolsky 1983).

Now, total parameter region is divided into two parts in terms of m_p and σ . As far away from the black hole $V_{\pm} \sim m_p^2$ (unit is dimensionless), if we choose $\sigma < m_p$, then particle can not enter into the potential field (Mukhopadhyay & Chakrabarti 1999). So the parameter space is divided into two parts accordingly. Then for the region $\sigma \geq m_p$, it is divided into two sub-regions whether the peak of the potential barrier (V_m) is greater than σ^2 or not (Mukhopadhyay & Chakrabarti 1999). In the region where $V_m > \sigma^2$, if $\sigma \leq \sigma_s$ then potential barrier diverges at a point defined as $r^2 = a^2 + \frac{am}{\sigma}$ (Chandrasekhar 1983). This diverging potential is important for super-radiation for integral spin particle but for spin-half particle super-radiation is absent (Chandrasekhar 1983). So there are two cases of interest: (1) the waves do not ‘hit’ the potential barrier and (2) the waves do hit the potential barrier. First, we replace the potential barrier by a large number of steps. Then we treat it as the step-barrier

problem in quantum mechanics (Mathews & Walker 1970; Davydov 1976). Figure II.1 shows one such example of the potential barrier V_+ (Eqn. II.46) which is drawn for $a = 0.5$, $m_p = 0.8$ and $\sigma = 0.8$. In reality we use tens of thousands of steps with suitable variable widths so that the steps become indistinguishable from the actual function. The solution of Eqn. (II.45) at n th step can be written as (Davydov 1976; Chakrabarti & Mukhopadhyay 2000),

$$Z_{+,n} = A_n \exp[ik_n \hat{r}_{*,n}] + B_n \exp[-ik_n \hat{r}_{*,n}] \quad (\text{II.48})$$

when energy of the wave is greater than the height of the potential barrier. The standard junction condition is given as (Davydov 1976),

$$Z_{+,n} = Z_{+,n+1} \quad \text{and} \quad \frac{dZ_+}{d\hat{r}_*}|_n = \frac{dZ_+}{d\hat{r}_*}|_{n+1}. \quad (\text{II.49})$$

The reflection and transmission coefficients at n th junction are given by (Chakrabarti & Mukhopadhyay 2000):

$$R_n = \frac{A_{n+1}(k_{n+1} - k_n) + B_{n+1}(k_{n+1} + k_n)}{A_{n+1}(k_{n+1} + k_n) + B_{n+1}(k_{n+1} - k_n)}; \quad T_n = 1 - R_n. \quad (\text{II.50})$$

At each of the n steps these conditions were used to connect solutions at successive steps. Here, k is the wave number ($k = \sqrt{\sigma^2 - V_{\pm}}$) of the wave and k_n is its value at n th step. We use the ‘no-reflection’ inner boundary condition: $R \rightarrow 0$ at $\hat{r}_* \rightarrow -\infty$.

For the cases where waves hit on the potential barrier, inside the barrier (where $\sigma^2 < V_+$) we use the wave function of the form (Chakrabarti & Mukhopadhyay 2000)

$$Z_{+,n} = A_n \exp[-\alpha_n \hat{r}_{*,n}] + B_n \exp[\alpha_n \hat{r}_{*,n}] \quad (\text{II.51})$$

where, $\alpha_n = \sqrt{V_{\pm} - \sigma^2}$, as in usual quantum mechanics.

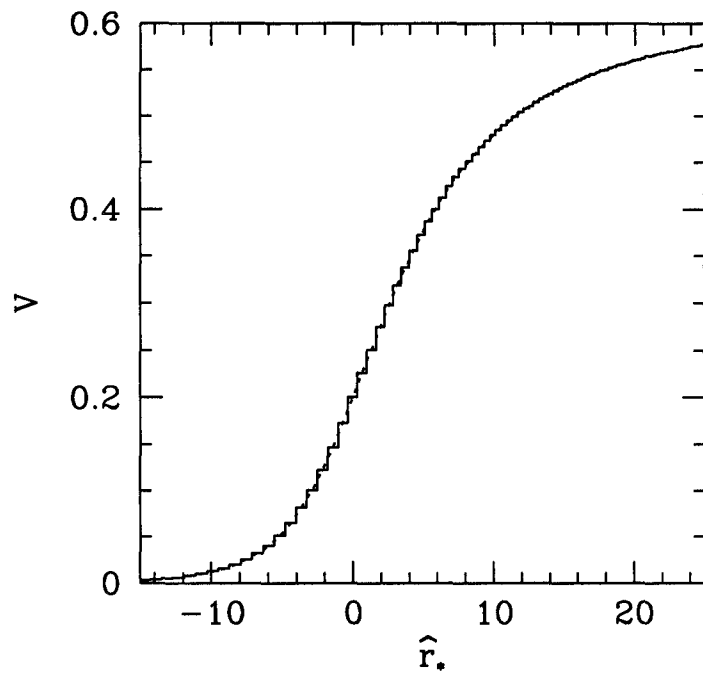


Fig. II.1 : Behaviour of V_+ (smooth dotted curve) for $a = 0.5$, $m_p = 0.8$, $\sigma = 0.8$. This is approximated as a collection of steps. In reality tens of thousand steps were used with varying step size which mimic the potential with arbitrary accuracy.

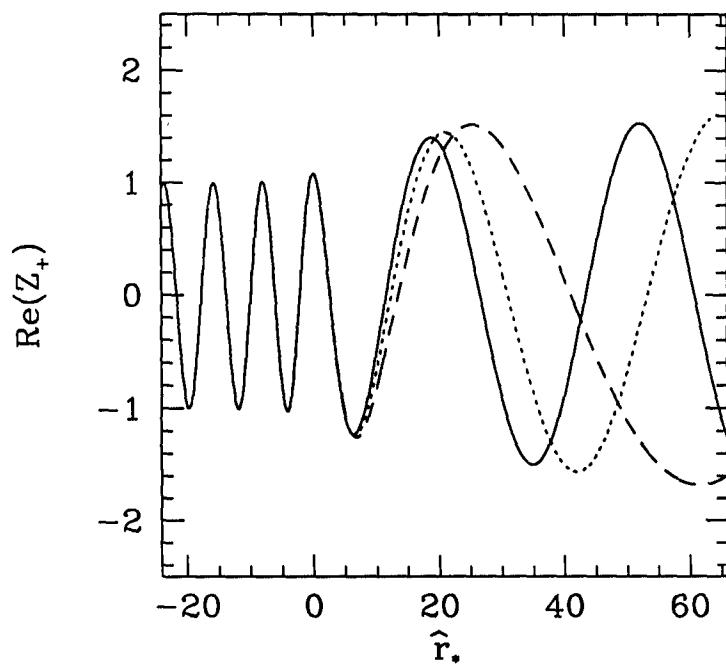


Fig. II.2a: Amplitude of $\text{Re}(Z_+)$ of waves with varying mass as functions of \hat{r}_* . $m_p = 0.78$ (solid), $m_p = 0.79$ (dotted) and $m_p = 0.80$ (long-dashed) are used. Other parameters are $a = 0.5$ and $\sigma = 0.8$.

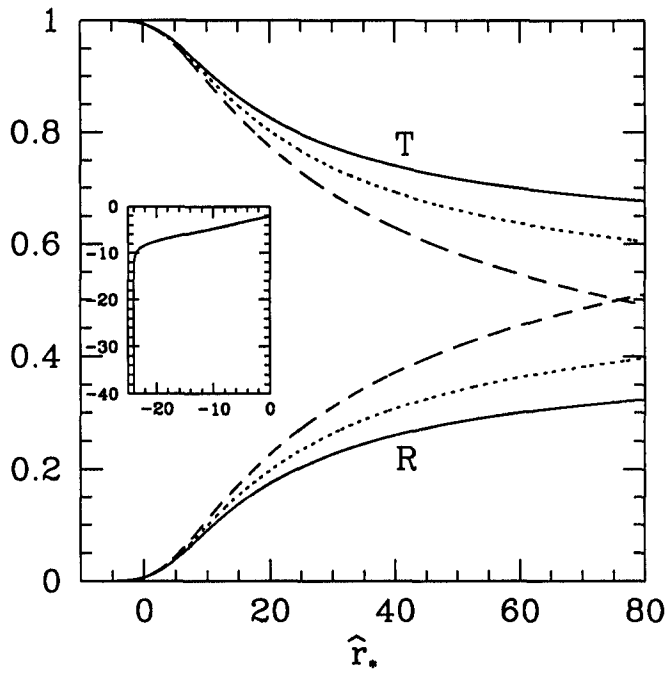


Fig. II.2b: Reflection (R) and transmission (T) coefficients of waves with varying mass as functions of \hat{r}_* . $m_p = 0.78$ (solid), $m_p = 0.79$ (dotted) and $m_p = 0.80$ (long-dashed) are used. Other parameters are $a = 0.5$ and $\sigma = 0.8$. Inset shows R in logarithmic scale which falls off exponentially just outside the horizon.

2.3 Examples of Solutions

Figure II.2a shows three solutions (amplitudes of $\text{Re}(Z_+)$) for parameters: $a = 0.5$, $\sigma = 0.8$ and $m_p = 0.78, 0.79$, and 0.80 respectively in solid, dotted and long-dashed curves. The energy σ^2 is always higher compared to the height of the potential barrier (Fig. II.1) and therefore the particles do not ‘hit’ the barrier. k goes up and therefore the wavelength goes down monotonically as the wave approaches a black hole. It is to be noted that though ours is apparently a ‘crude’ method, it has flexibility and is capable of presenting insight into the problem, suppressing any other method such as ODE solver packages. This is because one can choose (a) variable steps depending on steepness of the potential to ensure uniform accuracy, and at the same time (b) virtually infinite number of steps to follow the potential as closely as possible. In Fig. II.2b, we present the instantaneous values of the reflection R and transmission T coefficients (i.e., R_n and T_n of Eqn. II.50) for the same three cases. As the particle mass is decreased, k goes up and corresponding R goes down consistent with the limit that as $k \rightarrow \infty$, there would be no reflection at all as in a quantum mechanical problem. For instance, in the inset, we show R in logarithmic scale very close to the horizon. All the three curves merge, indicating that the solutions are independent of the mass of the particle and a closer inspection shows that here, the slope of the curve depends only on σ . The exponential dependence of R_n close to the horizon becomes obvious. Asymptotically, $V_{\pm} = m_p^2$ (Eqn. II.46), thus, as m_p goes down, the wavelength goes down.

Figures II.3(a-b) compare a few solutions where the incoming particles ‘hit’ the potential barrier. We choose, $a = 0.95$, $\sigma = 0.168$ and mass of the particle $m_p = 0.16, 0.164, 0.168$ respectively in solid, dotted and long-dashed curves. Inside the

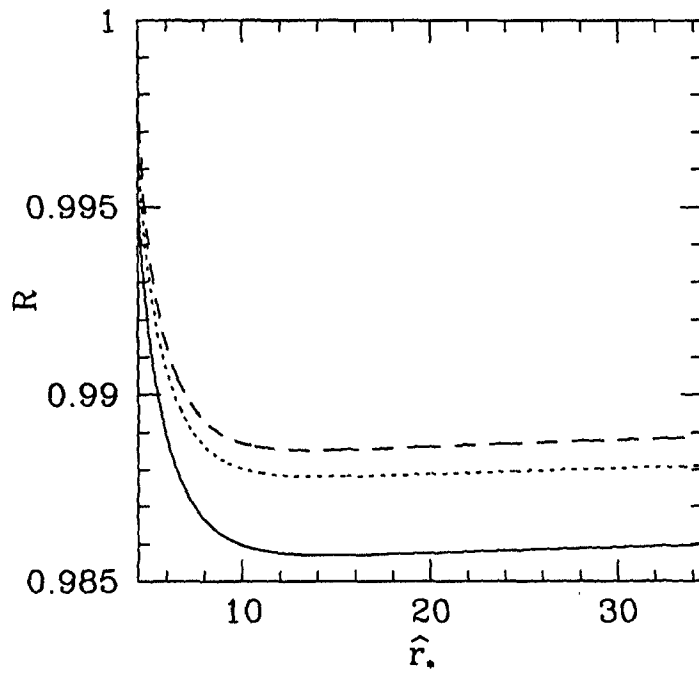


Fig. II.3a: Reflection (R) coefficient of waves with varying mass as functions of \hat{r}_* . $m_p = 0.16$ (solid), $m_p = 0.164$ (dotted) and $m_p = 0.168$ (long-dashed) are used. Other parameters are $a = 0.95$ and $\sigma = 0.168$.

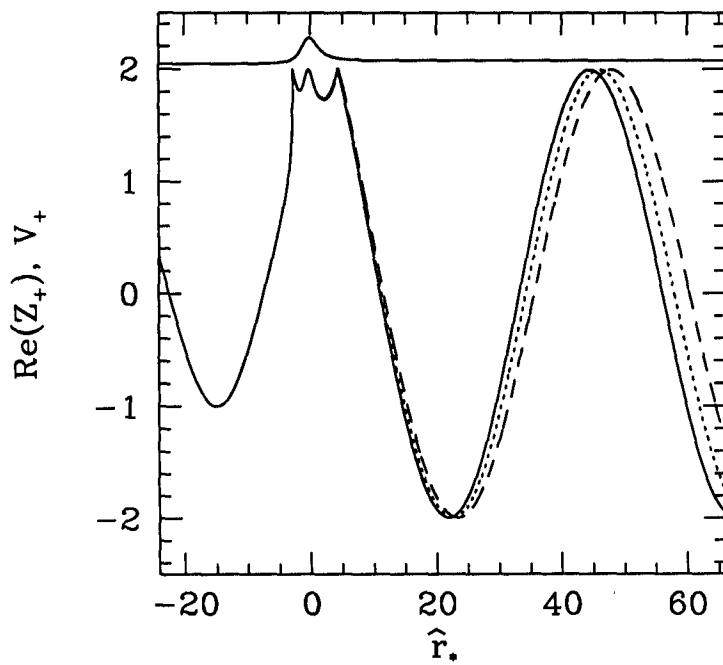


Fig. II.3b: Amplitude of $\text{Re}(Z_+)$ of waves with varying mass as functions of \hat{r}_* . $m_p = 0.16$ (solid), $m_p = 0.164$ (dotted) and $m_p = 0.168$ (long-dashed) are used. Nature of potential with $m_p = 0.168$ is drawn shifting vertically by 2.05 unit for clarity. Other parameters are $a = 0.95$ and $\sigma = 0.168$.

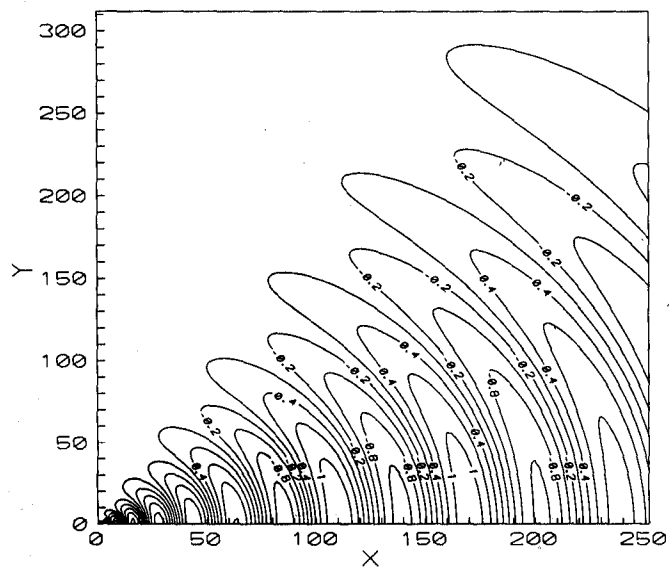


Fig. II.4a: Contours of constant amplitude are plotted in the meridional plane around a black hole. Radial direction on equatorial plane is along X axis and the vertical direction is along Y . Both radial and theta solutions have been combined. Parameters are $a = 0.5$, $m_p = 0.8$ and $\sigma = 0.8$.

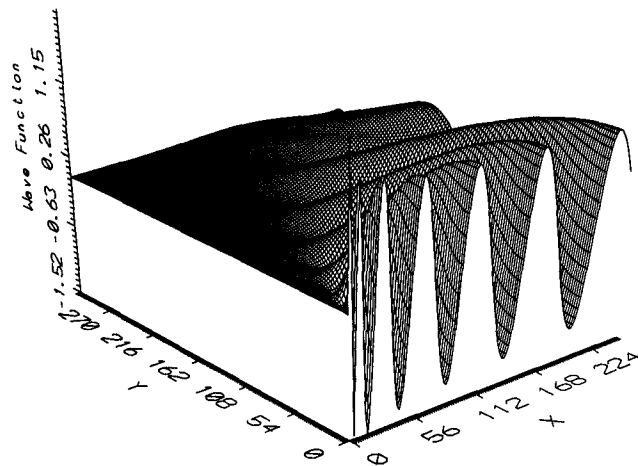


Fig. II.4b: Three dimensional view of $R_{-1/2}S_{-1/2}$ are plotted in the meridional plane around a black hole. Both radial and theta solutions have been combined. Parameters are $a = 0.5$, $m_p = 0.8$ and $\sigma = 0.8$.

barrier, the wave decays before coming back to a sinusoidal behaviour, before entering into a black hole. In Fig. II.3b, we plotted the potential (shifted by 2.05 along vertical axis for clarity). Here too, the reflection coefficient goes down as k goes up consistent with the classical result that as the barrier height goes up more and more, reflection is taking place strongly. Note however, that the reflection is close to a hundred percent. Tunneling causes only a few percent to be lost into the black hole.

Figures II.4(a-b) show the nature of the complete wave function when both the radial and the angular solutions (Chakrabarti 1984) are included. Figure II.4a shows contours of constant amplitude of the wave ($R_{-1/2}S_{-1/2}$) in the meridional plane – X is along radial direction in the equatorial plane and Y is along the vertical direction. The parameters are $a = 0.5$, $m_p = 0.8$ and $\sigma = 0.8$. Some levels are marked. Two successive contours have amplitude difference of 0.1. In Fig. II.4b a three-dimensional nature of the complete solution is given. Both of these figures clearly show how the wavelength varies with distance. Amplitude of the spherical wave coming from a large distance also gets weaker along the vertical axis and the wave is forced to fall generally along the equatorial plane, possibly due to the dragging of the inertial frame.

3 Conclusions

Here we write the Dirac equation in curved space-time and particularly in Kerr geometry. From this, the behaviour of non-integral spin particles (more clearly spin-half particle) can be studied in curved space-time. From the form of the equation and its solution it is clear that in curved space the particles behave differently from that in a flat space-time. The Newman-Penrose formalism is used to write the equation where the basis system is null. Dirac equation is separated into angular and radial parts. Similar separation can be possible on the background of Dyon black hole (Semiz 1992). The solution of angular part of the Dirac equation is first reviewed. The exact solution is possible for $\frac{m_p}{\sigma} = 1$, otherwise the solution is approximate (Chakrabarti 1984). Unlike in the case of a Kerr black hole, the solution of the angular equation around a Schwarzschild black hole is independent of the azimuthal or meridional angles (Chakrabarti 1984; Press & Teukolsky 1973; Teukolsky & Press 1974). This is expected because of symmetry of the space-time.

Finally we study the scattering of massive, spin-half particles from a Kerr black hole, particularly the nature of the radial wave functions and the reflection and transmission coefficients. The radial Dirac equation is solved using the method described above. The space dependent transmission and reflection coefficients are calculated. Spatial dependency of the transmission and reflection coefficients are very clear from the behaviour of the potential which is space-dependent. As the particle is moving in the potential field, the potential is changing. As a result transmission and reflection of the particle are changing. The reflection and transmission coefficients were found to distinguish strongly the solutions of different rest masses and different energies. The solution might be of immense use in the study of the spectrum of particles emitted

from a black hole horizon (Hawking radiation). We showed few illustrative cases as examples. The physical region was classified into two parts, depending on whether the particle ‘hits’ the potential barrier or not. Again, the region, where particle hits on the barrier, is divided into two parts, one is super-radiant region and other is non-super-radiant region. We chose one illustrative example in each of the regions. We emphasize that the most ‘interesting’ region to study would be close to $m_p \sim \sigma$. Our method of obtaining solutions should be valid for any black hole geometry which is asymptotically flat so that radial waves could be used at a large distance.

In the literature, reflection and transmission coefficients are defined at a single point. These definitions are meaningful only if the potential varies in a small region while studies are made from a large distance of it. In the present case, the potential changes over a large distance and we are studying in these regions as well. Although we used the words ‘reflection’ and ‘transmission’ coefficients, in this thesis very loosely, our definitions are very rigorous and well defined. These quantities are simply the instantaneous values and in our belief more physical. The problem at hand is very similar to the problem of reflection and transmission of acoustic waves from a strucked string of non-constant density where reflection and transmission occurs at each point.

It is noted that all the cases where potentials diverge at a certain r arise for $\sigma \leq \sigma_s$, with the negative values of azimuthal quantum number (here, $m = -1/2$) and the positive Kerr parameter, a . For positive values of m and positive values of a , potential does not diverge at any point for all values of σ . If we change the spin orientation of the black hole (negative values of a) and take positive m again divergence of the potential will arise. Thus, it seems that the cases with opposite sign of a and m are physically more interesting.

It is seen that for different physical parameters the solutions are different. The waves scattered off are distinctly different in different parameter regions. In a way, therefore, black holes can act as a mass spectrograph! Another interesting application of our method would be to study the interactions of Hawking radiations in regions just outside the horizon.

REFERENCES-II

- Chakrabarti S.K., 1984, Proc. R. Soc. Lond. A 391, 27
- Chakrabarti S.K., Mukhopadhyay B., 2000, MNRAS 317, 979
- Chandrasekhar S., 1976, Proc. R. Soc. Lond. A 349, 571
- Chandrasekhar S., 1983, The Mathematical Theory Of Black Holes, Clarendon Press: London
- Davydov A.M., 1976, Quantum Mechanics (Second Ed.), Pergamon Press: Oxford
- Goldberg J.N., Macfarlane A.J., Newman E.T., Rohrlich F., Sudarsan E.C.G., 1967, J. Math. Phys. 8, 2155
- Jin W.M., 1998, Class. Quantum Grav. 15, 3163
- Mathews J., Walker R.L., 1970, Mathematical Methods Of Physics (Second Ed.), The Benjamin/Cummings Publishing Company: California
- Mukhopadhyay B., 1999, Ind. J. Phys. 73(B), 855
- Mukhopadhyay B., 2000, Class. Quantum Grav. 17, 2017
- Mukhopadhyay B., Chakrabarti S.K., 1998, Mini-Workshop on Appl. Math., Islam J.N. (ed.), SUST Publication: Sylhet, Bangladesh, 251
- Mukhopadhyay B., Chakrabarti S.K., 1999, Class. Quantum Grav. 16, 3169
- Mukhopadhyay B., Chakrabarti S.K., 2000, Nucl. Phys. B 582, 627
- Newman E., Penrose R., 1966, J. Math. Phys. 7, 863
- Page D.N., 1976, Phys. Rev. D 14, 1509
- Press W.H., Teukolsky S.A., 1973, ApJ 185, 649
- Semiz I., 1992, Phys. Rev. D 46, 5414
- Shapiro S.L., Teukolsky S.A., 1983, Black Holes, White Dwarfs and Neutron Stars,

A Wiley-Interscience Publication: New York

Teukolsky S.A., 1972, Phys. Rev. Lett. 29, 1114

Teukolsky S.A., 1973, ApJ 185, 635

Teukolsky S.A., Press W.H., 1974, ApJ 193, 443

Weinberg S., 1972, Gravitation and Cosmology: Principle and Applications of the General Theory of Relativity, John Wiley & Sons.: New York, Chichester

Banilata Mukherjee

31.10.2000

THE LIST OF PUBLICATIONS

In Refereed Journals

1. Chakrabarti, S.K. and **Mukhopadhyay, B.**, Neutron Disks Around Black Holes - Astronomy and Astrophysics, Vol.-344, Page-105, 1999; astro-ph/9904342.
2. **Mukhopadhyay, B.** and Chakrabarti, S.K., Semi-analytical Solution of Dirac equation in Schwarzschild Geometry - Classical and Quantum Gravity, Vol.-16, No.-10, Page -3165, 1999; gr-qc/9907100.
3. **Mukhopadhyay, B.**, Dirac equation in Kerr Geometry - Indian Journal of Physics, Vol.-73B (6), Page-855, 1999; gr-qc/9910018.
4. **Mukhopadhyay, B.**, Nucleosynthesis around Black Holes - Indian Journal of Physics, Vol.-73B (6), Page-917, 1999; astro-ph/9910080.
5. **Mukhopadhyay, B.** and Chakrabarti S.K., Nucleosynthesis in Accretion Flows around Black Holes - Astronomy and Astrophysics, Vol.-353, Page-1029, 2000; astro-ph/9912568.
6. **Mukhopadhyay, B.**, Behaviour of spin-half particle around a charged black hole - Classical and Quantum Gravity, Vol.-17, No.-9, Page-2017, 2000; gr-qc/0003061.
7. **Mukhopadhyay, B.** and Chakrabarti, S.K., Solution of Dirac equation around a spinning black hole - Nuclear Physics B, Vol.-582, Page-627, 2000; gr-qc/0007016.
8. Chakrabarti, S.K., **Mukhopadhyay, B.**, Scattering of Dirac Waves off Quantum Black Holes - Mont. Not. Royal Astron. Soc., Vol.-317, Page-979, 2000; astro-ph/0007277.

9. **Mukhopadhyay, B.**, Chakrabarti, S.K., Stability of Accretion Flows in Presence of Nuclear Reactions (Submitted).
10. **Mukhopadhyay, B.**, Instantaneous Reflection and Transmission Coefficients and a Special Method to Solve Wave Equation (Submitted); math-ph/9908011.

In Proceedings

1. **Mukhopadhyay, B.**, Nucleosynthesis in Advective Accretion Disk around Galactic and Extra-Galactic Black Holes - Proc. International Conference On The Observational Evidences For Black Hole, Edited by Sandip K. Chakrabarti, Calcutta (1-17 Jan. 1998), Kluwer Academic Press: Dordrecht, Page-105; astro-ph/9807106.
2. **Mukhopadhyay, B.** and Chakrabarti, S.K., The Complete Solution of Dirac Equation in Kerr Geometry - Proc. Mini Workshop on Applied Mathematics, Shyllet, Bangladesh (1-3 Sept. 1998), SUST Publication: Sylhet, Bangladesh, Page-251.
3. Chakrabarti, S.K. & **Mukhopadhyay, B.**, Dirac Equation in Kerr Geometry and its Solution - Il Nouvo Cimento (In press), in Proc. of International Centre for Relativistic Astrophysics Workshop, Edited by Remo Ruffini, 1999; astro-ph/0007253.
4. **Mukhopadhyay, B.**, Nucleosynthesis in accretion disk around compact object - To appear in Proc. of 9th Marcel Grossmann Meeting, Rome, 2000.
5. **Mukhopadhyay, B.**, Behaviour of spin-1/2 particle in curved space-time - To appear in Proc. of 9th Marcel Grossmann Meeting, Rome, 2000.

In Abstract Proceedings

1. **Mukhopadhyay, B.** and Chakrabarti, Sandip K., Nucleosynthesis in Advective Accretion Disks Around Black Holes - Proc. of the 19th Texas Symposium on Relativistic Astrophysics and Cosmology, held in Paris, France, Dec. 14-18, 1998. Eds.: J. Paul, T. Montmerle, and E. Aubourg (CEA Saclay).
2. **Mukhopadhyay, B.** and Chakrabarti, Sandip K., Solution of Dirac Equation in Kerr Geometry - Proc. of the 19th Texas Symposium on Relativistic Astrophysics and Cosmology, held in Paris, France, Dec. 14-18, 1998. Eds.: J. Paul, T. Montmerle, and E. Aubourg (CEA Saclay).
3. **Mukhopadhyay, B.** and Raychaudhuri, S., Rules for Difference of Number of Complete and Non-Complete Set of Operators in a Particular Representation - Proc. of Indian Science Congress, 1998.
4. **Mukhopadhyay, B.**, The Method to Solve the Non-analytic Differential Equation Analytically - Proc. of Indian Science Congress, 1999.
5. **Mukhopadhyay, B.**, Space Dependent Reflection and Transmission Coefficients - Proc. of Indian Science Congress, 2000.

In Popular Magazine/Newspaper

1. **Mukhopadhyay, B.**, Nucleosynthesis around a Black Hole - Universe and Beyond, 1999.
2. **Mukhopadhyay, B.**, An article "Hole's A Heady Brew" in a newspaper "The Telegraph", India on 17th January, 2000.

THE RE-PRINT OF PUBLICATIONS

NUCLEOSYNTHESIS IN ADVECTIVE ACCRETION DISKS AROUND GALACTIC AND EXTRA-GALACTIC BLACK HOLES

B. MUKHOPADHYAY

*S. N. Bose National Centre For Basic Sciences JD Block, Salt
Lake, Sector-III, Calcutta-700091, India*

1. Introduction

Many of the observational evidences for black hole rely on the fact that the incoming gas has the potential to become as hot as its virial temperature $T_{\text{virial}} \sim 10^{13}$ °K (Rees, 1984). This flow is usually cooled down through bremsstrahlung and Comptonization effects and hard and soft states are produced depending on the degree by which this cooling takes place (Chakrabarti & Titarchuk, 1995). The generally sub-Keplerian, advective flow after deviating from a Keplerian disk, especially in the hard states, remains sufficiently hot to cause a significant amount of nuclear reactions around a black hole before plunging in it. The energy generated could be high enough to destabilize the flow and the modified composition may be dispersed through winds to change the metallicity of the galaxy (Chakrabarti, Jin & Arnett, 1987 [CJA]; Jin, Arnett & Chakrabarti, 1988; Chakrabarti, 1988; Mukhopadhyay & Chakrabarti, 1998). Earlier works have been done in cooler thick accretion disks only. Below, we present a few examples of nuclear reactions in advective flows and discuss the implications. Results of more detailed study could be seen in Mukhopadhyay & Chakrabarti (1998) [MC98].

2. Physical Systems Under Considerations

Black hole accretion is by definition advective, i.e., matter must have *radial* motion, and transonic, i.e., matter must be supersonic (Chakrabarti 1996 [C96] and references therein). The supersonic flow must be sub-Keplerian and therefore deviate from the Keplerian disk away from the black hole. The study of viscous, transonic flows was initiated by Paczyński & Bisnovatyi-Kogan (1981).

By and large, we follow C'96 for thermodynamical parameters along a flow and Chakrabarti & Titarchuk (1995) [C'T95] and Chakrabarti (1997a) [C'97a] to compute the temperature of the Comptonized flow in the advective region which may or may not have shocks. According to these solutions, a black hole accretion may be thought to be similar to a sandwich whose sub-Keplerian flow rate (\dot{m}_h) in the 'bread' part progressively increases and that (\dot{m}_d) in the 'meat' part progressively decreases as flow moves in towards the black hole. Finally at $x = x_K$, the equatorial flow also deviates from a Keplerian disk and for $x < x_K$ the entire flow is sub-Keplerian. Among the major reactions which are taking place inside the disk, we note that, due to hotter nature of the advective disks, especially when the accretion rate is low and Compton cooling is negligible, the major process of hydrogen burning is the rapid proton capture process (which operates at $T \gtrsim 5 \times 10^8 \text{K}$) as opposed to the PP chain (which operates at much lower temperature $T \sim 0.01 - 0.2 \times 10^9 \text{K}$) and CNO (which operates at $T \sim 0.02 - 0.5 \times 10^9 \text{K}$). The present paper being exploratory in nature, we do not include nuclear heating and cooling in determining the structure and stability of the accretion flow. We do not assume here heating due to magnetic dissipation (see, Shapiro, 1973 and Bisnovatyi-Kogan, 1998).

For simplicity, we take the solar abundance as the abundance of the Keplerian disk. Furthermore, Keplerian disk being cooler, no composition change is assumed inside it. In other words, our computation starts only from the time when matter is launched from the Keplerian disk ($x = x_K$). Most of the cases were repeated with initial abundance same as the output of big-bang nucleosynthesis (hereafter referred to as 'big-bang abundance').

According to C'T95, and C'97a, for two component accretion flows, for $\dot{m}_d \lesssim 0.1$ and $\dot{m}_h \lesssim 1$ the black hole remains in hard states. Lower rate in Keplerian disks *generally* implies a lower viscosity and a larger x_K ($x_K \sim 30 - 1000$; see, C'96 and C'97a). In this parameter range the protons remain hot, typically, $T_p \sim 1 - 10 \times 10^9$ degrees or so. This is because the efficiency of emission is lower ($f = 1 - Q^-/Q^+ \sim 0.1$, where, Q^+ and Q^- are the heat generation [due to viscous processes] and heat loss rates respectively. Also see, Rees [1984], where it is argued that \dot{m}/α^2 is a good indication of the cooling efficiency of the hot flow.). We have studied a large region of parameter space in details where $0.0001 \lesssim \alpha \lesssim 1$, $0.001 \lesssim \dot{m} \lesssim 100$, $0.01 \lesssim F_{Compt} \lesssim 0.95$, $4/3 \lesssim \gamma \lesssim 5/3$ are chosen. Here, F_{Compt} is the factor by which the proton temperature is reduced due to bremsstrahlung and Comptonization effects. Results with several sets of initial conditions are in MC'98. Since shocks can form in advective disks for a large region of parameter space (C'96 and references therein) we use a case with a standing shock in this paper.

In selecting the reaction network we kept in mind the fact that hotter

flows may produce heavier elements through triple- α and rapid proton and α capture processes. Furthermore due to photo dissociation significant neutrons may be produced and there is a possibility of production of neutron rich isotopes. Thus, we consider sufficient number of isotopes on either side of the stability line. The network thus contains protons, neutrons, till ^{72}Ge - altogether 255 nuclear species. The standard reaction rates were taken [MC98].

3. Results

We present now with a typical case which contained a shock wave in the advective region. We use the mass of the black hole $M/M_{\odot} = 10$, H-stress viscosity parameter $\alpha_{\text{H}} = 0.07$, the location of the inner sonic point $x_{\text{in}} = 2.9115$ and the value of the specific angular momentum at that point $\lambda_{\text{in}} = 1.6$, the polytropic index $\gamma = 4/3$ as free parameters. The net accretion rate $\dot{m} = 1$, which is the sum of (very low) Keplerian component and the sub-Keplerian component. Results of C95 and C97a for $\dot{m}_K \sim 0.1$ and $\dot{m}_h \sim 0.9$, fix $P_{\text{Compt}} = 0.03$, $x_K = 101$. This factor is used to convert the temperature distribution of solutions of C96 (which does not explicitly uses Comptonization) to temperature distribution *with* Comptonization. The proton temperature and velocity distribution computed in this manner are shown in Figs. 1(a-b). (velocity is measured in units of 10^{10} cm sec $^{-1}$).

In Fig. 1c, we show the composition change close to the black hole both for the shock-free branch (dotted curves) and the shocked branch of the solution (solid curves). Only prominent elements are plotted. The difference between the shocked and the shock-free cases is that in the shock case the similar burning takes place farther away from the black hole because of much higher temperature in the post-shock region. A significant amount of the neutron (with a final abundance of $Y_n \sim 10^{-3}$) is produced due to photo-dissociation process. Note that closer to the black hole, ^{12}C , ^{16}O , ^{24}Mg and ^{28}Si are all destroyed completely, even though at around $r = 3$ or so, the abundance of some of them went up first before going down. Among the new species which are formed closer to the black hole are ^{30}Si , ^{46}Ti , ^{50}Cr . Note that the final abundance of ^{20}Ne is significantly higher than the initial value. Thus a significant metallicity could be supplied by winds from the centrifugal barrier. In Fig. 1d, we show all the energy release/absorption components for the shocked flow. The viscous energy generation (Q^+) and the loss of energy (Q_-) from the disk (short dashed) are shown. These quantities, had the advective regime had Keplerian distribution, are also plotted (dotted). Solid curve represents the nuclear energy release/absorption for the shocked flow and the long dashed curve is that for the shock-free flow. Dot-dashed curve represents the nuclear energy release/absorption for big-

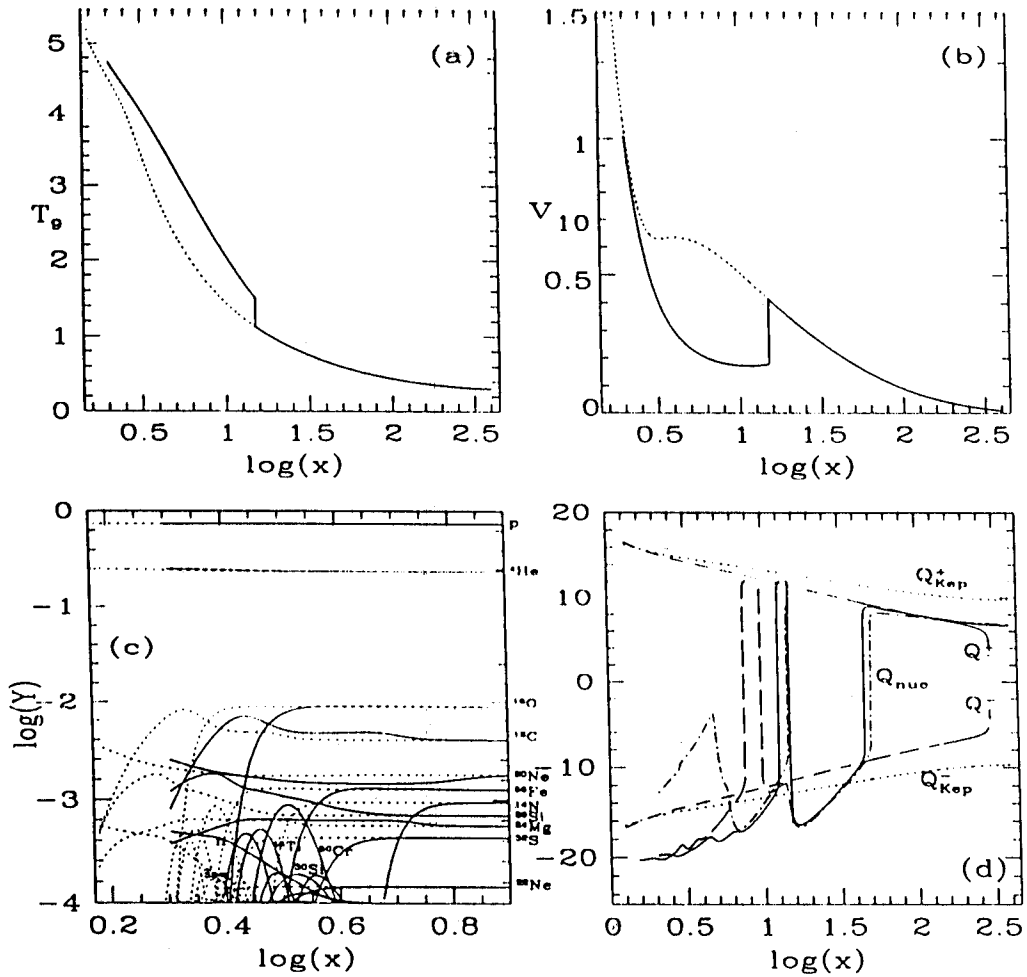


Fig. 1 : Variation of (a) proton temperature (T_p), (b) radial velocity v_{10} , (c) matter abundance Y_i in logarithmic scale and (d) various forms of specific energy release and absorption rates as functions of logarithmic radial distance (x in units of Schwarzschild radius). See text for parameters. Solutions in the stable branch with shocks are solid curves and those without the shock are dotted in (a-c). Curves in (d) are described in the text. At the shock temperature and density rise significantly and cause a significant change in abundance even farther out. Shock induced winds may cause substantial contamination of the galactic composition when parameters are chosen from these regions.

bang abundance. As matter leaves the Keplerian flow, the rapid proton capture (rp -) processes (such as, $p + {}^{18}\text{O} \rightarrow {}^{15}\text{N} + {}^4\text{He}$ etc.) burn hydrogen and releases energy to the disk. At around $x = 45$, $D \rightarrow n + p$ disso-

ciates D and the endothermic reaction causes the nuclear energy release to become 'negative', i.e., a huge amount of energy is absorbed from the disk. At around $x = 14$ the energy release is again dominated by the original rp -processes. Excessive temperature at around $x = 12.6$ breaks ${}^3\text{He}$ down into deuterium. This type of reactions absorb a significant amount of energy from the flow. When big-bang abundance is chosen to be the initial abundance, the net composition does not change very much, but the dominating reactions themselves are somewhat different because the initial compositions are different. For instance, in place of rapid proton capture reactions as above, the fusion of deuterium into ${}^4\text{He}$ plays dominant role via $D + D \rightarrow {}^3\text{He} + n$, $D + p \rightarrow {}^3\text{He}$, $D + D \rightarrow p + T$, ${}^3\text{He} + D \rightarrow p + {}^4\text{He}$. This is because no heavy elements were present to begin with. Endothermic reactions at around $x = 20 - 40$ are dominated by deuterium dissociation as before. However, after the complete destruction of deuterium, the exothermic reaction is momentarily dominated by neutron capture processes (due to the same neutrons which are produced earlier via $D \rightarrow n + p$) such as $n + {}^3\text{He} \rightarrow p + T$ which produces the spike at around $x = 14.5$. Following this, ${}^3\text{He}$ and T are destroyed as in solar abundance case and reaches the minimum in the energy release curve at around $x = 6$. The tendency of going back to the exothermic region is stopped due to the photo-dissociation of ${}^4\text{He}$ via ${}^4\text{He} \rightarrow p + T$ and ${}^4\text{He} \rightarrow n + {}^3\text{He}$. At the end of the big-bang abundance calculation, a significant amount of neutrons are produced. It is interesting to note that the radial dependence as well as the magnitude of the energy release due to rp -process and that due to viscous dissipation (Q^+) are *very* similar (save the region where endothermic reactions dominate). This suggests that even with nuclear reactions, at least some part of the advective disk may be perfectly stable.

We now present another interesting case where lower accretion rate ($\dot{m} = 0.01$) but higher viscosity (0.2) were used and the efficiency of emission is intermediate ($f = 0.2$). That means that the temperature of the flow is high ($F_{\text{Compt}} = 0.1$, maximum temperature $T_9^{\text{max}} = 13$). $x_K = 8.4$ in this case, if the high viscosity is due to stochastic magnetic field, protons would be drifted towards the black hole due to magnetic viscosity, but the neutrons will not be drifted (Rees et al., 1982) till they decay. This principle has been used to do the simulation in this case. The modified composition in one sweep is allowed to interact with freshly accreting matter with the understanding that the accumulated neutrons do not drift radially. After few iterations or sweeps the steady distribution of the composition may be achieved. Figure 2 shows the neutron distributions in iteration numbers 1, 7, 14 & 21 respectively (from bottom to top curves) in the advective region. The formation of a 'neutron torus' (Hogan & Applegate, 1987) is very apparent in this result and generally in all the hot advective flows. Details

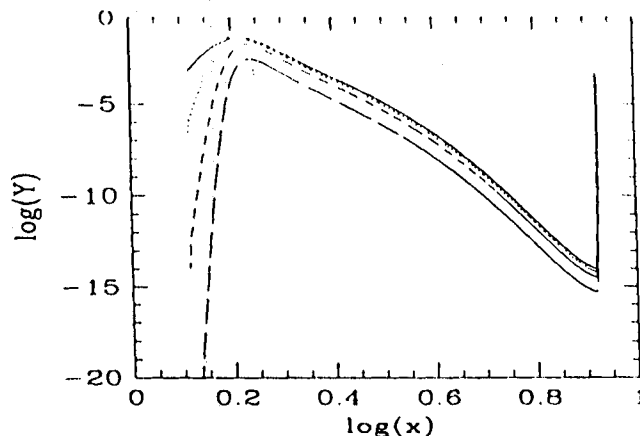


Fig. 2 : The convergence of the neutron abundance through successive iterations in a very hot advective disk. From bottom to top curves 1, 7, 14 and 21 iteration results are shown. A neutron torus with a significant abundance is formed in this case.

are in Chakrabarti & Mukhopadhyay (1998).

4. Discussions and Conclusions

In this paper, we have explored the possibility of nuclear reactions in advective accretion flows around black holes. Although this region is not fully self-consistently computed yet, particularly near the region where the advective disk joins with a standard Keplerian disk, we have used the best model that is available in the literature so far (C96). Temperature in this region is controlled by the efficiencies of bremsstrahlung and Comptonization processes (CT96, C97a) and possible heating and cooling due to magnetic fields (Shapiro, 1973; Bisnovatyi-Kogan, 1998). For a higher Keplerian rate and higher viscosity, the inner edge of the Keplerian component comes closer to the black hole and the advective region becomes cooler (CT95). However, as the viscosity is decreased, the inner edge of the Keplerian component moves away and the Compton cooling becomes less efficient.

The composition changes especially in the centrifugal pressure supported denser region, where matter is hotter and slowly moving. Since centrifugal pressure supported region can be treated as an effective surface of the black hole which may generate winds and outflows in the same way as the stellar surface, one could envisage that the winds produced in this

region would carry away modified composition (Chakrabarti, 1997b; Das & Chakrabarti 1998; Das, 1998). In very hot disks, a significant amount of free neutrons are produced which, while coming out through winds may recombine with outflowing protons at a cooler environment to possibly form deuteriums a process originally suggested by Ramadurai & Rees (1985) in the context of ion tori around black holes. A few related questions have been asked lately: Can lithium in the universe be produced in black hole accretion (Jin 1990; Yi & Narayan, 1997)? We believe that this is not possible. The spallation reactions may produce such elements when only He-He reactions are considered. But when the full network is used we find that the hotter disks where spallation would have been important also photo-dissociate heliums to deuteriums and then to protons and neutrons before any significant lithiums could be produced. Another question is: Could the metallicity of the galaxy be explained, at least partially, by nuclear reactions? We believe that this is quite possible. Details are in MC98.

An interesting possibility of formation of the neutron torus was also discussed by Hogan & Applegate (1987): Can a neutron torus be formed around a black hole? We find that in the case of hot inflows, such formation of neutron tori is a very distinct possibility (Chakrabarti & Mukhopadhyay, 1998). Presence of a neutron torus around a black hole would help the formation of neutron rich species as well, a process hitherto attributed to the supernovae explosions only.

The advective disks as we know today do not perfectly match with a Keplerian disk. The shear, i.e., $d\Omega/dx$ is always very small in the advective flow compared to that of a Keplerian disk near the outer boundary of the advective region. We believe that such behavior is unphysical and had the viscosity α parameter or the cooling function were allowed to be changed continuously, such deviation would not have occurred. Thus some improvements of the disk model at the transition region is needed, but since major reactions are closer to the black hole, we believe that such modifications of the model would not change our conclusions. The neutrino luminosity is generally very large compared to the photon luminosity in case of hot disk (Mukhopadhyay & Chakrabarti 1998). In the first Case that we discussed above, neutrinos typically carry an energy of around 10^{30} ergs sec^{-1} gm^{-1} . Assuming that a typical neutrino is of energy ~ 1 MeV, and appreciable neutrinos are emitted only from a region of a radial extent of the order of a Schwarzschild radius where the disk is also around a Schwarzschild radius thick and the density is around 10^{-9} gm sec^{-1} . In presence of hot advective disks, the number of neutrinos that should be detected per square cm area on the surface of earth would be at least a few per second provided the source is a $10M_{\odot}$ black hole at a distance of 10kpc. On the other hand, neutrino luminosity from a cool advective disk is low (around 10^{15} ergs

$\text{sec}^{-1} \text{ gm}^{-1}$) and no appreciable number of neutrino are expected. Thus, probably one way to check if hot, and stable advective disks exist is to look for neutrinos from the suspected black hole candidates, especially in the hard states.

In all the cases, even when the nuclear composition changes are not very significant, we note that the nuclear energy release due to exothermic reactions or absorption of energy due to endothermic reactions is of the same order as actual radiation from the disk. Unlike the gravitational energy release due to viscous processes, nuclear energy release strongly depends on temperatures. Thus, the additional energy source or sink may destabilize the flow. This aspect has not been studied in this work yet. A realistic way to do this is to include the nuclear energy also in time dependent studies of the black hole accretion (e.g., Molteni, Lanzafame & Chakrabarti, 1994; Molteni, Ryu & Chakrabarti, 1997). Such works are in progress and the results would be reported elsewhere.

References

- Bisnovaty-Kogan, G., 1998, this volume.
 Chakrabarti, S. K., Jin, L. & Arnett, W.D. *ApJ*, **313**, 674 [CJA], 1987
 Chakrabarti, S. K., *ApJ*, **464**, 623 [C96] 1996
 Chakrabarti, S. K., *ApJ*, **324**, 391 1988
 Chakrabarti, S. K., *ApJ*, **484**, 313 [C97a], 1997a
 Chakrabarti, S. K., *ApJ* (submitted), 1997b
 Chakrabarti, S.K., & Mukhopadhyay, B. (submitted), 1998
 Chakrabarti, S.K., & Titarchuk, *ApJ*, **455**, 623 [C95], 1995
 Das, T.K. & Chakrabarti, S.K., *ApJ* (submitted), 1998
 Das, T.K., 1998, this volume
 Hawley, J.W., Smarr, L.L. & Wilson, J.R., *Astrophys. J.*, **277**, 296, 1984
 Hawley, J.F., Smarr, L.L., & Wilson, J.R., *ApJS*, **55**, 211, 1985
 Hogan, C.J. & Applegate, J.H. *Nat*, **390**, 236, 1987
 Jin, L., Arnett, W.D. & Chakrabarti, S.K. *ApJ*, **336**, 572, 1989
 Jin, L., *ApJ*, **356**, 501, 1990
 Molteni, D., Lanzafame, G., & Chakrabarti, S.K., *ApJ*, **425**, 161, 1994
 Molteni, D., Ryu, D., & Chakrabarti, S. K., *ApJ*, **470**, 460, 1997
 Mukhopadhyay, B. & Chakrabarti, S.K., *ApJ*, 1998, (submitted) [MC98]
 Paczyński, B. & Bisnovaty-Kogan, G., *Acta Astron.*, **31**, 283, 1981
 Ramadurai, S. & Rees, M.J., *MNRAS*, **215**, 53P-56P, 1985
 Rees, M.J., *Ann. Rev. Astron. Astrophys.*, **22**, 471, 1984
 Shapiro, S.L., *ApJ*, **180**, 531, 1973
 Yi, I. & Narayan, R., *Astrophys. J.*, **486** 383, 1997

The complete solution of dirac equation in kerr geometry

Banibrata Mukhopadhyay and Sandip K. Chakrabarti

S. N. Bose National Centre For Basic Sciences, JD Block, Salt Lake, Sector-III, Calcutta-700091
e-mail: *bm@boson.bose.res.in* and *chakraba@boson.bose.res.in*

Abstract. In 1976 Chandrasekhar separated the Dirac equation in Kerr geometry in radial and angular parts. Chakrabarti in 1984 solved the angular equation and found the corresponding eigenvalues for different Kerr parameters. Chandrasekhar solved the radial equation asymptotically and the reflection and transmission coefficients were calculated by him for few Kerr parameters. In the present paper, we solve the complete radial equation and calculate analytical expressions of radial wave functions for a set of Kerr and wave parameters. From the solution we get the reflection and transmission coefficients, which are now space dependent.

1. Introduction

One of the most important solutions of Einstein's equation is that of the spacetime around and inside an isolated black hole. The spacetime at a large distance is flat and Minkowskian where usual quantum mechanics is applicable, while the spacetime closer to the singularity is so curved that no satisfactory quantum field theory could be developed as yet. An intermediate situation arises when a weak perturbation (due to, say, gravitational, electromagnetic or Dirac waves) originating from infinity impinges on a black hole, interacting with it. The resulting wave is partially transmitted into the black hole through the horizon and partially scatters off from it to infinity. In the linearized ('test field') approximation this problem has been attacked in the past by several authors [1-4]. The master equations of Teukolsky [2] which govern these linear perturbations for integral spin (e.g., gravitational and electromagnetic) fields were solved numerically by Press and Teukolsky [5] and Teukolsky and Press [6]. Chandrasekhar [3-4] separated the Dirac equation in Kerr geometry into radial and angular parts. Subsequently, Chakrabarti [7] solved the angular part of the Dirac equation in Kerr geometry and gave the eigenvalues of the equation. Chandrasekhar [4] calculated the asymptotic behavior of the radial part of the Dirac equation for massless particles (neutrino) and indicated how the form would be modified for when the Dirac particles are massive. In the present paper, we present a complete solution of the Dirac equation.

2. Basic equations of the problem

The radial parts of the Dirac equation are Banibrata

$$\Delta^{\frac{1}{2}} D_0 R_{-\frac{1}{2}} = (\lambda + im_p r) \Delta^{\frac{1}{2}} R_{+\frac{1}{2}} \quad (1)$$

$$\Delta^{\frac{1}{2}} D_0 \Delta^{\frac{1}{2}} R_{+\frac{1}{2}} = (\lambda - im_p r) R_{-\frac{1}{2}} \quad (2)$$

where $D_n = \partial_r + \frac{iK}{\Delta} + 2n \frac{(r-M)}{\Delta}$, $\Delta = r^2 + a^2 - 2Mr$, $K = (r^2 + a^2)\sigma + am$

where, a = Kerr parameter, n = integer, σ = frequency of incident wave of the particle, M = mass of the black hole, m = azimuthal quantum number, m_p = mass of the particle, λ = eigenvalue of the Dirac equation which was calculated in [7], $R_{+1/2}(R_{-1/2})$ = radial wave function with spin up (down).

The radial equation here is in coupled form. We can decouple it and express the equation either in terms of spin up or spin down wave function. However it is more convenient to follow Chandrasekhar's [4] approach by which he changed the basis and independent variable r and

transformed the coupled equation into two independent one dimensional wave equations since they are easier to solve.

We first define

$$r_* = r + \frac{2Mr_+ + am/\sigma}{r_+ - r_-} \log\left(\frac{r}{r_+} - 1\right) - \frac{2Mr_- + am/\sigma}{r_+ - r_-} \log\left(\frac{r}{r_-} - 1\right)$$

where $r) r_+$ and $\frac{d}{dr_*} = \frac{\Delta}{\omega^2} \frac{d}{dr}$, $\omega^2 = r^2 + \alpha^2$, $\alpha^2 = a^2 + (am/\sigma)$

and choose

$$\Delta^{\frac{1}{2}} R_{+\frac{1}{2}} = P_{+\frac{1}{2}}, R_{-\frac{1}{2}} = P_{-\frac{1}{2}}$$

In terms of r^* , the operators take the form: $D_0 = \frac{\omega^2}{\Delta} \left(\frac{d}{dr_*} + i\sigma \right)$ and $D'_0 = \frac{\omega^2}{\Delta} \left(\frac{d}{dr_*} - i\sigma \right)$

We choose $\theta = \tan^{-1}(m_p r / \lambda)$ which yields

$$\cos \theta = \frac{\lambda}{\sqrt{(\lambda^2 + m_p^2 r^2)}}, \sin \theta = \frac{m_p r}{\sqrt{(\lambda^2 + m_p^2 r^2)}} \text{ and } (\lambda \pm im_p r) = \exp(\pm i\theta) \sqrt{(\lambda^2 + m_p^2 r^2)}$$

Following exactly Chandrasekhar's [4] approach we write

$$P_{+\frac{1}{2}} = \Psi_{+\frac{1}{2}} \exp\left[-\frac{1}{2} i \tan^{-1}\left(\frac{m_p r}{\lambda}\right)\right] \text{ and } P_{-\frac{1}{2}} = \Psi_{-\frac{1}{2}} \exp\left[+\frac{1}{2} i \tan^{-1}\left(\frac{m_p r}{\lambda}\right)\right]$$

Finally a choice of $\hat{r}_* = r_* + \frac{1}{2\sigma} \tan^{-1}\left(\frac{m_p r}{\lambda}\right)$ yields $d\hat{r}_* = \left(1 + \frac{\Delta}{\omega^2} \frac{\lambda m_p}{2\sigma} \frac{1}{\lambda^2 + m_p^2 r^2}\right) dr_*$

With these definitions, the differential equations (1 and 2) are re-written as

$$\left(\frac{d}{d\hat{r}_*} - W\right) Z_+ = i\sigma Z_- \tag{3a}$$

$$\left(\frac{d}{d\hat{r}_*} + W\right) Z_- = i\sigma Z_+ \tag{3b}$$

where $Z_{\pm} = \Psi_{+\frac{1}{2}} \pm \Psi_{-\frac{1}{2}}$ and $W = \frac{\Delta^{\frac{1}{2}} (\lambda^2 + m_p^2 r^2)^{3/2}}{\omega^2 (\lambda^2 + m_p^2 r^2) + \lambda m_p \Delta / 2\sigma}$

From these equations, we readily obtain the pair of independent one-dimensional wave-equations,

$$\left(\frac{d^2}{d\hat{r}_*^2} + \sigma^2\right) Z_{\pm} = V_{\pm} Z_{\pm} \tag{4}$$

where

$$V_{\pm} = W^2 \pm \frac{dW}{d\hat{r}_*}$$

$$= \frac{\Delta^{\frac{1}{2}} (\lambda^2 + m_p^2 r^2)^{3/2}}{[\omega^2 (\lambda^2 + m_p^2 r^2) + \lambda m_p \Delta / 2\sigma]^2} \left[\Delta^{\frac{1}{2}} (\lambda^2 + m_p^2 r^2)^{3/2} \pm ((r-M)(\lambda^2 + m_p^2 r^2) + 3m_p^2 r \Delta) \right]$$

$$\mp \frac{\Delta^{\frac{3}{2}} (\lambda^2 + m_p^2 r^2)^{5/2}}{[\omega^2 (\lambda^2 + m_p^2 r^2) + \lambda m_p \Delta / 2\sigma]^3} \left[2r(\lambda^2 + m_p^2 r^2) + 2m_p^2 \omega^2 r + \lambda m_p (r-M) / \sigma \right]$$

3. The method to solve the equation

From eq. (4) it is clear that it is not analytically solvable unless very special case is chosen because of the non-trivial form of V_{\pm} . But for a particular set of parameters (such as specific angular momentum of the Kerr black hole, particle mass, particle energy) we observe that the nature of the potential is well behaved although the mathematical expression of the potential is complicated. So if expression of potential is fitted with a function with the presence of which the differential equation can be solved analytically then equation can be solved by replacing that expression of analytic function in place of potential expression in the differential equation. Using this procedure the differential wave equation is solved here by WKB approximation method. Solving the equation we get the reflection and transmission coefficient (which was calculated by Chandrasekhar [4] asymptotically). Also we impose space dependence on the coefficients so at each point from infinity to black hole horizon we find how reflection and transmission coefficient change. Here is one important point to note, that is the transformation of spatial co-ordinate r to r^* (and \hat{r}^*) is taken not only for mathematical simplicity but there is also physical significance. In case of initial equation which was a function of r , the black hole horizon is at r_+ . By decoupling the equation we obtain also two independent wave equations. Here we see the coefficients of the first order derivative term and linear term are not well behaved with respect to r (they are diverging functions). But by transforming those in terms of r^* (and \hat{r}^*) we get well behaved functions and horizon also is shifted to $-\infty$.

4. Solution

We present here the solution of eq. (4) for a few sets of parameters. The choice of parameters is generally made in such a way that there is significant interaction between the particle and the black hole, the Compton wavelength of the incoming wave should be of same order as Kerr radius. So,

$$G \left[M + \sqrt{M^2 - a^2} \right] / c^2 \sim \frac{h}{m_p c}$$

Here we are choosing $G = h = c = 1$, so

$$m_p \sim \left[M + \sqrt{M^2 - a^2} \right]^{-1}$$

Again for the case of Kerr geometry, frequency of the incoming particle (or wave) will be of the same order as inverse of time. So,

$$\frac{c^3}{G \left[M + \sqrt{M^2 - a^2} \right]} \sim \sigma$$

Using suitable units as before, we can write,

$$m_p \sim \sigma \sim \left[M + \sqrt{M^2 - a^2} \right]^{-1}$$

Case I

The parameters chosen here are given below,

Kerr parameter, $a = 0.5$

Mass of the black hole, $M = 1$

Mass of the particle, $m_p = 0.7999$

Orbital quantum number, $l = 1/2$

Azimuthal quantum number, $m = -1/2$

Frequency of the incoming wave, $\sigma = 0.8$

The derived parameters are,

$$\text{Corresponding black hole horizon, } r_+ = M + \sqrt{M^2 - a^2} \cong 1.86603$$

Corresponding $\sigma_r = 1$
 Corresponding $\sigma_s = 0.066987$
 Corresponding parameter $\alpha^2 = -0.0625$
 Corresponding eigenvalue $\lambda = 0.918573$ [7].

Here it is clear that σ is in between σ_r and σ_s and $\alpha^2 < 0$, $r_* > |\alpha|$ so this is strictly non super-radiant, i.e., $\sigma \leq \sigma_s$ [4].

From eq. (4) we observe there are two wave equations of corresponding potentials V_+ and V_- . The nature of potentials are shown in Fig. 1a. It is clear from the Fig. 1a that potential V_+ (solid curve) is well behaved. It is monotonically decreasing as the particle approaches the black hole, and the total energy chosen in this case (σ^2) is always higher compared to V_- . Here we concentrate to study the equation with potential V_+ . The expression of the potential is fitted with a few piecewise continuous analytic functions which are of the form

$$V_j = a'_j + b'_j \exp(-\hat{r}_* / c'_j)$$

The index j refers to different choices of the constants a' , b' , c' in different ranges of \hat{r}^* .

Now we re-write equation (4) as

$$\frac{d^2 Z_+}{d\hat{r}_*^2} + (\sigma^2 - V_+) Z_+ = 0 \quad (5)$$

let $k(\hat{r}_*) = \sqrt{(\sigma^2 - V_+)}$, $u(\hat{r}_*) = \int k(\hat{r}_*) d\hat{r}_* + \text{constant}$, so

$$k_j^2 = a_j + b_j \exp\left(\frac{-\hat{r}_*}{c_j}\right) \quad (6)$$

$$\text{and } u_j = \int k_j d\hat{r}_* = -2c_j k_j(\hat{r}_*) + c_j \sqrt{a_j} \log \left| \frac{\sqrt{a_j} + k_j(\hat{r}_*)}{\sqrt{a_j} - k_j(\hat{r}_*)} \right| + \text{constant} \quad (7)$$

Here, k is the wave number of the incoming wave and u as the *Eiconal*.

The solution of the equation (5) is,

$$Z_+ = \frac{A_+}{\sqrt{k}} \exp(iu) + \frac{A_-}{\sqrt{k}} \exp(-iu) \quad (8)$$

In this case all along $\sigma^2 > V_+$ and also $\frac{1}{k} \frac{dk}{d\hat{r}^*} \ll k$, so WKB approximation is valid in the whole

region. The equation (8) is the second order approximate solution. In Fig. 1b we show the nature of V_+ (solid curve), k (dashed curve) and $E (= \sigma^2)$ (short-dashed curve). In Fig. 1c the nature of the *Eiconal* u is shown. In the solution (eq. 8) first term represents the term corresponding incident wave and second term corresponds to the reflected wave. Now we will introduce space dependence on A_+ and A_- to get more accurate solution.

We write,

$$W_+ = \exp(iu) / \sqrt{k} \quad (9a)$$

$$\text{and } W_- = \exp(-iu) / \sqrt{k} \quad (9b)$$

$$\text{and } k^2(\hat{r}_*) = f(\hat{r}_*)$$

Defining

$$X = \left[\frac{1}{4} \frac{f''}{f} - \frac{5}{16} \left(\frac{f'}{f} \right)^2 \right]$$

we can write

$$W_{\pm}'' + [f + X] W_{\pm} = 0 \quad (10)$$

where, the single prime and double prime indicate single and double derivatives with respect to \hat{r}^* respectively. The original Z_+ equation takes the form

$$Z_+'' + f Z_+ = 0 \quad (11)$$

Now considering A_{\pm} to be the osculating parameter and following the approach of Mathews and Walker [9] we get,

$$A_{\pm} = \pm \frac{Z_+ W_{\mp}' - Z_{\mp}' W_{\pm}}{W_+ W_{-}' - W_{\mp}' W_{\pm}} \quad (12)$$

Differentiating eq. (12) and using eq. (10) and eq. (11) we can eliminate Z_{\pm}' and W_{\pm}' , and obtain

$$\frac{dA_+}{d\tilde{r}_0} = -\frac{i}{2} \frac{X}{k} [A_+ + A_- e^{-2iu}] \quad (13a)$$

$$\frac{dA_-}{d\tilde{r}_0} = +\frac{i}{2} \frac{X}{k} [A_- + A_+ e^{+2iu}] \quad (13b)$$

Now multiplying (13a) by e^{+iu} and (13b) by e^{-iu} and then adding, we get

$$e^{+iu} \frac{dA_+}{d\tilde{r}_0} + e^{-iu} \frac{dA_-}{d\tilde{r}_0} = 0 \quad (14)$$

Now for simplicity we are considering A_{\pm} to be real, so in eq. (14) separating real and imaginary parts we get ,

$$\frac{dA_+}{d\tilde{r}_0} + \frac{dA_-}{d\tilde{r}_0} = 0 \quad (15a)$$

$$\text{and } \frac{dA_+}{d\tilde{r}_0} - \frac{dA_-}{d\tilde{r}_0} = 0 \quad (15b)$$

Using either of the above equations we can find out analytical expression of A_+ and A_- . We choose eq. (15b) from where we obtain,

$$A_+ = A_- + c \quad (16)$$

This is a relation between A_+ and A_- up to this order of approximation. Here, c is an arbitrary integral constant which can be calculated by boundary condition.

Also another necessary condition

$$A_+^2 + A_-^2 = k \quad (17)$$

is imposed here since sum of the reflection and the transmission coefficient must be unity with respect to the transmission of the very previous point.

To determine c we need the value of coefficient A_{\pm} at least at one point, so we will calculate the asymptotic values. For this we consider a square potential barrier of same area under the curve as our given potential of the problem and of constant height as height at infinity of our potential. With respect to this barrier if we find the value of the coefficients, which will be the asymptotic values of the reflection and transmission coefficients for the original potential of our problem. By remembering the value of k at infinity and if T and R are the asymptotic values of transmission and reflection coefficients respectively then value of constant c can be calculated as

$$c = \left[\sqrt{kT} - \sqrt{kR} \right]_{\infty} = -0.032629 = -c'$$

So now we can write

$$A_+ = A_- - c' \quad (18)$$

and

$$A_+ = \sqrt{(k - A_+^2)} - c' \quad (19)$$

This gives,

$$A_{\pm} = \frac{c}{2} \pm \frac{\sqrt{(2k - c^2)}}{2} \quad (20)$$

But the solution with these coefficients has some disadvantage that it does not satisfy inner boundary condition at the horizon, i.e., unit transmission and zero reflection coefficients. For this, functions A_{\pm} must be shifted by introducing two different constants. So expressions of A_+ and A_- change to

$$A_+ = c_1 + \frac{c}{2} + \frac{\sqrt{2k - c^2}}{2} \quad (21a)$$

$$A_- = c_2 - \frac{c}{2} + \frac{\sqrt{2k - c^2}}{2} \quad (21b)$$

Now to maintain the sum of the reflection and transmission coefficients to unity, we must have

$$A_+^2 + A_-^2 = \left(c_1 + \frac{c}{2}\right)^2 + \left(c_2 - \frac{c}{2}\right)^2 + (c_1 + c_2)\sqrt{2k - c^2} + \frac{(2k - c^2)}{2} = h(\text{say}) = \left(\frac{h}{k}\right)k \quad (22)$$

It is advisable to choose the modified coefficients of the wave function as follows:

$$a_+ = \frac{A_+}{\sqrt{h/k}} \quad (23a)$$

$$a_- = \frac{A_-}{\sqrt{h/k}} \quad (23b)$$

so that

$$a_+^2 + a_-^2 = k \quad (24)$$

and the reflection and transmission coefficients are a_-^2/k and a_+^2/k respectively which are explicitly written as:

$$T = \frac{\left(c_1 + \frac{c}{2}\right)}{h} \left(c_1 + \frac{c}{2} + \sqrt{2k - c^2}\right) + \frac{2k - c^2}{4h} \quad (25a)$$

$$R = \frac{\left(c_2 - \frac{c}{2}\right)}{h} \left(c_2 - \frac{c}{2} + \sqrt{2k - c^2}\right) + \frac{2k - c^2}{4h} \quad (25b)$$

It is clear that difference between a_+ and a_- are not constant now and $da_+/d\hat{r}_*$ is not same as $da_-/d\hat{r}_*$. Also it can be easily checked by putting back this fourth order corrected solution into original differential equation that solution is still satisfying the equation up to consideration $\frac{1}{k} \frac{dk}{d\hat{r}_*} \ll 1$.

In Fig. 1d, variation of reflection and transmission coefficients are shown. It is seen that as matter comes close towards the black hole, the barrier height goes down. As a result, penetration probability increases resulting in the rise of the transmission coefficient.

Similarly, one can also solve the wave equation with potential V .

The radial wave functions $R_{+1/2}$ and $R_{-1/2}$ which are of spin up and spin down particles respectively of the original Dirac equation are given below,

$$\text{Re} \left(R_{\frac{1}{2}} \Delta^{\frac{1}{2}} \right) = \frac{a_+ \cos(u - \theta) + a_- \cos(u + \theta)}{2\sqrt{k}} + \frac{a'_+ \cos(u' - \theta) + a'_- \cos(u' + \theta)}{2\sqrt{k'}} \quad (26a)$$

$$\text{Im} \left(R_{\frac{1}{2}} \Delta^{\frac{1}{2}} \right) = \frac{a_+ \sin(u - \theta) - a_- \sin(u + \theta)}{2\sqrt{k}} - \frac{a'_+ \sin(u' - \theta) - a'_- \sin(u' + \theta)}{2\sqrt{k'}} \quad (26b)$$

$$\text{Re} \left(R_{-\frac{1}{2}} \right) = \frac{a_+ \cos(u + \theta) + a_- \cos(u - \theta)}{2\sqrt{k}} - \frac{a'_+ \cos(u' + \theta) + a'_- \cos(u' - \theta)}{2\sqrt{k'}} \quad (26c)$$

$$\text{Im} \left(R_{-\frac{1}{2}} \right) = \frac{a_+ \sin(u + \theta) - a_- \sin(u - \theta)}{2\sqrt{k}} - \frac{a'_+ \sin(u' + \theta) - a'_- \sin(u' - \theta)}{2\sqrt{k'}} \quad (26d)$$

where $a'_+/\sqrt{k'}$ and $a'_-/\sqrt{k'}$ are the transmitted and reflected amplitudes respectively for the wave of corresponding potential V .

Case II

The parameters chosen here are given below,

- Kerr parameter, $a = 0.95$
- Mass of the black hole, $M = 1$
- Mass of the particle, $m_p = 0.1684208$
- Orbital quantum number, $l = 1/2$
- Azimuthal quantum number, $m = -1/2$
- Frequency of the incoming wave, $\sigma = 0.210526$

The derived parameters are,

$$\text{Corresponding black hole horizon, } r_+ = M + \sqrt{(M^2 - a^2)} \cong 1.31225$$

$$\text{Corresponding } \sigma_c = 0.526316$$

$$\text{Corresponding } \sigma_s = 0.180987$$

$$\text{Corresponding parameter } \alpha^2 = -1.353754$$

$$\text{Corresponding eigenvalue } \lambda = 0.930115 [7].$$

It is clear that the values of σ , σ_c and σ_s indicate the region is non super-radiant, i.e., $\sigma \leq \sigma_s$ [4]. As before, the form of the potentials are complicated and the analytical solution is not possible. We employ the method as in the previous Section. We use the equation containing V_+ (eq. 4). In Fig. 2a, we show the nature of V_+ and V_- . Unlike the case in the previous Section, here σ^2 is no longer greater than V_+ at all radii. As a result, k^2 may attain negative values in some region. The potential and therefore the corresponding k is fitted with a few piecewise smooth functions such as

$$k_j^2 = (\sigma^2 - V) = a_j + b_j \exp(\hat{r}_* / c_j) \quad (27a)$$

$$k_l^2 = (\sigma^2 - V) = a_l + b_l \hat{r}_* - c_l \hat{r}_*^2 \quad (27b)$$

Similar forms are used even when $V > \sigma^2$. The corresponding u s obtained by integrating these k s yield the following forms:

$$u_j = -2c_j k_j - c_j \sqrt{a_j} \log \left| \frac{k_j - \sqrt{a_j}}{k_j + \sqrt{a_j}} \right| + \text{constant} \quad (28a)$$

$$u_l = \frac{\left(\hat{r}_* - \frac{b_l}{2c_l} \right) k_l}{2} + \frac{\sqrt{c_l}}{2} \left(\frac{a_l}{c_l} + \frac{b_l^2}{4c_l^2} \right) \sin^{-1} \left(\frac{\hat{r}_* - \frac{b_l}{2c_l}}{\sqrt{\left(\frac{a_l}{c_l} + \frac{b_l^2}{4c_l^2} \right)}} \right) + \text{constant} \quad (28b)$$

In Fig. 2b, nature of V_+ (solid curve), parameter k (dashed curve) and energy E (short-dashed curve) are shown. In Fig. 2c, parameter u is shown. Here, WKB approximation can still be applied but it is not valid in the whole range of \hat{r}_* since $\frac{1}{k} \frac{dk}{d\hat{r}_*} \ll k$ is not satisfied in the range $\hat{r}_* = -4$ to -1

and 1 to 7. In those two ranges, we have to employ a different method. There the solutions will be linear combination of Airy functions [8] because the potential is a linear function of \hat{r}_* in those intervals. At the junctions one has to match the solutions including Airy functions with the solution obtained by WKB method.

In the region where the WKB approximation valid, reflection and transmission coefficients and the wave function can be calculated easily by following the method described in Case I. In other regions, the equation reduces to

$$\frac{d^2 Z_+}{d\hat{r}_*^2} - x Z_+ = 0$$

where $x = \beta^{1/3}(\hat{r}_* - p)$ is chosen positive and p is the critical point where the total energy and potential energy are matching.

For the region $x > 0$ the solution of eq. (29) will be

$$Z_+(x) = x^{\frac{1}{2}} \left[C_1 I_{+\frac{1}{3}}(\xi) + C_2 I_{-\frac{1}{3}}(\xi) \right]$$

where $\xi = \frac{2}{3} x^{3/2}$.

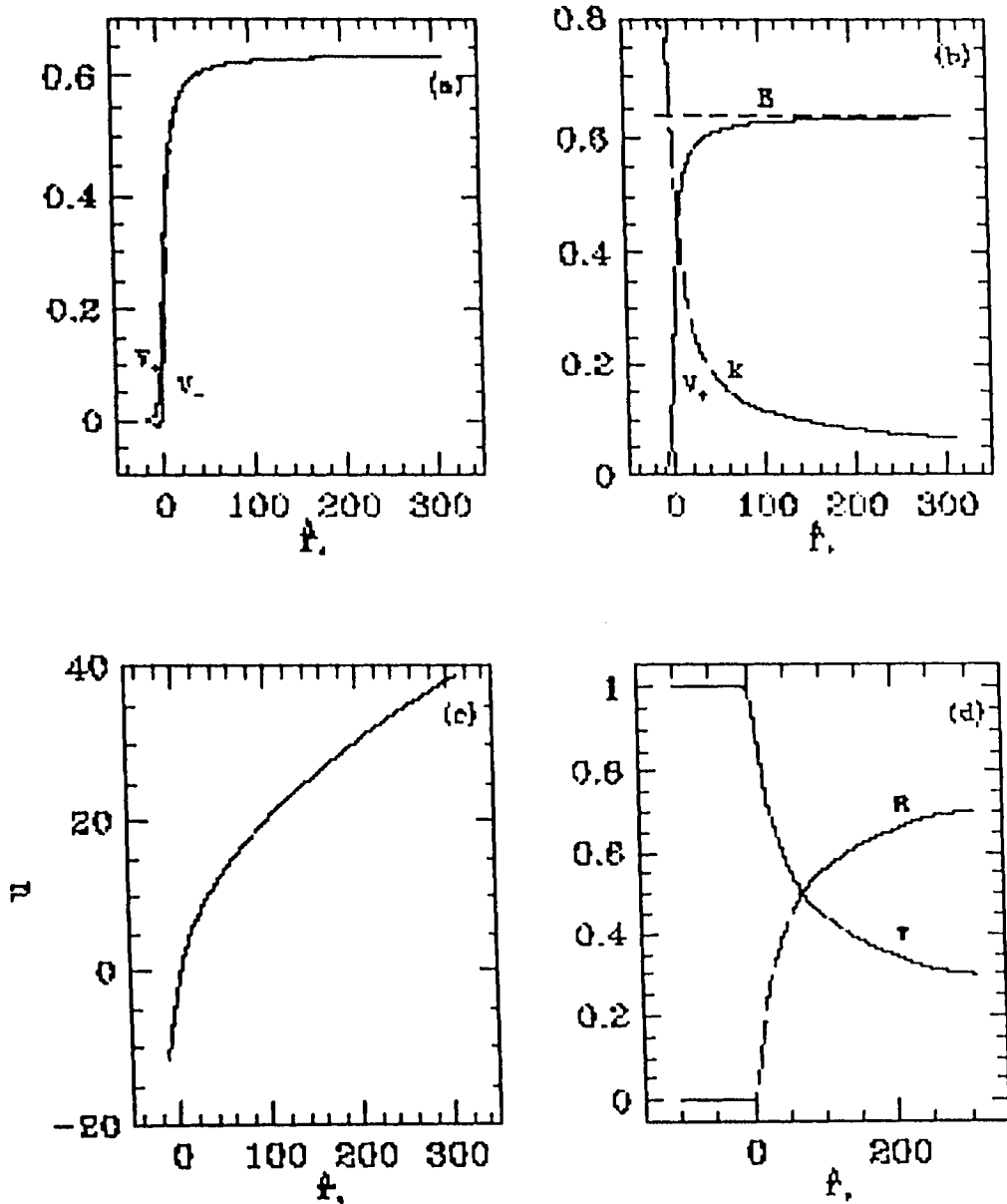


Figure 1. Behaviour of (a) V_+ (solid curve) and V_- (dashed curve), (b) V_+ (solid curve), k (dashed curve), total energy E (short-dashed curve), (c) eiconal u , (d) transmission (T , solid curve) and reflection (R , dashed curve) coefficients as functions of \hat{f} .

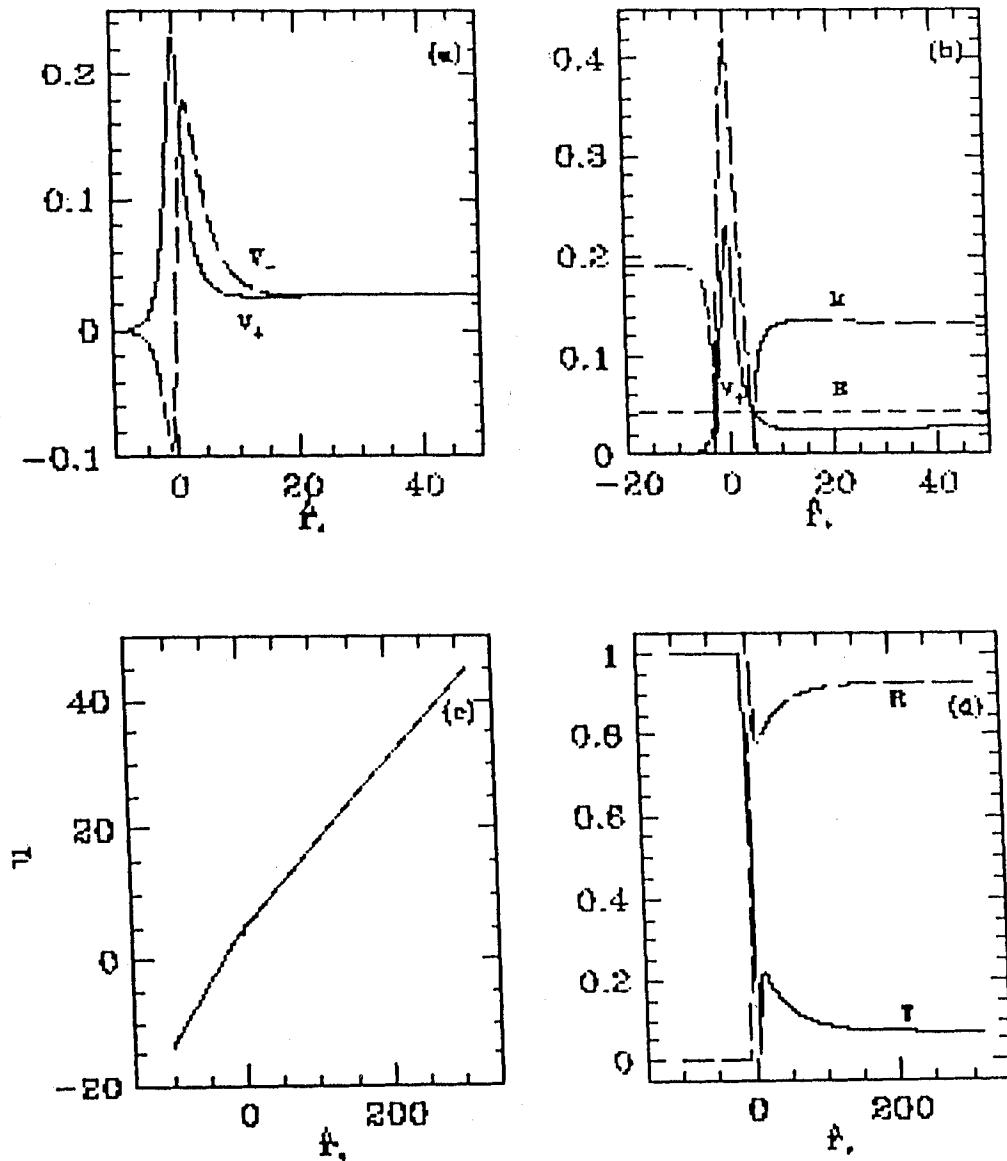


Figure 2. Behaviour of (a) V_+ (solid curve) and V_- (dashed curve), (b) V_+ (solid curve), k (dashed curve), total energy E (short-dashed curve), (c) eiconal u , (d) transmission (T , solid curve) and reflection (R , dashed curve) coefficients as functions of $\hat{\omega}$.

For the case $x < 0$ the corresponding solution will be

$$Z_+(x) = |x|^{1/2} \left[D_1 J_{+1/3}(\xi) + D_2 J_{-1/3}(\xi) \right]$$

where J_{\pm} and I_{\pm} are the Bessel functions and the modified Bessel functions of order $1/3$ respectively.

In terms of Airy functions the solutions can be written as

$$Z_+ = \frac{3}{2}(C_2 - C_1)Ai(x) + \frac{\sqrt{3}}{2}(C_2 + C_1)Bi(x) \quad \text{for } x > 0$$

$$Z_+ = \frac{3}{2}(D_2 + D_1)Ai(x) + \frac{\sqrt{3}}{2}(D_2 - D_1)Bi(x) \quad \text{for } x(0)$$

By matching boundary conditions it is easy to show that the solution corresponding $x > 0$ and that corresponding $x < 0$ are continuous when $C_1 = -D_1$ and $C_2 = D_2$. Following this process at all the junctions, we get the solution from 7 to 1 (in \hat{r}_* co-ordinate) around the critical point $\hat{r}_* = 4.45475$ as

$$Z_+ = 75.682216Ai(x) - 41.393114Bi(x)$$

Similarly the solution from -1 to -4 i.e. around the critical point $\hat{r}_* = -2.8053$ can be calculated as

$$Z_+ = -19.43945Ai(x) + 17.69174Bi(x)$$

It is to be noted that in the region $\hat{r}_* = 1$ to -1 , even though the potential energy dominates over the total energy, WKB approximation method is still valid. Here the solution will take the form $\exp(-u)/\sqrt{k}$ and $\exp(+u)/\sqrt{k}$.

Asymptotic values of the reflection and the transmission coefficients are obtained by suitably modeling the exact potential in terms of the square-well potential. This yields the integral constant c as -0.355337 . Using this, and eqs. 25(a-b), reflection and transmission coefficients are calculated, behaviors of which are shown in Fig. 2d. The constants c_1 and c_2 of eqs. 25(a-b) were calculated as before. Note the decaying nature of the reflection coefficient inside the potential barrier.

Case III

The parameters chosen here are given below,

Kerr parameter, $a = 0.95$

Mass of the black hole, $M = 1$

Mass of the particle, $m_p = 0.10526315799$

Orbital quantum number, $l = 1/2$

Azimuthal quantum number, $m = -1/2$

Frequency of the incoming wave, $\sigma = 0.105263158$

The derived parameters are,

Corresponding black hole horizon, $r_+ = M + \sqrt{M^2 - a^2} \cong 1.31225$

Corresponding $\sigma_c = 0.526316$

Corresponding $\sigma_r = 0.180987$

Corresponding parameter $\alpha^2 = -3.609999$

Corresponding eigenvalue $\lambda = 0.96970998$ [7].

It is clear that according to the definition of super-radiance and the choices of the parameters σ_c , σ_r and α^2 as above, this case should have belonged to the realm of super-radiance. However, unlike previous two cases, the relation between r and \hat{r}_* is not single valued in this region. Here, at both $r = r_+$ and $r = \infty$, the value of $\hat{r}_* = \infty$. With the decrement of r , \hat{r}_* is decreased initially up to a certain point $r = |\alpha|$. Subsequently, \hat{r}_* starts to rise and at the black hole horizon it diverges.

The behavior of potentials V_+ and V_- are shown in Fig. 3a. It is clear that at $r = |\alpha|$ the potential diverges and potential's nature is changed from repulsive to attractive. Here we will treat the equation of corresponding potential V_- . Here, we have divided our calculation into two parts, one for repulsive potential where particle is coming from infinity and most of them are reflecting back from the infinitely high barrier and another one for attractive potential where particle from the attractive potential field is coming outside (i.e. actually going to horizon but due to multivaluedness of the radial co-ordinate \hat{r}_* , with respect to r , the horizon is transformed to infinity). Here for the case of positive potential the potential is going sharply to infinity at the singular point so the wave with total energy σ^2 is hitting on the wall of the barrier. Here, as before the complicated form of the potential is fitted into a simple form by adjusting the parameters a_j , b_j , c_j . The attractive part of V_- is fitted as well.

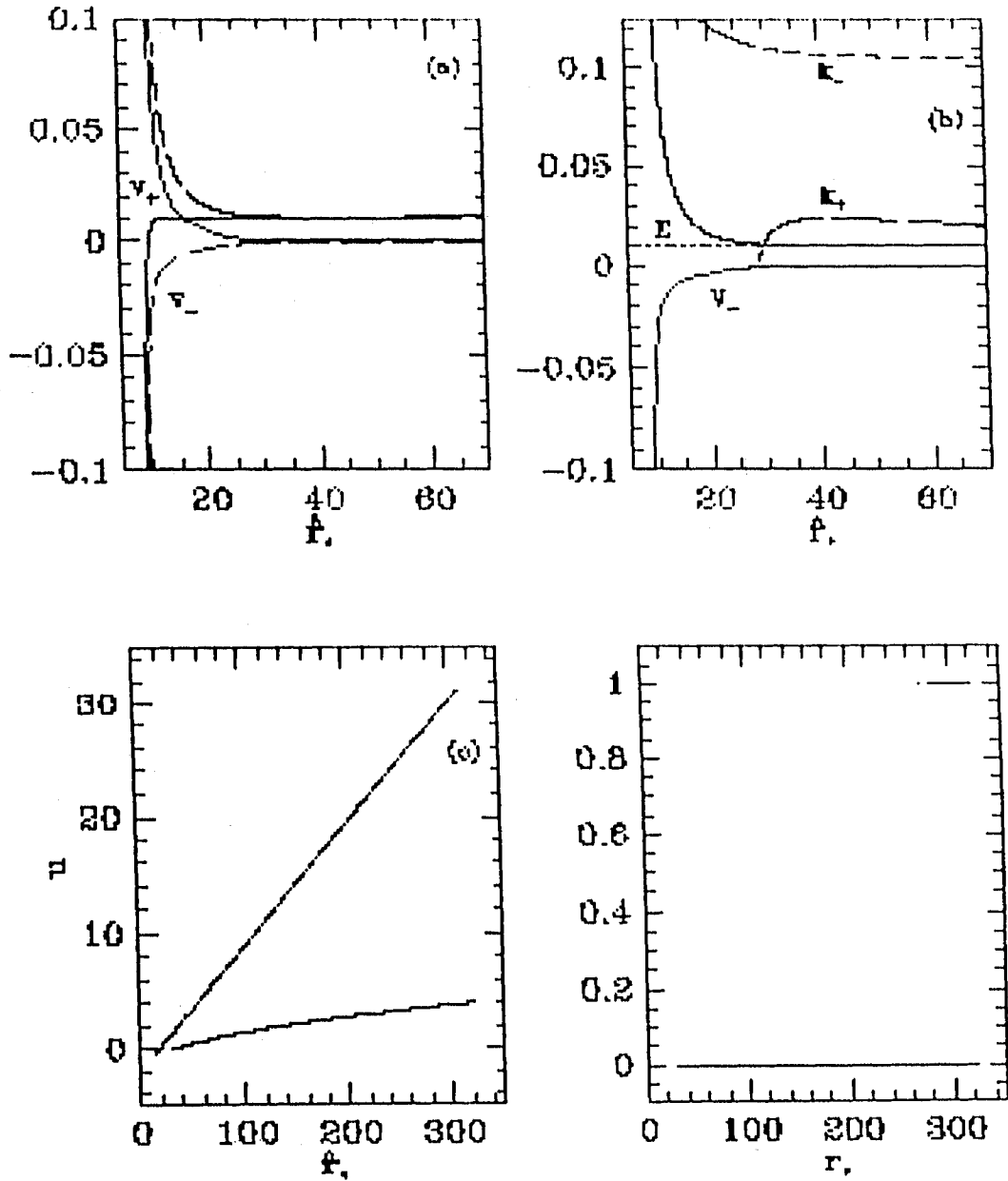


Figure 3. Behavior of (a) V_+ (solid curve) and V_- (dashed curve), (b) V_+ (solid curve), k for region where potential is positive (k_+ , dashed curve), k for region where potential is negative (k_- , short-dashed curve), total energy E (dotted curve), (c) eikonal u (d) transmission (T , solid curve) and reflection (R , dashed curve) coefficients as functions of \hat{r} .

As in the previous cases, we have computed k and u piecewise. In Fig. 3b nature of V_+ , k and E are shown. In Fig. 3c variation of u is shown. Here the WKB approximation method is valid up to \hat{r} equals to 40 (from infinity) since $\frac{1}{k} \frac{dk}{dr} \ll 1$ is not satisfied below this. The reflection and transmission coefficients and the wave function of the particle are calculated as in the previous case. Since the matter which tunnel through the infinitely high barrier face infinitely strong attractive field, the possibility of extraction of energy would be zero. In Fig. 3d the variations of transmission and reflection coefficients are shown.

The net transmission of the wave through the horizon is non-negative all along and therefore super-radiation is absent, although σ is less than σ_c . The non-existence of super-radiation is due to $(r-|\alpha|)^{-3}$ variation of the potential near the singular point. Because of existence of attractive field the extraction of energy is very very difficult, so the net transmission of the wave through horizon from ∞ is always positive.

Conclusion

In this paper, we analytically study scatterings of spin-half particles from a Kerr black hole, particularly the nature of the radial wave functions and the reflection and transmission coefficients. We chose a few illustrative cases.

Though we start with the WKB approximation method, we improvise on it so as to obtain spatial dependence of the coefficients of the wave function. This way we ensure that the analytical solution is closer to the exact solution.

We verify Chandrasekhar's [4] conjecture based on asymptotic solution that for spin-1/2 particle the phenomenon of super-radiance is absent. We believe that this is due to the very way the potential develops a singularity at $r = |\alpha|$. Here $V_-(\hat{r}_*) \propto (r - |\alpha|)^{-3}$, which results in an attractive potential in some region very close to the black hole. In contrast, the $V_-(\hat{r}_*) \propto (r - |\alpha|)^{-4}$ when electromagnetic and gravitational waves are scattered off the black hole [4] which does not create an attractive part in the potential and possibly exhibit the phenomenon of super-radiance.

References

- [1] S. Teukolsky (1972): "Rotating Black Holes: Separable Wave Equations for Gravitational and Electromagnetic Perturbations" *PRL* **29**, 1114-1118.
- [2] S. Teukolsky (1973): "Perturbations of a Rotating Black Hole. I. Fundamental Equations for Gravitational, Electromagnetic and Neutrino-Field Perturbations" *ApJ* **185**, 635-648.
- [3] S. Chandrasekhar (1976): "The Solution of Dirac's Equation in Kerr Geometry" *Proc. R. Soc. Lond. A* **349**, 571-575.
- [4] S. Chandrasekhar (1983): *The Mathematical Theory Of Black Holes*. London: Clarendon Press.
- [5] W. H. Press and S. Teukolsky (1973): Perturbations of a Rotating Black Hole. II. Dynamical Stability of the Kerr Metric, *ApJ* **185**, 649-674.
- [6] S. Teukolsky and W. H. (1974): "Press Perturbations of a Rotating Black Hole. III - Interaction of the Hole with Gravitational and Electromagnetic Radiation" *ApJ* **193**, 443-461.
- [7] S. K. Chakrabarti (1984): "On Mass-Dependent Spheroidal Harmonics of Spin One-Half" *Proc. R. Soc. Lond. A* **391**, 27-38.
- [8] A.S. Davydov (1976): (Second Ed.) *Quantum Mechanics*. Oxford, New York: Pergamon Press.
- [9] J. Mathews and R. L. Walker (1970): (Second Ed.) *Mathematical Methods Of Physics*. California: The Benjamin/Cummings Publishing Company.
- [10] M. Abramowitz and I. A. Stegun (1972): *Handbook Of Mathematical Functions*. Washington: National Bureau of Standards.

Neutron disks around black holes

Sandip K. Chakrabarti and Banibrata Mukhopadhyay

S.N. Bose National Centre for Basic Sciences, JD Block, Salt Lake, Calcutta 700091, India

Received 6 October 1998 / Accepted 13 January 1999

Abstract. We study nucleosynthesis in low accretion rate hot advective flows around black holes. We find that matter is generally photo-dissociated into protons and neutrons inside the disk. These neutrons stay around black holes for longer time because they are not coupled to magnetic fields while the protons accrete into the hole. We find the nature of the resulting neutron disks and estimate the rate at which these disks contaminate the surroundings.

Key words: stars: neutron – nucleosynthesis – black hole physics – accretion, accretion disks

1. Introduction

Angular momentum in accretion disks around black holes must deviate from a Keplerian distribution, since the presence of ion, radiation or inertial pressure gradient forces become as significant as the gravitational and centrifugal forces (see Chakrabarti 1996a; Chakrabarti 1996b and references therein). The inertial pressure close to a black hole is high, because, on the horizon, the inflow velocity must be equal to the velocity of light. For causality, the velocity of sound must be less than the velocity of light. In fact, in the extreme equation of state of $P = \frac{c^2}{3}\rho$ (where c is the velocity of light and P and ρ are the isotropic pressure and mass density respectively), the sound speed is only $c/\sqrt{3}$. Thus, the flow must pass through a sonic point and become supersonic before entering into the horizon. A flow which must pass through a sonic point must also be sub-Keplerian (Chakrabarti 1996b and references therein), and this causes the deviation. If the accretion rate is low, the flow cools down only by inefficient bremsstrahlung and Comptonization processes, unless the magnetic field is very high (Shvartsman 1971; Rees 1984; Bisnovatyi-Kogan 1998). This hot flow can undergo significant nucleosynthesis depending on the inflow parameters. Earlier, in the context of thick accretion disks calculations of changes in composition inside an accretion disk were carried out (Chakrabarti et al. 1987; Hogan & Applegate 1987; Arai & Hashimoto 1992; Hashimoto et al. 1993), but the disk models used were not completely self-consistent, in that neither the radial motion, nor the cooling and heating processes were in-

cluded fully self-consistently. Second, only high accretion rates were used. As a result, the viscosity parameter required for a significant nuclear burning was extremely low ($\alpha_{vis} < 10^{-4}$). In the present paper, we do the computation after including the radial velocity in the disk and the heating and cooling processes. We largely follow the solutions of Chakrabarti (1996b) to obtain the thermodynamic conditions along a flow.

Close to a black hole horizon, the viscous time scale is so large compared to the infall time scale that the specific angular momentum λ of matter remains almost constant and sub-Keplerian independent of viscosity (Chakrabarti 1996a,b; Chakrabarti 1989). Because of this, as matter accretes, the centrifugal force λ^2/x^3 increases much faster compared to the gravitational force GM/x^2 (where G and M are the gravitational constant and the mass of the black hole respectively, λ and x are the dimensionless angular momentum and the radial distance from the black hole). As a result, close to the black hole (at $x \sim \lambda^2/GM$) matter may even virtually stop to form standing shocks (Chakrabarti 1989). Shock or no-shock, as the flow slows down, the kinetic energy of matter is converted into thermal energy in the region where the centrifugal force dominates. Hard X-rays and γ -rays are expected from here (Chakrabarti & Titarchuk, 1995). In this centrifugal pressure supported hot 'boundary layer' (CENBOL) of the black hole (Chakrabarti et al. 1996) we find that for low accretion rates, ${}^4\text{He}$ of the infalling matter is completely photo-dissociated and no ${}^7\text{Li}$ could be produced. In this region, about ten to twelve percent of matter is found to be made up of pure neutrons. These neutrons should not accrete very fast because of very low magnetic viscosity associated with neutral particles (Rees et al. 1982) while protons are dragged towards the central black hole along with the field lines. Of course, both the neutrons and protons would have 'normal' ionic viscosity, and some slow accretion of protons (including those produced after neutron decay) would still be possible. In contrast to neutron stars, the *neutron disks* which we find are not dense. Nevertheless, they can participate in the formation of neutron rich isotopes and some amount of deuterium. They can be eventually dispersed into the galaxy through jets and outflows, which come out of CENBOL (Chakrabarti 1998; Das & Chakrabarti 1998) thereby possibly influencing the metallicity of the galaxy.

On the equatorial plane, where the viscosity is the highest, a Keplerian disk deviates to become sub-Keplerian *very close*

to the black hole (Chakrabarti & Titarchuk 1995; Wiita 1982). Away from the equatorial plane, viscosity is lower and the flow deviates from a Keplerian disk farther out. This is because the angular momentum transport is achieved by viscous stresses. Weaker the viscosity, longer is the distance through which angular momentum goes to match with a Keplerian disk. When the viscosity of the disk is decreased on the whole, the Keplerian disk recedes from the black hole forming quiescence states when the objects become very faint in X-rays (Ebisawa et al. 1996). Soft photons from the Keplerian disk are intercepted by this sub-Keplerian boundary layer (CENBOL) and photons are energized through Compton scattering process. For higher Keplerian rates, electrons and protons cool down completely and the black hole is in a *soft state* (Tanaka & Lewin 1995). Here, bulk motion Comptonization produces the power-law tail of slope $\alpha \sim 1.5$ (Chakrabarti & Titarchuk 1995; Titarchuk et al. 1997). For lower Keplerian rates, the Compton cooling is incomplete and the temperature of the boundary layer remains close to the virial value,

$$T_p \sim \frac{1}{2k} m_p c^2 \frac{x_g}{x} = 5.2 \times 10^{11} \left(\frac{10}{x/x_g} \right) \text{ } ^\circ\text{K.} \quad (1)$$

In this case, bremsstrahlung is also important and the black hole is said to be in a *hard state* with energy spectral index α ($F_\nu \sim \nu^{-\alpha}$, where ν is the frequency of the photon) close to 0.5. In Eq. (1), m_p is the mass of the proton, $x_g = 2GM/c^2$ is the Schwarzschild radius of the black hole, and c is the velocity of light. (In future, we measure the distances and velocities in units of x_g and c .) In this low Keplerian rate, electrons are cooler typically by a factor of $(m_p/m_e)^{1/2}$ unless the magnetic field is very high. Present high energy observations seem to support the apparently intriguing aspects of black hole accretion mentioned above. For instance, the constancy of (separate) spectral slopes in soft and hard states has been observed by many (Ebisawa et al. 1994; Miyamoto et al. 1991; Ramos et al. 1997; Grove et al. 1998; Vargas et al. 1997). ASCA observations of Cygnus X-1 seem to indicate that the inner edge of the Keplerian component is located at around $15R_g$ (instead of $3R_g$) (Gilfanov et al. 1997). HST FOS observations of the black hole candidate A0620-00 in quiescent state seems to have very faint Keplerian features (McClintock et al. 1995) indicating the Keplerian component to be farther out at low accretion rates. Bulk motion Comptonization close to the horizon has been considered to be a possible cause of the power-law tail in very soft states (Crary et al. 1996; Ling et al. 1997; Cui et al. 1997). However, some alternative modes may not be ruled out to explain some of these features.

This observed and predicted dichotomy of states of black hole spectra motivated us to investigate the nuclear reactions thoroughly for both the states, but we report here the results obtained in the more important case, namely, when the flow is hotter, i.e., for hard states. We use 255 nuclear elements in the thermo-nuclear network starting from protons, neutrons, deuterium etc. till ${}^{72}\text{Ge}$ and the nuclear reaction rates valid for high temperatures. We assume that accretion on the galactic black hole is taking place from a disk where matter is supplied

from a normal main sequence star. That is, we choose the abundance of the injected matter to be that of the sun. Because of very high temperature, the result is nearly independent of the initial composition, as long as reasonable choices are made. When accretion rates are higher, the advective region becomes cooler and very little nucleosynthesis takes place. The results are presented elsewhere (Mukhopadhyay 1998; Mukhopadhyay & Chakrabarti 1998).

As hot matter approaches a black hole, photons originated by the bremsstrahlung process, as well as those intercepted from the Keplerian disk, start to photo-dissociate deuterium and helium in the advective region. There are two challenging issues at this stage which we address first: (a) Thermodynamic quantities such as density and temperature inside a disk are computed using a *thin disk* approximation, i.e., the vertical height $h(x)$ at a radial distance x very small compared to x ($h(x) \ll x$), and assuming the flow to be instantaneously in vertical equilibrium. However, at a low rate, it is easy to show that the disk is optically thin in the vertical direction $\int_0^{h(x)} \rho \sigma dh < 1$ (σ is the Thomson scattering cross-section). However, soft photons from the Keplerian disk enter radially and $\int_1^{x_*} \rho \sigma dx > 1$, generally. In fact, this latter possibility changes the soft photons of a few keV from a Keplerian disk to energies up to $\sim 1\text{MeV}$ by repeated Compton scattering (Sunyaev & Titarchuk 1980; Chakrabarti & Titarchuk 1995) while keeping the photon number strictly constant. The spectrum of the resultant photons emitted to distant observers becomes a power law $F_\nu \sim \nu^{-\alpha}$ instead of a blackbody, where $\alpha \sim 0.5$ for hard state and $\alpha \sim 1.5$ for soft states of a black hole. (b) Now that the spectrum is not a blackbody, strictly speaking, the computation of photo-disintegration rate that is standard in the literature (which utilizes a Planckian spectrum) cannot be followed. Fortunately, this may not pose a major problem. As we shall show, the standard photo-disintegration rate yields a lower limit of the actual rate that takes place in the presence of power-law photon spectra. Thus, usage of the correct rate obtainable from a power-law spectrum would, if anything, strengthen our assertion about the photo-disintegration around a black hole. After photo-disintegration by these hard photons, all that are left are protons and neutrons. The exact location where the dissociation actually starts may depend on the detailed photon spectrum, i.e., optical depth of this boundary layer and the electron temperature.

The plan of the present paper is the following: in the next section, we present briefly the hydrodynamical model using which the thermodynamic quantities such as the density and temperature inside the inner accretion disk are computed. We also present the model parameters we employ. In Sect. 3, we present results of nucleosynthesis inside a disk. Finally, in Sect. 4, we present our concluding remarks.

2. Model determining the thermodynamic conditions

We chose the units of distance, time and mass to be $2GM/c^2$, $2GM/c^3$ and M where, G is the gravitational constant, M is the mass of the black hole, and c is the velocity of light. To keep the problem tractable without sacrificing the salient features,

we use a well understood model of the accretion flow close to the black hole. We solve the following equations (Chakrabarti 1996a,b) to obtain the thermodynamic quantities:

(a) The radial momentum equation:

$$\vartheta \frac{d\vartheta}{dx} + \frac{1}{\rho} \frac{dP}{dx} + \frac{\lambda_{Kep}^2 - \lambda^2}{x^3} = 0, \quad (2a)$$

(b) The continuity equation:

$$\frac{d}{dx}(\Sigma x \vartheta) = 0, \quad (2b)$$

(c) The azimuthal momentum equation:

$$\vartheta \frac{d\lambda(x)}{dx} - \frac{1}{\Sigma x} \frac{d}{dx}(x^2 W_{x\phi}) = 0, \quad (2c)$$

(d) The entropy equation:

$$\begin{aligned} \Sigma v T \frac{ds}{dx} &= \frac{h(x)\vartheta}{\Gamma_3 - 1} \left(\frac{dp}{dx} - \Gamma_1 \frac{p}{\rho} \right) \\ &= Q_{mag}^+ + Q_{nuc}^+ + Q_{vis}^+ - Q^- \\ &= Q^+ - g(x, \dot{m}) Q^+ = f(\alpha, x, \dot{m}) Q^+. \end{aligned} \quad (2d)$$

Here, Q^+ and Q^- are the heat gained and lost by the flow, and \dot{m} is the mass accretion rate in units of the Eddington rate. Here, we have included the possibility of magnetic heating Q_{mag}^- (due to stochastic fields; Shvartsman 1971; Shapiro, 1973; Bisnovatyi-Kogan, 1998) and nuclear energy release Q_{nuc}^+ as well (cf. Taam & Fryxall 1985) while the cooling is provided by bremsstrahlung, Comptonization, and endothermic reactions and neutrino emissions. A strong magnetic heating might equalize ion and electron temperatures (e.g. Bisnovatyi-Kogan 1998) but this would not affect our conclusions. On the right hand side, we wrote Q^+ collectively proportional to the cooling term for simplicity (purely on dimensional grounds). We use the standard definitions of Γ (Cox & Giuli 1968),

$$\begin{aligned} \Gamma_3 &= 1 + \frac{\Gamma_1 - \beta}{4 - 3\beta}, \\ \Gamma_1 &= \beta + \frac{(4 - 3\beta)^2(\gamma - 1)}{\beta + 12(\gamma - 1)(1 - \beta)} \end{aligned}$$

and $\beta(x)$ is the ratio of gas pressure to total pressure,

$$\beta(x) = \frac{\rho k T / \mu m_p}{\rho k T / \mu m_p + \bar{a} T^4 / 3 + B(x)^2 / 4\pi}$$

Here, \bar{a} is the Stefan constant, k is the Boltzman constant, m_p is the mass of the proton, μ is the mean molecular weight. Using the above definitions, Eq. (2d) becomes,

$$\frac{4 - 3\beta}{\Gamma_1 - \beta} \left[\frac{1}{T} \frac{dT}{dx} - \frac{1}{\beta} \frac{d\beta}{dx} - \frac{\Gamma_1 - 1}{\rho} \frac{d\rho}{dx} \right] = f(\alpha, x, \dot{m}) Q^+. \quad (2e)$$

In this paper, we shall concentrate on solutions with constant β . Actually, we study in detail only the special cases, $\beta = 0$ and $\beta = 1$, so we shall liberally use $\Gamma_1 = \gamma = \Gamma_3$. We note here that unlike *self-gravitating* stars where $\beta = 0$ causes instability, here this is not a problem. Similarly, we shall consider the case

for $f(\alpha, x, \dot{m}) = \text{constant}$, though as is clear, $f \sim 0$ in the Keplerian disk region and probably much greater than 0 near the black hole depending on the efficiency of cooling (governed by \dot{m} , for instance). We use the Paczyński-Wiita (1980) potential to describe the black hole geometry. Thus, λ_{Kep} , the Keplerian angular momentum is given by, $\lambda_{Kep}^2 = x^3 - 2(x-1)^2$, exactly same as in general relativity. $W_{x\phi}$ is the vertically integrated viscous stress, $h(x)$ is the half-thickness of the disk at radial distance x (both measured in units of $2GM/c^2$) obtained from vertical equilibrium assumption (Chakrabarti 1989) $\lambda(x)$ is the specific angular momentum, ϑ is the radial velocity, s is the entropy density of the flow. The constant α above is the Shakura-Sunyaev (1973) viscosity parameter modified to include the pressure due to radial motion ($\Pi = W - \Sigma \vartheta^2$, where W and Σ are the integrated pressure and density respectively; see Chakrabarti & Molteni (1995) in the viscous stress. With this choice, $W_{x\phi}$ keeps the specific angular momentum continuous across of the shock.

For a complete run, we supply the basic parameters, namely, the location of the sonic point through which flow must pass just outside the horizon X_{out} , the specific angular momentum at the inner edge of the flow λ_{in} , the polytropic index γ , the ratio f of advected heat flux $Q_+ - Q_-$ to heat generation rate Q^+ , the viscosity parameter α_{vis} and the accretion rate \dot{m} . The derived quantities are: x_{tr} where the Keplerian flow deviates to become sub-Keplerian, the ion temperature T_p , the flow density ρ , the radial velocity v_r and the azimuthal velocity λ/x of the entire flow from x_{tr} to the horizon. Temperature of the ions obtained from above equations is further corrected using a cooling factor F_{Comp} obtained from the results of radiative transfer of Chakrabarti & Titarchuk (1995). Electrons cool due to Comptonization, but they cause the ion cooling also since ions and electrons are coupled by Coulomb interaction. F_{Comp} , chosen here to be constant in the advective region, is the ratio of the ion temperature computed from hydrodynamic (Chakrabarti 1996b) and radiation-hydrodynamic (Chakrabarti & Titarchuk 1995) considerations.

3. Results of nucleosynthesis calculations

In the first example, we start with a relativistic flow (polytropic index $\gamma = 4/3$) with the accretion rate $\dot{M} = 0.01 \dot{M}_{Edd}$, where, \dot{M}_{Edd} is the Eddington accretion rate. We use the mass of the central black hole to be $M = 10 M_\odot$ throughout. We choose a very high viscosity and the corresponding α parameter (Shakura & Sunyaev 1973) is 0.2 in the sub-Keplerian regime. The cooling is not as efficient as in a Keplerian disk: $Q^- \sim 0.9 Q^+$, where, Q^+ and Q^- are the heat generation and heat loss rates respectively. The specific angular momentum at the inner edge is $\lambda_{in} = 1.65$ (in units of $2GM/c$). The flow deviates from a Keplerian disk at 4.15 Schwarzschild radii. It is to be noted that Q^- includes *all possible* types of cooling, such as bremsstrahlung, Comptonization as well as cooling due to neutrino emissions. We assume that the flow is magnetized so that only ions have larger viscosity. Due to poor supply of the soft photons from Keplerian disks, the Comptonization in the boundary layer is

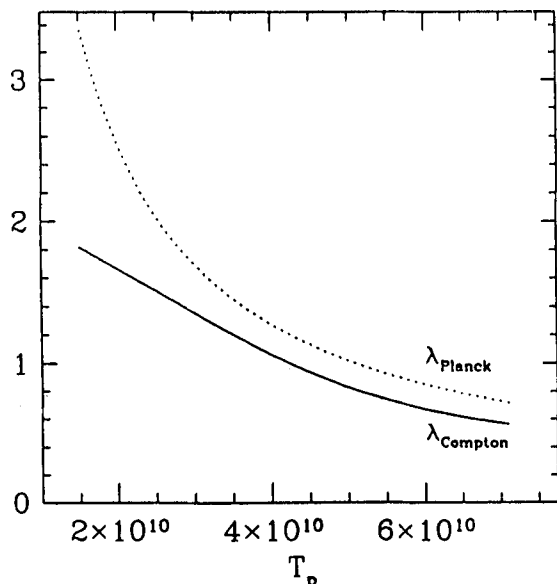


Fig. 1. Comparison of wavelength λ_{Planck} at peak blackbody intensity (dotted) with the mean (taken between 2 and 50 keV) wavelength of the Comptonized power law spectrum (solid) of the emitted X-rays. Wavelengths are measured in units of 10^{-11} cm.

not complete: we assume a standard value (Chakrabarti, & Titarchuk 1995) in this regime: $F_{Comp} \sim 0.1$, i.e., ions (in the radiation-hydrodynamic solution) are one-tenth as hot as obtained from the hydrodynamic solutions. [For high accretion rate, $\dot{m} \gtrsim 0.3$, $F_{Comp} \sim 0.001$ and ions and electrons both cool to a few KeV ($\sim 10^7$ oK)]. The typical density and temperature near the marginally stable orbit are $\rho_{x=3} \sim 8.5 \times 10^{-8} \text{ gm cm}^{-3}$ and 7.5×10^9 oK respectively where the thermonuclear depletion rates $N_A < \sigma v >$ for the $D \rightarrow p + n$, ${}^4\text{He} \rightarrow D + D$ and ${}^4\text{He} + {}^4\text{He} \rightarrow {}^7\text{Li} + p$ reactions are given by $1.6 \times 10^{14} \text{ gm}^{-1} \text{ s}^{-1}$, $4 \times 10^{-3} \text{ gm}^{-1} \text{ s}^{-1}$ and $1.9 \times 10^{-12} \text{ gm}^{-1} \text{ s}^{-1}$ respectively. Here, N_A is the element abundance on the left, σ is the reaction cross-section, v is the Maxwellian average velocity of the reactants. At these rates, the time scales of these reactions are given by, 4×10^5 s, 5×10^{11} s and 4×10^{20} s respectively indicating that the deuterium burning is the fastest of the reactions. In fact, it would take about a second to burn initial deuterium with $Y_D = 10^{-5}$. The ${}^7\text{Li}$ does not form at all because the ${}^4\text{He}$ dissociates to D much faster.

The above depletion rates have been computed assuming Planckian photon distribution corresponding to ion temperature T_p . The wavelength λ_{Planck} at which the brightness is highest at $T = T_p$ is shown in Fig. 1 in the dashed curve (in units of 10^{-11} cm). Also shown is the average wavelength of the photon $\lambda_{Compton}$ (solid curve) obtained from the spectrum $F_\nu \sim \nu^{-\alpha}$. The average has been performed over the region 2 to 50 keV of the photon energy in which the hard component is usually observed

$$\langle F_\nu \rangle = \frac{\int_{\nu_{min}}^{\nu_{max}} F_\nu d\nu}{\int_{\nu_{min}}^{\nu_{max}} d\nu} = \nu_{Compton}^{-\alpha} \quad (3)$$

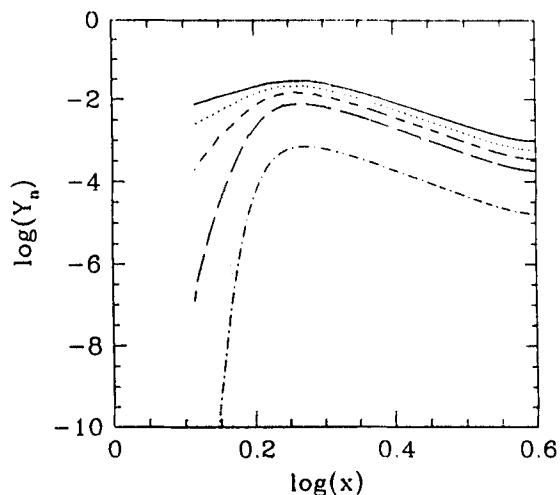


Fig. 2. Formation of a steady neutron torus in a hot inflow. Intermediate iteration results (from bottom to top: 1st, 11th, 21st, 31st and 41st iterations respectively) of the logarithmic neutron abundance Y_n in the flow as a function of the logarithmic radial distance (x in units of Schwarzschild radius) are shown.

where, ν_{min} and ν_{max} are computed from 2 and 50 keV respectively. The average becomes a function of the energy spectral index α ($F_\nu \propto \nu^{-\alpha}$), which in turn depends on the ion and electron temperatures of the medium. We follow Chakrabarti & Titarchuk (1995) to compute these relations. We note that $\lambda_{Compton}$ is lower compared to λ_{Planck} for all ion temperatures we are interested in. Thus, the disintegration rate with Planckian distribution that we employed in this paper is clearly a lower limit. Our assertion of the formation of a neutron disk should be strengthened when Comptonization is included.

Fig. 2 shows the result of the numerical simulation for the disk model mentioned above. Logarithmic abundance of neutron Y_n is plotted against the logarithmic distance from the black hole. First simulation produced the dash-dotted curve for the neutron distribution, forming a miniature neutron torus. As fresh matter is added to the existing neutron disk, neutron abundance is increased as neutrons do not fall in rapidly. Thus the simulation is repeated several times in order to achieve a converging steady pattern of the neutron disk. Although fresh neutrons are deposited, the stability of the distribution is achieved through neutron decay and neutron capture reactions. Results after every ten iterations are plotted. The equilibrium neutron torus remains around the black hole indefinitely. The neutron abundance is clearly very significant (more than five per cent!).

We study yet another case where the accretion rate is smaller ($\dot{m} = 0.001$) and the viscosity is so small ($\alpha = 0.01$) and the disk so hot that the sub-Keplerian flow deviates from a Keplerian disk farther away at $x = 85.1$. The polytropic index is that of a mono-atomic (ionized) hot gas $\gamma = 5/3$. The Compton cooling factor is as above since it is independent of the accretion rates as long as the rate is low (Sunyaev & Titarchuk 1980; Chakrabarti & Titarchuk 1995). The cooling is assumed to be very inefficient because of lower density: $Q^- \sim 0.1Q^+$.

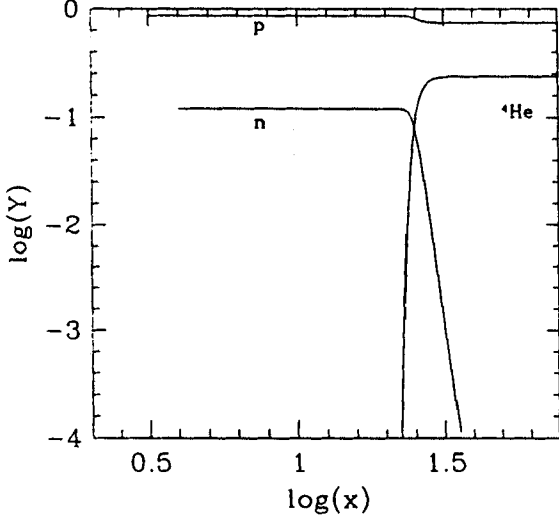


Fig. 3. Variation of matter abundance Y_i in logarithmic scale in a hot flow around a galactic black hole. Entire ${}^4\text{He}$ is photodissociated at around $x = 30x_g$ and the steady neutron disk is produced for $x < 30$ which is not accreted.

The specific angular momentum at the inner edge of the disk is $\lambda_{in} = 1.55$. In Fig. 3, we show the logarithmic abundances of proton (p), helium (${}^4\text{He}$) and neutron (n) as functions of the logarithmic distance from the black hole. Note that ${}^4\text{He}$ dissociates completely at a distance of around $x = 30$ where the density and temperatures are $\rho = 2.29 \times 10^{-11} \text{ gm cm}^{-3}$ and $T = 6.3 \times 10^9 \text{ }^\circ\text{K}$. Maximum temperature attained in this case is $T_{max} = 3.7 \times 10^{10} \text{ }^\circ\text{K}$. Both the neutrons and protons are enhanced for $x \lesssim 30$, the boundary layer of the black hole. This neutron disk also remains stable despite neutron decay, since new matter moves in to maintain equilibrium. The ${}^7\text{Li}$ abundance is insignificant.

4. Concluding remarks

In this paper, we have shown that hot flows may produce neutron disks around black holes, where neutron abundance is significant. However, unlike neutron stars, the formation of which is accompanied by the production of neutron rich isotopes, neutron disks do not produce significant neutron rich elements. Some fragile elements, such as deuterium, could be produced in the cooler outflows as follows:

Neutrons and protons may be released in space through winds which are produced in the centrifugal barrier. These winds are common in black hole sources and earlier they have been attributed to the dispersal of magnetic fields to the galactic medium (Daly & Loeb 1990; Chakrabarti et al. 1994). Recently, Chakrabarti (1998) and Das & Chakrabarti (1998), through a first ever self-consistent calculation of outflows out of accretion, found that significant winds can be produced and for low enough accretion rates, disks may even be almost evacuated causing the formation of quiescence and inactive states such as what is observed in V404 Cyg and our Galactic centre. If the

temperature of the wind falls off as $1/z$ and density as $z^{-3/2}$ (as is expected from an outflow of insignificant rotation), the deuterium synthesis rate $n + p \rightarrow D$, increases much faster very rapidly than the reverse ($D \rightarrow n + p$) process. For instance, with density and temperature mentioned as in the earlier section, at $z = 30x_g$, the forward rate ($N_A < \sigma v >$) is 0.12×10^{-5} while the reverse rate is much higher: 6.7×10^{13} . This results in the dissociation of deuterium. However, at $z = 300x_g$, the above rates are 1.8×10^{-8} and 9.6×10^{-6} respectively and at $z = 3000x_g$, the above rates are 1.3×10^{-8} and $\sim 10^{-165}$ respectively. Thus a significant deuterium could be produced farther out, say, starting from a distance of $\sim 10^3 x_g$. Ramadurai & Rees (1985) suggested deuterium formation on the surface of ion tori. As we establish here, this process may be feasible, only if these tori are vertically very thick: $z(x) \sim 10^3 x_g$. In any case, deuterium would be expected to form in winds and disperse.

In a typical case of a disk with an accretion rate of $\dot{M} \sim \dot{M}_{Edd}$, the temperature is lower, but the density is higher. In that case, the photo-dissociation of ${}^4\text{He}$ is insignificant and typically the change in abundances of some of the elements, such as ${}^{16}\text{O}$, ${}^{20}\text{Ne}$ etc. could be around $\Delta Y \sim 10^{-3}$ not as high as that of the neutron as in above cases where $\Delta Y_n \sim 0.1$. One could estimate the contamination of the galactic metallicity due to nuclear reactions as we do for realistic models. Assume that, on an average, all the N stellar black holes of equal mass M have a non-dimensional accretion rate of around $\dot{m} \sim 1$ ($\dot{m} = \dot{M}/\dot{M}_{Edd}$). Let ΔY_i be the typical change in composition of this matter during the run and let f_w be the fraction of the incoming flow that goes out as winds and outflows, then in the lifetime of a galaxy (say, 10^{10} yrs), the total 'change' in abundance of a particular species deposited to the surroundings by all the stellar black holes is given by:

$$(\Delta Y_i) \cong 10^{-9} \left(\frac{\dot{m}}{1} \right) \left(\frac{N}{10^6} \right) \left(\frac{\Delta Y_i}{10^{-3}} \right) \left(\frac{f_w}{0.1} \right) \left(\frac{M}{10 M_\odot} \right) \times \left(\frac{T_{gal}}{10^{10}} \right) \left(\frac{M_{gal}}{10^{13} M_\odot} \right)^{-1}. \quad (4)$$

We here assume a conservative estimate that there are 10^6 such stellar black holes (their number varies from 10^7 (van den Heuvel 1992, 1998) to several thousands (Romani, 1998) depending on assumptions made) and the mass of the host galaxy is around $10^{13} M_\odot$ and the lifetime of the galaxy during which such reactions are going on is about 10^{10} Yrs. We believe that $< \Delta Y_i > \sim 10^{-9}$ is quite reasonable for a typical case when $\Delta Y_i \sim 10^{-3}$ and a fraction of ten percent of matter is blown off as winds. When $\Delta Y_i \sim 0.1$ or the outflow rate is higher (particularly in presence of strong centrifugal barrier) the contamination would be even higher.

It is to be noted that our assertion of formation of neutron disks around a black hole for very low accretion rate $\dot{M} \sim 0.001-0.01 \dot{M}_{Edd}$ is different from that of the earlier results, (Hogan & Applegate 1987) where $\dot{M} \sim 10 \dot{M}_{Edd}$ was believed to be the more favourable accretion rate. This is because in last decades the emphasis was on super-Eddington thick accretion

tori. More recent computations suggest that advective regions are not as hot when the rates are very high. Another assertion of our work is that ${}^7\text{Li}$ should not be produced in accretion disks at all. This is not in line with earlier suggestions (Jin 1990) also. That is because unlike earlier case where the spallation reaction ${}^4\text{He} + {}^1\text{He}$ was dealt with in isolation, we study this in relation to other reactions prevalent in the disk. We find that ${}^4\text{He}$ could be dissociated much before it can contribute to spallation. However, our work supports Ramadurai & Rees' (1985) conjecture that deuterium may be produced in the outer regions of the disk provided the disk is at least as thick as $10^3 x_g$.

In the process of performing the simulation we were faced with a challenge which was never addressed earlier in the literature. The problem arises because the inflow under consideration is optically thin vertically, but optically thick horizontally. As a result, photons emitted form a power-law spectrum. Question naturally arises, whether these power-law photons are capable of photo-disintegration. We find that the answer is yes and that the calculation of usual photo-disintegration gives a lower limit of the changes in the composition. In the extreme conditions close to the black hole, such processes are sufficiently effective to produce neutron disks around black holes.

Acknowledgements. We thank Mr. A. Ray for carefully reading the manuscript.

References

- Arai K., Hashimoto M., 1992, *A&A* 254, 191
 Bisnovatyi-Kogan G., 1998, In: Chakrabarti S.K. (ed.) *Observational Evidence for Black Holes in the Universe*. Kluwer Academic Publishers, Dordrecht, Reidel, p. 1
 Chakrabarti S.K., 1989, *ApJ* 347, 365
 Chakrabarti S.K., 1996a, *Phys. Rep.* 266, 229
 Chakrabarti S.K., 1996b, *ApJ* 464, 664
 Chakrabarti S.K., 1998, In: Chakrabarti S.K. (ed.) *Observational Evidence for Black Holes in the Universe*. Kluwer Academic Publishers, Dordrecht, Reidel, p. 19
 Chakrabarti S.K., Molteni D., 1995, *MNRAS* 272, 80
 Chakrabarti S.K., Titarchuk L., 1995, *ApJ* 455, 623
 Chakrabarti S.K., Jin L., Arnett W.D., 1987, *ApJ* 313, 674
 Chakrabarti S.K., Rosner R., Vainshtein S.I., 1994, *Nat* 368, 434
 Chakrabarti S.K., Titarchuk L.G., Kazanas D., Ebisawa K., 1996, *A&AS* 120, 163
 Cox J.P., Giuli R.T., 1968, *Principles of Stellar Structure*. Gordon & Breach, New York
 Cray D.J., Kouveliotou C., van Paradijs J., et al., 1996, *ApJ* 462, L71
 Cui W., Zhang S.N., Focke W., Swank J.H., 1997, *ApJ* 484, 383
 Daly R.A., Loeb A., 1990, *ApJ* 364, 451
 Das T.K., Chakrabarti S.K., 1998, *ApJ* (submitted)
 Ebisawa K., Ogawa M., Aoki T., et al., 1994, *PASJ* 46, 375
 Ebisawa K., Titarchuk L., Chakrabarti S.K., 1996, *PASJ* 48, 59
 Gilfanov M., Churazov E., Sunyaev R.A., 1997, In: Meyer-Hofmeister E., Spruit H. (eds.) *Accretion Disks – New Aspects*. Springer Verlag, Heidelberg, p. 45
 Grove J.E., Johnson W.N., Kroeger R.A., et al., 1998, *ApJ* 500, 899
 Hashimoto M., Eriguchi Y., Arai K., Müller E., 1993, *A&A* 268, 131
 Hogan C.J., Applegate J.H., 1987, *Nat* 390, 236
 Jin L., 1990, *ApJ* 356, 501
 Ling J., Wheaton W.A., Wallyn P., et al., 1997, *ApJ* 484, 375
 McClintock J., Home K., Remillard R.A., 1995, *ApJ* 442, 358
 Miyamoto S., Kimura K., Kitamoto S., Dotani T., Ebisawa K., 1991, *ApJ* 383, 784
 Mukhopadhyay B., 1998, In: Chakrabarti S.K. (ed.) *Observational Evidence for Black Holes in the Universe*. Kluwer Academic Publishers, Dordrecht, Reidel, p. 105
 Mukhopadhyay B., Chakrabarti S.K., 1998, *ApJ* (submitted)
 Paczyński B., Wiita P.J., 1980, *A&A* 88, 23
 Ramadurai S., Rees M.J., 1985, *MNRAS* 215, 53p
 Ramos E., Kafatos M., Fruscione A., et al., 1997, *ApJ* 482, 167
 Rees M.J., 1984, *ARA&A* 22, 471
 Rees M.J., Begelman M.C., Blandford R.D., Phinney E.S., 1982, *Nat* 295, 17
 Romani R.W., 1998, *A&AS* 133, 583
 Shakura N.I., Sunyaev R.A., 1973, *A&A* 24, 337
 Shapiro S.L., 1973, *ApJ* 180, 531
 Shvartsman V.F., 1971, *Sov. Astron. AJ* 15, 377
 Sunyaev R.A., Titarchuk L.G., 1980, *A&A* 86, 121
 Tanaka Y., Lewin W.H.G., 1995, In: Lewin W.H.G., van Paradijs J., van den Heuvel E.P.J. (eds.) *X Ray Binaries*. Cambridge University Press, England, p. 126
 Taam R.E., Fryxall B.A., 1985, *ApJ* 294, 303
 Titarchuk, L., Mastichiadis A., Kylafis N., 1997, *ApJ* 487, 834
 van den Heuvel E.P.J., 1992, *Proc. Internatl. Space year. ESA ISY* 3, p. 29
 van den Heuvel E.P.J., 1998, In: Agrawal P.C., Vishwanath P.R. (eds.) *High Energy Astronomy and Astrophysics*. University Press, Hyderabad, p. 10
 Vargus M., Goldwurm A., Laurent P., et al., 1997, *ApJ* 476, L23
 Wiita P.J., 1982, *Comm. Astrophys.* 6, 251

Semi-analytical solution of Dirac equation in Schwarzschild geometry

Banibrata Mukhopadhyay and Sandip K Chakrabarti

Theoretical Astrophysics Group, S N Bose National Centre For Basic Sciences, J D Block, Salt Lake, Sector-III, Calcutta-700091, India

E-mail: bm@boson.bose.res.in and chakraba@boson.bose.res.in

Received 4 January 1999, in final form 18 June 1999

Abstract. Separation of the Dirac equation in the spacetime around a Kerr black hole into radial and angular coordinates was done by Chandrasekhar in 1976. In the present paper, we solve the radial equations in a Schwarzschild geometry semi-analytically using the WKB approximation method. Among other things, we present an analytical expression of the instantaneous reflection and transmission coefficients and the radial wave functions of the Dirac particles. The complete physical parameter space was divided into two parts depending on the height of the potential well and energy of the incoming waves. We show the general solution for these two regions. We also solve the equations using a quantum mechanical approach in which the potential is approximated by a series of steps and we have found that these two solutions agree. We compare solutions of different initial parameters and show how the properties of the scattered wave depend on these parameters.

PACS numbers: 0420, 0470, 0470D, 9530S

1. Introduction

The spacetime around an isolated black hole is flat and Minkowskian at a large distance where usual quantum mechanics is applicable, while the spacetime closer to the singularity is curved and no satisfactory quantum field theory has been developed as yet. However, occasionally, it is useful to look into an intermediate situation when a weak perturbation (due to, say, gravitational, electromagnetic or Dirac waves) originating from infinity scatters from a black hole. The resulting wave is partially transmitted into the black hole through the horizon and partially scatters off from it to infinity. In the linearized ('test field') approximation this problem has been attacked in the past by several authors [1–4]. These methods are mostly numerical and most of the solutions obtained so far are for particles of integral spin only. Chandrasekhar [3–4] separated the Dirac equation in Kerr geometry into radial and angular parts. These works were extended to other spacetimes, such as in Kerr–Newman geometry [5], and around dyon black holes [6]. Subsequently, Chakrabarti [7] solved the angular part of the Dirac equation in Kerr geometry and gave the eigenvalues of the equation. These and the present works mostly concern scattering off tiny black holes and thus changing the incoming solution appreciably into an outgoing solution. Scattering effects from larger black holes could be studied by phase shift analysis and this has also been done recently [8].

In the present paper, we attack a simpler problem to get a 'feel' for the complete solution when the black hole is non-rotating. In the next section, we present the basic equations. In

section 3, we classify the parameter space in terms of the physical and unphysical regions and present the method we adopt to solve the equations. In section 4, we present a complete solution. In section 5, we present solutions using a classical method in which the potential is approximated by a series of steps and then compare the solutions of these two methods. In section 6, we also compare solutions of various parameters and show how a Schwarzschild black hole distinguishes incoming particles of various masses. Finally, in section 7, we draw our conclusions.

2. Basic equations of the problem

Following Chandrasekhar [4], the radial part of the Dirac equation is easily reduced into a Schrödinger like equation. However, because the spin-spin coupling term is absent in the Schwarzschild geometry, the radial equation is much simpler to deal with. The eigenvalue of the angular equation for spin $\pm\frac{1}{2}$ is trivially obtained as $(l + \frac{1}{2})^2$ [7, 9–10] where l is the orbital quantum number. In what follows, we choose $l = \frac{1}{2}$ throughout for concreteness. This eigenvalue turns out to be the separation constant λ of the original Dirac equation [4]. Here we solve the equation for one possible value of separation constant λ (for $l = \frac{1}{2}$, λ is unity). In future we plan to explore the nature of the solutions for other orbital quantum numbers.

Presently, we need to solve only the following coupled radial equations [4]:

$$\Delta^{\frac{1}{2}} \mathcal{D}_0 R_{-\frac{1}{2}} = (1 + im_p r) \Delta^{\frac{1}{2}} R_{+\frac{1}{2}}, \quad (1)$$

$$\Delta^{\frac{1}{2}} \mathcal{D}_0^\dagger \Delta^{\frac{1}{2}} R_{+\frac{1}{2}} = (1 - im_p r) R_{-\frac{1}{2}}, \quad (2)$$

where

$$\mathcal{D}_n = \partial_r + \frac{iK}{\Delta} + 2n \frac{(r - M)}{\Delta},$$

$$\Delta = r^2 - 2Mr,$$

$$K = r^2 \sigma.$$

Here n is an integer, σ is the frequency of the incoming Dirac wave, M is the mass of the black hole, m is the azimuthal quantum number, m_p is the rest mass of the Dirac particle (p indicates particle), $R_{+\frac{1}{2}}$ ($R_{-\frac{1}{2}}$) is the radial wave function for spin up (down) particles. \mathcal{D}_0^\dagger is the complex conjugate operator. It should be noted that dimensionless units are chosen, so that $G = \hbar = c = 1$. The radial equation here is in coupled form. We can decouple it and express the equation either in terms of a spin up or spin down wavefunction. However, it is more convenient to follow Chandrasekhar's [4] approach by which the basis was changed along with the independent variable r . That way, the coupled equation was reduced into two independent one-dimensional wave equations since they are easier to solve.

We first define

$$r_* = r + 2M \log |r - 2M|, \quad (3)$$

where $r > r_+ (= 2M)$,

$$\frac{d}{dr_*} = \frac{\Delta}{r^2} \frac{d}{dr}, \quad (4)$$

and choose $\Delta^{\frac{1}{2}} R_{+\frac{1}{2}} = P_{+\frac{1}{2}}$, $R_{-\frac{1}{2}} = P_{-\frac{1}{2}}$.

In terms of r_* , the operators take the form:

$$D_0 = \frac{r^2}{\Delta} \left(\frac{d}{dr_*} + i\sigma \right)$$

and

$$D_0^\dagger = \frac{r^2}{\Delta} \left(\frac{d}{dr_*} - i\sigma \right).$$

We choose $\theta = \tan^{-1}(m_p r)$ which yields,

$$\cos \theta = \frac{1}{\sqrt{(1 + m_p^2 r^2)}}, \quad \sin \theta = \frac{m_p r}{\sqrt{(1 + m_p^2 r^2)}}$$

and

$$(1 \pm im_p r) = \exp(\pm i\theta) \sqrt{(1 + m_p^2 r^2)}.$$

Following exactly Chandrasekhar's [4] approach we write

$$P_{+\frac{1}{2}} = \psi_{+\frac{1}{2}} \exp \left[-\frac{1}{2} i \tan^{-1}(m_p r) \right] \tag{5}$$

and

$$P_{-\frac{1}{2}} = \psi_{-\frac{1}{2}} \exp \left[+\frac{1}{2} i \tan^{-1}(m_p r) \right]. \tag{6}$$

Finally, a choice of $\hat{r}_* = r_* + \frac{1}{2\sigma} \tan^{-1}(m_p r)$ yields $d\hat{r}_* = \left(1 + \frac{\Delta}{r^2} \frac{m_p}{2\sigma} \frac{1}{1+m_p^2 r^2} \right) dr_*$.

With these definitions, the differential equations (1) and (2) are re-written as

$$\left(\frac{d}{d\hat{r}_*} - W \right) Z_+ = i\sigma Z_- \tag{7a}$$

and

$$\left(\frac{d}{d\hat{r}_*} + W \right) Z_- = i\sigma Z_+, \tag{7b}$$

where $Z_\pm = \psi_{+\frac{1}{2}} \pm \psi_{-\frac{1}{2}}$ and

$$W = \frac{\Delta^{\frac{1}{2}} (1 + m_p^2 r^2)^{3/2}}{r^2 (1 + m_p^2 r^2) + m_p \Delta / 2\sigma}. \tag{8}$$

One important point to note: the transformation of spatial coordinate r to r_* (and \hat{r}_*) is taken not only for mathematical simplicity but also for a physical significance. When r is chosen as the radial coordinate, the decoupled equations for independent waves show diverging behaviour. However, by transforming those in terms of r_* (and \hat{r}_*) we obtain well behaved functions. The horizon is shifted from $r = r_*$ to $\hat{r}_* = -\infty$.

From the above set of equations, we readily obtain a pair of independent one-dimensional wave equations,

$$\left(\frac{d^2}{d\hat{r}_*^2} + \sigma^2 \right) Z_\pm = V_\pm Z_\pm, \tag{9}$$

where

$$V_\pm = W^2 \pm \frac{dW}{d\hat{r}_*} \tag{10}$$

$$\begin{aligned} &= \frac{\Delta^{\frac{1}{2}} (1 + m_p^2 r^2)^{3/2}}{[r^2 (1 + m_p^2 r^2) + m_p \Delta / 2\sigma]^2} \left[\Delta^{\frac{1}{2}} (1 + m_p^2 r^2)^{3/2} \pm \left((r - M)(1 + m_p^2 r^2) + 3m_p^2 r \Delta \right) \right] \\ &\mp \frac{\Delta^{\frac{3}{2}} (1 + m_p^2 r^2)^{5/2}}{[r^2 (1 + m_p^2 r^2) + m_p \Delta / 2\sigma]^3} [2r(1 + m_p^2 r^2) + 2m_p^2 r^3 + m_p(r - M)/\sigma]. \end{aligned} \tag{11}$$

3. Parameter space and method to solve equations

We obtain solutions by employing the Wentzel-Kramers-Brillouin (WKB) [11,12] method and then imposing strict boundary conditions on the horizon, so that the reflection coefficient is zero and the transmission coefficient is unity at the horizon. After establishing the general solution, we present here the solution of equation (9) for two sets of parameters as illustrative examples.

It is advisable to choose the parameters in such a way that there is a significant interaction between the particle and the black hole. This is possible when the Compton wavelength of the incoming wave is of the same order as the Schwarzschild radius of the black hole, i.e.,

$$\frac{2GM}{c^2} \sim \frac{\hbar}{m_p c}.$$

Here we are choosing $G = \hbar = c = 1$, so

$$m_p \sim \frac{1}{2M}.$$

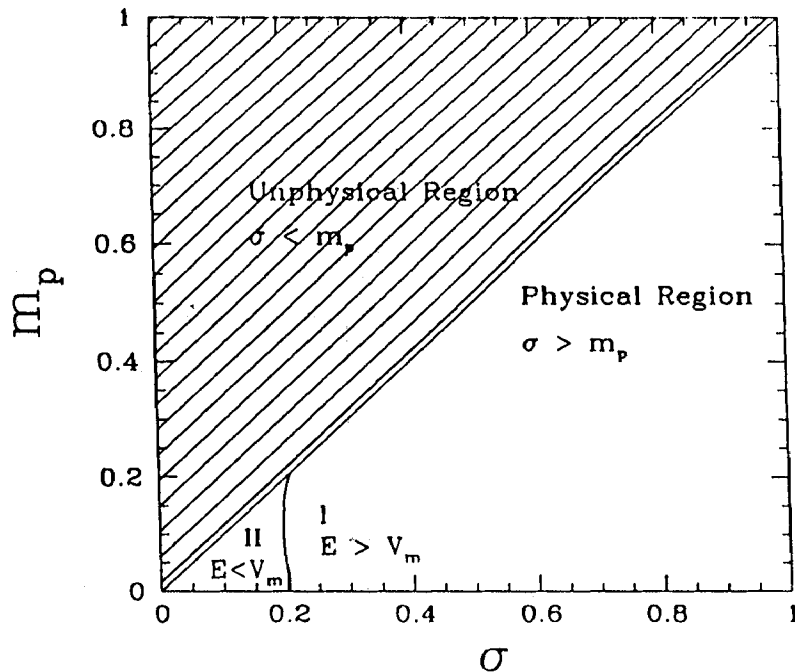
Again, in the case of Schwarzschild geometry, the frequency of the incoming particle (or wave) will be of the same order as the inverse of time. So,

$$\frac{c^3}{2GM} \sim \sigma.$$

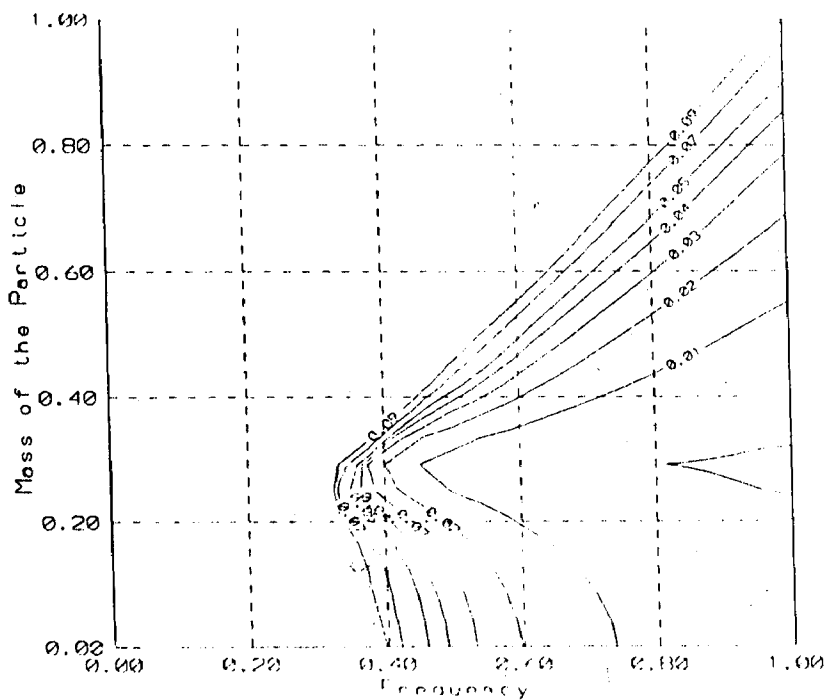
Using the units as before, one can write,

$$m_p \sim \sigma \sim (2M)^{-1}. \quad (12)$$

In principle one can choose any values of σ and m_p for a particular black hole and the corresponding solution is possible, but we shall concentrate upon the region of parameter space where the solution is expected to be interesting as pointed out above, namely the region close to $m_p = \sigma$. In figure 1(a), we draw this line. The parameter space is spanned by the frequency σ and the rest mass of the incoming particle m_p . It is clear that 50% of the total parameter space where $\sigma < m_p$ is unphysical, and one need not study this region. The rest of the parameter space ($\sigma > m_p$) is divided into two regions: I: $E > V_m$ and II: $E < V_m$, where V_m is the maximum of the potential. In region I, the wave is *locally* sinusoidal because the wave number k is real for the entire range of \hat{r}_* . In region II on the other hand, the wave is decaying when $E < V$, i.e. where the wave 'hits' the potential barrier, and in the rest of the region, the wave is propagating. We shall show solutions in these two regions separately. In region I whatever the physical parameters, the energy of the particle is always greater than the potential energy and the WKB approximation is generally valid in the whole range (i.e. $\frac{1}{k^2} \frac{dk}{d\hat{r}_*} \ll 1$). In region II, the energy of the particle is always less than the maximum height of the potential barrier. Thus, at two points (where $k = 0$) the total energy matches the potential energy and in the vicinity of these two points the WKB approximation method is not valid. These have to be dealt with separately. In figure 1(b), we show contours of constant $w_{\max} = \max(\frac{1}{k^2} \frac{dk}{d\hat{r}_*})$ for a given set (σ, m_p) of parameters. The labels show the actual values of w_{\max} . Clearly, except for parameters *very close* to the boundary of regions I and II, the WKB approximation is safely valid for any value of \hat{r}_* . One has to employ a different method (such as using Airy functions, see below) to find solutions in this region.



(a)



(b)

Figure 1. (a) Classification of the parameter space in terms of the energy and rest mass of the particles. The physical region $\sigma > m_p$ is further classified in terms of whether the particle actually 'hits' the barrier or not. (b) Contours of constant $u_{\max} = \max\left(\frac{1}{|T|} \frac{dk}{dl}\right)$ are shown to indicate that generally $w \ll 1$ and therefore the WKB approximation is valid in most of the physical region. Labels indicate the values of u .

4. The complete solution

4.1. Solutions of region I

In this region, for any set of parameters, the energy of the particle is always greater than the corresponding potential energy. We first re-write equation (9) as

$$\frac{d^2 Z_+}{d\hat{r}_*^2} + (\sigma^2 - V_+) Z_+ = 0. \quad (13)$$

This is simply the Schrödinger equation corresponding to the total energy of the wave σ^2 . This can be solved by the regular WKB method [11, 12]. Let

$$k(\hat{r}_*) = \sqrt{(\sigma^2 - V_+)}. \quad (14)$$

$$u(\hat{r}_*) = \int k(\hat{r}_*) d\hat{r}_* + \text{constant}. \quad (15)$$

Here, k is the wave number of the incoming wave and u is the *eikonal*. The solution of equation (13) is,

$$Z_+ = \frac{A_+}{\sqrt{k}} \exp(iu) + \frac{A_-}{\sqrt{k}} \exp(-iu), \quad (16)$$

with

$$A_+^2 + A_-^2 = k. \quad (17)$$

In this case all along $\sigma^2 > V_+$ and also $\frac{1}{k} \frac{dk}{d\hat{r}_*} \ll k$, so the WKB approximation is generally valid in the whole region. The quantity $\frac{1}{k^2} \frac{dk}{d\hat{r}_*}$ falls off rapidly with distance. Thus, WKB is strictly valid at long distance only.

It is clear that a standard WKB solution where A_+ and A_- are kept constant throughout should not be accurate, since the physical inner boundary condition on the horizon must be that the reflected component is negligible there. Thus the WKB approximation requires a slight modification in which the spatial dependence of A_{\pm} is allowed. On the other hand, at a large distance, where WKB is strictly valid, A_+ and A_- should tend to be constant, and hence their difference is also a constant:

$$A_+ - A_- = c. \quad (18)$$

Here, c is determined from the WKB solution at a large distance. This along with (17) gives

$$A_+(r) = -\frac{c}{2} + \frac{\sqrt{[2k(r) - c^2]}}{2}. \quad (19)$$

This spatial variation, strictly valid at large distances only, should not be extended to the horizon without correcting for the inner boundary condition. These values are to be shifted by, say, $A_{\pm h}$ respectively, so that on the horizon one obtains physical R and T . We first correct the reflection coefficient on the horizon as follows: Let A_{-h} be the value of A_- on the horizon (see equation (19)),

$$A_{-h} = +\frac{c}{2} + \frac{\sqrt{[2k(r_+) - c^2]}}{2}.$$

It is appropriate to use $\mathcal{A}_- = A_- - A_{-h}$, rather than A_- , since \mathcal{A}_- vanishes at $r = r_+$.

Incorporating these conditions, the solution (16) becomes,

$$Z_+ = \frac{A_+}{\sqrt{q}} \exp(iu) + \frac{\mathcal{A}_-}{\sqrt{q}} \exp(-iu) \quad (20)$$

with the usual normalization condition

$$\mathcal{A}_+^2 + \mathcal{A}_-^2 = q, \quad (21)$$

where $\mathcal{A}_+ = A_+ - A_{+h}$. Here, q is to be determined self-consistently by equating the asymptotic behaviour of this reflection coefficient with that obtained using the WKB method. This q in turn is used to compute $\mathcal{A}_+ = A_+ - A_{+h}$, and therefore the transmission coefficient T from equation (21). In this way, normalization of $R + T = 1$ is assured.

The normalization factor $q \rightarrow k$ as $\hat{r}_* \rightarrow \infty$ and the condition $\frac{1}{q} \frac{dq}{dr_*} \ll q$ are found to be satisfied whenever $\frac{1}{k} \frac{dk}{dr_*} \ll k$. This is the essence of our modification of the WKB. In a true WKB, A_{\pm} are constants and the normalization is with respect to an (almost) constant k . However, we are using it as if WKB is instantaneously valid everywhere. Our method may therefore be called the 'instantaneous' WKB approximation or IWKB for short. Using the new notation, the instantaneous values (i.e. local values) of the reflection and transmission coefficients are given by (see equation (20)),

$$R = \frac{\mathcal{A}_-^2}{q} \quad (22a)$$

$$T = \frac{\mathcal{A}_+^2}{q} \quad (22b)$$

Determination of A_{+h} is done by ensuring R obtained from equation (22a) is the same as that obtained by the actual WKB method at infinity.

To be concrete, we choose one set of parameters from region I. (A large number of solutions is compared in section 6 below.) Here, the total energy of the incoming particle is greater than the potential barrier height for all values of \hat{r}_* . We use mass of the black hole, $M = 1$; mass of the particle, $m_p = 0.8$, orbital quantum number, $l = \frac{1}{2}$, azimuthal quantum number, $m = -\frac{1}{2}$, frequency of the incoming wave, $\sigma = 0.8$.

From equation (9) we observe that there are two wave equations for the two potentials V_+ and V_- . The nature of the potentials is shown in figure 2. It is clear that potentials V_{\pm} are well behaved. They are monotonically decreasing as the particle approaches the black hole, and the total energy chosen in this case (σ^2) is always higher compared to V_{\pm} . For concreteness, we solve using potential V_+ . A similar procedure can be adopted using potential V_- to compute Z_- and its form would be

$$Z_- = \frac{A'_+ - A'_{+h} \exp(iu')}{\sqrt{q'}} - \frac{A'_- - A'_{-h} \exp(-iu')}{\sqrt{q'}}. \quad (20')$$

Note the occurrence of the negative sign in front of the reflected wave. This is to satisfy the asymptotic property of the wavefunctions which must conserve the Wronskian [4]. Since the coefficients should not change sign between infinity and the horizon (as that would amount to having zero amplitude, i.e. unphysical, absence of either the forward or the backward component) the same sign convention is followed throughout the space. Local values of the reflection and transmission coefficients could also be calculated in the same manner. In the solution (equations (20) and (20')), the first term represents the incident wave and the second term represents the reflected wave.

In figure 3 we show the nature of V_+ (solid curve), k (dashed curve) and $E (= \sigma^2)$ (short-dashed curve). The difference between E and V_+ and therefore k increases as the particle approaches the black hole.

In figure 4, variation of 'local' reflection and transmission coefficients is shown. It is observed that as matter comes close to the black hole, the barrier height goes down. As a result

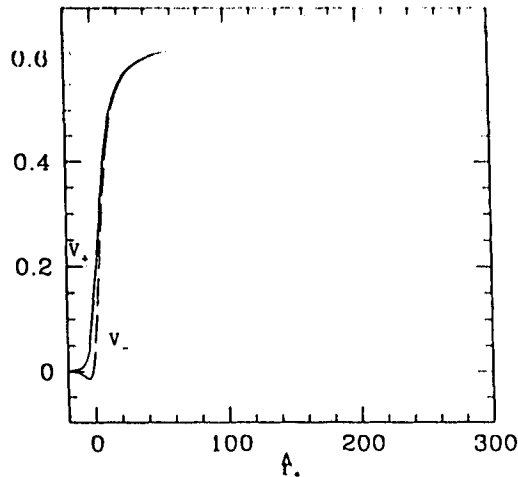


Figure 2. Behaviour of potentials V_+ (solid curve) and V_- (dashed curve), as a function of r_* . The parameters are chosen from region I of figure 1.

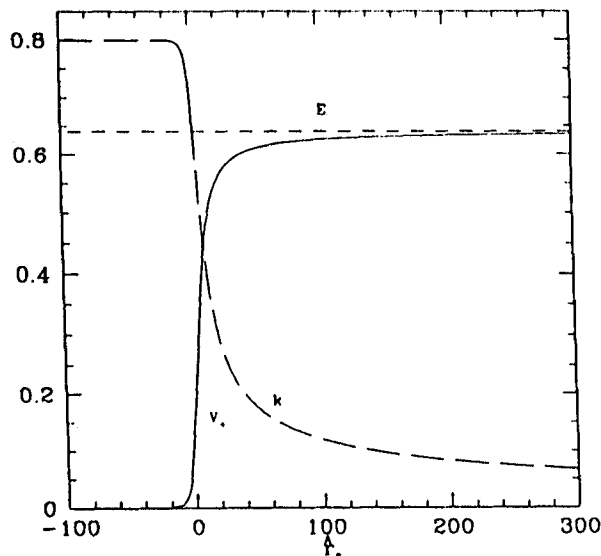


Figure 3. Behaviour of V_+ (solid curve), k (dashed curve) and total energy E (short-dashed curve) as functions of r_* .

the penetration probability increases, resulting in the rise of the transmission coefficients. At the same time the reflection coefficient tends to zero. It should be noted that, strictly speaking, the terms 'reflection' and 'transmission' coefficients are traditionally defined with respect to the asymptotic values. The spatial dependences that we show are to be interpreted as the instantaneous values. This is consistent with the spirit of the IWKB approximation that we are using.

The behaviour of the solutions with V_- is not very different from that shown in figures 3 and 4 except in a region very close to the black hole horizon where V_+ and V_- differ slightly (see figure 2).

Using the solutions of equations with potential V_+ and V_- , the radial wavefunctions $R_{+\frac{1}{2}}$ and $R_{-\frac{1}{2}}$, for spin up and spin down particles respectively, of the original Dirac equation are

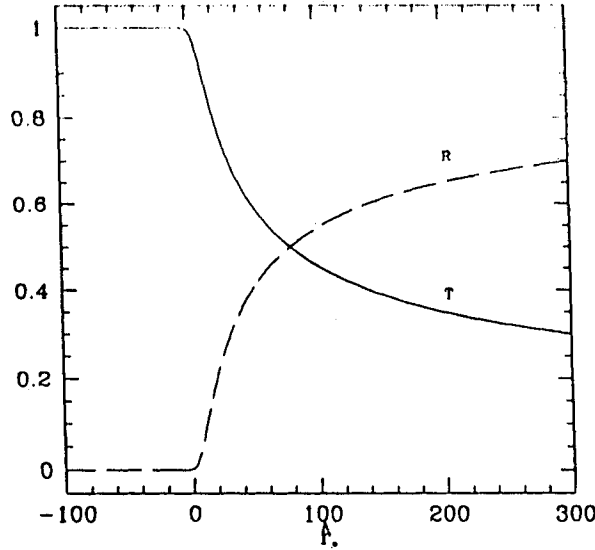


Figure 4. Behaviour of local transmission (T , solid curve) and reflection (R , dashed curve) coefficients as functions of \hat{r}_* . Close to the horizon, transmission is a hundred per cent and reflection is almost zero.

given below,

$$\text{Re} \left(R_{\frac{1}{2}} \Delta^{\frac{1}{2}} \right) = \frac{a_+ \cos(u - \theta) + a_- \cos(u + \theta)}{2\sqrt{k}} + \frac{a'_+ \cos(u' - \theta) - a'_- \cos(u' + \theta)}{2\sqrt{k'}} \tag{23a}$$

$$\text{Im} \left(R_{\frac{1}{2}} \Delta^{\frac{1}{2}} \right) = \frac{a_+ \sin(u - \theta) - a_- \sin(u + \theta)}{2\sqrt{k}} + \frac{a'_+ \sin(u' - \theta) + a'_- \sin(u' + \theta)}{2\sqrt{k'}} \tag{23b}$$

$$\text{Re} \left(R_{-\frac{1}{2}} \right) = \frac{a_+ \cos(u + \theta) + a_- \cos(u - \theta)}{2\sqrt{k}} - \frac{a'_+ \cos(u' + \theta) - a'_- \cos(u' - \theta)}{2\sqrt{k'}} \tag{23c}$$

$$\text{Im} \left(R_{-\frac{1}{2}} \right) = \frac{a_+ \sin(u + \theta) - a_- \sin(u - \theta)}{2\sqrt{k}} - \frac{a'_+ \sin(u' + \theta) + a'_- \sin(u' - \theta)}{2\sqrt{k'}}. \tag{23d}$$

Here, $a_+ = (\Lambda_+ - \Lambda_{+h})/\sqrt{(q/k)}$ and $a_- = (\Lambda_- - \Lambda_{-h})/\sqrt{(q/k)}$. Here, we have brought back k and k' so that these may resemble the original solution (equation (16)) using the WKB approximation. $\frac{a'_+}{\sqrt{k'}}$ and $\frac{a'_-}{\sqrt{k'}}$ are the transmitted and reflected amplitudes respectively for the wave of corresponding potential V_- .

Figure 5 shows the resulting wavefunctions for both the spin $+\frac{1}{2}$ and spin $-\frac{1}{2}$ particles respectively. The eikonals used in plotting these functions (see equation (23a-d)) have been calculated by approximating V_{\pm} in terms of polynomials (this was done since V_{\pm} as presented in equation (10) is not directly integrable) and using the definition $u(\hat{r}_*) = \int \sqrt{(\sigma^2 - V_{\pm})} d\hat{r}_*$. Note that the amplitude as well as the wavelength remain constant in regions where k is also constant. As discussed before, the wavefunctions are almost sinusoidal close to the horizon and at a very large distance (albeit with different frequencies). Since the net current ($|P_{+\frac{1}{2}}|^2 - |P_{-\frac{1}{2}}|^2$) is conserved, the probability of spin $+\frac{1}{2}$ is complimentary to the probability of spin $-\frac{1}{2}$ particles respectively.

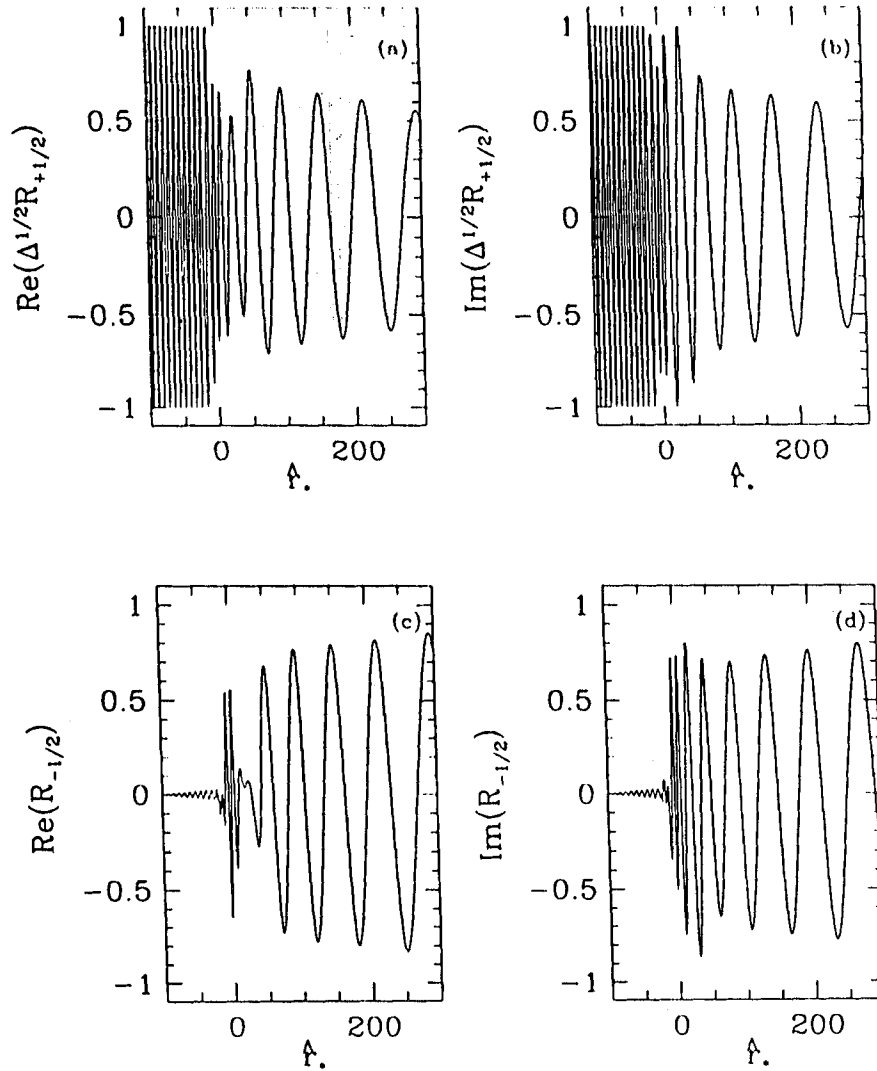


Figure 5. Behaviour of (a) $\text{Re}(R_{1/2}\Delta^{1/2})$, (b) $\text{Im}(R_{1/2}\Delta^{1/2})$, (c) $\text{Re}(R_{-1/2})$, (d) $\text{Im}(R_{-1/2})$ as functions of \hat{r}_* . Note the complimentary nature of the wavefunctions of the spin $+\frac{1}{2}$ and spin $-\frac{1}{2}$ particles. This is because the current is conserved.

4.2. Solutions of region II

Here we study the second region where for any set of physical parameters the total energy of the incoming particle is less than the maximum height of the potential barrier. Thus, the WKB approximation is not valid in the whole range of \hat{r}_* . In such regions, the solutions will be a linear combination of Airy functions because the potential is approximately linear in \hat{r}_* in those intervals. At the junctions one has to match the solutions with Airy functions along with the solution obtained by the WKB method. In the region where the WKB approximation is valid, local values of reflection and transmission coefficients and the wavefunctions can be calculated easily by following the same method described in case I. In other regions, the equation reduces to

$$\frac{d^2 Z_+}{d\hat{r}_*^2} - x Z_+ = 0, \quad (24)$$

where $x = \beta^{\frac{1}{2}}(\hat{r} - p)$, β is chosen to be positive and p is the critical point where the total energy and potential energy are equal.

Let $Z_+(x) = x^{\frac{1}{2}}Y(x)$ and considering region $x > 0$ the equation (24) reduces to

$$x^2 \frac{d^2 Y}{dx^2} + x \frac{dY}{dx} - \left(x^3 + \frac{1}{4}\right) Y(x) = 0. \tag{25}$$

By making yet another transformation,

$$\xi = \frac{2}{3}x^{\frac{3}{2}}, \tag{26}$$

we obtain,

$$\xi^2 \frac{d^2 Y}{d\xi^2} + \xi \frac{dY}{d\xi} - \left(\xi^2 + \frac{1}{9}\right) Y(\xi) = 0. \tag{27}$$

This is the modified Bessel equation. The solution of this equation is $I_{+\frac{1}{3}}(\xi)$ and $I_{-\frac{1}{3}}(\xi)$. Hence, the solution of equation (27) will be

$$Z_+(x) = x^{\frac{1}{2}}[C_1 I_{+\frac{1}{3}}(\xi) + C_2 I_{-\frac{1}{3}}(\xi)]. \tag{28}$$

When $x < 0$ the corresponding equation is

$$\xi^2 \frac{d^2 Y}{d\xi^2} + \xi \frac{dY}{d\xi} + \left(\xi^2 - \frac{1}{9}\right) Y(\xi) = 0, \tag{29}$$

which is the Bessel equation. The corresponding solution is

$$Z_+(x) = |x|^{\frac{1}{2}}[D_1 J_{+\frac{1}{3}}(\xi) + D_2 J_{-\frac{1}{3}}(\xi)], \tag{30}$$

where J_{\pm} and I_{\pm} are the Bessel functions and the modified Bessel functions of order $\frac{1}{3}$ respectively.

The Airy functions are defined as

$$Ai(x) = \frac{1}{3}x^{\frac{1}{2}}[I_{-\frac{1}{3}}(\xi) - I_{+\frac{1}{3}}(\xi)], \quad x > 0, \tag{31}$$

$$Ai(x) = \frac{1}{3}|x|^{\frac{1}{2}}[J_{-\frac{1}{3}}(\xi) + J_{+\frac{1}{3}}(\xi)], \quad x < 0, \tag{32}$$

$$Bi(x) = \frac{1}{\sqrt{3}}x^{\frac{1}{2}}[I_{-\frac{1}{3}}(\xi) + I_{+\frac{1}{3}}(\xi)], \quad x > 0, \tag{33}$$

$$Bi(x) = \frac{1}{\sqrt{3}}|x|^{\frac{1}{2}}[J_{-\frac{1}{3}}(\xi) - J_{+\frac{1}{3}}(\xi)], \quad x < 0. \tag{34}$$

In terms of Airy functions, the solutions (28) and (30) can be written as

$$Z_+ = \frac{3}{2}(C_2 - C_1)Ai(x) + \frac{\sqrt{3}}{2}(C_2 + C_1)Bi(x) \quad \text{for } x > 0, \tag{35}$$

$$Z_+ = \frac{3}{2}(D_2 + D_1)Ai(x) + \frac{\sqrt{3}}{2}(D_2 - D_1)Bi(x) \quad \text{for } x < 0. \tag{36}$$

By matching boundary conditions it is easy to show that the solution corresponding to $x > 0$ and that corresponding to $x < 0$ are continuous when $C_1 = -D_1$ and $C_2 = D_2$.

To have an explicit solution, we choose the following set of parameters: $M = 1, m_p = 0.1, l = \frac{1}{2}, m = -\frac{1}{2}$ and $\sigma = 0.15$.

In figure 6, we show the nature of V_+ and V_- . However, while solving, we use the equation containing V_+ (equation (9)). Unlike the case in the previous section, σ^2 is no longer greater than V_{\pm} at all radii. As a result, k^2 may attain negative values in some region. In figure 7, the

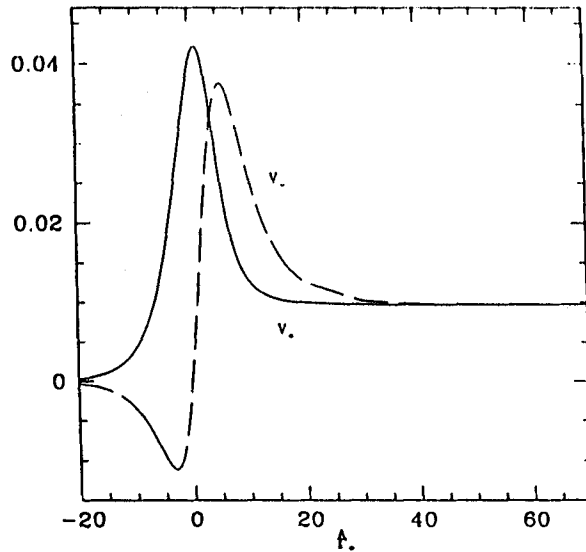


Figure 6. Behaviour of V_+ (solid curve) and V_- (dashed curve), as functions of \hat{f}_* . The parameters are chosen from region II of figure 1(a) and (b).

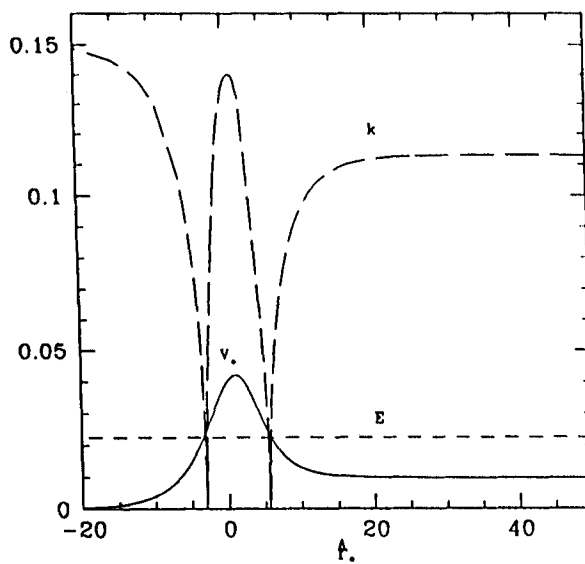


Figure 7. As figure 3. See text for the choice of parameters.

nature of V_+ (solid curve), parameter k (dashed curve) and energy E (short-dashed curve) are shown. Here, the WKB approximation can be applied in regions other than $\hat{f}_* \sim -6$ to -1 and 4 to 8 where k is close to zero and the condition $\frac{1}{k} \frac{dk}{d\hat{f}_*} \ll k$ is not satisfied. In the region $\hat{f}_* \sim 8$ to 4 around the turning point $\hat{f}_* \sim 5.6088$ the solution turns out as [13]

$$Z_+ = 1.858\,386Ai(x) + 0.600\,610\,914Bi(x). \tag{37}$$

Similarly, the solution from -1 to -6 , i.e. around the turning point $\hat{f}_* = -3.0675$, can be calculated as [13]

$$Z_+ = 1.978\,145Ai(x) + 0.716\,8807Bi(x). \tag{38}$$

It should be noted that in the region $\hat{f}_* \sim 4$ to -1 , even though the potential energy dominates over the total energy, the WKB approximation method is still valid. Here the solution will take

the form $\frac{\exp(-u)}{\sqrt{k}}$ and $\frac{\exp(+u)}{\sqrt{k}}$. Asymptotic values of the instantaneous reflection and transmission coefficients (which are traditionally known as the 'reflection' and 'transmission' coefficients respectively) are obtained from the WKB approximation. This yields the integral constant c as in case I. From equation (22a,b) local reflection and transmission coefficients are calculated, the behaviour of which is shown in figure 8. The constants A_{-h} and A_{+h} are calculated as before. Note the decaying nature of the reflection coefficient inside the potential barrier.

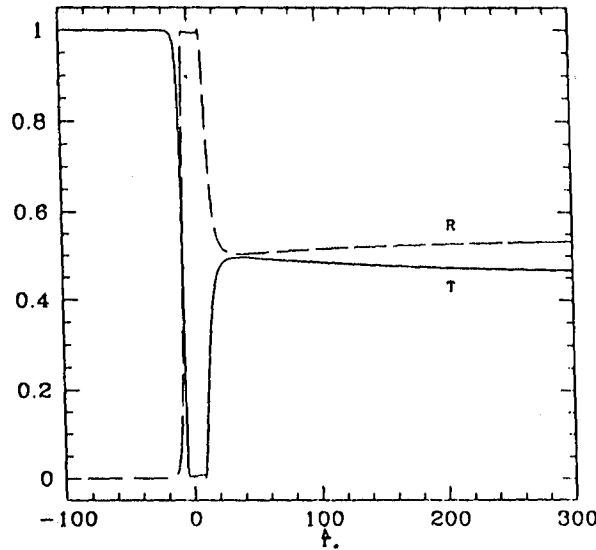


Figure 8. As figure 4. See text for the choice of parameters.

5. Solution of the equations by step-potential method

In the above sections we presented our semi-analytical solutions by the WKB method with an appropriate boundary condition at the horizon. A numerical approach would be to replace the potential $V(\hat{r}_*)$ by a collection of step functions as shown in figure 9(a). Here, the solid steps approximate the dashed potential for $m_p = 0.8$ and $\sigma = 0.8$. The standard junction conditions are of the type

$$Z_{+,n} = Z_{+,n+1} \tag{39a}$$

where

$$Z_{+,n} = A_n \exp[ik_n \hat{r}_{*,n}] + B_n \exp[-ik_n \hat{r}_{*,n}]$$

and

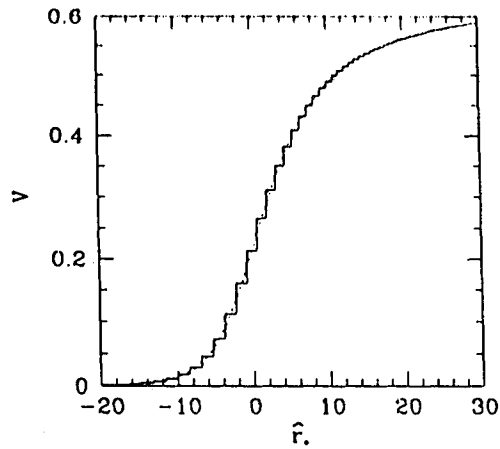
$$\frac{dZ_+}{d\hat{r}_*} \Big|_n = \frac{dZ_+}{d\hat{r}_*} \Big|_{n+1} \tag{39b}$$

where

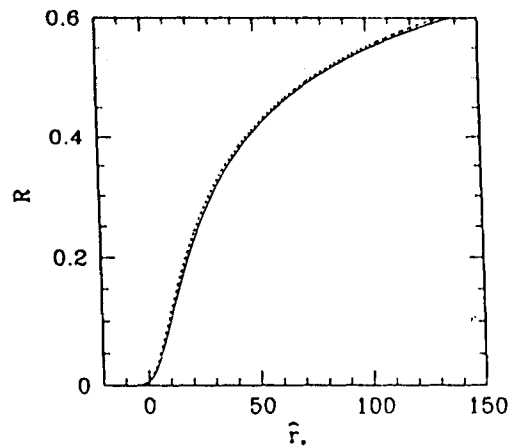
$$\frac{dZ_+}{d\hat{r}_*} \Big|_n = ik_n A_n \exp(ik_n \hat{r}_{*,n}) - ik_n B_n \exp(-ik_n \hat{r}_{*,n})$$

at each of the n steps were used to connect solutions at successive steps. As before, we use the inner boundary condition $R \rightarrow 0$ at $\hat{r}_* \rightarrow -\infty$. In reality, we used as many as 12 000 steps to accurately follow the shape of the potential. Smaller step sizes were used whenever k varied faster. Figure 9(b) shows the comparison of the instantaneous reflection coefficients in

both methods. The solid curve is from the WKB method of the previous section and the dotted curve is from the step-potential method as described here. The agreement is clearly excellent.



(a)



(b)

Figure 9. (a) Steps (solid) approximating a potential (dotted) thus reducing the problem to that of quantum mechanics. The parameters are $m_p = 0.8$ and $\sigma = 0.8$. (b) Comparison of variation of instantaneous reflection coefficient R with the radial coordinate \hat{r}_* using analytical WKB method (solid) and numerical step-potential method (dotted). The parameters are $m_p = 0.8$ and $\sigma = 0.8$.

6. Black hole: a mass spectrograph?

In order to show that the black hole scatters incoming waves of different rest masses (m_p) and of different energies (σ^2) quite differently, we show a collection of solutions in figures 10(a)–(d). In figure 10(a), we show reflection and transmission coefficients for waves with parameters $\sigma = 0.8$ (solid), 0.85 (dotted) and 0.90 (dashed) respectively with the same $m_p = 0.8$. As the energy of the particle rises comparable to the height of the potential (which is solely dependent on m_p at a large distance), the reflection coefficient goes down and the transmission coefficient goes up. In figure 10(b), the real parts of the wave Z_+ , corresponding to these three cases are shown. At $\hat{r}_* = 0$, the wave pattern is independent of σ as the phase factor is trivially the same in all cases. The dispersal of the wave with frequency is clear. Waves with smaller energy

and longer wavelength are scattered with higher amplitude of $\text{Re}(Z_+)$ as the fraction of the reflected wave goes up when the energy is reduced. This behaviour is valid until $R < 0.5$ since the amplitude of $\text{Re}(Z_+) = (1 + \sqrt{T/R})^{1/2}$. For $R > 0.5$, the amplitude of $\text{Re}(Z_+)$ goes down with energy. In figures 10(c), (d), solutions are shown varying the rest mass of the particles while keeping σ fixed at 0.8. The solid, dotted and dashed curves are for $m_p = 0.8, 0.76, 0.72$ respectively. The most interesting aspect is that close to the black hole $\hat{r}_* \lesssim 0$, the reflection and transmission coefficients as well as the nature of the wave are quite independent of the rest mass. This is understandable, as just outside the horizon the potential is insensitive to m_p . However, farther out, the amplitude of $\text{Re}(Z_+)$ goes up as before when m_p is raised, as a larger fraction of the wave is reflected from the potential (figure 10(c)).

This interesting behaviour for the first time shows that one could scatter a mixed wave off a black hole and each of the constituent waves would behave differently as in a prism or a mass spectrograph.

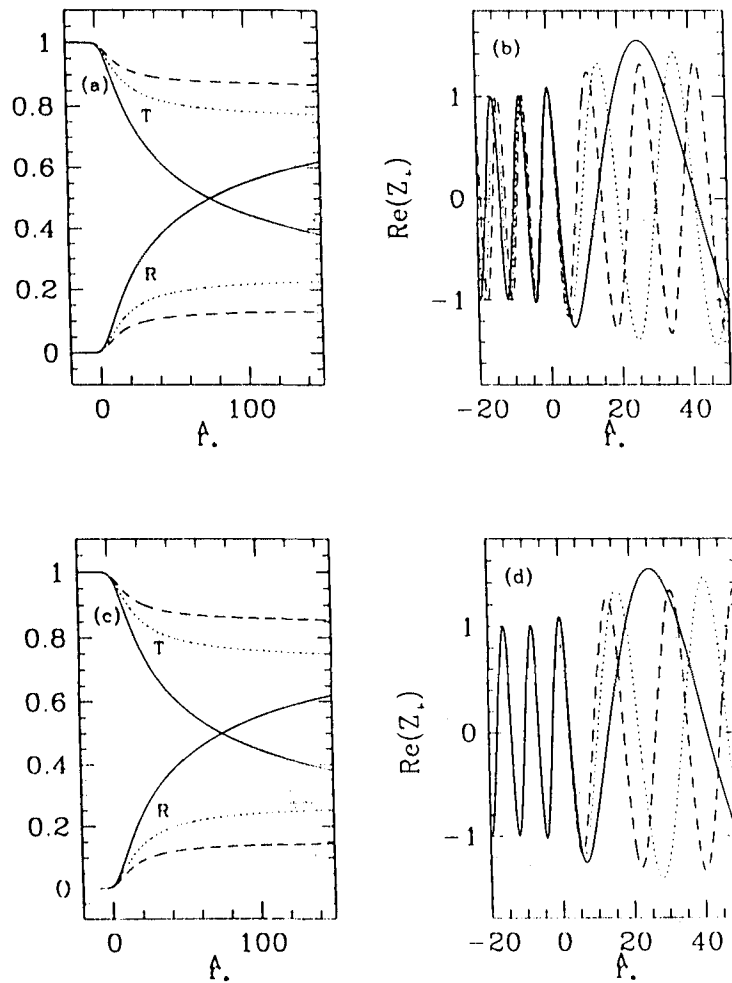


Figure 10. Comparison of (a) reflection and transmission coefficients and (b) the real amplitude of the wavefunction Z_+ for $m_p = 0.8$ and $\sigma = 0.80$ (solid), 0.85 (dotted) and 0.90 (dashed) respectively. (c), (d) Similar quantities for $m_p = 0.80$; (solid) 0.76 (dotted) and 0.72 (dashed) respectively keeping $\sigma = 0.8$ fixed. The higher reflection component enhances the wave amplitude, thus differentiating the incoming waves very clearly.

7. Concluding remarks

In this paper, we have analytically studied the scattering of spin-half particles from a Schwarzschild black hole. In particular, we have presented the nature of the radial wavefunctions and the reflection and transmission coefficients. Our main motivation was to give an analytical expression of the solution which could be useful for further study of interactions among Hawking radiations, for instance. We verified that these analytical solutions were indeed correct by explicitly solving the same set of equations numerically using the step-potential approach as described in section 5. We classified the entire parameter space in terms of the physical and unphysical regions and the physical region was further classified into two regions, depending on whether the particle ‘hits’ the potential barrier or not. We chose one illustrative example in each of the regions. We emphasize that the most ‘interesting’ region to study would be close to $m_p \sim \sigma$. However, we pointed-out (figure 1(b)) that for $m_p \leq 0.3$, WKB solutions cannot be trusted, and other methods (such as those using Airy functions) must be employed.

We used the well known WKB approximation method as well as the step-potential method of quantum mechanics to obtain the spatial dependence of the coefficients of the wavefunction. This in turn, allowed us to determine the reflection and transmission coefficients and the nature of the wavefunctions. The usual WKB method with constant coefficients and (almost) constant wave number k is successfully applied even when the coefficients and wave number are not constant everywhere. The solution from this ‘instantaneous’ WKB (IWKB for short) method agrees fully with that obtained from a purely classical numerical method where the potential is replaced by a collection of steps. The resulting waveforms satisfy the inner and the outer boundary conditions. Our method of obtaining solutions should be valid for any black hole geometries which are asymptotically flat so that radial waves could be used at a large distance. This way we ensure that the analytical solution is closer to the exact solution. In region II, in some regions, the WKB method cannot be applied and hence an Airy function approach or our step-potential approach could be used.

In the literature, reflection and transmission coefficients are defined at a single point. These definitions are meaningful only if the potential sharply changes in a small region while studies are made from a large distance. In the present case, however, the potential changes over a large distance and we are studying these regions as well. Although we used the words ‘reflection’ and ‘transmission’ coefficients in this paper very loosely, our definitions are very rigorous and well defined. These quantities are simply the instantaneous values. It is our belief these are more physical. The problem at hand is very similar to the problem of reflection and transmission of acoustic waves from a struck string of non-constant density where reflection and transmission occurs at each point.

Unlike in the case of a Kerr black hole, the solution of the angular equation around a Schwarzschild black hole is independent of the azimuthal or meridional angles [5–7]. This is expected because of symmetry of spacetime. However, otherwise the nature of the reflection and transmission coefficients was found to strongly distinguish solutions of different rest masses and different energies, as illustrated in figures 10(a)–(d). For instance, when the energy of the wave is increased for a given mass of the particle, the reflected component goes down. In regions where $R > 0.5$, $\text{Re}(Z_+)$ goes down with energy, but where $R < 0.5$, $\text{Re}(Z_+)$ goes up with energy. In any case, the waves scattered off are distinctly different. In a way therefore, black holes can act as a mass spectrograph! For instance a mixture of waves should be split into its components by the black hole. Our method is quite general and should also be used to study outgoing Hawking radiations. This is beyond the scope of this paper and will be dealt with in future.

References

- 856
857
858
859
860
861
862
863
864
865
866
867
868
869
870
871
872
873
874
875
876
877
878
879
880
881
882
883
884
885
886
887
888
889
890
891
892
893
894
895
896
897
898
899
900
- [1] Teukolsky S 1972 *Phys. Rev. D* **6** 364
- [2] Teukolsky S 1973 *Astrophys. J.* **185** 635
- [3] Chandrasekhar S 1976 *Proc. R. Soc. A* **349** 571
- [4] Chandrasekhar S 1983 *The Mathematical Theory of Black Holes* (London: Clarendon)
- [5] S. K. Chakrabarti 1984 *Proc. R. Soc. A* **391** 27
- [6] Senia 1997 *Phys. Rev. D* **46** 5414
- [7] Chakrabarti S K 1984 *Proc. R. Soc. A* **391** 27
- [8] H. W. 1998 *Trans. Quantum Chem.* **15** 1
- [9] N. S. and S. K. 1986 *Phys. Rev. D* **33** 786
- [10] Goldberg J N, Macfarlane A J, Newman E T, Rohrlich F and Sudarsan E C G 1967 *J. Math. Phys.* **8** 2155
- [11] Davydov A M 1976 *Quantum Mechanics* 2nd edn (Oxford: Pergamon)
- [12] S. K. Chakrabarti 1984 *Proc. R. Soc. A* **391** 27
- [13] Abramowitz M and Stegun I A (ed) 1973 *Handbook of Mathematical Functions* (Washington, DC: National Bureau of Standards).

Dirac equation in Kerr geometry

Banibrata Mukhopadhyay

Theoretical Astrophysics Group,

S. N. Bose National Centre For Basic Sciences

JD Block, Salt Lake, Sector-III, Calcutta-700091, India

e-mail: bm@boson.bose.res.in

Abstract. We are familiar with Dirac equation in flat space by which we can investigate the behaviour of half-integral spin particle. With the introduction of general relativistic effects the form of the Dirac equation will be modified. For the cases of different background geometry like Kerr, Schwarzschild etc. the corresponding form of the Dirac equation as well as the solution will be different. In 1972, Teukolsky wrote the Dirac equation in Kerr geometry. Chandrasekhar separated it into radial and angular parts in 1976. Later Chakrabarti solved the angular equation in 1984. In 1999 Mukhopadhyay and Chakrabarti have solved the radial Dirac equation in Kerr geometry in a spatially complete manner. In this review we will discuss these developments systematically and present some solutions.

Keywords : General relativity, gravitation, black holes, quantum aspects

PACS Nos. : 04.20.-q, 04.70.-s, 04.70.Dy, 95.30.Sf

1. Introduction

Behaviour of particles with half integral spin can be investigated through the study of Dirac equation. Generally, we are familiar with the Dirac equation and its solution when the space-time is flat. In the curved space-time where the influence of the gravity is introduced, the corresponding equation will be changed in form. Its solution will also be different. In 1972, Teukolsky [1] wrote the Dirac equation in curved space-time particularly in Kerr geometry [2] using Newman-Penrose formalism [3]. Through this modified Dirac equation we can study the behaviour of spin half particles around the spinning black holes. Due to presence of central black hole the space-time is influenced and behaviour of the particle is changed with respect to that of flat space. From the same equation of Teukolsky, Dirac equation for Schwarzschild metric [2] (Schwarzschild geometry), where the central black hole is static can be studied

[1] Teukolsky S 1972 *Phys. Rev. D* **18** 2163
 [2] Teukolsky S 1973 *Astrophys. J.* **185** 635
 [3] Chandrasekhar S 1976 *Proc. R. Soc. A* **349** 571
 [4] Chandrasekhar S 1983 *The Mathematical Theory of Black Holes* (London: Clarendon)
 [5] Page DN 1982 *Phys. Rev. D* **26** 3443
 [6] Senitzel 1992 *Phys. Rev. D* **46** 5414
 [7] Chakrabarti S K 1984 *Proc. R. Soc. A* **391** 27
 [8] Dirac P A M 1928 *Class. Quantum Grav.* **15** 105
 [9] Newman and Penrose 1966 *Math. Phys.* **7** 463
 [10] Goldberg J N, Macfarlane A J, Newman E T, Rohrlich F and Sudarsan E C G 1967 *J. Math. Phys.* **8** 2155
 [11] Davydov A M 1976 *Quantum Mechanics* 2nd edn (Oxford: Pergamon)
 [12] Sparrow and Calkins 1992 *Journal of Mathematical Physics* **33** 1000
 [13] Abramowitz M and Stegun I A (ed) 1993 *Handbook Of Mathematical Functions* (Washington, DC: National Bureau of Standards)

just by putting the angular momentum parameter a of the black hole to zero. So one can study how the behaviour of spin half particle in curved space time is influenced by the angular momentum of black hole. In 1976, Chandrasekhar and Chakrabarti [5] separated the Dirac equation in Kerr geometry into radial and angular parts and solved the radial part of the equation asymptotically. Chakrabarti [6] and Goldberg [7] solved the angular part analytically. Here we shall introduce the partially complete analytical solution of radial Dirac equation (6.7) So the complete solution of Dirac equation can be studied far away from the black hole the the modified Dirac equation for curved space-time (for Kerr and Schwarzschild geometry [2-3]) and its solution reduce into that of the flat space.

In this review we will first indicate how Dirac equation in curved space-time can be written using Newman-Penrose formalism [3]. Newman-Penrose formalism is one of the tetrad formalism where null basis are chosen instead of orthonormal basis. To fulfill the understanding of Dirac equation in this formalism we also need to know the ‘Spinor Analysis’ [3]. In the next Section, we will briefly describe this in the context of our present purpose. In §3 we will write the Dirac equation in Newman-Penrose formalism for flat and curved space-time. For curved space we will separate the Dirac equation under the background of Kerr geometry. In §4 and §5 we will briefly outline the angular and radial solution of Dirac equation respectively. In §6 we make concluding remarks.

2. Spinor analysis

In Minkowski space we consider a point x^i ($i = 0, 1, 2, 3$) on a null ray whose norm is defined as

$$(x^0)^2 - (x^1)^2 - (x^2)^2 - (x^3)^2 = 0. \tag{1}$$

Now, we consider two complex numbers ξ^0 and ξ^1 , and their complex conjugate numbers $\bar{\xi}^0$ and $\bar{\xi}^1$ in terms of which each point can be written as,

$$x^0 = \frac{1}{\sqrt{2}}(\xi^0 \bar{\xi}^0 + \xi^1 \bar{\xi}^1) \tag{2a}$$

$$x^1 = \frac{1}{\sqrt{2}}(\xi^0 \bar{\xi}^1 + \xi^1 \bar{\xi}^0) \tag{2b}$$

$$x^2 = \frac{1}{\sqrt{2}}(\xi^0 \bar{\xi}^1 - \xi^1 \bar{\xi}^0) \tag{2c}$$

$$x^3 = -\frac{i}{\sqrt{2}}(\xi^0 \bar{\xi}^0 - \xi^1 \bar{\xi}^1) \tag{2d}$$

Conversely, we can write,

$$\xi^0 \bar{\xi}^{0'} = \frac{1}{\sqrt{2}}(x^0 + x^3) \quad (3a)$$

$$\xi^0 \bar{\xi}^{1'} = \frac{1}{\sqrt{2}}(x^1 + ix^2) \quad (3b)$$

$$\xi^1 \bar{\xi}^{0'} = \frac{1}{\sqrt{2}}(x^1 - ix^2) \quad (3c)$$

$$\xi^1 \bar{\xi}^{1'} = \frac{1}{\sqrt{2}}(x^0 - x^3) \quad (3d)$$

Let,

$$\xi_{\star}^A = \alpha^A_B \xi^{B'} \quad (4a)$$

$$\bar{\xi}_{\star}^{A'} = \bar{\alpha}^{A'}_B \bar{\xi}^{B'} \quad (4b)$$

where, $(A, B, A', B' = 0, 1)$, are the linear transformations in complex two-dimensional spaces. The transformation of x^i is defined as,

$$x_{\star}^i = \beta_j^i x^j. \quad (5)$$

Now, using equation (2) and (3) we can write,

$$\begin{aligned} x_{\star}^0 &= \frac{1}{\sqrt{2}}(\alpha_0^0 \xi^0 + \alpha_1^0 \xi^1)(\bar{\alpha}_{0'}^0 \bar{\xi}^{0'} + \bar{\alpha}_{1'}^0 \bar{\xi}^{1'}) + \frac{1}{\sqrt{2}}(\alpha_0^1 \xi^0 + \alpha_1^1 \xi^1)(\bar{\alpha}_{0'}^1 \bar{\xi}^{0'} + \bar{\alpha}_{1'}^1 \bar{\xi}^{1'}) \\ &= \frac{1}{2}(\alpha_0^0 \bar{\alpha}_{0'}^0 + \alpha_0^1 \bar{\alpha}_{0'}^1)(x^0 + x^3) + \frac{1}{2}(\alpha_1^0 \bar{\alpha}_{1'}^0 + \alpha_1^1 \bar{\alpha}_{1'}^1)(x^0 - x^3) \\ &\quad + \frac{1}{2}(\alpha_0^0 \bar{\alpha}_{1'}^0 + \alpha_0^1 \bar{\alpha}_{1'}^1)(x^1 + ix^2) + \frac{1}{2}(\alpha_1^0 \bar{\alpha}_{0'}^0 + \alpha_1^1 \bar{\alpha}_{0'}^1)(x^1 - ix^2). \end{aligned} \quad (6)$$

Similarly, we can write down the relations between x_{\star}^1 , x_{\star}^2 and x_{\star}^3 with α 's and $\bar{\alpha}$'s. Therefore, keeping in mind (5) we can write,

$$\beta_0^0 + \beta_3^0 = \alpha_0^0 \bar{\alpha}_{0'}^0 + \alpha_0^1 \bar{\alpha}_{0'}^1,$$

$$\beta_0^0 - \beta_3^0 = \alpha_1^0 \bar{\alpha}_{1'}^0 + \alpha_1^1 \bar{\alpha}_{1'}^1,$$

$$\beta_1^0 - i\beta_2^0 = \alpha_0^0 \bar{\alpha}_{1'}^0 + \alpha_0^1 \bar{\alpha}_{1'}^1,$$

$$\beta_1^0 + i\beta_2^0 = \alpha_1^0 \bar{\alpha}_{0'}^0 + \alpha_1^1 \bar{\alpha}_{0'}^1.$$

Now, imposing the condition that the transformation (5) is Lorentzian we can write,

$$(\beta_0^0)^2 - (\beta_1^0)^2 - (\beta_2^0)^2 - (\beta_3^0)^2 = 1$$

So,

$$\left\| \begin{array}{cc} \alpha_0^0 \bar{\alpha}_{0'}^{0'} + \alpha_0^1 \bar{\alpha}_{0'}^{1'} & \alpha_0^0 \bar{\alpha}_{1'}^{0'} + \alpha_0^1 \bar{\alpha}_{1'}^{1'} \\ \alpha_1^0 \bar{\alpha}_{0'}^{0'} + \alpha_1^1 \bar{\alpha}_{0'}^{1'} & \alpha_1^0 \bar{\alpha}_{1'}^{0'} + \alpha_1^1 \bar{\alpha}_{1'}^{1'} \end{array} \right\| = 1. \quad (7)$$

This gives,

$$\left\| \begin{array}{cc} \alpha_0^0 & \alpha_1^0 \\ \alpha_0^1 & \alpha_1^1 \end{array} \right\| \left\| \begin{array}{cc} \bar{\alpha}_{0'}^{0'} & \bar{\alpha}_{1'}^{0'} \\ \bar{\alpha}_{0'}^{1'} & \bar{\alpha}_{1'}^{1'} \end{array} \right\| = \Delta \bar{\Delta} = 1 \quad (8)$$

Now we consider $\Delta = \bar{\Delta} = 1$, so individually each transformation of ξ is Lorentzian. So we can conclude if transformation (5) is Lorentzian, the necessary condition is transformation (4) is also Lorentzian.

Now we define spinors $\xi^A, \eta^{A'}$ of rank one as $\xi^A = \alpha_B^A \xi^B$ and $\eta^{A'} = \bar{\alpha}_{B'}^{A'} \eta^{B'}$. ($A, A', B, B' = 0$), where $\left\| \alpha_B^A \right\| = \left\| \bar{\alpha}_{B'}^{A'} \right\| = 1$. Since ξ^A and $\eta^{A'}$ are two spinors of same class,

$$\left\| \begin{array}{cc} \xi^0 & \xi^1 \\ \eta^0 & \eta^1 \end{array} \right\| = \xi^0 \eta^1 - \xi^1 \eta^0 \quad (9)$$

which is invariant under unimodular transformation, i.e.,

$$\epsilon_{AB} \xi^A \eta^B \rightarrow \text{invariant} \quad (10)$$

where, ϵ_{AB} is Levi-Civita symbol. Here as in the case of tensor analysis ϵ_{AB} and $\epsilon_{A'B'}$ are used to lower the spinor indices as, $\xi_A = \xi^C \epsilon_{CA}$.

Now, using above information the representation of position vector x^i can be written as

$$x^i \leftrightarrow \left| \begin{array}{cc} \xi^0 \bar{\xi}^{0'} & \xi^0 \bar{\xi}^{1'} \\ \xi^1 \bar{\xi}^{0'} & \xi^1 \bar{\xi}^{1'} \end{array} \right| = \frac{1}{\sqrt{2}} \left| \begin{array}{cc} x^0 + x^3 & x^1 + ix^2 \\ x^1 - ix^2 & x^0 - x^3 \end{array} \right| \quad (11)$$

Generally any vector X^i can be written in terms of spinor of rank two as,

$$X^i \leftrightarrow \left| \begin{array}{cc} \xi^{00'} & \xi^{01'} \\ \xi^{10'} & \xi^{11'} \end{array} \right| = \frac{1}{\sqrt{2}} \left| \begin{array}{cc} X^0 + X^3 & X^1 + iX^2 \\ X^1 - iX^2 & X^0 - X^3 \end{array} \right| = X^{AB'} \quad (12)$$

So a 4-vector is associated with a hermitian matrix such that,

$$\begin{aligned} (X^0)^2 - (X^1)^2 - (X^2)^2 - (X^3)^2 &= (X^0 + X^3)(X^0 - X^3) - (X^1 + iX^2)(X^1 - iX^2) \\ &= 2(\xi^{00'} \xi^{11'} - \xi^{01'} \xi_{10'}) = (\xi^{00'} \xi_{00'} + \xi_{11'} \xi^{11'} + \xi_{10'} \xi^{10'} + \xi^{01'} \xi_{01'}) = X_{AB'} X^{AB'}. \end{aligned}$$

From the definition of norms, we can write it in two different representations:

$$g_{ij} X^i X^j = \epsilon_{AC} \epsilon_{B'D'} X^{AB'} X^{CD'} \quad (13)$$

Therefore, we can transform $X^i \leftrightarrow X^{AB'}$ using,

$$X^i = \sigma_{AB'}^i X^{AB'} \quad (14a)$$

$$X^{AB'} = \sigma_i^{AB'} X^i \tag{14b}$$

where, $\sigma_i^{AB'}$ and $\sigma_{AB'}^i$ are nothing but Pauli matrices and their conjugate matrices with a factor $\frac{1}{\sqrt{2}}$.

A curved space-time is locally Minkowskian. At each point of space-time an orthonormal Dyad basis can be set up as $\zeta_{(a)}^A$ and $\zeta_{(a')}^{A'}$ ($a, a' = 0, 1$ and $A, A' = 0, 1$) for spinors.

We define, $\zeta_{(0)}^A = o^A$ and $\zeta_{(1)}^A = l^A$. The condition of orthonormality is $\epsilon_{AB} o^A l^B = o^0 l^1 - o^1 l^0 = o_B l^B = -o^A l_A = 1$.

Also it is clear that, $\epsilon^{(a)(b)} \zeta_{(a)}^A \zeta_{(b)}^B = \epsilon^{AB}$.

Then the null vectors are defined as

$$l^i \leftrightarrow o^A \bar{o}^{B'}, m^i \leftrightarrow o^A \bar{l}^{B'}, \bar{m}^i \leftrightarrow l^A \bar{o}^{B'}, n^i \leftrightarrow l^A \bar{l}^{B'}$$

Where, vectors obey relations of null tetrads such as,

$$l^i n_i = 1, m^i \bar{m}_i = -1 \text{ and all other products give zero.}$$

In this way using dyad basis we can set up four null vectors which are basis of Newman-Penrose formalism. Using (14) we can write the basis explicitly as

$$l^i = \sigma_{AB'}^i \zeta_{(0)}^A \bar{\zeta}_{(0')}^{B'} = \sigma_{AB'}^i o^A \bar{o}^{B'}, \tag{15a}$$

$$m^i = \sigma_{AB'}^i \zeta_{(0)}^A \bar{\zeta}_{(1')}^{B'} = \sigma_{AB'}^i o^A \bar{l}^{B'}, \tag{15b}$$

$$\bar{m}^i = \sigma_{AB'}^i \zeta_{(1)}^A \bar{\zeta}_{(0')}^{B'} = \sigma_{AB'}^i l^A \bar{o}^{B'}, \tag{15c}$$

$$n^i = \sigma_{AB'}^i \zeta_{(1)}^A \bar{\zeta}_{(1')}^{B'} = \sigma_{AB'}^i l^A \bar{l}^{B'}. \tag{15d}$$

Thus, in Newman-Penrose formalism the Pauli matrices change their forms as,

$$\sigma_{AB'}^i = \frac{1}{\sqrt{2}} \begin{vmatrix} l^i & m^i \\ \bar{m}^i & n^i \end{vmatrix} \tag{16a}$$

$$\sigma_i^{AB'} = \frac{1}{\sqrt{2}} \begin{vmatrix} n_i & -\bar{m}_i \\ -\bar{m}_i & l_i \end{vmatrix}. \tag{16b}$$

Therefore in this basis, the directional derivatives can be written as,

$$D = l^i \partial_i, \underline{\Delta} = n^i \partial_i, \delta = m^i \partial_i \text{ and } \delta^* = \bar{m}^i \partial_i.$$

Thus, the spinor equivalents of Newman-Penrose formalism are

$$\partial_{00'} = D, \partial_{11'} = \underline{\Delta}, \partial_{01'} = \delta, \partial_{10'} = \delta^*.$$

Due to the reason, as explained earlier $\nabla_i \leftrightarrow \nabla_{AB'}$, so we can write,

$$\nabla_i X_j = X_{j;i} \leftrightarrow \nabla_{AB'} X_{CD'} = X_{CD';AB'},$$

therefore,

$$X_{CD';AB'} = \sigma_{CD'}^j \sigma_{AB'}^i X_{j;i}. \tag{17}$$

For covariant derivatives spin coefficients Γ are introduced. In the Newman-Penrose formalism these different coefficients are assigned in terms of special symbols which are given below:

$$\Gamma_{(a)(b)(c)(d')}$$

(a)(b)	00	01 or 10	11
(c)(d')			
00'	κ	ε	π
10'	ρ	α	λ
01'	σ	β	μ
11'	τ	γ	ν

3. Dirac equation and its separation

Before going into discussion, we should mention about the unit of the system. Here we have chosen throughout $h = c = G = 1$, where $h =$ Planck constant, $c =$ speed of light and $G =$ gravitational constant. It is very clear that simultaneously all these quantities are chosen as unity implying the corresponding system is dimensionless.

The Dirac equation in flat space using Newman-Penrose formalism can be written as,

$$\sigma_{AB'}^i \partial_i P^A + i\mu_* \bar{Q}_{B'} = 0 \tag{18a}$$

$$\sigma_{AB'}^i \partial_i Q^A + i\mu_* \bar{P}_{B'} = 0. \tag{18b}$$

Here, P^A and $\bar{Q}^{A'}$ are the pair of spinors. $\mu_*/\sqrt{2}$ is the mass of the particles and $\sigma_{AB'}^i$ is nothing but Pauli matrix, because $1/\sqrt{2}$ factors are canceled in the equation.

In curved space time Dirac equation reduces to

$$\sigma_{AB'}^i P_{;i}^A + i\mu_* \bar{Q}^{C'} \epsilon_{C'B'} = 0, \tag{19a}$$

$$\sigma_{AB'}^i Q_{;i}^A + i\mu_* \bar{P}^{C'} \epsilon_{C'B'} = 0, \tag{19b}$$

where, $\sigma_{AB'}^i$ is same as defined in equation (16a).

Now, consider $B' = 0$, then (19a) reduces to

$$\sigma_{00'}^i P_{;i}^0 + \sigma_{10'}^i P_{;i}^1 - i\mu_* \bar{Q}^{1'} = 0$$

or,

$$(\partial_{00'} P^0 + \Gamma_{b00'}^0 P^b) + (\partial_{10'} P^1 + \Gamma_{b10'}^0 P^b) - i\mu_* \bar{Q}^{1'} = 0,$$

Therefore,

$$(D + \Gamma_{1000'} - \Gamma_{0010'}) P^0 + (\delta^* + \Gamma_{1100'} - \Gamma_{0110'}) P^1 - i\mu_* \bar{Q}^{1'} = 0 \tag{20}$$

Similarly, choosing $B' = 1$, we can get another similar type equation and then we can get corresponding conjugate equation of both by interchanging P and Q . Now choosing,

$$F_1 = P^0, F_2 = P^1, G_1 = \bar{Q}^{1'}, G_2 = -\bar{Q}^{0'}$$

and replacing various spin coefficients by their named symbols we get the the Dirac equation in Newman-Penrose formalism in its reduced form as.

$$(D + \varepsilon - \rho)F_1 + (\delta^* + \pi - \alpha)F_2 = i\mu_*G_1, \tag{21a}$$

$$(\underline{\Delta} + \mu - \gamma)F_2 + (\delta + \beta - \tau)F_1 = i\mu_*G_2, \tag{21b}$$

$$(D + \varepsilon^* - \rho^*)G_2 - (\delta + \pi^* - \alpha^*)G_1 = i\mu_*F_2, \tag{21c}$$

$$(\underline{\Delta} + \mu^* - \gamma^*)G_1 - (\delta^* + \beta^* - \tau^*)G_2 = i\mu_*F_1. \tag{21d}$$

3.1. Basis vectors of Newman-Penrose formalism in terms of Kerr geometry

The contravariant form of Kerr metric is given as [3],

$$g^{ij} = \begin{pmatrix} \Sigma^2/\rho^2\Delta & 0 & 0 & 2aMr/\rho^2\Delta \\ 0 & -\Delta/\rho^2 & 0 & 0 \\ 0 & 0 & -1/\rho^2 & 0 \\ 2aMr/\rho^2\Delta & 0 & 0 & -(\Delta - a^2\sin^2\theta)/\rho^2\Delta\sin^2\theta \end{pmatrix} \tag{22}$$

where, E is the energy, a is specific angular momentum of the black hole. $M =$ mass of the black hole, $\rho^2 = r^2 + a^2\cos^2\theta$ (should not confuse with the spin coefficient $\Gamma_{(0)(0)(1)(0')} = \rho$), $\Sigma^2 = (r^2 + a^2)^2 - a^2\Delta\sin^2\theta$, $\Delta = r^2 + a^2 - 2Mr$.

In Kerr geometry, the tangent vectors of null geodesics are: $\frac{dt}{d\tau} = \frac{(r^2+a^2)}{\Delta}E$, $\frac{dr}{d\tau} = \pm E$, $\frac{d\theta}{d\tau} = 0$, $\frac{d\phi}{d\tau} = \frac{a}{\Delta}E$, where τ is the proper time (not to be confused with spin coefficient $\Gamma_{(0)(0)(1)(1')} = \tau$).

Now, the basis of Newman-Penrose formalism can be defined in Kerr geometry as (in tetrad form),

$$l_i = \frac{1}{\Delta}(\Delta, -\rho^2, 0, -a\Delta\sin^2\theta), \tag{23a}$$

$$n_i = \frac{1}{2\rho^2}(\Delta, \rho^2, 0, -a\Delta\sin^2\theta), \tag{23b}$$

$$m_i = \frac{1}{\bar{\rho}\sqrt{2}}(iasin\theta, 0, -\rho^2, -i(r^2 + a^2)\sin\theta), \tag{23c}$$

$$l^i = \frac{1}{\Delta}(r^2 + a^2, \Delta, 0, a), \tag{23d}$$

$$n^i = \frac{1}{\bar{\rho}\sqrt{2}}(r^2 + a^2, -\Delta, 0, a), \tag{23e}$$

$$m_i = \frac{1}{\bar{\rho}\sqrt{2}}(i\sin\theta, 0, 1, i\operatorname{cosec}\theta), \quad (23f)$$

\bar{m}_i and \bar{m}^i are nothing but complex conjugates of m_i and m^i respectively.

3.2. Separation of Dirac equation into radial and angular parts

It is clear that the basis vectors basically become derivative operators when these are applied as tangent vectors to the function $e^{i(\sigma t + m\phi)}$. Here, σ is the frequency of the particle (not to be confused with spin coefficient $\Gamma_{(0)(0)(0)(1')} = \sigma$) and m is the azimuthal quantum number [3].

Therefore, we can write,

$$\bar{l} = D = \mathcal{D}_0, \quad \bar{n} = \underline{\Delta} = -\frac{\Delta}{2\rho^2}\mathcal{D}_0^\dagger, \quad \bar{m} = \delta = \frac{1}{\bar{\rho}\sqrt{2}}\mathcal{L}_0^\dagger, \quad \bar{m}^* = \delta^* = \frac{1}{\bar{\rho}^*\sqrt{2}}\mathcal{L}_0.$$

where,

$$\mathcal{D}_n = \partial_r + \frac{iK}{\Delta} + 2n\frac{r-M}{\Delta}, \quad (24a)$$

$$\mathcal{D}_n^\dagger = \partial_r - \frac{iK}{\Delta} + 2n\frac{r-M}{\Delta}, \quad (24b)$$

$$\mathcal{L}_n = \partial_\theta + Q + n\cot\theta \quad (25a)$$

$$\mathcal{L}_n^\dagger = \partial_\theta - Q + n\cot\theta. \quad (25b)$$

$$K = (r^2 + a^2)\sigma + am, \quad Q = a\sigma\sin\theta + m\operatorname{cosec}\theta.$$

The spin coefficients can be written as combination of basis vectors in Newman-Penrose formalism which are now expressed in terms of elements of different components of Kerr metric. So we are combining those different components of basis vectors in a suitable manner and get the spin coefficients as,

$$\kappa = \sigma = \lambda = \nu = \varepsilon = 0. \quad (26a)$$

$$\bar{\rho} = -\frac{1}{\bar{\rho}^*}, \quad \beta = \frac{\cot\theta}{\bar{\rho}^*2\sqrt{2}}, \quad \pi = \frac{i\sin\theta}{(\bar{\rho}^*)^2\sqrt{2}}.$$

$$\tau = -\frac{i\sin\theta}{\rho^2\sqrt{2}}, \quad \mu = -\frac{\Delta}{2\rho^2\bar{\rho}^*}, \quad \gamma = \mu + \frac{r-M}{2\rho^2}, \quad \alpha = \pi - \beta^*. \quad (26b)$$

Using the above definitions and results and choosing $f_1 = \bar{\rho}^*F_1$, $g_2 = \bar{\rho}G_2$, $f_2 = F_2$, $g_1 = G_1$ the Dirac equation is reduced to

$$\mathcal{D}_0f_1 + 2^{-1/2}\mathcal{L}_{1/2}f_2 = (i\mu_*r + a\mu_*\cos\theta)g_1, \quad (27a)$$

$$\Delta\mathcal{D}_{1/2}^\dagger f_2 - 2^{1/2}\mathcal{L}_{1/2}^\dagger f_1 = -2(i\mu_*r + a\mu_*\cos\theta)g_2, \quad (27b)$$

$$\mathcal{D}_0g_2 - 2^{-1/2}\mathcal{L}_{1/2}^\dagger g_1 = (i\mu_*r - a\mu_*\cos\theta)f_2, \quad (27c)$$

$$\Delta\mathcal{D}_{1/2}^\dagger g_1 + 2^{1/2}\mathcal{L}_{1/2}g_2 = -2(i\mu_*r - a\mu_*\cos\theta)f_1, \quad (27d)$$

Now we will separate the Dirac equation into radial and angular parts by choosing,

$$f_1(r, \theta) = R_{-1/2}(r)S_{-1/2}(\theta), f_2(r, \theta) = R_{1/2}(r)S_{1/2}(\theta),$$

$$g_1(r, \theta) = R_{1/2}(r)S_{-1/2}(\theta), g_2(r, \theta) = R_{-1/2}(r)S_{1/2}(\theta).$$

Replacing these f_i and g_i ($i = 1, 2$) into (27) and using separation constant λ we get,

$$\mathcal{L}_{\frac{1}{2}} S_{+\frac{1}{2}} = -(\lambda - am_p \cos \theta) S_{-\frac{1}{2}} \tag{28a}$$

$$\mathcal{L}_{\frac{1}{2}}^\dagger S_{-\frac{1}{2}} = +(\lambda + am_p \cos \theta) S_{+\frac{1}{2}} \tag{28b}$$

$$\Delta^{\frac{1}{2}} \mathcal{D}_0 R_{-\frac{1}{2}} = (\lambda + im_p r) \Delta^{\frac{1}{2}} R_{+\frac{1}{2}}, \tag{29a}$$

$$\Delta^{\frac{1}{2}} \mathcal{D}_0^\dagger \Delta^{\frac{1}{2}} R_{+\frac{1}{2}} = (\lambda - im_p r) R_{-\frac{1}{2}}, \tag{29b}$$

where, m_p is the mass of the particle which is nothing but $2^{1/2}\mu_*$. Also, $2^{1/2}R_{-1/2}$ is redefined as $R_{-1/2}$.

Equations (28) and (29) are the angular and radial Dirac equation respectively in coupled form with the separation constant λ [3].

4. Solution of angular Dirac equation

Decoupling equation (28) we obtain the eigenvalue equation for spin- $\frac{1}{2}$ particles as

$$\left[\mathcal{L}_{\frac{1}{2}} \mathcal{L}_{\frac{1}{2}}^\dagger + \frac{am_p \sin \theta}{\lambda + am_p \cos \theta} \mathcal{L}_{\frac{1}{2}}^\dagger + (\lambda^2 - a^2 m_p^2 \cos^2 \theta) \right] S_{-\frac{1}{2}} = 0. \tag{30}$$

Similarly, one can obtain decoupled equation for spin+ $\frac{1}{2}$ particles. Here, the separation constant λ is considered to be the eigenvalue of the equation. The exact solutions of this equation for λ and $S_{-\frac{1}{2}}$ is possible in terms of orbital angular momentum quantum number l and the spin of the particle s when the parameter $\rho_1 = \frac{m_p}{\sigma} = 1$. When the angular momentum of the black hole is zero i.e., Schwarzschild case, the equation is reduced in such a form that whose solution is nothing but standard spherical harmonics such as [8-9].

$$S_{-1/2}(\theta) e^{im\phi} =_{-\frac{1}{2}} Y_{lm}(\theta, \phi), \tag{31}$$

the eigenvalue i.e., the separation constant can be solved as,

$$\lambda^2 = (l + 1/2)^2. \tag{32}$$

Similarly, for spin+ $\frac{1}{2}$ particle one can solve $S_{+1/2}$ as

$$S_{+1/2}(\theta) e^{im\phi} =_{+\frac{1}{2}} Y_{lm}(\theta, \phi), \tag{33}$$

with same eigenvalue λ .

For any non-integral, massless, spin particle the solutions are [8-9]

$$S_{\pm s}(\theta) e^{im\phi} =_{\pm s} Y_{lm}(\theta, \phi), \tag{34}$$

$$\lambda^2 = (l + |s|)(l - |s| + 1). \tag{35}$$

In the case of Kerr geometry, when $a \neq 0$ the equation can be solved by perturbative procedure [5] with perturbative parameter $a\sigma$. The solution for $\rho_1 = m_p/\sigma = 1$ and $s = \pm \frac{1}{2}$ is [5]

$$\lambda^2 = \left(l + \frac{1}{2}\right)^2 + a\sigma(p + 2m) + a^2\sigma^2 \left[1 - \frac{y^2}{2(l + 1) + a\sigma x}\right], \tag{36}$$

$$\frac{1}{2}S_{lm} = \frac{1}{2}Y_{lm} + \frac{a\sigma y}{2(l + 1) + a\sigma x} \frac{1}{2}Y_{l+1m} \tag{37a}$$

$$-\frac{1}{2}S_{lm} = -\frac{1}{2}Y_{lm} - \frac{a\sigma y}{2(l + 1) + a\sigma x} -\frac{1}{2}Y_{l+1m} \tag{37b}$$

where,

$$p = F(l, l); \quad x = F(l + 1, l + 1); \quad y = F(l, l + 1) \tag{38}$$

and

$$F(l_1, l_2) = [(2l_2 + 1)(2l_1 + 1)]^{\frac{1}{2}} \langle l_2 1 m 0 | l_1 m \rangle [\langle l_2 1 \frac{1}{2} 0 | l_1 \frac{1}{2} \rangle + (-1)^{l_2-l} \langle l_2 1 m 0 | l_1 m \rangle [\langle l_2 1 \frac{1}{2} 0 | l_1 \frac{1}{2} \rangle + (-1)^{l_2-l} \rho_1 \sqrt{2} \langle l_2 1 - \frac{1}{2} 1 | l_1 \frac{1}{2} \rangle]]. \tag{39}$$

with $\langle \dots | \dots \rangle$ are the usual Clebsh-Gordon coefficients.

If $\rho_1 \neq 1$ then exact solution is not possible. In those cases the analytic expression of eigenvalue and angular wave-function are found as infinite series not in a compact form as the case $\rho_1 = 1$.

From the general convergence of series expansions one can truncate the infinite series upto certain order for particular values of l, s and m . For $l = \frac{1}{2}, s = -\frac{1}{2}$ and $m = -\frac{1}{2}$, up to third order in $a\sigma$, one obtains [5],

$$\lambda^2 = \left(l + \frac{1}{2}\right)^2 + a\sigma f_1(l, m) + (a\sigma)^2 f_2(l, m) + (a\sigma)^3 f_3(l, m), \tag{40}$$

$$-\frac{1}{2}S_{\frac{1}{2}-\frac{1}{2}} = -\sin\theta - \left(\sin^3\frac{\theta}{2} - \sin\theta\cos\frac{\theta}{2}\right) \left[\frac{2}{3}a\sigma(1 + \rho_1) + \frac{4}{15}(a\sigma)^2(1 - \rho_1^2)\right] + \frac{2}{5}(a\sigma)^2(1 - \rho_1^2) \left[\sin^5\frac{\theta}{2} - 6\sin^2\frac{\theta}{2}\cos^3\frac{\theta}{2} + 3\sin\frac{\theta}{2}\cos^4\frac{\theta}{2}\right]. \tag{41}$$

The accuracy of eigenvalues and eigenfunctions decreases as $a\sigma \rightarrow 1$.

5. Solution of radial Dirac equation

In the radial equation independent variable r is extended from 0 to ∞ . For mathematical simplicity we change the independent variable r to r_* as

$$r_* = r + \frac{2Mr_+ + am/\sigma}{r_+ - r_-} \log\left(\frac{r}{r_+} - 1\right) - \frac{2Mr_- + am/\sigma}{r_+ - r_-} \log\left(\frac{r}{r_-} - 1\right) \tag{42}$$

(for $r > r_+$), here in new r_* co-ordinate system horizon r_+ is shifted to $-\infty$ unless $\sigma \leq -\frac{am}{2Mr_+}$ [3], so the region is extended from $-\infty$ to ∞ . We also choose $R_{-\frac{1}{2}} = P_{-\frac{1}{2}}$, $\Delta^{\frac{1}{2}}R_{+\frac{1}{2}} = P_{+\frac{1}{2}}$. Then we are defining

$$(\lambda \pm im_p r) = \exp(\pm i\theta) \sqrt{(\lambda^2 + m_p^2 r^2)}$$

and

$$P_{+\frac{1}{2}} = \psi_{+\frac{1}{2}} \exp \left[-\frac{1}{2} i \tan^{-1} \left(\frac{m_p r}{\lambda} \right) \right],$$

$$P_{-\frac{1}{2}} = \psi_{-\frac{1}{2}} \exp \left[+\frac{1}{2} i \tan^{-1} \left(\frac{m_p r}{\lambda} \right) \right].$$

Finally choosing,

$$Z_{\pm} = \psi_{+\frac{1}{2}} \pm \psi_{-\frac{1}{2}}$$

and combining the differential equations (29) we get,

$$\left(\frac{d}{d\hat{r}_*} - W \right) Z_+ = i\sigma Z_-, \tag{43a}$$

and

$$\left(\frac{d}{d\hat{r}_*} + W \right) Z_- = i\sigma Z_+, \tag{43b}$$

where,

$$\hat{r}_* = r_* + \frac{1}{2\sigma} \tan^{-1} \left(\frac{m_p r}{\lambda} \right)$$

and

$$W = \frac{\Delta^{\frac{1}{2}}(\lambda^2 + m_p^2 r^2)^{3/2}}{\omega^2(\lambda^2 + m_p^2 r^2) + \lambda m_p \Delta / 2\sigma}. \tag{44}$$

where, $\omega^2 = \frac{K}{\sigma}$.

Now decoupling equations (43a-b) we get,

$$\left(\frac{d^2}{d\hat{r}_*^2} + \sigma^2 \right) Z_{\pm} = V_{\pm} Z_{\pm}. \tag{45}$$

where, $V_{\pm} = W^2 \pm \frac{dW}{d\hat{r}_*}$ and \hat{r}_* is extended from $-\infty$ (horizon) to $+\infty$.

The equation (45) is nothing but one dimensional Schrödinger equation [10] with potentials V_{\pm} and the energy of the particle σ^2 (since the system is dimensionless) in Cartesian co-ordinate system. The equation (45) can be solved by WKB approximation method [10-11]. The corresponding solution is [6-7],

$$Z_{\pm} = \frac{A_{\pm}}{\sqrt{k_{\pm}}} \exp(iu_{\pm}) \pm \frac{B_{\pm}}{\sqrt{k_{\pm}}} \exp(-iu_{\pm}) \tag{46}$$

where,

$$k_{\pm} = \sqrt{(\sigma^2 - V_{\pm})}, \quad (47)$$

and

$$u_{\pm} = \int k_{\pm} d\hat{r}_*. \quad (48)$$

Now we improve the solution by introducing space dependences on coefficients A_{\pm} and B_{\pm} [6-7] (this is beyond WKB approximation, because WKB deals with solutions with constant coefficients). It is seen that far away from a black hole, potential varies very slowly. Thus, in those regions one can safely write,

$$A_{\pm} - B_{\pm} = \text{Constant}(= c). \quad (49)$$

Since the sum of reflection and transmission coefficients must be unity,

$$A_{\pm}^2 + B_{\pm}^2 = k_{\pm}. \quad (50)$$

Near the horizon it is seen that potential height reduces to zero so the reflection in that region is almost zero and transmission is almost 100%. This is the *inner boundary condition*. Solving (49) and (50) we get analytical expression of space dependent reflection and transmission coefficients far away from the black hole which satisfy *outer boundary condition*. Combining the inner and outer boundary conditions, we get analytical expression of space dependent coefficient A_{\pm} and B_{\pm} which is valid in whole region $(-\infty$ to $+\infty)$. For details see [6-7]. The space dependency of A_{\pm} and B_{\pm} i.e. the transmission and reflection coefficients arises due to the variation of potential with distance. So from the analytical expressions one can easily find out at each point what fraction of incoming matter is going inward and what other fraction is going outward as a result of the interaction with the black hole. These space dependent transmission and reflection coefficients are given below [6-7].

$$T_{\pm} = \frac{a_{\pm}^2}{k_{\pm}} = \frac{(c_1 + \frac{\epsilon}{2})}{h_{\pm}} \left(c_1 + \frac{c}{2} + \sqrt{2k_{\pm} - c^2} \right) + \frac{2k_{\pm} - c^2}{4h_{\pm}} \quad (51a)$$

$$R_{\pm} = \frac{b_{\pm}^2}{k_{\pm}} = \frac{(c_2 - \frac{\epsilon}{2})}{h_{\pm}} \left(c_2 - \frac{c}{2} + \sqrt{2k_{\pm} - c^2} \right) + \frac{2k_{\pm} - c^2}{4h_{\pm}}. \quad (51b)$$

Here, a_{\pm} and b_{\pm} are defined as

$$a_{\pm} = \frac{A_{\pm}}{\sqrt{h_{\pm}/k_{\pm}}}, \quad (52a)$$

$$b_{\pm} = \frac{B_{\pm}}{\sqrt{h_{\pm}/k_{\pm}}} \quad (52b)$$

which are transmitted and reflected amplitudes of the solution with modified WKB method (going beyond WKB method) and

$$h_{\pm} = \left(c_1 + \frac{c}{2}\right)^2 + \left(c_2 - \frac{c}{2}\right)^2 + (c_1 + c_2)\sqrt{2k_{\pm} - c^2} + \frac{(2k_{\pm} - c^2)}{2}, \quad (53)$$

where, c_1 and c_2 are two constants introduced to satisfy the inner boundary condition. The final form of the solution is

$$Z_{\pm} = \frac{a_{\pm}}{\sqrt{k_{\pm}}} \exp(iu_{\pm}) \pm \frac{b_{\pm}}{\sqrt{k_{\pm}}} \exp(-iu_{\pm}). \quad (54)$$

Since the relation between Z_{\pm} and $R_{\pm\frac{1}{2}}$ is known, one can easily calculate the radial wave function $R_{\pm\frac{1}{2}}$.

6. Conclusions

In this review we write the Dirac equation in curved space-time and particularly in Kerr geometry. From this, the behaviour of non-integral spin particles can be studied in curved space-time. From the form of the equation and its solution it is clear that in curved space the particles behave in differently than in a flat space-time. The Newman-Penrose formalism is used to write the equation where the basis system is null. Dirac equation is separated into angular and radial parts. Similar separation can be possible on the background of Dyon black hole [12]. The solution of angular component of the Dirac equation is first reviewed. The exact solution is possible for $\frac{m\mu}{\sigma} = 1$, otherwise the solution is approximate [5]. Unlike in the case of a Kerr black hole, the solution of the angular equation around a Schwarzschild black hole is independent of the azimuthal or meridional angles [5, 13,14]. This is expected because of symmetry of the space-time.

The radial Dirac equation is solved using WKB approximation more clearly modified WKB approximation [6-7], where the space dependent transmission and reflection coefficients are calculated. Although WKB method is an approximate method, it is improvised in such a way that spatial dependence of the coefficients of the wave function is obtained. This way we ensure that the analytical solution is closer to the exact solution. The reflection and transmission coefficients were found to distinguish strongly the solutions of different rest masses and different energies. The solution might be of immense use in the study of the spectrum of particles emitted from a black hole horizon (Hawking radiation).

Acknowledgments

It is a great pleasure to thank Prof. Sandip K. Chakrabarti for many serious discussion and giving me the opportunity to write this review.

References

1. S Teukolsky *PRL* **29** 1114 (1972)
2. S Weinberg *Gravitation and Cosmology: Principle and Applications of the General Theory of Relativity*, (New York: John Wiley & Sons) (1972)
3. S Chandrasekhar *The Mathematical Theory Of Black Holes* (London: Clarendon Press) (1983)
4. S Chandrasekhar *Proc. R. Soc. Lond. A* **349** 571 (1976)
5. S K Chakrabarti *Proc. R. Soc. Lond. A* **391** 27 (1984)
6. B Mukhopadhyay and S K Chakrabarti *Proc. Roy. Soc A* (submitted) (1999)
7. B Mukhopadhyay and S K Chakrabarti *Class. Quant. Grav.* (in Press), (1999)
8. E Newman and R Penrose *J. Math. Phys.* **7** 863 (1966)
9. J N Goldberg, A J Macfarlane, E T Newman, F Rohrlich and E C G Sudarsan *J. Math. Phys.* **8** 2155 (1967)
10. A M Davydov *Quantum Mechanics*, (Second Ed.) (Oxford: Pergamon Press) (1976)
11. J Mathews and R L Walker *Mathematical Methods Of Physics* (Second Ed.) (California: The Benjamin/Cummings Publishing Company), (1970)
12. I Semiz *Phys. Rev. D* **46** 5414 (1992)
13. W H Press and S Teukolsky *Astrophys. J.* **185** 649 (1973)
14. S Teukolsky and W H Press *Astrophys. J.* **193** 443 (1974)

Nucleosynthesis around black holes

Banibrata Mukhopadhyay
Theoretical Astrophysics Group.
S. N. Bose National Centre For Basic Sciences
JD Block, Salt Lake, Sector-III. Calcutta-700091,
India
e-mail: bm@boson.bose.res.in

Abstract. Study of nucleosynthesis in accretion disks around black holes was initiated by Chakrabarti et al. (1987). In the present work we do the similar analysis using the state-of-the-art disk model, namely, Advective Accretion Disks. During the infall, matter temperature and density are generally increased which are first computed. These quantities are used to obtain local changes in composition, amount of nuclear energy released or absorbed, etc. under various inflow conditions. In the cases where the magnetic viscosity is dominant neutron torus may be formed. We also talk about the fate of Li^7 and D during the accretion. The outflowing winds from the disk could carry the new isotopes produced by nucleosynthesis and contaminate the surroundings. From the degree of contamination, one could pinpoint the inflow parameters.

Keywords : Accretion, black holes, nuclear astrophysics, origin and abundance of elements

PACS Nos. : 97.10.Gz, 04.70.-s, 98.80.Ft, 26.0

1. Introduction

There are many observational evidences where the incoming matter has the potential to become as hot as its virial temperature $T_{virial} \sim 10^{13}$ K [1]. Through various cooling effects, this incoming matter is usually cooled down to produce hard and soft states [2]. In the accretion disk, matter in the sub-Keplerian region generally remains hotter than Keplerian disks. The matter is so hot that after big-bang nucleosynthesis this is the most favourable temperature to produce significant nuclear reactions. The energy generation due to nucleosynthesis could be high enough to destabilize the flow and the modified composition may come out through winds to affect the metallicity of the galaxy [3-7]. Previous works on nucleosynthesis in disk was done for cooler

thick accretion disks. Since the sub-Keplerian region is much hotter than of Keplerian region and also than the central temperature ($\sim 10^7\text{K}$) of stars, presently we are interested to study nucleosynthesis in hot sub-Keplerian region of accretion disks.

2. Basic equations and physical systems

In 1981 Paczyński & Bisnovatyi-Kogan [8] initiated the study of viscous transonic flow although the global solutions of advective accretion disks were obtained much later [9] which we use here. In the advective disks, matter must have radial motion which is transonic. The supersonic flow must be sub-Keplerian and therefore must deviate from a Keplerian disk away from the black hole. The basic equations which matter obeys while falling towards the black hole from the boundary between Keplerian and sub-Keplerian region are given below (for details, see, [9]):

(a) The radial momentum equation:

$$\vartheta \frac{d\vartheta}{dx} + \frac{1}{\rho} \frac{dP}{dx} + \frac{\lambda_{Kep}^2 - \lambda^2}{r^3} = 0, \quad (1a)$$

(b) The continuity equation:

$$\frac{d}{dx}(\Sigma x \vartheta) = 0, \quad (1b)$$

(c) The azimuthal momentum equation:

$$\vartheta \frac{d\lambda(x)}{dx} - \frac{1}{\Sigma x} \frac{d}{dx}(x^2 W_{x\phi}) = 0, \quad (1c)$$

(d) The entropy equation:

$$\frac{2na\rho\vartheta h(x)}{\gamma} \frac{da}{dx} - \frac{a^2\vartheta h(x)}{\gamma} \frac{d\rho}{dx} = fQ^+ \quad (1d)$$

where the equation of state is chosen as $a^2 = \frac{\gamma P}{\rho}$. Here, λ is the specific angular momentum of the infalling matter. λ_{Kep} is that in the Keplerian region is defined as $\lambda_{Kep}^2 = \frac{x^3}{2(x-1)^2}$ [10], Σ is vertically integrated density, $W_{x\phi}$ is the stress tensor, a is the sound speed and $h(x)$ is the half thickness of the disk ($\sim ax^{1/2}(x-1)$), $n = \frac{1}{\gamma-1}$ is the polytropic index, f is the cooling factor which is kept constant throughout our study, Q^+ is the heat generation due to the viscous effect of the disk. For the time being we are neglecting the magnetic heating term.

During infall different nuclear reactions take place and nuclear energy is released. Here, our study is exploratory so in the heating term Q^+ , we do not include the heating due to nuclear reactions. (Work including nuclear energy

release term is in [6].) Another parameter β is defined as ratio of gas pressure to total pressure, which is assumed to be a constant value throughout a particular case. Actually, the factor β is used to take into account the cooling due to Comptonization. To compute the temperature of the Comptonized flow in the advective region which may or may not have shocks, we follow Chakrabarti & Titarchuk [2] and Chakrabarti's [11] works and method. The temperature is computed from.

$$T = \frac{a^2 \mu m_p \beta}{\gamma k}. \quad (2)$$

It is seen that due to hotter nature of the advective disk especially when accretion rate is low, Compton cooling is negligible, the major process of hydrogen burning is the rapid proton capture process, which operates at $T \gtrsim 0.5 \times 10^9 \text{K}$ which is much higher than the operating temperature of PP chain (operates at $T \sim 0.01 - 0.2 \times 10^9 \text{K}$) and CNO cycle (operates at $T \sim 0.02 - 0.5 \times 10^9 \text{K}$) which take place in the case of stellar nucleosynthesis where temperature is much lower. Also in stellar case, in different radii same sets of reaction take place but in the case of disk, in different radii different reactions (or different sets of reaction) can take place simultaneously. These are the basic differences between the nucleosynthesis in stars and disks.

For simplicity, we take the solar abundance as the initial abundance of the disk and our computation starts where matter leaves a Keplerian disk. According to [2] and [11], the black hole remains in hard states when viscosity and accretion rate are smaller. In this case, x_K (at radius x_K matter deviates from Keplerian to sub-Keplerian region) is large. In this parameter range the protons remain hot ($T_p \sim 1 - 10 \times 10^9 \text{K}$). The corresponding factor $f (= 1 - Q^+/Q^-)$ is not low enough to cool down the disk, (in [1], it is indicated that \dot{m}/α^2 is a good indication of the cooling efficiency of the hot flow), where Q^+ and Q^- are the heat gain and heat loss due to viscosity of the disk.

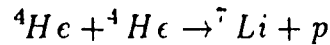
We have studied a large region of parameter space with $0.0001 \lesssim \alpha \lesssim 1$, $0.001 \lesssim \dot{m} \lesssim 100$, $0.01 \lesssim \beta \lesssim 1$, $4/3 \lesssim \gamma \lesssim 5/3$. We study a case with a standing shock as well. In selecting the reaction network we kept in mind the fact that hotter flows may produce heavier elements through triple- α and rapid proton and α capture processes. Furthermore due to photo-dissociation significant neutrons may be produced and there is a possibility of production of neutron rich isotopes. Thus, we consider sufficient number of isotopes on either side of the stability line. The network thus contains protons, neutrons, till ${}^{72}\text{Ge}$ - altogether 255 nuclear species. The standard reaction rates were taken [6].

3. Results

Here we present a typical case containing a shock wave in the advective region [6]. We express the length in the unit of one Schwarzschild radius which is

$\frac{2GM}{c^2}$ where M is the mass of the black hole, velocity is expressed in the unit of velocity of light c and the unit of time is $\frac{2GM}{c^3}$. We use the mass of the black hole $M/M_\odot = 10$ ($M_\odot =$ solar mass), Π -stress viscosity parameter $\alpha_\Pi = 0.05$, the location of the inner sonic point $x_{in} = 2.8695$, the value of the specific angular momentum at the inner edge of the black hole $\lambda_{in} = 1.6$, the polytropic index $\gamma = 4/3$ as free parameters. The net accretion rate $\dot{m} = 1$ in the unit of Eddington rate, cooling factor due to Comptonization $\beta = 0.03$, $x_K = 481$. The proton temperature (in the unit of 10^9), velocity distribution (in the units of 10^{10} cm sec $^{-1}$), density distribution (in the unit of 2×10^{-8} gm cm $^{-3}$) are shown in Fig. 1(a).

In Fig. 1b, we show composition changes close to the black hole both for the shock-free branch (dotted curves) and the shocked branch of the solution (solid curves). Only prominent elements are plotted. The difference between the shocked and the shock-free cases is that, in the shock case the similar burning takes place farther away from the black hole because of much higher temperature in the post-shock region. A significant amount of the neutron (with a final abundance of $Y_n \sim 10^{-3}$) is produced due to photo-dissociation process. Note that closer to the black hole, ^{12}C , ^{16}O , ^{24}Mg and ^{28}Si are all destroyed completely. Among the new species which are formed closer to the black hole are ^{30}Si , ^{46}Ti , ^{50}Cr . Note that the final abundance of ^{20}Ne is significantly higher than the initial value. Thus a significant metallicity could be supplied by winds from the centrifugal barrier. In Fig. 1c we show the change of abundance of neutron (n), deuterium (D) and lithium (7Li). It is noted that near black hole a significant amount of neutron is formed although initially neutron abundance was almost zero. Also D and 7Li are totally burnt out near black hole which is against the major claim of Yi & Narayan [13] which found significant lithium in the disk. It is true that due to spallation reaction, i.e.,



7Li may be formed in the disk but due to photo-dissociation in high temperature all 4He are burnt out before forming 7Li i.e. the formation rate of 4He from D is much slower than the burning rate of it. Yi & Narayan [13] do not include the possibility of photo-dissociation in the hot disk.

In Fig. 1d, we show nuclear energy release/absorption for the flow in units of erg sec $^{-1}$ gm $^{-1}$. Solid curve represents the nuclear energy release/absorption for the shocked flow and the dotted curve is that for unstable shock-free flow. As matter leaves the Keplerian region, the rapid proton capture such as, $p + ^{18}O \rightarrow ^{15}N + ^4He$ etc., burn hydrogen and releases energy to the disk. At around $x = 50$, $D \rightarrow n + p$ dissociates D and the endothermic reaction causes the nuclear energy release to become 'negative', i.e., a huge amount of energy is absorbed from the disk. At around $x = 15$ the energy release is again dominated by the original processes because no deuterium is left to burn. Due to excessive temperature, immediately 3He breaks down into deuterium and

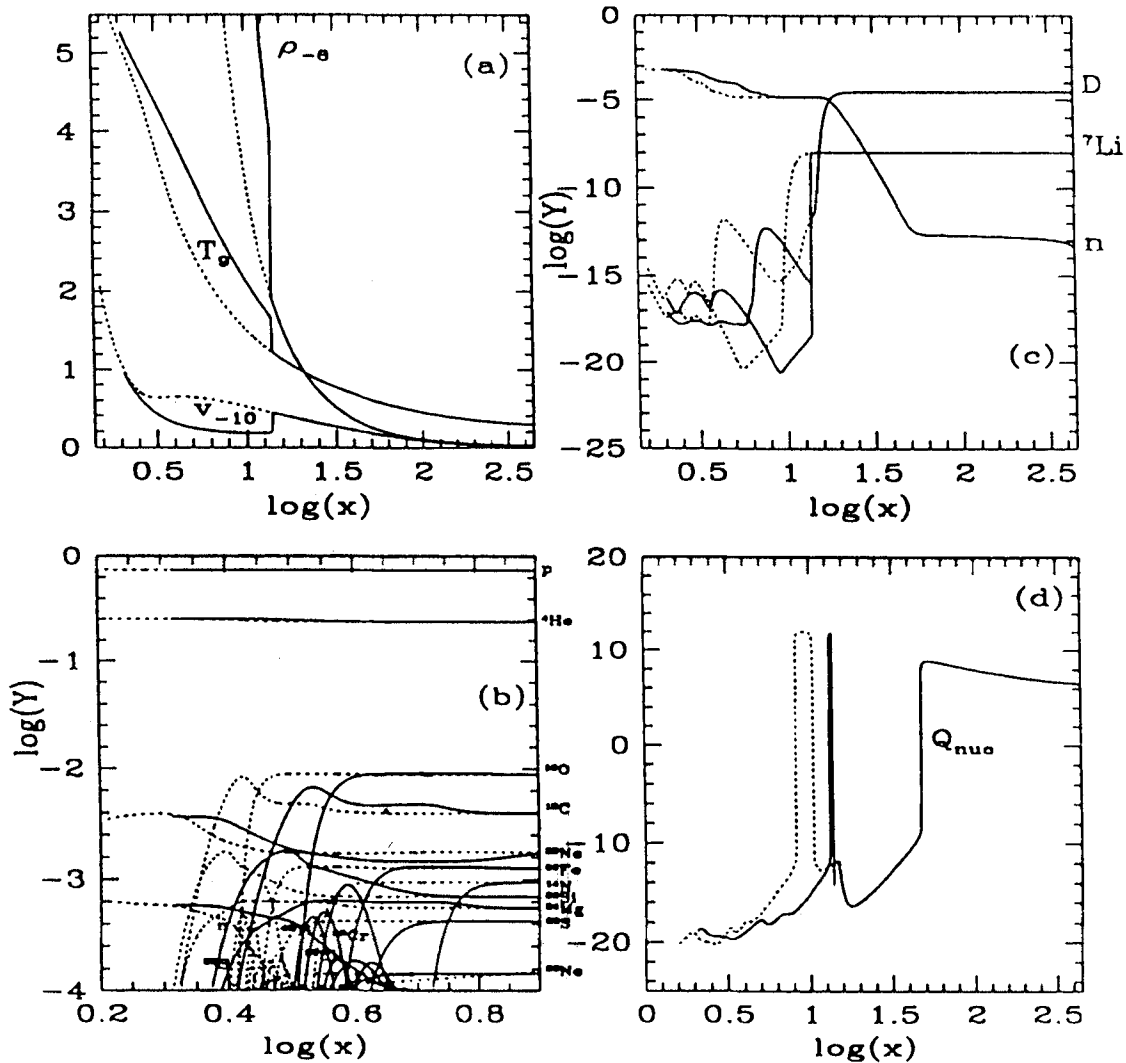


Figure 1. Variation of (a) proton temperature (T_9), radial velocity v_{10} and density distribution ρ_{-8} (b) matter abundance Y in logarithmic scale (c) neutron, deuterium and lithium abundance Y in logarithmic scale and (d) nuclear energy release and absorption as a functions of logarithmic radial distance x . See text for parameters. Solutions in the stable branch with shocks are solid curves and those without the shock are dotted in (a-d). At the shock, temperature and density rise and velocity lower significantly and cause a significant change in abundance even farther out. Shock induced winds may cause substantial contamination of the galactic composition when parameters are chosen from these regions [6].

through dissociation of D again a huge amount of energy is absorbed from the disk. It is noted that energy absorption due to photo-dissociation as well as the magnitude of the energy release due to proton capture process and that due to

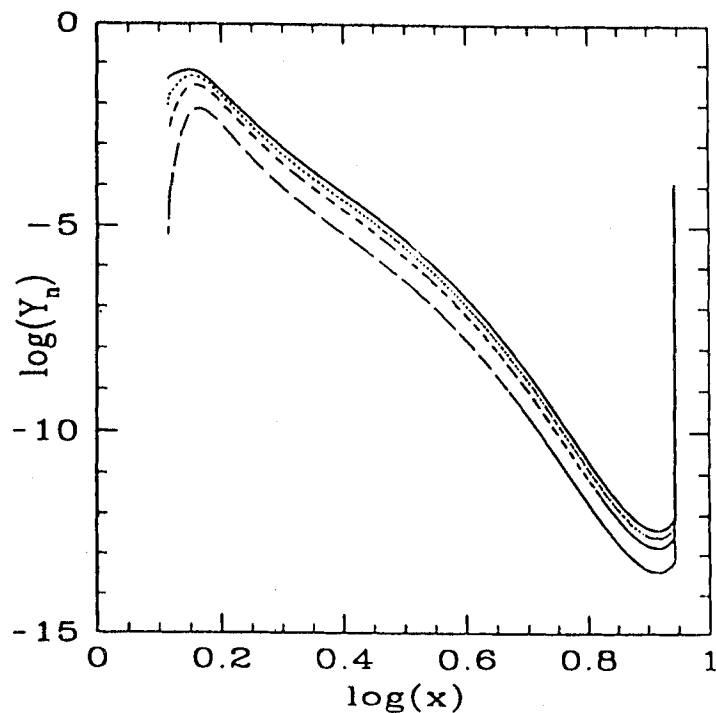


Figure 2. The convergence of the neutron abundance through successive iterations in a very hot advective disk. From bottom to top curves 1st, 4th, 7th and 11th iteration results are shown. A neutron torus with a significant abundance is formed in this case [15].

viscous dissipation (Q^+) are very similar (save the region where endothermic reactions dominate). This suggests that even with nuclear reactions, at least some part of the advective disk may be perfectly stable.

We now present another interesting case where lower accretion rate ($\dot{m} = 0.01$) but higher viscosity (0.2) were used and the efficiency of cooling is not 100% ($f = 0.1$). That means that the temperature of the flow is high ($\beta = 0.1$, maximum temperature $T_9^{max} = 11$). In this case $x_K = 8.8$, if the high viscosity is due to stochastic magnetic field, protons would be drifted towards the black hole due to magnetic viscosity, but the neutrons will not be drifted [13] till they decay. This principle has been used to do the simulation in this case. The modified composition in one sweep is allowed to interact with freshly accreting matter with the understanding that the accumulated neutrons do not drift radially. After few iterations or sweeps the steady distribution of the composition may be achieved. Figure 2 shows the neutron distributions in iteration numbers 1, 4, 7 & 11 respectively (from bottom to top curves) in the advective region. The formation of a 'neutron torus' is very apparent in this result and generally in all the hot advective flows. In 1987 Hogan &

Applegate [14] showed that formation of neutron torus is possible with high accretion rate. But high accretion rate means high rate of photon to dump into sub-Keplerian region and high rate of inverse Compton process through which matter cool down, that is why photo-dissociation will be less prominent. Also formation of neutron is possible through the photo-dissociation of deuterium in the hot disk which is physically possible prominently in our parameter region, where neutron torus is formed. Details are in Chakrabarti & Mukhopadhyay [15].

4. Discussions and conclusions

In this paper, we have explored the possibility of nuclear reactions in advective accretion flows around black holes. Temperature in this region is controlled by the efficiencies of bremsstrahlung and Comptonization processes [2, 7]. For a higher Keplerian rate and higher viscosity, the inner edge of the Keplerian component comes closer to the black hole and the advective region becomes cooler [2, 9]. However, as the viscosity is decreased, the inner edge of the Keplerian component moves away and the Compton cooling becomes less efficient.

The composition changes especially in the centrifugal pressure supported denser region, where matter is hotter and slowly moving. Since centrifugal pressure supported region can be treated as an effective surface of the black hole which may generate winds and outflows in the same way as the stellar surface, one could envisage that the winds produced in this region would carry away modified composition [16-18]. In very hot disks, a significant amount of free neutrons are produced which, while coming out through winds may recombine with outflowing protons at a cooler environment to possibly form deuteriums. A few related questions have been asked lately: Can lithium in the universe be produced in black hole accretion [12,19]? We believe that this is not possible. When the full network is used we find that the hotter disks where spallation would have been important also heliums photo-dissociate into deuteriums and then to protons and neutrons before any significant production of lithiums. Another question is: Could the metallicity of the galaxy be explained, at least partially, by nuclear reactions? We believe that this is quite possible. Details are in [6].

Another important thing which we find that in the case of hot inflows formation of neutron tori is a very distinct possibility [15]. Presence of a neutron torus around a black hole would help the formation of neutron rich species as well, a process hitherto attributed to the supernovae explosions only. It can also help production of Li on the companion star surface (see [6] and references therein).

The advective disks as we know today do not perfectly match with a Keplerian disk. The shear, i.e., $d\Omega/dr$ is always very small in the advective flow compared to that of a Keplerian disk near the outer boundary of the advective

region. Thus some improvements of the disk model at the transition region is needed. Since major reactions are closer to the black hole, we believe that such modifications of the model would not change our conclusions. The neutrino luminosity in a steady disk is generally very small compared to the photon luminosity [6], but occasionally, it is seen to be very high. In these cases, we predict that the disk would be unstable. Neutrino luminosity from a cool advective disk is low.

In all the cases, even when the nuclear composition changes are not very significant, we note that the nuclear energy release due to exothermic reactions or absorption of energy due to endothermic reactions is of the same order as the gravitational binding energy release. Like the energy release due to viscous processes, nuclear energy release strongly depends on temperatures. This additional energy source or sink may destabilize the flow [6].

Acknowledgments

I would like to thank Prof. Sandip K. Chakrabarti for introducing me to this subject and helpful discussion throughout the work.

References

1. M J Rees *Ann. Rev. Astron. Astrophys.* **22** 471 (1984)
2. S K Chakrabarti and L G Titarchuk *Astrophys J.* **455** 623 (1995)
3. S K Chakrabarti, L Jin and W D Arnett *Astrophys. J.* **313** 674 (1987)
4. L Jin, W D Arnett and S K Chakrabarti *Astrophys. J.* **336** 572 (1989)
5. S K Chakrabarti *Astrophys. J.* **324** 391 (1988)
6. B Mukhopadhyay and S K Chakrabarti *Astron. Astrophys.* (1999) in press
7. B Mukhopadhyay in *Observational Evidences for Black Holes in the Universe*, (Ed.) S K Chakrabarti (Dordrecht: Kluwer Academic Publishers) 105 (1998)
8. B Paczyński and G Bisnovatyi-Kogan *Acta Astron.* **31** 283 (1981)
9. S K Chakrabarti *Astrophys. J.* **464** 664 (1996)
10. B Paczyński and P J Wiita *Astron. Astrophys.* **88** 23 (1980)
11. S K Chakrabarti *Astrophys. J.* **484** 313 (1997)
12. I Yi and R Narayan *Astrophys. J.* **486** 383 (1997)
13. M J Rees et al., *Nat*, **295**, 17 (1982)
14. C J Hogan and J H Applegate *Nat* **390** 236 (1987)
15. S K Chakrabarti and B Mukhopadhyay *Astron. Astrophys.* **344** 105 (1999)
16. S K Chakrabarti *Astron. Astrophys.* (1999) in press
17. T K Das and S K Chakrabarti *Class. Quant. Grav.* (1999) in press
18. T K Das in *Observational Evidences for Black Holes in the Universe* (Ed.) S. K. Chakrabarti (Dordrecht: Kluwer Academic Publishers) 113 (1998)
19. L Jin *Astrophys. J.* **356** 501 (1990)

Nucleosynthesis in accretion flows around black holes

Banibrata Mukhopadhyay and Sandip K. Chakrabarti

S.N. Bose National Centre for Basic Sciences, JD Block, Salt Lake, Sector-III, Calcutta-700091, India

Received 21 January 1999 / Accepted 7 October 1999

Abstract. Significant nucleosynthesis is possible in the centrifugal pressure-supported dense and hot region of the accretion flows which deviate from Keplerian disks around black holes. We compute composition changes and energy generations due to such nuclear processes. We use a network containing 255 species and follow the changes in composition. Highly viscous, high-accretion-rate flows deviate from a Keplerian disk very close to the black hole and the temperature of the flow is very small due to Compton cooling. No significant nucleosynthesis takes place in these cases. Low-viscosity and lower-accretion-rate hot flows deviate farther out and significant changes in composition are possible in these cases. We suggest that such changes in composition could be contributing to the metallicities of the galaxies. Moreover, the radial variation of the energy generation/absorption specifically due to proton capture and photo-dissociation reactions could cause instabilities in the inner regions of the accretion flows. For most of these cases sonic point oscillations may take place. We discuss the possibility of neutrino emissions.

Key words: accretion, accretion disks – black hole physics – stars: neutron – shock waves – nuclear reactions, nucleosynthesis, abundances

1. Introduction

In Chakrabarti & Mukhopadhyay (1999, hereafter referred to as Paper I) we studied the result of nucleosynthesis in hot, highly viscous accretion flows with small accretion rates and showed that neutron tori can form around a black hole. In the present paper, we study nucleosynthesis in disks in other parameter space, where the photo-dissociation may not be complete and other reactions may be important, and show that depending on the accretion parameters, abundances of new isotopes may become abnormal around a black hole. Thus, observation of these isotopes may give a possible indication of black holes at the galactic center or in a binary system.

Earlier, Chakrabarti (1986) and Chakrabarti et al. (1987, hereafter CJA) initiated discussions of nucleosynthesis in sub-Keplerian disks around black holes and concluded that for very

low viscosity (α parameter less than around 10^{-4}) and high accretion rates (typically, ten times the Eddington rate) there could be significant nucleosynthesis in thick disks. Radiation-pressure-supported thick accretion flows are cooler and significant nucleosynthesis was not possible unless the residence time of matter inside the accretion disk was made sufficiently high by reducing viscosity. The conclusions of this work were later verified by Arai & Hashimoto (1992) and Hashimoto et al. (1993).

However, the theory of accretion flows which contain a centrifugal-pressure-supported hotter and denser region in the inner part of the accretion disk has been developed more recently (Chakrabarti 1990, hereafter C90 and Chakrabarti 1996, hereafter C96). The improvement in the theoretical understanding can be appreciated by comparing the numerical simulation results done in the eighties (e.g. Hawley et al. 1984, 1985) and in the nineties (e.g. Molteni et al. 1994; Molteni et al. 1996; Ryu et al. 1997). Whereas in the eighties the matching of theory and numerical simulations was poor, the matching of the results obtained recently is close to perfect. It is realized that in a large region of the parameter space, especially for lower accretion rates, the deviated flow would be hot and a significant nuclear reaction is possible without taking resort to very low viscosity.

We arrive at a number of the important conclusions: (a) Significant nucleosynthesis is possible in the accretion flows. Whereas most of the matter of modified composition enters inside the black hole, a fraction may go out through the winds and will contaminate the surroundings in due course. The metallicity of the galaxies may also be influenced. (b) Generation or absorption of energy due to exothermic and endothermic nuclear reactions could seriously affect the stability of a disk. (c) Hot matter is unable to produce Lithium (7Li) or Deuterium (D) since when the flow is hot, photo-dissociation (photons partially locally generated and the rest supplied by the nearby Keplerian disk (Shakura & Sunyaev 1973) when the region is optically thin) is enough to dissociate all the elements completely into protons and neutrons. Even when photo-dissociation is turned off (low opacity cases or when the system is fundamentally photon-starved) Li was not found to be produced very much. (d) Most significantly, we show that one does not require a very low viscosity for nucleosynthesis in contrary to the conclusions of the earlier works in thick accretion disk (e.g., CJA).

In Paper I, we already presented the basic equations which govern accretion flows around a compact object, so we do not

Send offprint requests to: B. Mukhopadhyay (bm@boson.bose.res.in)

present them here. The plan of the present paper is the following: we present a set of solutions of these equations in the next section which would be used for nucleosynthesis work. When nucleosynthesis is insignificant, we compute thermodynamic quantities ignoring nuclear energy generation, otherwise we include it. The detailed method is presented here. We divide all the disks into three categories: ultra-hot, moderately hot, and cold. In Sect. 3, we present the results of nucleosynthesis for these cases. We find that in ultra-hot cases, the matter is completely photo-dissociated. In moderately hot cases, proton-capture processes along with dissociation of deuterium and ${}^3\text{He}$ are the major processes. In the cold cases, no significant nuclear reactions go on. In Sect. 4, we discuss the stability properties of the accretion disks in presence of nucleosynthesis and conclude that only the very inner edge of the flow is affected. Nucleosynthesis may affect the metallicities of the galaxies as well as Li abundance in companions in black hole binaries. In Sect. 5, we discuss these issues and draw our conclusions.

2. Typical solutions of accretion flows

In our work below, we choose a Schwarzschild black hole and use the Schwarzschild radius $2GM/c^2$ to be the unit of the length scale where G and c are the gravitational constant and the velocity of light respectively. We choose c to be the unit of velocity. We also choose the cgs unit when we find it convenient to do so. The nucleosynthesis work is done using cgs units and the energy release rates are in that unit as well.

A black hole accretion disk must, by definition, have *radial* motion, and it must also be transonic, i.e., matter must be supersonic (C90) while entering through the horizon. The supersonic flow must be sub-Keplerian and therefore deviate from the Keplerian disk away from the black hole. The location where the flow may deviate will depend on the cooling and heating processes (which depend on viscosity). Several solutions of the governing equations (see Eq. 2(a-d) of Paper 1) are given in C96. By and large, we follow this paper to compute thermodynamical parameters along a flow. However, we have considered Comptonization as in Chakrabarti & Titarchuk (1995, hereafter CT95) and Chakrabarti (1997, hereafter C97). Due to computational constraints, we include energy generation due to nuclear reactions (Q_{nuc}) only when it is necessary (namely, when $|Q_{\text{nuc}}|$ is comparable to energy generation due to viscous effects), and we do not consider energy generation due to magnetic dissipation (due to reconnection effects, for instance). In Fig. 1, we show a series of solutions which we employ to study nucleosynthesis processes. We plot the ratio λ/λ_K (Here, λ and λ_K are the specific angular momentum of the disk and the Keplerian angular momentum respectively.) as a function of the logarithmic radial distance. The coefficient of the viscosity parameters are marked on each curve. The other parameters of the solution are in Table 1. These solutions are obtained with constant $f = 1 - Q^-/Q^+$ and Q^+ include only the viscous heating. In presence of significant nucleosynthesis, the solutions are obtained by choosing $f = 1 - Q^-/(Q^+ + Q_{\text{nuc}})$, where Q_{nuc} is the net energy generation or absorption due to exothermic and

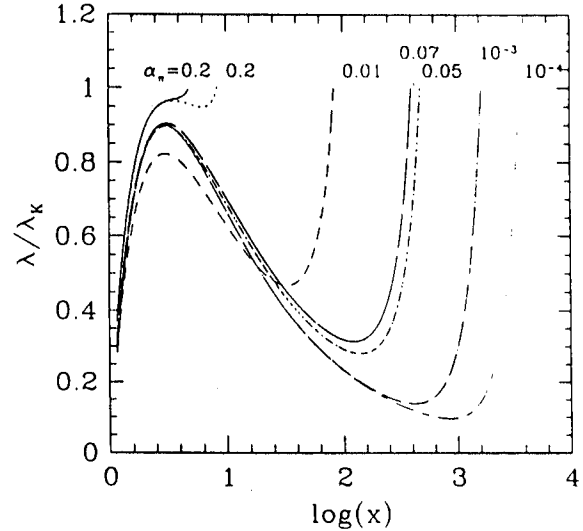


Fig. 1. Variation of λ/λ_K with logarithmic radial distance for a few solutions which are employed to study nucleosynthesis. The viscosity parameter α_{H} is marked on each curve. $x = x_K$ where $\lambda/\lambda_K = 1$, represents the location where the flow deviates from a Keplerian disk. Note that except for the dashed curve marked 0.01 (which is for $\gamma = 5/3$, and the rest are for $\gamma = 4/3$), x_K generally rises with decreasing α_{H} . Thus, high viscosity flows must deviate from the Keplerian disk closer to the black hole.

endothermic reactions. The motivation for choosing the particular cases are mentioned in the next section. At $x = x_K$, the ratio $\lambda/\lambda_K = 1$ and therefore x_K represents the transition region where the flow deviates from a Keplerian disk. First, note that when other parameters (basically, specific angular momentum and the location of the inner sonic point) remain roughly the same, x_K changes inversely with viscosity parameter α_{H} (C96). (The only exception is the curve marked with 0.01. This is because it is drawn for $\gamma = 5/3$; all other curves are for $\gamma = 4/3$.) If one assumes, as Chakrabarti & Titarchuk (1995) and Chakrabarti (1997) did, that the alpha viscosity parameter *decreases* with vertical height, then it is clear from the general behaviour of Fig. 1 that x_K would go up with height. The disk will then look like a sandwich with higher viscosity Keplerian matter flowing along the equatorial plane. As the viscosity changes, the sub-Keplerian and Keplerian flows redistribute (Chakrabarti & Molteni 1995) and the inner edge of the Keplerian component also recedes or advances. This fact that the inner edge of the disk should move in and out when the black hole goes into soft or hard state (as observed by, e.g., Giffanov et al. 1997; Zhang et al. 1997) is thus naturally established from this disk solution.

In C90 and C96, it was pointed out that in a large region of the parameter space, especially for intermediate viscosities, centrifugal-pressure-supported shocks would be present in the hot, accretion flows. In these cases a shock-free solution passing through the outer sonic point was present. However, this branch is not selected by the flow and the flow passes through the higher entropy solution through shocks and the inner sonic points in-

stead. This assertion has been repeatedly verified independently by both theoretical (Yang & Kafatos 1995, Nobuta & Hanawa 1994; Lu & Yuan 1997; Lu et al. 1997) and numerical simulations (with independent codes, Chakrabarti & Molteni 1993; Sponholz & Molteni 1994; Ryu et al. 1995; Molteni et al. 1996 and references therein). When the shock forms, the temperature of the flow suddenly rises and the flow slows down considerably, raising the residence time of matter significantly. This effect of shock-induced nucleosynthesis is also studied in the next section and, for comparison, the changes in composition in the shock-free branch were also computed, although it is understood that the shock-free branch is unstable. Our emphasis is not on shocks per se, but on the centrifugal-pressure-dominated region where the accreting matter slows down. When the shock does not form, the rise in temperature is more gradual. We generally follow the results of CT95 and C97 to compute the temperature of the Comptonized flow in the sub-Keplerian region which may or may not have shocks. Basically we borrow the mean factor $F_{\text{Compt}} \lesssim 1$ by which the temperature of the flow at a given radius x ($< x_K$) is reduced due to Comptonization process from the value dictated by the single-temperature hydrodynamic equations. This factor is typically $1/30 \sim 0.03$ for very low ($\lesssim 0.1$) mass accretion rate of the *Keplerian component* (which supplies the soft photons for the Comptonization) and around $1/100 \sim 0.01$ or less for higher Keplerian accretion rates. In presence of magnetic fields, some dissipation is present due to reconnections. Its expression is $Q_{\text{mag}} = \frac{3B^2}{16\pi r\rho}$ (Shvartsman 1971; Shapiro 1973). We do not assume this heating in this paper.

The list of major nuclear reactions such as PP chain, CNO cycle, rapid proton capture and alpha (α) processes, photo-dissociation etc. which may take place inside a disk are already given in CJA, and we do not repeat them here. Suffice it to say that due to the hotter nature of the sub-Keplerian disks, especially when the accretion rate is low and Compton cooling is negligible, the major process of hydrogen burning is some rapid proton capture process (which operates at $T \gtrsim 0.5 \times 10^9$ K) and mostly (p, α) reactions as opposed to the PP chain (which operates at much lower temperature $T \sim 0.01\text{--}0.2 \times 10^9$ K) and CNO cycle (which operates at $T \sim 0.02\text{--}0.5 \times 10^9$ K) as in CJA.

Typically, accretion onto a stellar-mass black hole takes place from a binary companion which could be a main sequence star. In a supermassive black hole at a galactic center, matter is presumably supplied by a number of nearby stars. Because it is difficult to establish the initial composition of the inflow, we generally take the solar abundance as the abundance of the Keplerian disk. Furthermore, the Keplerian disk being cooler, and the residence time inside it being insignificant compared to the hydrogen burning time scale, we assume that for $x \gtrsim x_K$, the composition of the gas remains the same as that of the companion star, namely, solar. Thus our computation starts only from the time when matter is launched from the Keplerian disk. Occasionally, for comparison, we run the models with an initial abundance same as the output of big-bang nucleosynthesis (hereafter referred to as 'big-bang abundance'). These cases are

particularly relevant for nucleosynthesis around proto-galactic cores and the early phase of star formations. We have also tested our code with an initial abundance same as the composition of late-type stars since in certain cases they are believed to be companions of galactic black hole candidates (Martin et al. 1992, 1994; Filippenko et al. 1995; Harlaftis et al. 1996).

2.1. Selection of models

In selecting models for which the nucleosynthesis should be studied, the following considerations were made. According to CT95, and C97, there are two essential components of a disk. One is Keplerian (of rate \dot{m}_d) and the other is sub-Keplerian halo (of rate \dot{m}_h). For $\dot{m}_d \lesssim 0.1$ and $\dot{m}_h \lesssim 1$, the black hole remains in hard states. A lower Keplerian accretion rate generally implies a lower viscosity and a larger x_K ($x_K \sim 30\text{--}1000$; see, C96 and C97). In this parameter range the protons remain hot, typically, $T_p \sim 1\text{--}10 \times 10^9$ degrees or so. This is because the efficiency of emission is lower ($f = 1 - Q^- / Q^+ \sim 0.1$, where, Q^+ and Q^- are the height-integrated heat generation and heat loss rates [ergs $\text{cm}^{-2} \text{sec}^{-1}$] respectively. Also, see Rees (1984), where it is argued that \dot{m}/α^2 is a good indication of the cooling efficiency of the hot flow.). Thus, we study a group of cases (Group A) where the net accretion rate $\dot{m} \sim 1.0$ and the viscosity parameter $\alpha \sim 0.001\text{--}0.1$. The Comptonization factor $F_{\text{Compt}} \sim 0.03$, i.e., the cooling due to Comptonization reduces the mean temperature roughly by a factor of around 30, which is quite reasonable. Here, although the density of the gas is low, the temperature is high enough to cause significant nuclear reactions in the disk.

When the net accretion rate is very low ($\dot{m} \lesssim 0.01$) such as in a quiescence state of an X-ray novae, the dearth of soft photons keeps the temperature of the sub-Keplerian flow to a very high value and a high Comptonization factor $F_{\text{Compt}} \sim 0$.[†] could be used (Group B). Here significant nuclear reaction takes place, even though the density of matter is very low. Basically, the entire amount of matter is photo-dissociated into protons and neutrons in this case even when opacity is very low.

In the event the inflow consist of both the Keplerian (accretion rate \dot{m}_d) and sub-Keplerian (accretion rate \dot{m}_h) matter as the modern theory predicts, there would be situations where the *net* accretion rate is high, say $\dot{m} = \dot{m}_d + \dot{m}_h \sim 1\text{--}5$, and yet the gas temperature is very high ($T > 10^9$). This happens when viscosity is low to convert sub-Keplerian inflow into a Keplerian disk. Here, most of the inflow is in the sub-Keplerian component and very little ($\dot{m}_d \sim 0.01$) matter is in the Keplerian flow. Dearth of soft photons keeps the disk hot, while the density of reactants is still high enough to have profuse nuclear reactions. The simple criteria for the cooling efficiency (that $\dot{m}/\alpha^2 > 1$ would cool the disk, see Rees 1984) will not hold since the radiation source (Keplerian disk) is different from the cooling body (sub-Keplerian disk).

One could envisage yet another set of cases (Group C), where the accretion rate is very high ($\dot{m} \sim 10\text{--}100$), and the soft photons are so profuse that the sub-Keplerian region of the disks becomes very cold. In this case, typically, viscosity is very high

0.2. x_K becomes low ($x_K \sim 3-10$). The efficiency of cooling is very high ($Q^+ \approx Q^-$, i.e., $f \approx 0$). The Comptonization factor is low $F_{\text{Compt}} \lesssim 0.01$. The black hole is in a soft state. There is no significant nuclear reaction in these cases. In the protogalactic phase when the supply of matter is very high, while the viscosity may be so low (say, 10^{-4}) that the entire amount is not accreted, one can have an ultra-cold accretion flow with $F_{\text{Compt}} \sim 10^{-3}$. In this case also not much nuclear reaction goes on.

The above simulations have been carried out with polytropic index $\gamma = 4/3$. In reality, the polytropic index could be in between $4/3$ and $5/3$. If $\gamma < 1.5$ then shocks would form as in some of the above cases. However, for $\gamma > 1.5$, standing shocks would not form (C96). We have included one illustrative example of a shock-free case with $\gamma = 5/3$ which is very hot and we have presented the result in Group B. In this case the Keplerian component is far away and the intercepted soft photons are very few.

2.2. Selection of the reaction network

In selecting the reaction network we kept in mind the fact that hotter flows may produce heavier elements through triple- α and proton and α capture processes. Similarly, due to photo-dissociation, significant neutrons may be produced. Thus, we consider a sufficient number of isotopes on either side of the stability line. The network thus contains protons, neutrons, till ^{72}Ge – altogether 255 nuclear species. The network of coupled non-linear differential equation is linearized and evolved in time along the solution of C96 obtained from a given set of initial parameters of the flow. This well proven method is widely used in the literature (see Arnett & Truran 1969; Woosley et al. 1973).

The reaction rates were taken from Fowler et al. (1975) including updates by Harris et al. (1983). Other relevant references from where rates have been updated are: Thielemann (1980); Wallace & Woosley (1981); Wagoner et al. (1967); Fuller et al. (1980, 1982). For details of the procedure of adopting reaction rates, see, CJA and Jin et al. (1989, hereinafter JAC). The solar abundance which was used as the initial composition of the inflow was taken from Anders & Ebihara (1982).

3. Results

In this section, we present a few major results of our simulations using different parameter groups as described above. For a complete solution of the sub-Keplerian disks (C96) we need to provide (a) the mass of the black hole M , (b) the viscosity parameter α_{II} , (c) the cooling efficiency factor f , (d) the Comptonization factor F_{Compt} , (e) the net accretion rate of the flow \dot{m} , (f) the inner sonic point location x_{in} through which the flow must pass and finally, (g) the specific angular momentum λ_{in} at the inner sonic point.

The following table gives the cases we discuss in this paper. The Π -stress viscosity parameter α_{II} , the location of the inner sonic point x_{in} and the value of the specific angular momentum at that point λ_{in} are free parameters. The net accretion rate \dot{m} ,

the Comptonization factor F_{Compt} and the cooling efficiency f are related quantities (CT96, C97). For extremely inefficient cooling, $f \sim 1.0$, and for extremely efficient cooling $f = 0$ or even negative. The derived quantities, such as the value of maximum temperature T_9^{max} of the flow (in units of 10^9 K), density of matter (in cgs units) at T_9^{max} , x_K , the location from where the Keplerian disk on the equatorial plane becomes sub-Keplerian are also provided in the table. In the rightmost column, we present whether the inner edge of the disk is stable (S) or unstable (U) in the presence of the accretion flow. Three groups are separated as the parameters are clearly from three distinct regimes.

The basis of our three groupings are clear from the Table. Very low $\dot{m}/\alpha_{\text{II}}^2$ in Group B makes the cooling efficiency to be very small. Thus we choose a relatively large $f \sim 0.2-0.5$. It also makes the cooling due to Comptonization to be very low ($F_{\text{Compt}} \sim 0.1$). Thus the disks could be ultra-hot. Intermediate $\dot{m}/\alpha_{\text{II}}^2$ in Group A means that the efficiency of cooling is intermediate $f \sim 0.1$ and the Compton cooling of the sub-Keplerian region is average: $F_{\text{Compt}} \sim 0.03$. The sub-Keplerian disk in this case is neither too hot nor too cold. Extremely high $\dot{m}/\alpha_{\text{II}}^2$ causes a strong cooling in Group C. Thus, we choose $f = 0$, and a very efficient Compton cooling $F_{\text{Compt}} \sim 0.01-0.001$. As a result, the disk is also very cold. Now, we present our numerical results in these cases.

3.1. Nucleosynthesis in moderately hot flows

Case A.1: In this case, the termination of the Keplerian component in the weakly viscous flow takes place at $x = 1655.7$. The soft photons intercepted by the sub-Keplerian region reduce the temperature of this region but not by a large factor. The net accretion rate $\dot{m} = 1$ is the sum of (very low) Keplerian component and the sub-Keplerian component. Using computations of CT95 and C97 for $\dot{m}_K \sim 0.1$ and $\dot{m}_B \sim 0.9$, we find that the electron temperature T_e is around 60 keV $T_9 \sim 0.6$ (T_9 is the temperature in units of 10^9 K) and the ion temperature is around $T_9 = 2.5$. This fixes the Comptonization factor to about $F_{\text{Compt}} = 0.03$. This factor is used to reduce the temperature distribution of solutions of C96 (which does not explicitly use Comptonization) to temperature distribution with Comptonization. The ion temperature (in T_9) and density (in units of 10^{-10} gm cm $^{-3}$ to bring in the same plot) distribution computed in this manner are shown in Fig. 2a. Fig. 2b gives the velocity distribution (velocity is measured in units of 10^{10} cm sec $^{-1}$). Note the sudden rise in temperature and slowing down of matter close to the centrifugal barrier $x \sim 30$. Fig. 2c shows the changes in composition as matter is accreted onto the black hole. Only those species with abundance $Y_i \gtrsim 10^{-4}$ have been shown for clarity. Also, compositions closer to the black hole are shown, as variations farther out are negligible. Most of the burning of species takes place below $x = 10$. A significant amount of the neutrons (with a final abundance of $Y_n \sim 10^{-3}$) is produced by the photo-dissociation process. Note that closer to the black hole, ^{12}C , ^{16}O , ^{21}Mg and ^{28}Si are all destroyed completely, even though at around $x = 5$ or so, the abundance of

Table 1.

Model	M/M_{\odot}	γ	x_{in}	λ_{in}	αn	\dot{m}	t	F_{Compt}	x_K	T_9^{max}	ρ_{max}	S/U
A.1	10	4/3	2.7945	1.65	0.001	1	0.1	0.03	1655.7	5.7	6.2×10^{-7}	S
A.2	10	4/3	2.9115	1.6	0.07	1	0.1	0.03	401.0	4.7	4.9×10^{-7}	S
A.3	10^6	4/3	2.9115	1.6	0.07	1	0.1	0.03	401.0	4.7	4.9×10^{-12}	U
B.1	10	4/3	2.8695	1.6	0.05	0.01	0.5	0.1	481.4	16.5	3.9×10^{-9}	S
B.2	10	4/3	2.8695	1.6	0.05	4	0.5	0.1	481.4	16.5	1.6×10^{-8}	U
B.3	10	5/3	2.4	1.5	0.01	0.001	0.5	0.1	84.4	47	3.3×10^{-10}	S
B.4	10	4/3	2.795	1.65	0.2	0.01	0.2	0.1	8.4	13	1.1×10^{-8}	S
C.1	10	4/3	2.795	1.65	0.2	100	0.0	0.01	4.8	0.8	1.1×10^{-4}	S
C.2	10^6	4/3	2.795	1.65	10^{-4}	100	0.0	0.001	3657.9	0.2	6.2×10^{-10}	S

some of them went up first before going down. Among the new species which are formed closer to the black hole are ^{30}Si , ^{46}Ti , ^{50}Cr . The final abundance of ^{20}Ne is significantly higher than the initial value. This was not dissociated as the residence time in hotter region was insufficient. Thus a significant metallicity could be supplied by winds from the centrifugal barrier.

Fig. 2d shows the energy release and absorption due to exothermic and endothermic nuclear reactions (Q_{nuc}) that are taking place inside the disk (solid). Superposed on it are the energy generation rate Q^+ (long dashed curve) due to viscous process and the energy loss rate Q^- in the sub-Keplerian flows. For comparison, we also plot the hypothetical energy generation and loss rates (short dashed curves marked as Q_{Kep}^+ and Q_{Kep}^- respectively) if the disk had purely Keplerian angular momentum distribution even in the sub-Keplerian regime. All these quantities are in units of 3×10^6 and they represent height-integrated energy release rate ($\text{ergs cm}^{-2} \text{sec}^{-1}$). Note that these Q s are in logarithmic scale (if $Q < 0$, $-\log(|Q|)$ is plotted). As matter leaves the Keplerian flow, the proton capture (p, α) processes (such as $^{18}\text{O}(p, \alpha)^{15}\text{N}$, $^{15}\text{N}(p, \alpha)^{12}\text{C}$, $^6\text{Li}(p, \alpha)^3\text{He}$, $^7\text{Li}(p, \alpha)^4\text{He}$, $^{11}\text{B}(p, \gamma)^3\alpha$, $^{17}\text{O}(p, \alpha)^{14}\text{N}$, etc.) burn hydrogen and release energy to the disk. (Since the temperature of the disk is very high, PP chains or CNO cycles are not the dominant processes for the energy release.) At around $x = 40$, the deuterium starts burning ($D(\gamma, n)p$) and the endothermic reaction causes the nuclear energy release to become 'negative', i.e., a huge amount of energy is absorbed from the disk. At the completion of the deuterium burning (at around $x = 20$) the energy release tends to go back to the positive value to the level dictated by the original proton capture processes. Excessive temperature at around $x = 5$ breaks ^3He down into deuterium ($^3\text{He}(\gamma, p)D$, $D(\gamma, n)p$). Another major endothermic reaction which is dominant in this region is $^{17}\text{O}(\gamma, n)^{16}\text{O}$. These reactions absorb a significant amount of energy from the flow. Note that the nuclear energy release or absorption is of the same order as the energy release due to viscous process. This energy was incorporated in computing thermodynamic quantities following these steps:

- Compute thermodynamic quantities without nuclear energy
- Run nucleosynthesis code and compute Q_{nuc}
- Fit Q_{nuc} using piecewise analytical functions and include this into the definition of f ,

$$f = 1 - \frac{Q^-}{Q^+ + Q_{nuc}} \quad (1)$$

- Do sonic point analysis once more using this extra heating/cooling term and compute thermodynamic quantities.
- Repeat from step (b) till the results converge. In this case, there is virtually no difference in the solution and the solution appear to be completely stable under nucleosynthesis.

Case A.2: Here we choose the same net accretion rate, but with a larger viscosity. As a result, the Keplerian component moves closer. The Comptonization is still not very effective, and the flow is moderately hot as above with $F_{Compt} = 0.03$. The flow deviates from a very hot (sufficient to cause the flow to pass through the outer sonic point) Keplerian disk at $x_K = 401.0$, and after passing through an outer sonic point at $x = 50$, and through a shock at $x_S = 15$, the flow enters into the black hole through the inner sonic point at $x = 2.9115$. We show the results both for the shock-free branch (i.e., the one which passes through only the outer sonic point before plunging into the black hole, dotted curves) and the shocked branch of the solution (solid curves). Fig. 3a shows the comparison of the temperatures and densities (scaled in the same way as in Fig. 2a). The temperature and density jump sharply at the shock. Fig. 3b shows the comparison of the radial velocities. The velocity sharply drops at the shock. Both of these effects hasten the nuclear burning in the case which includes the shock. Fig. 3c shows the comparison of the abundances of only those species whose abundances reached a value of at least 10^{-4} . The difference between the shocked and the shock-free cases is that in the shock case similar burning takes place farther away from the black hole because of much higher temperature in the post-shock region.

The nature of the (height integrated) nuclear energy release is very similar to Case A.1 as the major reactions which take place inside the disk are basically same, except that the exact locations where any particular reactions take place are different since they are temperature sensitive. In Fig. 3d, we show all the energy release/absorption components for the shocked flow (solid curve). For comparison, we include the nuclear energy curve of the shock-free branch (very long dashed curve). Note that in the post-shock region, hotter and denser flow of the shocked-branch causes a particular nuclear reaction to take place farther away from a black hole when compared with the behaviour in the shock-free branch as is also reflected in the

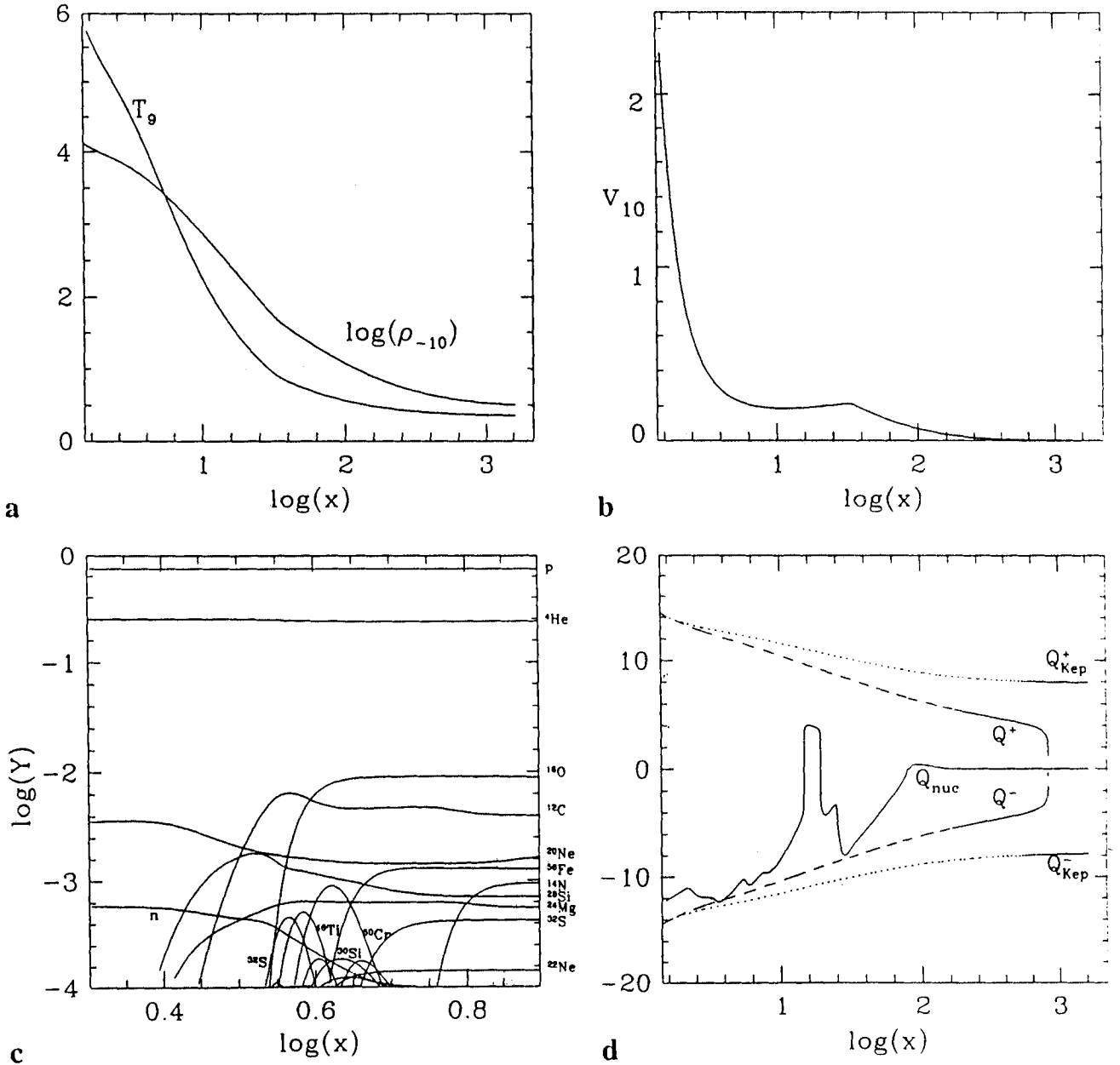


Fig. 2a–d. Variation of **a** ion temperature (T_9) and density (ρ_{-10}), **b** radial velocity v_{10} , **c** matter abundance Y_i in logarithmic scale and **d** various forms of height-integrated specific energy release and absorption rates (in $\text{ergs cm}^{-2} \text{sec}^{-1}$) when the model parameters are $M = 10M_\odot$, $\dot{m} = 1.0$, $\alpha_{\text{ff}} = 0.001$ as functions of logarithmic radial distance (x in units of Schwarzschild radius). Q is in logarithmic scale. See text and Table 1 for other parameters of Case A.1 which is considered here. The centrifugal barrier slows down and heats up matter where a significant change in abundance takes place ($\Delta Y_i \sim 10^{-3}$).

composition variation in Fig. 3c. The viscous energy generation (Q^+) and the loss of energy (Q^-) from the disk (long dashed) and shown. As before, these quantities, if the inner part had Keplerian distribution, are also plotted (short dashed). When big-bang abundance is chosen to be the initial abundance, the net composition does not change very much, but the dominating reactions themselves are somewhat different because the initial compositions are different. The dot-dashed

curve shows the energy release/absorption in the shocked flow when big-bang abundance is chosen. All these quantities are, as before, in units of 3×10^6 and they represent height-integrated energy release rate ($\text{ergs cm}^{-2} \text{sec}^{-1}$). For instance, in place of proton capture reactions for computations with solar abundance, the fusion of deuterium into ^4He plays a dominant role via the following reactions: $D(D, n)^3\text{He}$, $D(p, \gamma)^3\text{He}$, $D(D, p)^3\text{He}$, $^3\text{He}(D, p)^4\text{He}$. This is because no heavy elements

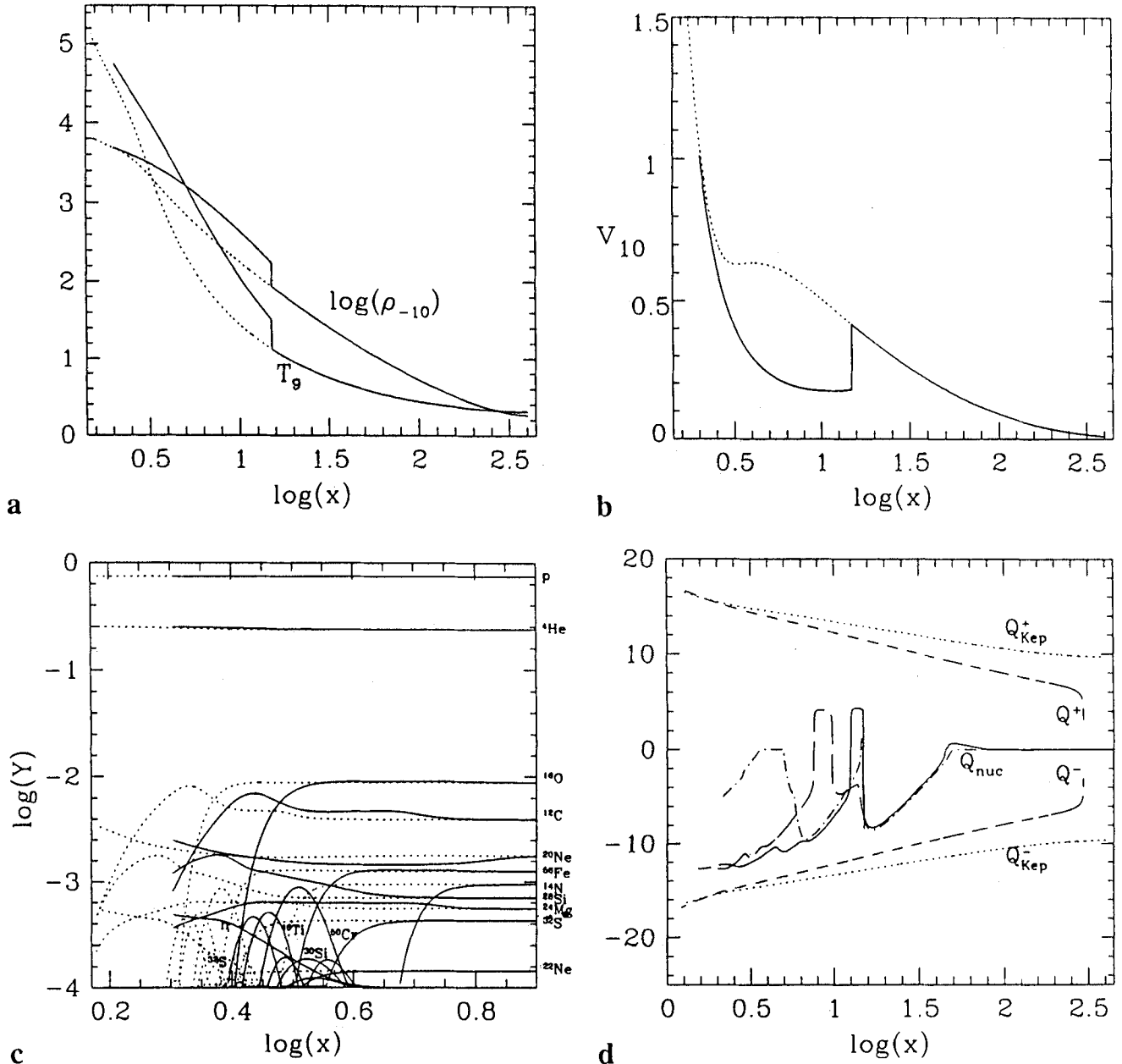


Fig. 3a–d. Variation of a ion temperature (T_9) and density (ρ_{-10}), b radial velocity v_{10} , c matter abundance Y , in logarithmic scale and d various forms of specific energy release and absorption rates when the model parameters are $M = 10M_{\odot}$, $\dot{m} = 1.0$, $\alpha_{\text{ff}} = 0.07$ as functions of logarithmic radial distance (x in units of Schwarzschild radius). See text and Table 1 for other parameters of Case A.2 which is considered here. Solutions in the stable branch with shocks are solid curves and those without the shock are dotted in (a–c). Curves in d are described in the text. At the shock temperature and density rise significantly and cause a significant change in abundance even farther out. Shock-induced winds may cause substantial contamination of the galactic composition when parameters are chosen from these regions.

were present to begin with and proton capture processes involving heavy elements such as were prevalent in the solar abundance case cannot take place here. Endothermic reactions at around $x = 20$ – 40 are dominated by deuterium dissociation as before. However, after the complete destruction of deuterium, the exothermic reaction is momentarily dominated by neutron capture processes (due to the same neutrons which are

produced earlier via $D(\gamma, n)p$) such as $^3\text{He}(n, p)\text{T}$ which produces the spike at around $x = 14.5$. Following this, ^3He and T are destroyed as in the solar abundance case (i.e., $^3\text{He}(\gamma, p)\text{D}$, $\text{D}(\gamma, n)p$, $\text{T}(\gamma, n)\text{D}$) and reaches the minimum in the energy release curve at around $x = 6$. The tendency of going back to the exothermic region is stopped due to the photo-dissociation of ^4He via $^4\text{He}(\gamma, p)\text{T}$ and $^4\text{He}(\gamma, n)^3\text{He}$. At the end of the

big-bang abundance calculation, a significant amount of neutrons are produced. The disk was found to be perfectly stable under nuclear reactions.

Case A.3: This case is exactly same as A.2 except that the mass of the black hole is chosen to be $10^6 M_\odot$. The temperature and velocity variations are similar to the above case. Because the accretion rate (in non-dimensional units) is the same, the density (which goes as \dot{m}/r^2v) is lower by a factor of 10^{-5} . Tenuous plasma should change its composition significantly only at higher temperatures than in the previous case. However, the increase in residence time by a factor of around 10^5 causes the nuclear burning to take place farther out even at a lower temperature. This is exactly what is seen. Fig. 4a shows the comparison (without including nuclear energy) of the composition of matter when the flow has a shock (solid curves) and when the flow is shock-free (dashed curve). We recall that the shock-free flow is in reality not stable. It is kept only for comparison purposes. Note that unlike earlier cases, a longer residence time also causes to burn all the ^{20}Ne that was generated from ^{16}O .

In Fig. 4b, we show a comparison of various height-integrated energy release and absorption curves as in Fig. 3d (in $\text{ergs cm}^{-2} \text{sec}^{-1}$). The nuclear energy remains negligibly small till around $x = 100$. After that the endothermic reactions dominate. This is due to the dissociation of D , ^3He and ^7Li and also of ^{12}C , ^{16}O , ^{20}Ne etc. all of which produce ^4He . The solid curve is for the branch with a shock and the very long dashed curve is for the shock-free branch. A small amount of neutrons are produced ($Y_n \sim 10^{-3}$) primarily due to the dissociation of D . These considerations are valid for solar abundance as the initial composition. In the case of big-bang abundance (dash-dotted curve), similar reactions take place but no elements heavier than ^7Li are involved. The three successive dips are due to dissociation of D , ^3He and ^4He respectively.

Below $x = 10$, $|Q_{\text{mic}}|$ is larger compared to Q^+ by 3–4 orders of magnitude. This is because of the superposition of a large number of photo-dissociation effects. We expect that in this case the disk would be unstable. This is exactly what we see. In Fig. 4c, we show the effects of nuclear reactions more clearly. The dotted curve and the solid curves are, as in Fig. 3b, the variation of velocity for the solution without and with shocks, respectively. The dot-dashed curve represents velocity variation without shock when nuclear reaction is included. The dashed curve is the corresponding solution when nucleosynthesis of the shocked branch is included. Both branches are unstable since the steady flow is subsonic at the inner edge. In these cases, the flow is expected to pass through the inner sonic point in a time-dependent manner and some sort of quasi-periodic oscillations cannot be ruled out.

3.2. Nucleosynthesis in hot flows

Case B.1: This case is chosen with such a set of parameters that a standing shock forms at $x_s = 13.9$. A very low accretion rate is chosen so that the Compton cooling is negligible and the flow remains very hot (Comptonization factor $F_{\text{Compt}} = 0.1$). We show the results both for the shock-free branch (dashed)

and the shocked branch (solid) of the solution. Fig. 5a shows the comparison of the temperatures and densities (in units of $10^{-20} \text{ gm cm}^{-3}$ to bring in the same plot). Fig. 5b shows the comparison of the radial velocities. This behaviour is similar to that shown in Case A.2. Because the temperature is suitable for photo-dissociation, we chose a very small set of species in the network (only 21 species up to ^{11}B are chosen). Fig. 5c shows the comparison of the abundances of proton (p), ^4He and neutron (n). In the absence of the shock, the breaking up of ^4He into n and p takes place much closer to the black hole, while the shock hastens it due to higher temperature and density. Although initially the flow starts with $Y_p = 0.7425$ and $^4\text{He} = 0.2380$, at the end of the simulation, only proton ($Y_p \sim 0.8786$) and neutron ($Y_n \sim 0.1214$) remain and the rest of the species become insignificant.

Fig. 5d shows the comparison of the height-integrated nuclear energy release (units are as Fig. 2d). As the flow leaves the Keplerian disk at $x_K = 481.4$, the deuterium and ^9Be are burnt instantaneously at the cost of some energy from the disk. At the end of deuterium burning at around $x = 200$, the np and proton capture processes (mainly via $^{11}\text{B}(p, \gamma)^{12}\text{C}$ which releases significant energy) and neutron capture ($^3\text{He}(n, p)^3\text{H}$) take place, but further in, ^3He (via $^3\text{He}(\gamma, p)^3\text{H}$) first and ^4He (mainly via $^4\text{He}(\gamma, n)^3\text{He}$ and $^4\text{He}(\gamma, p)^3\text{H}$, $T(\gamma, n)^3\text{H}$) subsequently, are rapidly dissociated. As soon as the entire helium is burnt out, the energy release becomes negligible. This is because there is nothing left other than free protons and neutrons and hence no more reactions take place and no energy is released or absorbed. The solid curve is for the branch with a shock and the very long dashed curve is for the shock-free branch. Inclusion of an opacity factor (which reduces photo-dissociation) shifts the burning towards the black hole. The disk is found to be completely stable even in presence of nucleosynthesis.

Case B.2: As discussed in Sect. 2, in extreme hard states, a black hole may accrete very little matter in the Keplerian component and very large amount of matter in the sub-Keplerian component. To simulate this we used B.1 parameters, but $\dot{m} = 4$. The resulting solution is found to be unstable when shocks are present. In Fig. 5b, we superimposed velocity variation without nuclear energy (same as with nuclear energy as far as Case B.1 is concerned) and with nuclear energy. The dash-dotted curve next to the un-shocked branch and dashed curve next to the shocked branch show the resulting deviation. While the branch without shock still remains stable, the other branch is distinctly unstable as the steady-state solution is sub-sonic at the inner edge. The only solution available must be non-steady with oscillations near the sonic point.

Case B.3: In this case, accretion rate is chosen to be even smaller ($\dot{m} = 0.001$) and the polytropic index is chosen to be $5/3$. The maximum temperature reaches $T_9^{\text{max}} = 47$. After leaving the Keplerian flow, the temperature and velocity of the flow monotonically increases. Because of excessive temperature, D and ^3He are photo-dissociated immediately after the flow leaves the Keplerian disk at $x_K = 84.4$. At around $x = 30$, all ^4He is photo-dissociated exactly as in Case B.1. Subsequently, the flow contains only protons and neutrons and there is no more energy

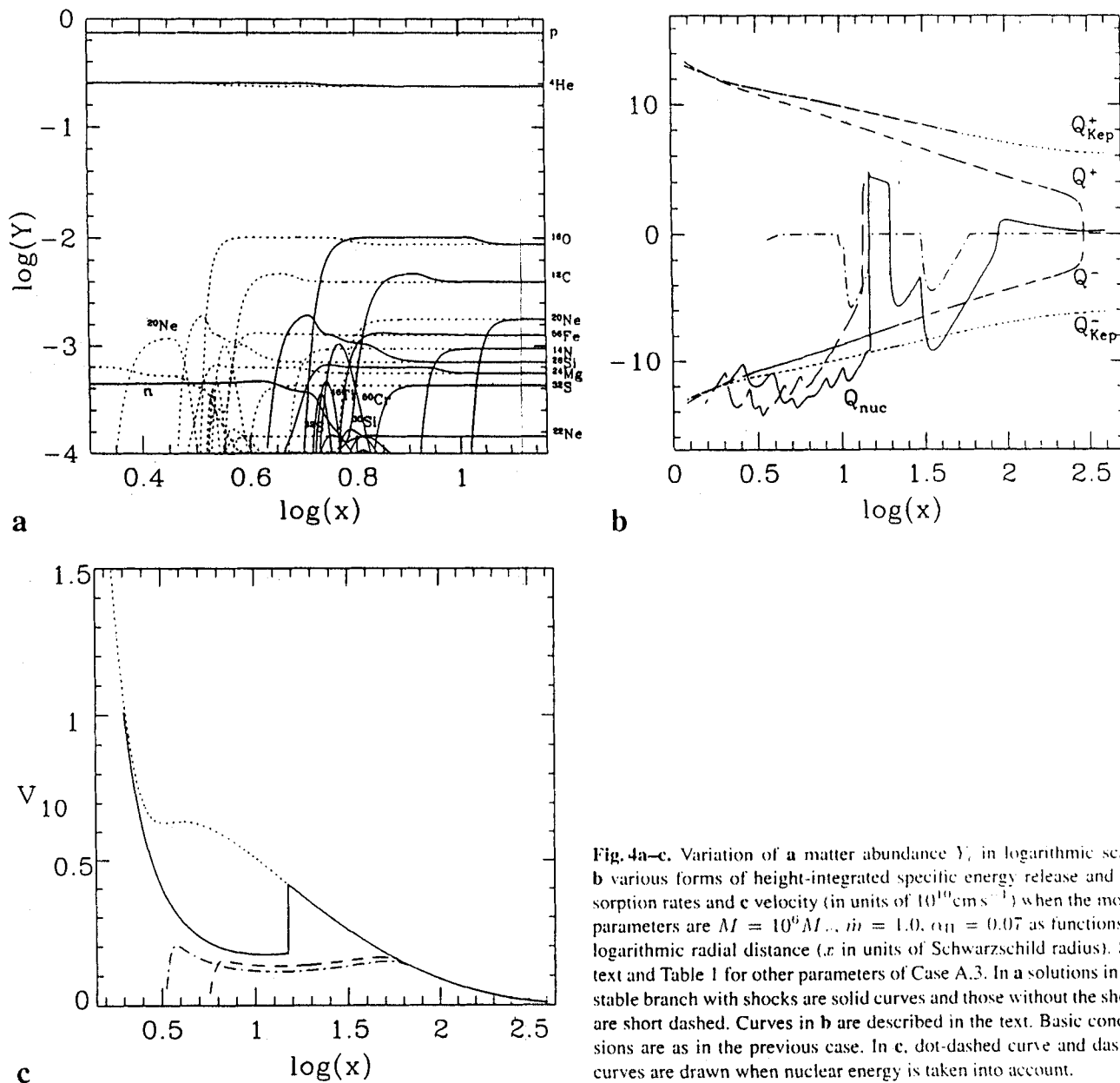


Fig. 4a–c. Variation of a matter abundance Y , in logarithmic scale, b various forms of height-integrated specific energy release and absorption rates and c velocity (in units of $10^{10} \text{ cm s}^{-1}$) when the model parameters are $M = 10^6 M_{\odot}$, $\dot{m} = 1.0$, $\alpha_{\text{H}} = 0.07$ as functions of logarithmic radial distance (x in units of Schwarzschild radius). See text and Table 1 for other parameters of Case A.3. In a solutions in the stable branch with shocks are solid curves and those without the shock are short dashed. Curves in b are as described in the text. Basic conclusions are as in the previous case. In c, dot-dashed curve and dashed curves are drawn when nuclear energy is taken into account.

release from the nuclear reactions. This behaviour is clearly seen in Fig. 6. The notations are the same as in the previous run. This ultra-hot case is found to be stable since the energy released took place far away from the black hole where the matter was moving slowly and therefore the rate (Q_{nuc}) was not high compared to that due to viscous dissipation (units are as Fig. 2d).

Case B.4: In this case, the net accretion rate is low ($\dot{m} = 0.01$) but viscosity is high and the efficiency of emission is intermediate ($f = 0.2$). That means that the temperature of the flow is high ($F_{\text{Compt}} = 0.1$, maximum temperature $T_{\text{p}}^{\text{max}} = 13$). Matter deviates from a Keplerian disk at around $x_K = 8.4$. Assuming that the high viscosity is due to stochastic magnetic

field, protons would be drifted towards the black hole due to magnetic viscosity, but the neutrons will not be drifted (Rees et al. 1982). They will generally circle around the black hole till they decay. This principle has been used to do the simulation in this case. The modified composition in one sweep is allowed to interact with freshly accreting matter with the understanding that the accumulated neutrons do not drift radially. After few iterations or sweeps the steady distribution of the composition is achieved. Fig. 7a shows the neutron distribution in the sub-Keplerian region. The formation of a 'neutron torus' is very apparent in this result. In fact, the formation of a neutron disk is very generic in all the hot, highly viscous accretion flows as also

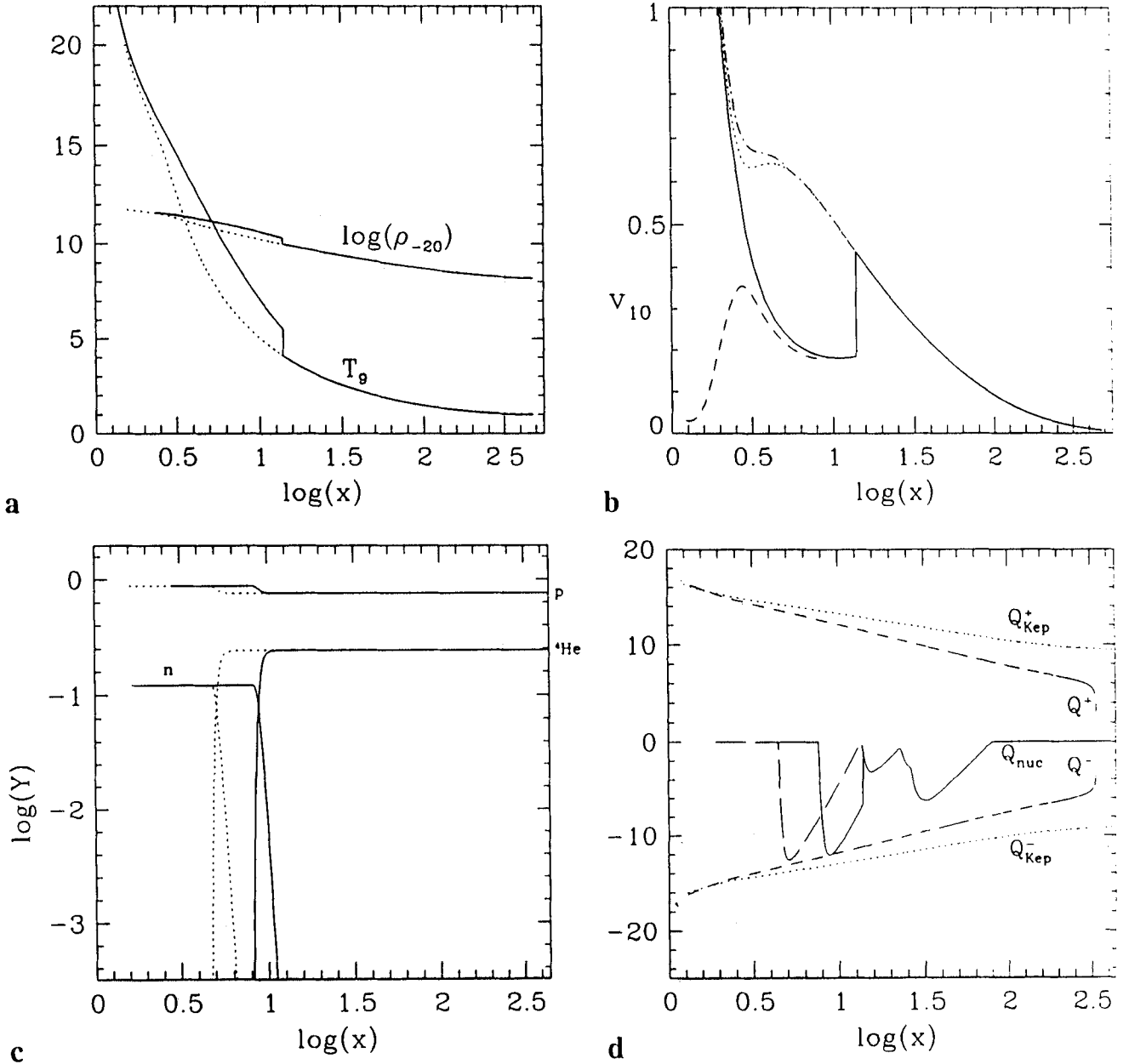


Fig. 5a–d. Variation of **a** ion temperature (T_9) and density (ρ_{-20}), **b** radial velocity v_{10} , **c** matter abundance Y , in logarithmic scale and **d** various forms of height-integrated specific energy release and absorption rates when the model parameters are $M = 10M_\odot$, $\dot{m} = 0.01$, $\alpha_{\text{H}} = 0.05$ as functions of logarithmic radial distance (x in units of Schwarzschild radius). See text and Table 1 for other parameters of Case B.1 which is considered here. Solutions in the stable branch with shocks are solid curves and those without the shock are short dashed in a–c. Curves in d are described in the text. The ultra-hot temperature of the flow photo-dissociates ${}^4\text{He}$ into protons and neutrons. The shocked branch (which is stable) causes such dissociation farther out from the black hole than the unstable shock-free branch. In b, dot-dashed curve and dashed curves are drawn when nuclear energy is taken into account and $\dot{m} = 1$ is chosen (Case B.2).

seen in Cases B.1–B.3 (for details, see, Paper 1). The nuclear reactions leading to the neutron torus formation are exactly same as previous cases and are not described here. However, we wish to present the energy release curve in Fig. 7b, only to impress the fact that the degree of absorption of nuclear energy from a

given annulus of the disk is generally correlated with the amount of neutrons deposited in that annulus. This is because no significant reactions other than photo-dissociation are taking place in the disk.

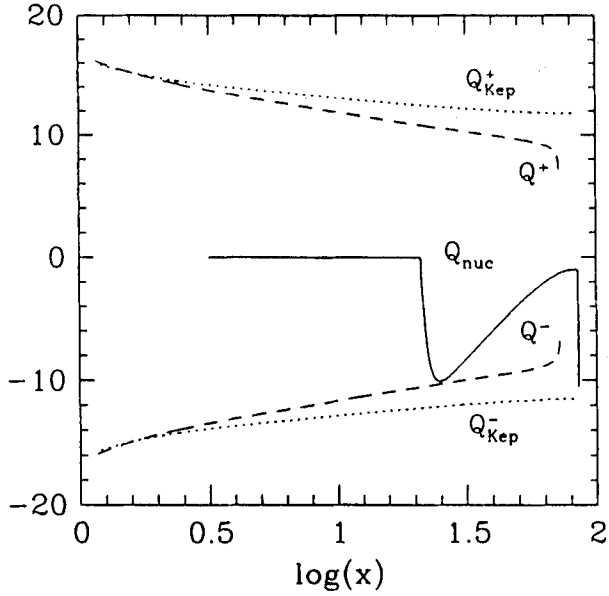
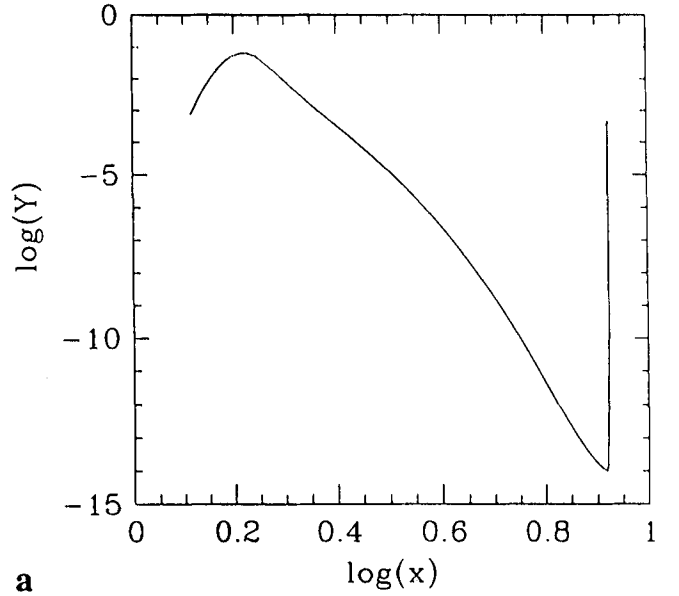


Fig. 6. Specific nuclear energy rate variation curve (solid) for a $\gamma = 5/3$, ultra-hot case ($T_9^{\max} = 44$) as functions of logarithmic radial distance (x in units of Schwarzschild radius). The entire initial abundance is photo-dissociated at $x \gtrsim 30$. The viscous energy generation curve (Q^+) and absorption curve (Q^-) [both long dashed] are presented for comparison. Q_{Kep}^{\pm} (dotted) curves are the specific energy generation and absorption rates provided the inner disks were Keplerian. Q s are in units of $\text{ergs cm}^{-2} \text{sec}^{-1}$. See Table 1 for parameters of Case B.3.

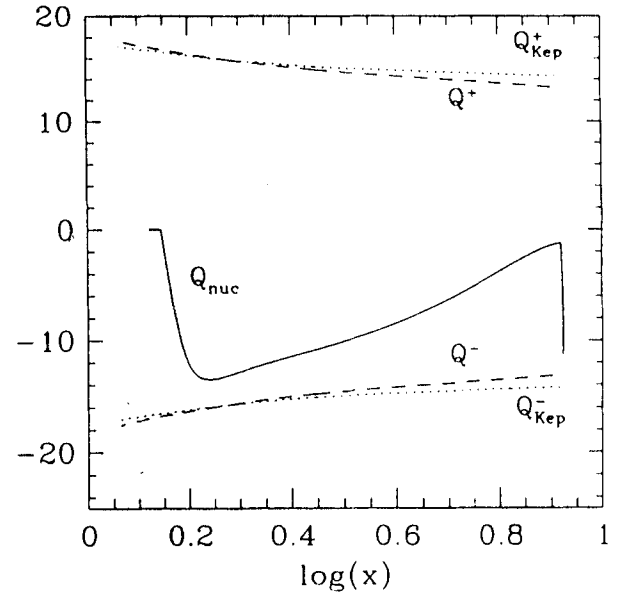
3.3. Nucleosynthesis in cooler flows

Case C.1: Here we choose a high-viscosity flow with a very high accretion rate. Matter deviates from the Keplerian disk very close to the black hole $x_K = 4.8$. The flow in the centrifugal barrier is cooler (temperature maximum $T_9^{\max} = 0.8$). Fig. 8a shows the variation of the temperature and density (in units of $10^{-5} \text{ gm cm}^{-3}$ to bring in the same plot) of the flow. Fig. 8b shows the velocity variation. Clearly, high viscosity removes the centrifugal barrier completely and matter falls in almost freely. Due to very short residence time, no significant change in the composition takes place. Only a small amount of proton capture (mainly due to $^{11}\text{B}(p, \gamma)^{12}\text{C}$, $^{16}\text{O}(p, \alpha)^{13}\text{N}$, $^{15}\text{N}(p, \alpha)^{12}\text{C}$, $^{18}\text{O}(p, \alpha)^{15}\text{N}$, $^{19}\text{F}(p, \alpha)^{16}\text{O}$) takes place. A small amount of deuterium dissociation also take place, but it does not change the energetics significantly. Fig. 8c shows the height-integrated energy release curves (units same as in Case A.1). Since the contribution due to nuclear reactions (Q_{nuc}) is very much smaller than the viscous energy release, the flow is not found to be unstable in this case.

Case C.2: This is a test case for the proto-galactic accretion flow. In the early phase of galaxy formation, the supply of matter is high, and the temperature of the flow is very low. The viscosity may or may not be very high, but we choose very low (presumably, radiative) viscosity ($\alpha = 10^{-4}$). The motivation is to use similar parameters as were used in JAC while studying the nucleosynthesis in thick accretion disks. The central mass



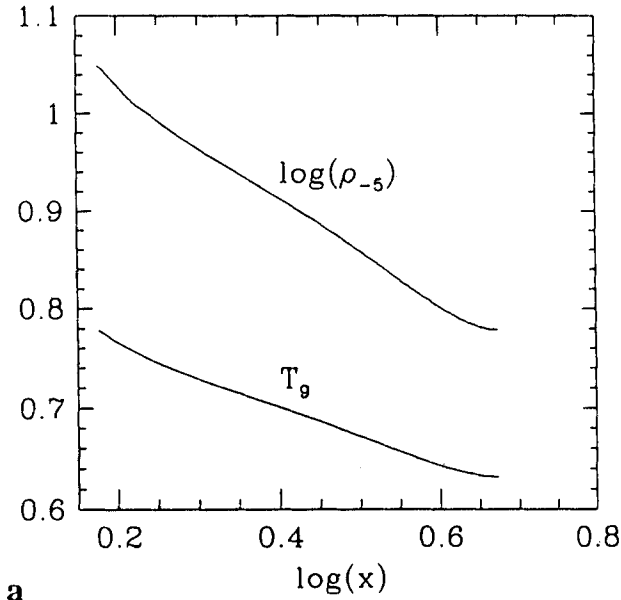
a



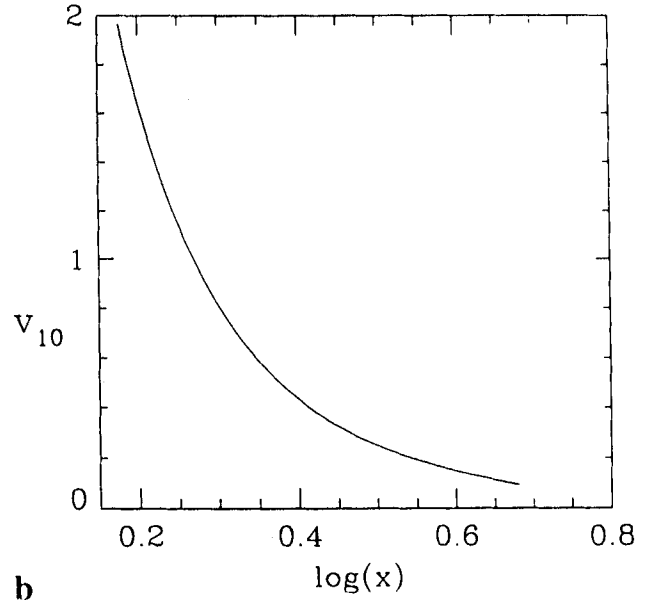
b

Fig. 7a and b. Formation of a neutron torus in a hot inflow. a Neutron abundance as a function of the logarithmic radial distance (x in units of Schwarzschild radius). b Various height-integrated specific energy release and absorption rates (units same as in Fig. 2d). Note the correlation of the neutron abundance with the degree of nuclear energy absorption. This is due to the endothermic nature of the photo-dissociation. See, Table 1 for parameters of Case B.4.

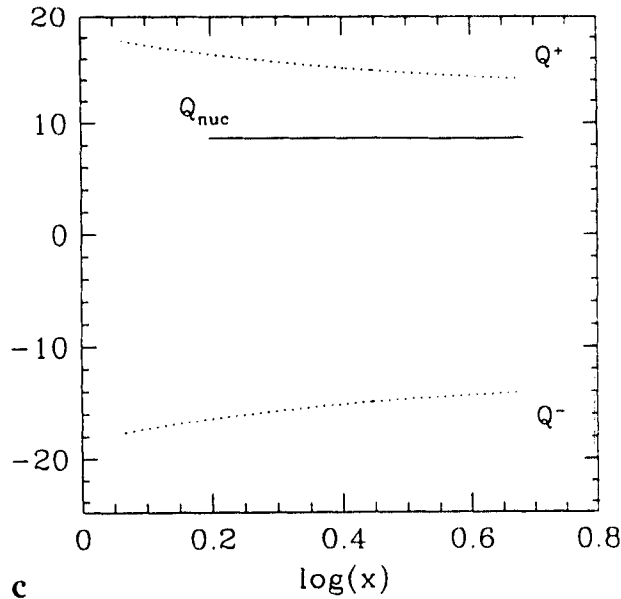
$M = 10^6 M_{\odot}$, the maximum temperature is $T_9^{\max} \sim 0.2$ and the Comptonization factor $F_{\text{Compt}} = 0.001$. The temperature variation is similar to Fig. 2a when scaled down by a factor of 30 (basically by the ratio of the F_{Compt} values). The velocity variation is similar to Fig. 2b and is not repeated here. Due to the low temperature, there is no significant change in the nuclear abundance. Note that since thick accretion disks are rotation



a



b



c

Fig. 8a–c. Variation of a ion temperature (T_9) and density (ρ_{-5}) b radial velocity v_{10} , and c various forms of specific energy release and absorption rates (units same as in Fig. 2d) when the model parameters are $M = 100M_\odot$, $\dot{m} = 10$, $\alpha_{11} = 0.2$ as functions of logarithmic radial distance (x in units of Schwarzschild radius). See text and Table 1 for other parameters of Case C.1. considered here. Not much nucleosynthesis takes place in this case.

dominated, the residence time was very long in CJA simulation and there was significant change in composition even at lower temperatures. But in this case the flow radial velocity is very high and the residence time is shorter. The nuclear energy release is negligible throughout and is not shown.

4. Nucleosynthesis induced instability

CJA, while studying nucleosynthesis in cooler, mainly rotating disks, suggested that as long as the nuclear energy release is smaller than the gravitational energy release, the disk would be stable. In the present paper, we find that this suggestion is still valid. Indeed, even when momentarily the nuclear energy release or absorption is as high as the gravitational energy re-

lease (through viscous dissipation), the disk may be stable. For instance, in case A.1 (Fig. 2d) at around $x = 4$ these rates are similar. Yet the velocity, temperature and density distributions (Fig. 2a,b) remain unchanged. In Case A.3, Q_{nuc} is several magnitudes greater than viscous energy release Q_- and the thermodynamic quantities are indeed disturbed to the extent that the flow with same injected quantities (with the same density and velocity and their gradients) at the outer edge does not become supersonic at the inner edge. In these cases, the flow must be unsteady in an effort to search for the 'right' sonic point to enter into the black hole. On the other hand, ultra-hot cases like B.2 show deviation in non-shocked solution while the shocked solution is unstable.

The general behaviour suggests that the present model of accretion disks is more stable under nuclear reactions compared to the earlier, predominantly rotating model. Here, the radial velocity (v) spreads energy release or absorption radially to a distance $v\tau_D(\rho, T) = vN_D/\dot{N}_D$ cm, where, N_D is the number density of, say, Deuterium and \dot{N}_D is its depletion rate. For a free fall, $v \sim x^{-1/2}$, while for most nuclear reactions, $\tau_D(\rho, T) \sim x^n$, with $n \gg 1$ (since reaction rates are strongly dependent on density and temperature). Thus, Q_{nuc} for the destruction of a given element spreads out farther away from the black hole, but steepens closer to it. Large dQ_{nuc}/dx causes instability since the derivatives such as dv/dx at the inner regions (including the sonic point) become imaginary.

5. Discussions and conclusions

In this paper, we have explored the possibility of nuclear reactions in inner accretion flows. Because of high radial motion and ion pressure, matter deviates from a Keplerian disk close to the black hole. The temperature in this region is controlled by the efficiencies of bremsstrahlung and Comptonization processes (CT96, C97) and possible heating by magnetic fields (Shapiro 1973): for a higher Keplerian rate and higher viscosity, the inner edge of the Keplerian component comes closer to the black hole and the sub-Keplerian region becomes cooler (CT95). The nucleosynthesis in this soft state of the black hole is quite negligible. However, as the viscosity is decreased to around 0.05 or less, the inner edge of the Keplerian component moves away and the Compton cooling becomes less efficient due to the paucity of the supply of soft photons. The sub-Keplerian region, though cooler by a factor of about $F_{Compt} = 0.01$ to 0.03 from that of the value obtained through purely hydrodynamical calculations of C96, is still high enough to cause significant nuclear reactions to modify compositions. The composition changes very close to the black hole, especially in the centrifugal-pressure-supported denser region, where matter is hotter and slower.

The degree of change in compositions which takes place in the Group A and B calculations, is very interesting and its importance must not be underestimated. Since the centrifugal-pressure-supported region can be treated as an effective surface of the black hole which may generate winds and outflows in the same way as the stellar surface (Chakrabarti 1998a,b; Das & Chakrabarti 1999), one could envisage that the winds produced in this region would carry away a modified composition and contaminate the atmosphere of the surrounding stars and the galaxy in general.

One could estimate the contamination of the galactic metallicity due to nuclear reactions. For instance, in Case A.1, ^{12}C , ^{16}O , ^{20}Ne , ^{30}Si , ^{44}Ca and ^{52}Cr are found to be over-abundant in some region of the disk. Assume that, on an average, all the N stellar black holes are of equal mass M and have a non-dimensional accretion rate of around $\dot{m} \sim 1$ ($\dot{m} = \dot{M}/\dot{M}_{Edd}$). Let ΔY_i (few times 10^{-3}) be the typical change in composition of this matter during the run and let f_w be the fraction of the incoming flow that goes out as winds and outflows (could be from ten percent to more than a hundred percent when disk evacua-

tion occurs), then in the lifetime of a galaxy (say, 10^{10} yrs), the total 'change' in abundance of a particular species deposited in the surroundings by all the stellar black holes is given by:

$$\langle \Delta Y_i \rangle_{\text{small}} \cong 10^{-7} \left(\frac{\dot{m}}{1} \right) \left(\frac{N}{10^6} \right) \left(\frac{\Delta Y_i}{10^{-3}} \right) \left(\frac{f_w}{0.1} \right) \left(\frac{M}{10M_{\odot}} \right) \left(\frac{T_{\text{gal}}}{10^{10}} \text{Yr} \right) \left(\frac{M_{\text{gal}}}{10^{11} M_{\odot}} \right)^{-1}. \quad (2)$$

The subscript 'small' is used here to represent the contribution from small black holes. We also assume a conservative estimate that there are 10^6 such stellar black holes in a galaxy, the mass of the host galaxy is around $10^{11} M_{\odot}$ and the lifetime of the galaxy during which such reactions are going on is about 10^{10} Yrs. We also assume that $\Delta Y_i \sim 10^{-3}$ and a fraction of ten percent of matter is blown off as winds. The resulting $\langle \Delta Y_i \rangle \sim 10^{-7}$ may not be very significant if one considers averaging over the whole galaxy. However, for a lighter galaxy ($M_{\text{gal}} = 10^9 M_{\odot}$), $\langle \Delta Y_i \rangle \sim 10^{-5}$. This would significantly change the average abundances of ^{30}Si , ^{44}Ca and ^{52}Cr . On the other hand, if one concentrates on the region of the outflows only, the change in abundance is the same as in the disk, and should be detectable (e.g., through line emissions). One such observation of stronger iron-line emission was reported for SS433 (Lamb et al. 1983; see also Arnould & Takahashi 1999, for a recent discussion on galactic contaminations).

When we consider a case like A.3, we find that ^{12}C , ^{16}O , ^{20}Ne , and ^{28}Si are increased by about 10^{-3} in some regions. In this case, the average change of abundance due to accretion onto the massive black hole situated at the galactic centre would be,

$$\langle \Delta Y_i \rangle_{\text{big}} \cong f_w \times 10^{-8} \left(\frac{\dot{m}}{1} \right) \left(\frac{\Delta Y_i}{10^{-3}} \right) \left(\frac{f_w}{0.1} \right) \left(\frac{M}{10^6 M_{\odot}} \right) \left(\frac{T_{\text{gal}}}{10^{10}} \text{Yr} \right) \left(\frac{M_{\text{gal}}}{10^{11} M_{\odot}} \right)^{-1}. \quad (3)$$

Here, we have put 'big' as the subscript to indicate the contribution from the massive black hole. Even for a lighter galaxy, e.g., of mass $M_{\text{gal}} = 10^9 M_{\odot}$, $\Delta Y_i = 10^{-6}$ which may not be significant. If one considers only the regions of outflows, contamination may not be negligible.

A few related questions have been asked lately: Can lithium be produced in black hole accretion? We believe not. The spallation reactions (Jin 1990; Yi & Narayan 1997) which may produce such elements assuming that a helium beam hits a helium target in a disk. Using a full network, rather than only He-He reaction, we find that the hotter disks where spallation would have been important also photo-dissociate (particularly due to the presence of photons from the Keplerian disk) helium to deuterium and then to protons and neutrons before any significant lithium could be produced. Even when photo-dissociation is very low (when the Keplerian disk is far away, for instance), or when late-type stellar composition is taken as the initial composition, we find that the ^7Li production is insignificant, particularly if one considers more massive black holes ($M \sim 10^5 M_{\odot}$).

Recently, it has been reported by several authors (Martin et al. 1992; 1994; Filippenko et al. 1995; Harlaftis et al. 1996)

that a high abundance of *Li* is observed in late type stars which are also companions of black hole and neutron star candidates. This is indeed surprising since the theory of stellar evolution predicts that these stars should have at least a factor of ten lower *Li* abundance. These workers have suggested that this excess *Li* could be produced in the hot accretion disks. However, in Paper I as well as in our Cases A and B computations we showed that *Li* is not likely to be produced in accretion disks. Indeed, we ran several cases with a mass fraction of He as high as 0.5 to 0.98, but we are still unable to produce *Li* with a mass fraction more than 10^{-10} . Recent work of Guessoum & Kazanas (1999) agrees with our conclusion that profuse neutrons would be produced in the disk. They further suggested that these energetic neutrons can produce adequate *Li* through spallation reactions with the *C*, *N*, and *O* that is present in the atmospheres of these stars. For instance, in Cases B.1 and B.3 we see that neutrons could have an abundance of ~ 0.1 in the disk. Since the production rate is similar to what Guessoum & Kazanas (1999) found, *Li* should also be produced on stellar surface at a similar rate.

What would be the neutrino flux on earth if nucleosynthesis does take place? The energy release by neutrinos (the pair neutrino process, the photoneutrino process and the plasma neutrino process) can be calculated using the prescription of Beaudet et al. (1967, hereafter BPS; see also Itoh et al. 1996) provided the pairs are in equilibrium with the radiation field. However, in the case of accretion disks, the situation is significantly different from that inside a star (where matter is in static equilibrium). Because of rapid infall, matter density is much lower and the infall time scale could be much shorter compared to the time-scale of various neutrino processes, especially the pair and photoneutrino processes. As a result, the pair density need not attain equilibrium. One important thing in this context is the opacity (τ_{pair}) of the pair process. Following treatments of Colpi et al. (1984) we find that $\tau_{\text{pair}} < 1$ for all our cases, and therefore pair process is expected to be negligible (for Case B.2, τ_{pair} is the highest [0.9]). Park (1990a,b), while studying pair creation processes in spherical accretion, shows that even in the most favourable condition, the ratio of positron (n_+) and ion (n_i) is no more than 0.05. A simple analysis suggests that neutrino production rate is many orders of magnitude smaller compared to what the equilibrium solutions of BPS and Itoh et al. would predict. Thus, we can safely ignore the neutrino luminosity.

When the nuclear energy release or absorption is comparable to the gravitational energy release through viscous processes, we find that the disk is still stable. Stability seems to depend on how steeply the energy is released or absorbed in the disk. This in turn depends on $\tau_D v$, the distance traversed inside the disk by the element contributing the highest change of energy before depleting significantly. Thus, an ultra-hot case (Group B) can be stable even though a hot (Group A) case can be unstable as we explicitly showed by including nuclear energy release. In these 'unstable' cases, we find that the steady flow does not satisfy the inner boundary condition and becomes subsonic close to the horizon. This implies that in these cases the flow must become non-steady, constantly searching for the supersonic branch to enter into the black hole. This can induce oscillations as have

been found elsewhere (Ryu et al. 1997). In such cases, one is required to do time dependent simulations (e.g., Molteni et al. 1994, 1996) to include nuclear reactions. This will be attempted in future.

Acknowledgements. We thank the referee for many helpful comments. This research is partially supported by DST grant under the project "Analytical and numerical studies of astrophysical flows around black holes and neutron stars" with SKC.

References

- Anders E., Ebihara M., 1982, *Geochim. Cosmochim. Acta* 46, 2363
 Arai K., Hashimoto M., 1992, *A&A* 254, 191
 Arnett W.D., Truran J., 1969, *ApJ* 157, 339
 Arnould M., Takahashi K., 1999, *Rep. Prog. Phys.* 62, 395
 Beaudet G., Petrosian V., Salpeter E.E., 1967, *ApJ* 150, 979 (BPS)
 Chakrabarti S.K., 1986, in *Accretion Processes in Astrophysics*, Audouze J., Tran Thanh Van, J., (eds.) Editions Frontières: Paris, p.155
 Chakrabarti S.K., 1990, *Theory of Transonic Astrophysical Flows*, Singapore: World Scientific
 Chakrabarti S.K., 1996, *ApJ* 464, 623 (C96)
 Chakrabarti S.K., 1997, *ApJ* 484, 313 (C97)
 Chakrabarti S.K., 1998a, *Ind. J. Phys.* 72(B), 183
 Chakrabarti S.K., 1998b, in: *Observational Evidence for Black Holes in the Universe*, Chakrabarti S.K. (ed.), Kluwer Academic Publishers, Dordrecht, p. 19
 Chakrabarti S.K., Molteni D., 1993, *ApJ* 417, 671
 Chakrabarti S.K., Molteni D., 1995, *MNRAS* 272, 80
 Chakrabarti S.K., Mukhopadhyay B., 1999, *A&A* 344, 105 (Paper 1)
 Chakrabarti S.K., Titarchuk L., 1995, *ApJ* 455, 623 (CT95)
 Chakrabarti S.K., Jin L., Arnett W.D., 1987, *ApJ* 313, 674 (CJA)
 Colpi M., Maraschi L., Treves A., 1984, *ApJ* 280, 319
 Das T.K. & Chakrabarti, S.K. 1999, *Class. Quantum Grav.* 16, 3879.
 Filippenko A.V., Matheson T., Barth A.J., 1995, *ApJ* 455, L139
 Fowler W.A., Caughlan G.R., Zimmerman B.A., 1975, *ARA&A* 13, 69
 Fuller G.M., Fowler W.A., Newmann M.J., 1980, *ApJS* 42, 447
 Fuller G.M., Fowler W.A., Newmann M.J., 1982, *ApJS* 48, 279
 Gillfanov M., Churazov E., Sunyaev R.A., 1997, in *Accretion Disks - New Aspects*, Meyer-Hofmeister E., Spruit H. (eds.), Springer (Heidelberg).
 Guessoum N., Kazanas D., 1999, *ApJ* 512, 332
 Harlatis E.T., Horne K., Filippenko, A.V., 1996, *PASP* 168, 762
 Harris M.J., Fowler W.A., Caughlan G.R., Zimmerman, B.A., 1983, *ARA&A* 21, 165
 Hashimoto M., Eriguchi Y., Arai K., Müller E., 1993, *A&A* 268, 131
 Hawley J.W., Smarr L.L., Wilson J.R., 1984, *ApJ* 277, 296
 Hawley J.F., Smarr L.L., Wilson J.R., 1985, *ApJS* 55, 211
 Itoh N., Hayashi H., Nishikawa A., Kohyama Y., 1996, *ApJS* 102, 411
 Jin L., 1990, *ApJ* 356, 501
 Jin L., Arnett W.D., Chakrabarti S.K., 1989, *ApJ* 336, 572 (JAC)
 Lamb R.C., Ling J.C., Mahoney W.A. et al., 1983, *Nat* 305, 37
 Lu J.F., Yuan F., 1997, *PASJ* 49, 525
 Lu J.F., Yu K.N., Yuan F., Young E.C.M., 1997, *A&A* 321, 665
 Martin E.L., Rebolo R., Casares J., Charles P.A., 1992, *Nat* 358, 129
 Martin E.L., Rebolo R., Casares J., Charles P.A., 1994, *ApJ* 791, 435
 Molteni D., Lanzafame G., Chakrabarti S.K., 1994, *ApJ* 425, 161
 Molteni D., Ryu D., Chakrabarti S.K., 1996, *ApJ* 470, 460
 Nobuta K., Hanawa T., 1994, *PASJ* 46, 257

- Park M., 1990a, *ApJ* 354, 64
Park M., 1990b, *ApJ* 354, 83
Rees M.J., 1984, *ARA&A* 22, 471
Rees M.J., Begelman M.C., Blandford R.D., Phinney E.S., 1982, *Nat* 295, 17
Ryu D., Brown J.G.L., Ostriker J.P., Loeb A., 1995, *ApJ* 452, 364
Ryu D., Chakrabarti S.K., Molteni D., 1997, *ApJ* 474, 378
Shakura N.I., Sunyaev R.A., 1973, *A&A* 24, 337
Shapiro S.L., 1973, *ApJ* 180, 531
Shvartsman V.F., 1971, *Sov. Astron. A.J.* 15, 377
Sponholz H., Molteni D., 1994, *MNRAS* 271, 233
Thelemann F.-K., 1980, Ph.D. Thesis, Max-Planck-Institut, Munich and Technische Hochschule, Darmstadt
Wagoner R., Fowler W.A., Hoyle F., 1967, *ApJ* 148, 3
Wallace R.K., Woosley S.E., 1981, *ApJS* 231, 26
Woosley S.E., Arnett W.D., Clayton D.D., 1973, *ApJS* 231, 26
Yang R., Kafatos M., 1995, *A&A* 295, 238
Yi I., Narayan R., 1997, *ApJ* 486, 38
Zhang S.N., Ebisawa K., Sunyaev R., et al., 1997, *ApJ* 479, 381

Behaviour of a spin- $\frac{1}{2}$ particle around a charged black hole

Banibrata Mukhopadhyay

Theoretical Astrophysics Group, S N Bose National Centre For Basic Sciences, JD Block,
Salt Lake, Sector-III, Calcutta 700091, India

E-mail: bm@bosc.nbose.res.in

Received 20 January 2000

Abstract. The Dirac equation is separable in curved spacetime and its solution has been found for both spherically and axially symmetric geometry. However, most work on this subject has been done without considering the charge of the black hole. Here we consider the spherically symmetric charged black-hole background, namely the Reissner–Nordström black hole. Due to the presence of the charge of the black-hole, charge–charge interaction will be important for the case of an incoming charged particle (e.g. an electron, proton, etc). Therefore, both gravitational and electromagnetic gauge fields should be introduced. Naturally the behaviour of the particle will be changed from that in the Schwarzschild geometry. We compare both the solutions. In the case of a Reissner–Nordström black hole there is a possibility of super-radiance unlike in the Schwarzschild case. We also check this branch of the solution.

PACS numbers: 04.20, 04.70, 04.70D, 95.30S

1. Introduction

Chandrasekhar separated the Dirac equation in the Kerr geometry into radial and angular parts [1] in 1976. His separation method can be extended to the Schwarzschild geometry and corresponding separated equations can be found. However, he did not consider the charge of the black hole. If we consider the black hole to be charged then electromagnetic interaction is important for an incoming particle with charge. To study the behaviour of a spin- $\frac{1}{2}$ particle, the Dirac wave is treated as a perturbation in spacetime which is asymptotically flat [1]. Far away from the black hole its influence on the particle is not significant. As it comes closer, it feels the curvature of the spacetime and the corresponding behaviour start to change with respect to that of flat space. Particle behaviour around a black hole without charge has been studied in the past by several authors [1–6]. In this paper, we will introduce charge in the black hole. Here, we study a simpler problem to gain insight into the solution when the black hole is non-rotating but charged. We have to solve the Dirac equation in an electromagnetic field around a Reissner–Nordström black hole. Thus we will study the particle in *crossed* electromagnetic and gravitational fields. It is very clear that the potential felt by the incoming Dirac wave will be different from that for the Schwarzschild black hole [5]. For an incoming uncharged particle such as a neutron, the electromagnetic field does not play a part and the Dirac equation will be reduced to being the same as in the Schwarzschild case except for the redefinition of the horizon. For a charged incoming particle such as an electron, proton, etc, an electromagnetic gauge field should be introduced. One can also study the neutrino wave whose behaviour is known for the Kerr geometry [7]. In the next section, we present the basic

Dirac equations and separate them in this crossed field. In section 3, we study the behaviour of the potential and the possibility of super radiance. In section 4, we present a complete solution. Finally, in section 5, we draw our conclusions.

2. Dirac equation and its separation

By introducing an electromagnetic interaction and gravitational effect the covariant derivatives take the form as

$$D_\mu = \partial_\mu + iq_1 A_\mu + q_2 \Gamma_\mu^{\dot{}}. \quad (1)$$

The derivative of the spinor P^A can be written as

$$D_\mu P^A = \partial_\mu P^A + iq_1 A_\mu P^A + q_2 \Gamma_{\mu\nu}^A P^\nu, \quad (2)$$

where q_1 and q_2 are coupling constants. q_1 is the charge of the incoming particle (say $q_1 = q$) and q_2 is chosen throughout as 1. A_μ and $\Gamma_{\mu\nu}^A$ are the electromagnetic and gravitational gauge (spin coefficients) fields, respectively. Thus, following [7] the Dirac equation in the Newman–Penrose formalism can be written as

$$\sigma_{\Lambda B'}^\mu D_\mu P^A + i\mu_p \bar{Q}^{C'} \epsilon_{C'B'} = 0, \quad (3a)$$

$$\sigma_{\Lambda B'}^\mu D_\mu Q^A + i\mu_p \bar{P}^{C'} \epsilon_{C'B'} = 0, \quad (3b)$$

where, for any vector X_i , according to the spinor formalism [7] $\sigma_{\Lambda B'}^i X_i = X_{\Lambda B'}$; $\Lambda, B' = 0, 1$. Here, we introduce a null tetrad $(\bar{l}, \bar{n}, \bar{m}, \bar{\bar{m}})$ to satisfy orthogonality relations, $\bar{l} \cdot \bar{n} = 1$, $\bar{m} \cdot \bar{\bar{m}} = -1$ and $\bar{l} \cdot \bar{m} = \bar{n} \cdot \bar{\bar{m}} = \bar{l} \cdot \bar{\bar{m}} = \bar{n} \cdot \bar{m} = 0$ following Newman and Penrose [8]. $2^{1/2}\mu_p$ is the mass of the Dirac particle. In terms of this new basis in the Newman–Penrose formalism Pauli matrices can be written as

$$\sigma_{\Lambda B'}^\mu = \frac{1}{\sqrt{2}} \begin{pmatrix} l^\mu & m^\mu \\ \bar{m}^\mu & n^\mu \end{pmatrix}. \quad (4)$$

Using equations (2), (3a), (4) and choosing $B = 0$ and subsequently $B = 1$ we obtain

$$l^\mu (\partial_\mu + iq A_\mu) P^0 + \bar{m}^\mu (\partial_\mu + iq A_\mu) P^1 + (\Gamma_{1000} - \Gamma_{0010'}) P^0 + (\Gamma_{1100} - \Gamma_{0110'}) P^1 - i\mu_p \bar{Q}^{1'} = 0, \quad (5a)$$

$$m^\mu (\partial_\mu + iq A_\mu) P^0 + n^\mu (\partial_\mu + iq A_\mu) P^1 + (\Gamma_{1001} - \Gamma_{0011'}) P^0 + (\Gamma_{1101} - \Gamma_{0111'}) P^1 + i\mu_p \bar{Q}^{0'} = 0. \quad (5b)$$

Next, by taking complex conjugation of equation (3b), writing various spin coefficients using their named symbol [7] and choosing

$$P^0 = F_1, \quad P^1 = F_2, \quad \bar{Q}^{1'} = G_1, \quad \bar{Q}^{0'} = -G_2$$

we obtain

$$l^\mu (\partial_\mu + iq A_\mu) F_1 + \bar{m}^\mu (\partial_\mu + iq A_\mu) F_2 + (\epsilon - \rho) F_1 + (\pi - \alpha) F_2 = i\mu_p G_1, \quad (6a)$$

$$m^\mu (\partial_\mu + iq A_\mu) F_1 + n^\mu (\partial_\mu + iq A_\mu) F_2 + (\mu - \gamma) F_2 + (\beta - \tau) F_1 = i\mu_p G_2, \quad (6b)$$

$$l^\mu (\partial_\mu + iq A_\mu) G_2 - m^\mu (\partial_\mu + iq A_\mu) G_1 + (\epsilon^* - \rho^*) G_2 - (\pi^* - \alpha^*) G_1 = i\mu_p F_2, \quad (6c)$$

$$n^\mu (\partial_\mu + iq A_\mu) G_1 - \bar{m}^\mu (\partial_\mu + iq A_\mu) G_2 + (\mu^* - \gamma^*) G_1 - (\beta^* - \tau^*) G_2 = i\mu_p F_1. \quad (6d)$$

These are the Dirac equations in the Newman-Penrose formalism in curved spacetime in the presence of an electromagnetic interaction.

Now we write the basis vectors of the null tetrad in terms of elements of the Reissner-Nordström geometry [7, 9] as

$$l^\mu = \frac{1}{\Delta}(r^2, \Delta, 0, 0), \quad (7a)$$

$$n^\mu = \frac{1}{2r^2}(r^2, -\Delta, 0, 0), \quad (7b)$$

$$m^\mu = \frac{1}{r\sqrt{2}}(0, 0, 1, i \operatorname{cosec} \theta), \quad (7c)$$

$$\bar{m}^\mu = \frac{1}{r\sqrt{2}}(0, 0, 1, -i \operatorname{cosec} \theta), \quad (7d)$$

where $\Delta = r^2 - 2Mr + Q_*^2$ and $G = \hbar = c = 1$ are chosen. Here M is the mass of the black hole, Q_* is the charge of the black hole, G is the gravitational constant, \hbar is Planck's constant and c is the speed of light.

We consider the spin- $\frac{1}{2}$ wavefunction as the form of $e^{i(\sigma t + m\phi)} f(r, \theta)$ where σ is the frequency of the incoming wave and m is the azimuthal quantum number. The temporal and azimuthal dependences are chosen to be the same but radial and polar dependences are chosen differently for different spinors. Thus we write

$$\begin{aligned} f_1 &= e^{i(\sigma t + m\phi)} r F_1, & f_2 &= e^{i(\sigma t + m\phi)} F_2, \\ g_1 &= e^{i(\sigma t + m\phi)} G_1, & g_2 &= e^{i(\sigma t + m\phi)} r G_2. \end{aligned} \quad (8)$$

Now we strictly consider the static field so the magnetic potentials are chosen to be zero, i.e. $A^\mu = (A', 0, 0, 0)$. A' is nothing but the corresponding scalar potential of the field as (in this spherically symmetric spacetime)

$$A' = \frac{q Q_*}{r - r_+}, \quad (9)$$

where $r_+ = \text{location of the horizon} = M + \sqrt{M^2 - Q_*^2}$.

So using equations (7)–(9) and writing various spin coefficients in terms of the Reissner-Nordström metric elements (actually in terms of basis vectors) [7] equation (6) reduces to

$$\mathcal{D}_0 f_1 + 2^{-1/2} \mathcal{L}_{1/2} f_2 = i\mu_{\rho r} g_1 \quad (10a)$$

$$\Delta \mathcal{D}_{1/2}^\dagger f_2 - 2^{1/2} \mathcal{L}_{1/2}^\dagger f_1 = -2i\mu_{\rho r} g_2 \quad (10b)$$

$$\mathcal{D}_0 g_2 - 2^{-1/2} \mathcal{L}_{1/2}^\dagger g_1 = i\mu_{\rho r} f_2 \quad (10c)$$

$$\Delta \mathcal{D}_{1/2}^\dagger g_1 + 2^{1/2} \mathcal{L}_{1/2} g_2 = -2i\mu_{\rho r} f_1 \quad (10d)$$

where

$$\begin{aligned} \mathcal{D}_n &= \frac{d}{dr} + \frac{ir^2\sigma}{\Delta} + \frac{iqQ_*r^2}{\Delta(r-r_+)} + 2n \frac{r-M}{\Delta}, \\ \mathcal{D}_n^\dagger &= \frac{d}{dr} - \frac{ir^2\sigma}{\Delta} - \frac{iqQ_*r^2}{\Delta(r-r_+)} + 2n \frac{r-M}{\Delta}. \end{aligned} \quad (11)$$

$$\begin{aligned}\mathcal{L}_n &= \frac{d}{d\theta} + Q + n \cot \theta, \\ \mathcal{L}_n^\dagger &= \frac{d}{d\theta} - Q + n \cot \theta, \\ Q &= m \operatorname{cosec} \theta.\end{aligned}\tag{12}$$

Now considering $f_1(r, \theta) = R_{-1/2}(r)S_{-1/2}(\theta)$, $f_2(r, \theta) = R_{1/2}(r)S_{1/2}(\theta)$, $g_1(r, \theta) = R_{1/2}(r)S_{-1/2}(\theta)$, $g_2(r, \theta) = R_{-1/2}(r)S_{+1/2}(\theta)$ and following Chandrasekhar [7] we can separate the Dirac equation into radial and angular parts as

$$\Delta^{1/2} \mathcal{D}_0 R_{-1/2} = (\lambda + im_p r) \Delta^{1/2} R_{1/2},\tag{13a}$$

$$\Delta^{1/2} \mathcal{D}_0^\dagger \Delta^{1/2} R_{1/2} = (\lambda - im_p r) R_{-1/2},\tag{13b}$$

$$\mathcal{L}_{1/2} S_{1/2} = -\lambda S_{-1/2},\tag{14a}$$

$$\mathcal{L}_{1/2}^\dagger S_{-1/2} = \lambda S_{1/2}.\tag{14b}$$

Here m_p is the normalized rest mass of the incoming particle and λ is the separation constant.

3. Nature of the potential in a decoupled system

Equations (14a) and (14b) are the same as the angular equation in the Schwarzschild geometry whose solution is given in [2, 10, 11] as

$$\lambda^2 = \left(l + \frac{1}{2}\right)^2, \quad R_{\pm 1/2} = \text{standard spherical harmonics} = {}_{\pm 1/2} Y_m^l(\theta).\tag{15}$$

It is clear that the separation constant depends on the orbital angular momentum quantum number l .

Equations (13a) and (13b) are in coupled form. Following Chandrasekhar's [7] and Mukhopadhyay and Chakrabarti's [5] approach we can decouple it as

$$\left(\frac{d^2}{d\hat{r}_*^2} + \sigma^2\right) Z_\pm = V_\pm Z_\pm,\tag{16}$$

where

$$\begin{aligned}\hat{r}_* &= r_* + \frac{1}{2\sigma} \tan^{-1} \frac{m_p r}{\lambda} + \frac{q Q_*}{\sigma} \left[\log(r - r_-) + \left\{ \frac{2r_+}{r_+ - r_-} - \frac{r_+^2}{(r_+ - r_-)^2} \right\} \log\left(\frac{r - r_+}{r - r_-}\right) \right. \\ &\quad \left. - \frac{r_+^2}{(r - r_-)(r - r_+)} \right],\end{aligned}\tag{17}$$

$$r_* = r - 3M + \frac{r_+^2}{r_+ - r_-} \log(r - r_+) - \frac{r_-^2}{r_+ - r_-} \log(r - r_-),\tag{18}$$

$$r_\pm = M \pm \sqrt{M^2 - Q_*^2}, \quad Z_\pm = \Delta^{1/2} R_{1/2} e^{i\Theta/2} \pm R_{-1/2} e^{-i\Theta/2}, \quad \Theta = m_p r / \lambda.\tag{19}$$

In the extreme case when $M = Q^*$, the expression for \hat{r}_* and r_* are given as

$$\hat{r}_* = r_* + \frac{1}{2\sigma} \tan^{-1} \frac{m_p r}{\lambda} + \frac{q Q_*}{\sigma} \left[\log(r - M) - \frac{2M^2}{(r - M)^2} - \frac{2M}{r - M} \right],\tag{17'}$$

$$r_* = r - M + 2M \log(r - M) - \frac{M^2}{r - M}.\tag{18'}$$

Here, \hat{r}_* varies from $-\infty$ to $+\infty$ (Cartesian coordinate). If we compare equation (16) with the one-dimensional Schrödinger equation in a Cartesian coordinate system, the energy E of the incoming particle can be written as $E \propto \sigma^2$ and the potential (V_{\pm}) felt by the particle is given as

$$\begin{aligned}
 V_{\pm} = & \frac{\Delta(\lambda^2 + m_p^2 r^2)^3}{\left[r^2(\lambda^2 + m_p^2 r^2) (1 + Q_* q / (r - r_*) \sigma) + \Delta \lambda m_p / 2\sigma \right]^2} \\
 & \pm \frac{\Delta(\lambda^2 + m_p^2 r^2)}{\left[r^2(\lambda^2 + m_p^2 r^2) (1 + Q_* q / (r - r_*) \sigma) + \Delta \lambda m_p / 2\sigma \right]^3} \\
 & \times \left[\left\{ r^2(\lambda^2 + m_p^2 r^2) \left(1 + \frac{Q_* q}{(r - r_*) \sigma} \right) + \frac{\Delta \lambda m_p}{2\sigma} \right\} \right. \\
 & \times \frac{(\lambda^2 + m_p^2 r^2)^{1/2}}{\Delta^{1/2}} \{ (r - M)(\lambda^2 + m_p^2 r^2) + 3\Delta r m_p^2 \} - \Delta^{1/2} (\lambda^2 + m_p^2 r^2)^{3/2} \\
 & \times \left[2r(\lambda^2 + m_p^2 r^2) \left(1 + \frac{Q_* q}{(r - r_*) \sigma} \right) + 2r^3 m_p^2 \left(1 + \frac{Q_* q}{(r - r_*) \sigma} \right) \right. \\
 & \left. \left. - r^2(\lambda^2 + m_p^2 r^2) \frac{Q_* q}{(r - r_*)^2 \sigma} + \frac{(r - M)\lambda m_p}{\sigma} \right] \right]. \quad (20)
 \end{aligned}$$

From the expression of V_{\pm} it is very clear that the potential depends strictly on the charge of the particle as well as of the black hole. More precisely, it depends on the Coulomb interaction between the charge of the black hole and the incoming particle. When the charge of the black hole or particle, or both, are chosen to be zero the potential reduces to being the same as in the Schwarzschild geometry [5]. When the factor $Q_* q / \sigma$ is positive, the potential varies smoothly. When $Q_* q / \sigma$ becomes negative, V_{\pm} diverges at a certain location $r = \alpha$. For the second case, the factor $(1 + Q_* q / (r - r_*) \sigma)$ vanishes at $r = r_* - Q_* q / \sigma > r_*$ and then becomes negative. At $r = \alpha > r_*$ the denominator of V_{\pm} vanishes. For all other cases $\alpha < r_*$ always, so there is no scope to diverge the potential. Thus for the positive energy solution when the electromagnetic scalar potential in the field is of an attractive nature, the corresponding potential diverges, again for the negative energy solution the potential diverges for the repulsive electromagnetic scalar potential. For the integral spin particle, it is found that when the potential diverges energy extraction is possible, i.e. super-radiation occurs in the spacetime [7]. On the other hand, for the case of a spin- $\frac{1}{2}$ particle in the Kerr geometry, although at a certain parameter region the potential diverges, super-radiation does not exist [7]. In the case of a spherically symmetric Schwarzschild geometry the potential does not diverge at all and there is no scope for super-radiation [5]. Here it is interesting to note that although our spacetime is spherically symmetric, due to the presence of the electromagnetic interaction term a region exists which is expected to be super-radiant.

Figure 1 shows the behaviour of the potential V_+ for different values of black-hole charge, where $\sigma = 0.8$, $m_p = 0.8$, $l = \frac{1}{2}$, $q = 1$ are chosen; $\alpha < r_*$. When $Q_* = 0$ (solid curve), the potential reduces to being the same as in the Schwarzschild case shown in figure 2 by Mukhopadhyay and Chakrabarti [5]. It is also seen that with increasing black-hole charge, the barrier height decreases. An increase of the black-hole charge indicates an increase of the electromagnetic coupling and a corresponding repulsive scalar potential opposes the attractive gravitational field. So the net effect decreases. Figure 2 shows the change of potential barrier for different values of particle charge, where $\sigma = 0.8$, $m_p = 0.8$, $l = \frac{1}{2}$, $Q_* = 0.6$ are chosen; $\alpha < r_*$. The solid curve indicates the potential felt by a neutron-like particle.

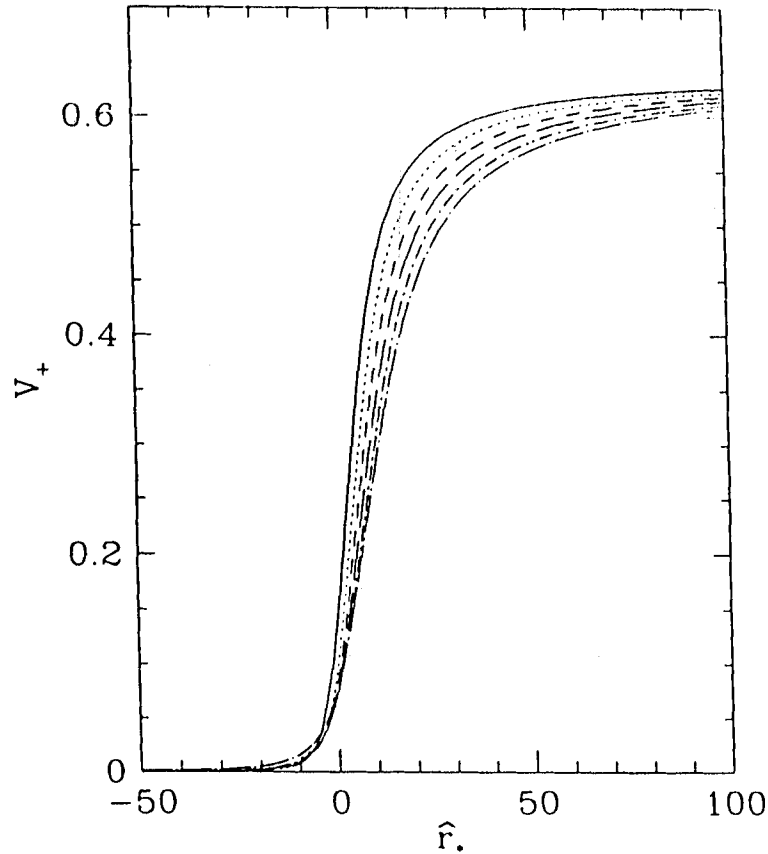


Figure 1. Behaviour of the potential for different values of the black-hole charge. The fixed parameters are: $\sigma = 0.8$, $m_p = 0.8$, $l = \frac{1}{2}$ and $q = 1$. From the upper to the lower curves the charge Q_* of the black hole is chosen as 0, 0.2, 0.4, 0.6, 0.8, 0.998.

Now we come to the case when Q_*q/σ is negative. For these cases the $\hat{r}_* - r$ relation is multivalued. For both $r \rightarrow \infty$ and $r \rightarrow r_+$, $\hat{r}_* \rightarrow \infty$. As explained above the net potential barrier diverges at a certain location in this parameter region. From equation (20) it is very clear that near $r = \alpha$, the potential varies as $1/(r - \alpha)^3$. So it has two branches, one repulsive and one attractive on either side of the singular point. As a result super-radiation is absent for the case of Reissner–Nordström geometry as in other cases [5, 7]. We can choose any combination of Q_* , q and σ in such a way that Q_*q/σ is negative.

In figure 3 we show how the nature of the potential (V_+) changes with the rest mass of the incoming particle where $\sigma = 0.8$, $Q_* = 0.5$, $l = \frac{1}{2}$, $q = 1$ are chosen. The solid curve shows the nature of the neutrino wave. It is very clear from the figure that with the increase of rest mass of the incoming particle the gravitational interaction increases and the corresponding potential barrier attains a high value.

4. The complete solution

Now we will find the spatially complete solution. As mentioned earlier a solution of the angular part is known which is the same as in the Schwarzschild case [5, 10, 11]. For the radial solution we need to solve a decoupled radial equation. The solution of equation (16) for the potential V_+ and V_- , using the instantaneous WKB approximation (IWKB) method [5, 6], can

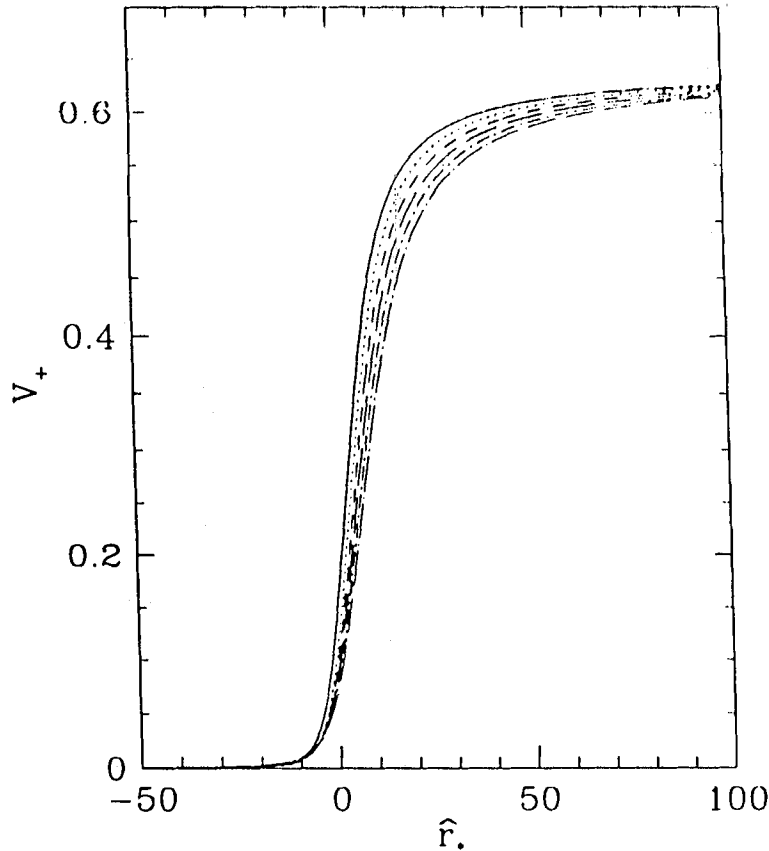


Figure 2. Behaviour of the potential for different values of the incoming particle charge. The fixed parameters are: $\sigma = 0.8$, $m_p = 0.8$, $l = \frac{1}{2}$ and $Q_* = 0.6$. From the upper to the lower curves the charge q of the particle is chosen as 0, 0.2, 0.4, 0.6, 0.8, 1.

be written as

$$Z_+ = \sqrt{T_+[k_+(\hat{r}_*)]} \exp(iu_+) + \sqrt{R_+[k_+(\hat{r}_*)]} \exp(-iu_+), \quad (21a)$$

$$Z_- = \sqrt{T_-[k_-(\hat{r}_*)]} \exp(iu_-) + \sqrt{R_-[k_-(\hat{r}_*)]} \exp(-iu_-), \quad (21b)$$

where

$$k_{\pm}(\hat{r}_*) = \sqrt{(\sigma^2 - V_{\pm})}, \quad (22)$$

$$u_{\pm}(\hat{r}_*) = \int k_{\pm}(\hat{r}_*) d\hat{r}_* + \text{constant}, \quad (23)$$

with

$$T_+(r) + R_+(r) = 1, \quad T_-(r) + R_-(r) = 1 \quad \text{instantaneously.} \quad (24)$$

Here, k is the wavenumber of the incoming wave and u is the *eiconal*, T_{\pm} and R_{\pm} are instantaneous transmission and reflection coefficients [5], respectively. Using this method at each location, instantaneously, the WKB method is applied. This solution is valid when $(1/k)(dk/d\hat{r}_*) \ll k$, otherwise a different method [5] should be used.

In figure 4, the comparison of the instantaneous reflection and transmission coefficients for the Schwarzschild and Reissner–Nordström geometries is shown. The parameters chosen are given in the figure caption. With decreasing barrier height, the transmission coefficient

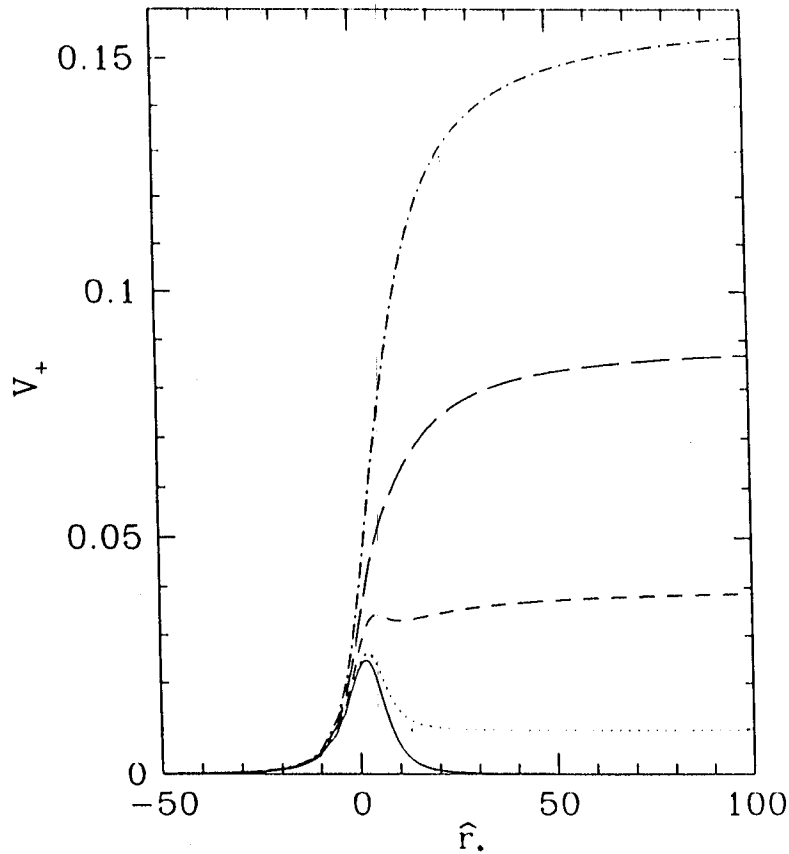


Figure 3. Behaviour of the potential for different values of the rest mass of the incoming particle. The fixed parameters are: $\sigma = 0.8$, $Q_* = 0.5$, $l = \frac{1}{2}$ and $q = 1$. From the upper to the lower curves the mass m_p of the particle is chosen as 0.4, 0.3, 0.2, 0.1, 0.

increases and the reflection coefficient decreases. It can be seen that by the introduction of the electromagnetic coupling, the potential barrier height reduces so that the corresponding transmission probability increases with respect to that of the Schwarzschild case (the behaviour for the Schwarzschild case is shown graphically in [5]) for a particular set of parameters. So the presence of the black-hole charge decreases the curved nature of spacetime.

Now recombining Z_+ and Z_- one can easily find the original radial Dirac wavefunctions $R_{1/2}$ and $R_{-1/2}$ [5]. Finally, we will have a complete solution as $J(r, \theta) = R_{1/2}(r)S_{1/2}(\theta)$.

5. Conclusions

In this paper, we have studied analytically the scattering of spin- $\frac{1}{2}$ particles around a Reissner–Nordström black hole. Our main motivation is to show analytically how the spin- $\frac{1}{2}$ particles behave in the presence of an electromagnetic interaction in curved spacetime. We introduced the gravitational and electromagnetic gauge fields. Since no such study had been carried out previously we started from scratch. Firstly, we wrote the corresponding dynamical equation of a spin- $\frac{1}{2}$ particle, namely the Dirac equation in a combined gravitational and electromagnetic background. Due to the curvature of the spacetime a gravitational gauge field (here, spin coefficients for the Reissner–Nordström geometry) was introduced. The electromagnetic

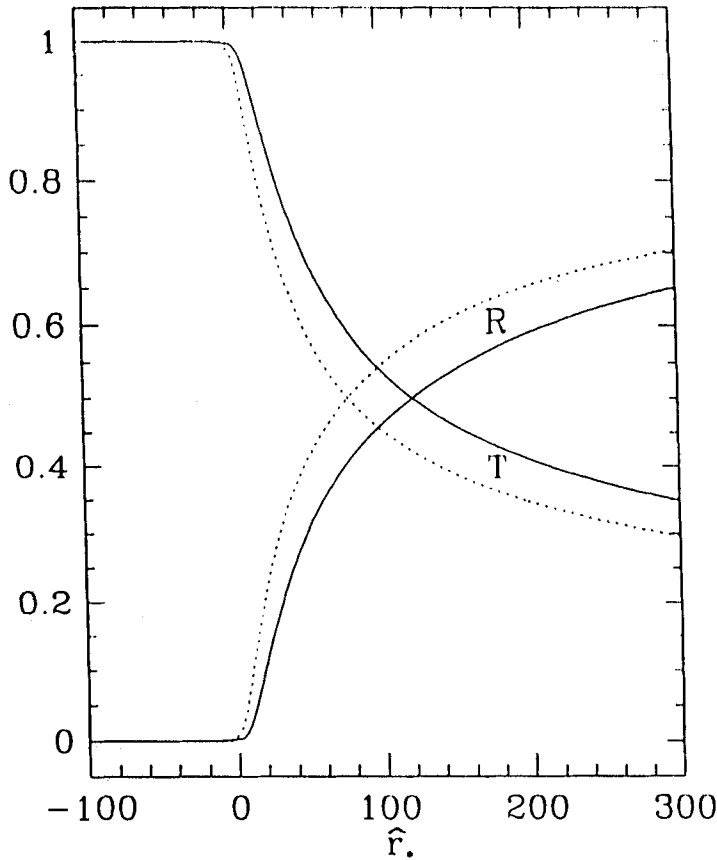


Figure 4. Instantaneous reflection (R) and transmission (T) coefficients for Reissner–Nordström (solid curves) and Schwarzschild (dotted curves) black holes. The physical parameters are chosen as $\sigma = 0.8$, $m_p = 0.8$, $l = \frac{1}{2}$, $q = 1$. For the Reissner–Nordström case $Q_* = 0.5$.

interaction comes into the game because of the charge of the black hole. Here, we have considered a steady-state problem and the corresponding components of the electromagnetic vector potential are set to zero. We then separated the equation into radial and angular parts. It is seen that in the case of a spherically symmetric spacetime, the presence of a charge of the gravitating object does not affect the behaviour of the incoming particles in the polar direction. Only the radial part of the equation is influenced. We then decoupled the radial Dirac equation. Now the potential is dependent on charge–charge coupling in the spacetime. If the charge of the black hole reduces to zero, the potential reduces to that of the Schwarzschild case. With the presence of a repulsive (or attractive) charge–charge interaction for a positive (or negative) energy solution the magnitude of the curvature effect reduces. This is because of the opposing nature of the two simultaneous interactions.

There is one interesting sector of the solution (which was absent in the uncharged spherically symmetric spacetime). If the charge–charge interaction is of an attractive nature for the positive energy solution (or repulsive for the negative energy solution) then the potential at a certain location ($r = \alpha$) diverges. However, because of the $1/(r - \alpha)^3$ variance of the potential super-radiation is absent.

Here we study the behaviour of the potential by varying the charge of the black hole, the charge of the incoming particle and the rest mass of the incoming particle. We also study the space-dependent reflection and transmission coefficients and display them graphically for

one set of physical parameters. It is seen that as the potential barrier height decreases, the corresponding transmission probability increases. We solve the radial Dirac equation by the IWKB method.

Acknowledgments

I am grateful to Professor Sandip K Chakrabarti regarding selection of this problem. I also would like to thank Kaushik Ghosh for helpful comments during my work.

References

- [1] Chandrasekhar S 1976 *Proc. R. Soc. A* **349** 571
- [2] Chakrabarti S K 1984 *Proc. R. Soc. A* **391** 27
- [3] Jin W M 1998 *Class. Quantum Grav.* **15** 3163
- [4] Semiz I 1992 *Phys. Rev. D* **46** 5414
- [5] Mukhopadhyay B and Chakrabarti S K 1999 *Class. Quantum Grav.* **16** 3165
- [6] Mukhopadhyay B 1999 *Ind. J. Phys. B* **73** 855
- [7] Chandrasekhar S 1983 *The Mathematical Theory of Black Holes* (London: Clarendon)
- [8] Newman E and Penrose R 1962 *J. Math. Phys.* **3** 566
- [9] Kinnersley W 1969 *J. Math. Phys.* **10** 1195
- [10] Newman E and Penrose R 1966 *J. Math. Phys.* **7** 863
- [11] Goldberg J N, Macfarlane A J, Newman E T, Rohrlich F and Sudarsan E C G 1967 *J. Math. Phys.* **8** 2155



ELSEVIER

Nuclear Physics B 582 (2000) 627–645

NUCLEAR
PHYSICS B

www.elsevier.nl/locate/npe

Solution of Dirac equation around a spinning black hole

Banibrata Mukhopadhyay¹, Sandip K. Chakrabarti²

Theoretical Astrophysics Group, S.N. Bose National Centre For Basic Sciences, JD Block, Salt Lake, Sector-III, Calcutta-700091, India

Received 13 March 2000; revised 10 May 2000; accepted 18 May 2000

Abstract

Chandrasekhar separated the Dirac equation for spinning and massive particles in Kerr geometry in radial and angular parts. Chakrabarti solved the angular equation and found the corresponding eigenvalues for different Kerr parameters. The radial equations were solved asymptotically by Chandrasekhar. In the present paper, we use the WKB approximation to solve the spatially complete radial equation and calculate analytical expressions of radial wave functions for a set of Kerr and wave parameters. From these solutions we obtain local values of reflection and transmission coefficients. © 2000 Elsevier Science B.V. All rights reserved.

PACS: 04.20.-q; 04.70.-s; 04.70.Dy; 95.30.Sf

Keywords: Black holes; Kerr geometry; Dirac waves

1. Introduction

One of the most important solutions of Einstein's equation is that of the spacetime around and inside an isolated black hole. The spacetime at a large distance is flat and Minkowskian where usual quantum mechanics is applicable, while the spacetime closer to the singularity is so curved that no satisfactory quantum field theory could be developed as yet. An intermediate situation arises when a weak perturbation (due to, say, gravitational, electromagnetic or Dirac waves) originating from infinity impinges on a black hole, interacting with it. The resulting wave is partially transmitted into the black hole through the horizon and partially scatters off to infinity. In the linearized ("test field") approximation this problem has been attacked in the past by several authors [1–4]. The master equations of Teukolsky [2] which govern these linear perturbations for integral spin (e.g., gravitational and electromagnetic) fields were solved numerically by Press and

¹ bm@boson.bose.res.in

² chakraba@boson.bose.res.in

Teukolsky [5] and Teukolsky and Press [6]. While the equations governing the massive Dirac particles were separated by Chandrasekhar [3]. So far, only the angular eigenfunction and eigenvalue (which happens to be the separation constant) have been obtained [7]. Particularly interesting is the fact that whereas gravitational and electromagnetic radiations were found to be amplified in some range of incoming frequencies, Chandrasekhar [4] predicted that no such amplifications should take place for Dirac waves because of the very nature of the potential experienced by the incoming fields. However, these later conclusions were drawn using asymptotic solutions and no attempt has so far been made to determine the nature of the radial wave functions, both incoming and outgoing, for the Dirac wave perturbations. He also speculated that one needs to look into the problem for negative eigenvalues (λ) where one *might* come across super-radiance for Dirac waves.

In the present paper, we revisit this important problem to study the nature of the radial wave functions as a function of the Kerr parameter, rest mass and frequency of incoming particle. We also verify that super-radiance is indeed absent for the Dirac field. Unlike the works of Press and Teukolsky [5] and Teukolsky and Press [6] where numerical (shooting) methods were used to solve the master equations governing gravitational and electromagnetic waves, we use an approximate analytical method for the massive Dirac wave. The details of the method would be presented below.

The plan of the paper is as follows: in the next section, we present the equation governing the Dirac waves (waves for half-integral massive spin particles) as they were separated into radial and angular coordinates. We then briefly present the nature of the angular eigenvalues and eigenfunctions. In Section 3, we present our method of solution and present the *spatially complete* radial wave functions. Finally, in Section 4, we draw our conclusions.

2. The Dirac equation in Kerr geometry

Chandrasekhar [3] separated the Dirac equation in Kerr geometry into radial (R) and angular (S) wave functions. Below, we present these equations from Chandrasekhar [4] using the same choice of units: we choose $\hbar = 1 = G = c$.

The equations governing the radial wave-functions $R_{\pm\frac{1}{2}}$ corresponding to spin $\pm\frac{1}{2}$, respectively, are given by:

$$\Delta^{1/2} \mathcal{D}_0 R_{-1/2} = (\lambda + im_p r) \Delta^{1/2} R_{+1/2}, \quad (1a)$$

$$\Delta^{1/2} \mathcal{D}_0^\dagger \Delta^{1/2} R_{+\frac{1}{2}} = (\lambda - im_p r) R_{-1/2}, \quad (1b)$$

where, the operators \mathcal{D}_n and \mathcal{D}_n^\dagger are given by,

$$\mathcal{D}_n = \partial_r + \frac{iK}{\Delta} + 2n \frac{(r-M)}{\Delta}, \quad (2a)$$

$$\mathcal{D}_n^\dagger = \partial_r - \frac{iK}{\Delta} + 2n \frac{(r-M)}{\Delta}, \quad (2b)$$

and

$$\Delta = r^2 + a^2 - 2Mr, \tag{3a}$$

$$K = (r^2 + a^2)\sigma + am. \tag{3b}$$

Here, a is the Kerr parameter, n is an integer or half-integer, σ is the frequency of incident wave, M is the mass of the black hole, m_p is the rest mass of the Dirac particle, λ is the eigenvalue of the Dirac equation and m is the azimuthal quantum number.

The equations governing the angular wave-functions $S_{\pm\frac{1}{2}}$ corresponding to spin $\pm\frac{1}{2}$, respectively, are given by:

$$\mathcal{L}_{\frac{1}{2}} S_{+\frac{1}{2}} = -(\lambda - am_p \cos\theta) S_{-\frac{1}{2}}, \tag{4a}$$

$$\mathcal{L}_{\frac{1}{2}}^\dagger S_{-\frac{1}{2}} = +(\lambda + am_p \cos\theta) S_{+\frac{1}{2}}, \tag{4b}$$

where, the operators \mathcal{L}_n and \mathcal{L}_n^\dagger are given by,

$$\mathcal{L}_n = \partial_\theta + Q + n \cot\theta, \tag{5a}$$

$$\mathcal{L}_n^\dagger = \partial_\theta - Q + n \cot\theta \tag{5b}$$

and

$$Q = a\sigma \sin\theta + m \operatorname{cosec}\theta. \tag{6}$$

Note that both the radial and the angular sets of equations, i.e., Eqs. 1(a), 1(b) and Eqs. 4(a), 4(b) are coupled equations. Combining Eqs. 4(a), 4(b), one obtains the angular eigenvalue equations for the spin- $\frac{1}{2}$ particles as [7]

$$\left[\mathcal{L}_{\frac{1}{2}} \mathcal{L}_{\frac{1}{2}}^\dagger + \frac{am_p \sin\theta}{\lambda + am_p \cos\theta} \mathcal{L}_{\frac{1}{2}}^\dagger + (\lambda^2 - a^2 m_p^2 \cos^2\theta) \right] \hat{S}_{-\frac{1}{2}} = 0. \tag{7}$$

There are exact solutions of this equation for the eigenvalues λ and the eigenfunctions $S_{-\frac{1}{2}}$ when $\rho = m_p/\sigma = 1$ in terms of the orbital quantum number l and azimuthal quantum number m . These solutions are [7]:

$$\lambda^2 = \left(l + \frac{1}{2} \right)^2 + a\sigma(p + 2m) + a^2\sigma^2 \left[1 - \frac{y^2}{2(l+1) + a\sigma x} \right], \tag{8}$$

and

$$\frac{1}{2} S_{lm} = \frac{1}{2} Y_{lm} - \frac{a\sigma y}{2(l+1) + a\sigma x} \frac{1}{2} Y_{l+1m}, \tag{9}$$

where

$$p = F(l, l); \quad x = F(l+1, l+1); \quad y = F(l, l+1)$$

and

$$F(l_1, l_2) = [(2l_2 + 1)(2l_1 + 1)]^{1/2} \langle l_2 1 m 0 | l_1 m \rangle \\ \times \left[\langle l_2 1 \frac{1}{2} 0 | l_1 \frac{1}{2} \rangle + (-1)^{l_2-l} \langle l_2 1 m 0 | l_1 m \rangle \left[\langle l_2 1 \frac{1}{2} 0 | l_1 \frac{1}{2} \rangle + (-1)^{l_2-l} \rho \sqrt{2} \langle l_2 1 - \frac{1}{2} 1 | l_1 \frac{1}{2} \rangle \right] \right] \tag{10}$$

with $\langle \dots | \dots \rangle$ are the usual Clebsh–Gordon coefficients. For other values of ρ one has to use perturbation theories. Solutions upto sixth order using perturbation parameter $a\sigma$ is

given in Chakrabarti [7]. The eigenvalues λ are required to solve the radial equations which we do now.

This radial equations (1a), (1b) are in coupled form. One can decouple them and express the equation either in terms of spin up or spin down wave functions $R_{\pm\frac{1}{2}}$ but the expression loses its transparency. It is thus advisable to use the approach of Chandrasekhar [4] by changing the basis and independent variable r to

$$r_* = r + \frac{2Mr_+ + am/\sigma}{r_+ - r_-} \log\left(\frac{r}{r_+} - 1\right) - \frac{2Mr_- + am/\sigma}{r_+ - r_-} \log\left(\frac{r}{r_-} - 1\right) \quad (11)$$

(for $r > r_+$),

$$\frac{d}{dr_*} = \frac{\Delta}{\omega^2} \frac{d}{dr}, \quad (12)$$

$$\omega^2 = r^2 + \alpha^2, \quad \alpha^2 = a^2 + am/\sigma, \quad (13)$$

to transform the set of coupled Eqs. 1(a), 1(b) into two independent one dimensional wave equations given by:

$$\left(\frac{d}{dr_*} - i\sigma\right) P_{+\frac{1}{2}} = \frac{\Delta^{1/2}}{\omega^2} (\lambda - im_p r) P_{-\frac{1}{2}}, \quad (14)$$

$$\left(\frac{d}{dr_*} + i\sigma\right) P_{-\frac{1}{2}} = \frac{\Delta^{1/2}}{\omega^2} (\lambda + im_p r) P_{+\frac{1}{2}}. \quad (15)$$

Here, $\mathcal{D}_0 = \frac{\omega^2}{\Delta} \left(\frac{d}{dr_*} + i\sigma\right)$ and $\mathcal{D}_0^\dagger = \frac{\omega^2}{\Delta} \left(\frac{d}{dr_*} - i\sigma\right)$ were used and wave functions were redefined as $R_{-\frac{1}{2}} = P_{-\frac{1}{2}}$ and $\Delta^{1/2} R_{+\frac{1}{2}} = P_{+\frac{1}{2}}$.

We now define a new variable,

$$\theta = \tan^{-1}(m_p r/\lambda), \quad (16)$$

which yields

$$\cos\theta = \frac{\lambda}{\sqrt{\lambda^2 + m_p^2 r^2}} \quad \text{and} \quad \sin\theta = \frac{m_p r}{\sqrt{\lambda^2 + m_p^2 r^2}}$$

and

$$(\lambda \pm im_p r) = \exp(\pm i\theta) \sqrt{\lambda^2 + m_p^2 r^2}, \quad (17)$$

so the coupled equations take the form

$$\left(\frac{d}{dr_*} - i\sigma\right) P_{+\frac{1}{2}} = \frac{\Delta^{1/2}}{\omega^2} (\lambda^2 + m_p^2 r^2)^{1/2} P_{-\frac{1}{2}} \exp\left[-i \tan^{-1}\left(\frac{m_p r}{\lambda}\right)\right], \quad (18a)$$

and

$$\left(\frac{d}{dr_*} + i\sigma\right) P_{-\frac{1}{2}} = \frac{\Delta^{1/2}}{\omega^2} (\lambda^2 + m_p^2 r^2)^{1/2} P_{+\frac{1}{2}} \exp\left[i \tan^{-1}\left(\frac{m_p r}{\lambda}\right)\right]. \quad (18b)$$

Then, defining,

$$P_{+\frac{1}{2}} = \psi_{+\frac{1}{2}} \exp\left[-\frac{i}{2} \tan^{-1}\left(\frac{m_p r}{\lambda}\right)\right] \quad (19a)$$

and

$$P_{-\frac{1}{2}} = \psi_{-\frac{1}{2}} \exp \left[+\frac{1}{2} i \tan^{-1} \left(\frac{m_p r}{\lambda} \right) \right], \tag{19b}$$

we obtain,

$$\frac{d\psi_{+\frac{1}{2}}}{dr_*} - i\sigma \left(1 + \frac{\Delta \lambda m_p}{\omega^2} \frac{1}{2\sigma} \frac{1}{\lambda^2 + m_p^2 r^2} \right) \psi_{+\frac{1}{2}} = \frac{\Delta^{1/2}}{\omega^2} (\lambda^2 + m_p^2 r^2)^{1/2} \psi_{-\frac{1}{2}} \tag{20a}$$

and

$$\frac{d\psi_{-\frac{1}{2}}}{dr_*} + i\sigma \left(1 + \frac{\Delta \lambda m_p}{\omega^2} \frac{1}{2\sigma} \frac{1}{\lambda^2 + m_p^2 r^2} \right) \psi_{-\frac{1}{2}} = \frac{\Delta^{1/2}}{\omega^2} (\lambda^2 + m_p^2 r^2)^{1/2} \psi_{+\frac{1}{2}}. \tag{20b}$$

Further choosing $\hat{r}_* = r_* + \frac{1}{2\sigma} \tan^{-1} \left(\frac{m_p r}{\lambda} \right)$ so that $d\hat{r}_* = \left(1 + \frac{\Delta \lambda m_p}{\omega^2} \frac{1}{2\sigma} \frac{1}{\lambda^2 + m_p^2 r^2} \right) dr_*$, the above equations become,

$$\left(\frac{d}{d\hat{r}_*} - i\sigma \right) \psi_{+\frac{1}{2}} = W \psi_{-\frac{1}{2}}, \tag{21a}$$

and

$$\left(\frac{d}{d\hat{r}_*} + i\sigma \right) \psi_{-\frac{1}{2}} = W \psi_{+\frac{1}{2}}, \tag{21b}$$

where

$$W = \frac{\Delta^{1/2} (\lambda^2 + m_p^2 r^2)^{3/2}}{\omega^2 (\lambda^2 + m_p^2 r^2) + \lambda m_p \Delta / 2\sigma}. \tag{22}$$

Now letting $Z_{\pm} = \psi_{+\frac{1}{2}} \pm \psi_{-\frac{1}{2}}$ we can combine the differential equations to give,

$$\left(\frac{d}{d\hat{r}_*} - W \right) Z_+ = i\sigma Z_-, \tag{23a}$$

and

$$\left(\frac{d}{d\hat{r}_*} + W \right) Z_- = i\sigma Z_+. \tag{23b}$$

From these equations, we readily obtain a pair of independent one-dimensional wave equations,

$$\left(\frac{d^2}{d\hat{r}_*^2} + \sigma^2 \right) Z_{\pm} = V_{\pm} Z_{\pm}, \tag{24}$$

where

$$\begin{aligned} V_{\pm} = W^2 \pm \frac{dW}{d\hat{r}_*} = & \frac{\Delta^{1/2} (\lambda^2 + m_p^2 r^2)^{3/2}}{[\omega^2 (\lambda^2 + m_p^2 r^2) + \lambda m_p \Delta / 2\sigma]^2} \\ & \times [\Delta^{1/2} (\lambda^2 + m_p^2 r^2)^{3/2} \pm ((r - M)(\lambda^2 + m_p^2 r^2) + 3m_p^2 r \Delta)] \\ & \mp \frac{\Delta^{3/2} (\lambda^2 + m_p^2 r^2)^{5/2}}{[\omega^2 (\lambda^2 + m_p^2 r^2) + \lambda m_p \Delta / 2\sigma]^3} \\ & \times [2r(\lambda^2 + m_p^2 r^2) + 2m_p^2 \omega^2 r + \lambda m_p (r - M) / \sigma]. \end{aligned} \tag{25}$$

One important point to note: the transformation of spatial coordinate r to r_* (and \hat{r}_*) is taken not only for mathematical simplicity but also for a physical significance. When r is chosen as the radial coordinate, the decoupled equations for independent waves show diverging behaviour. However, by transforming those in terms of r_* (and \hat{r}_*) we obtain well behaved functions. The horizon is shifted from $r = r_+$ to $\hat{r}_* = -\infty$ unless $\sigma \leq \sigma_s = -am/(2Mr_+)$ (Eq. (11)). In this connection, it is customary to define σ_c where $\alpha^2 = 0$ (Eq. (13)). Thus, $\sigma_c = -m/a$. If $\sigma \leq \sigma_s$, the region is expected to be super-radiant [4] because for integral spin particles for $\sigma \leq \sigma_s$ there exhibit super-radiation.

3. Solution of the radial equation

Out of the total physical parameter space, in one region (region I) the total energy of the particle is always greater than the height of potential barrier and in the other region (region II) the energy is less than of the maximum height of the potential barrier. In region II, the wave hits the wall of barrier and tunnels through it. One has to treat these two cases a little differently.

The usual WKB approximation [8] is used to obtain the zeroth order solution. We improve the solution by properly incorporating the inner and outer boundary conditions. After establishing the general solution, we present here the solution of Eq. (24) for three sets of parameters as illustrative examples. For those examples the choice of parameters is made in such a way that there is a significant interaction between the particle and the black hole, i.e., when the Compton wavelength of the incoming wave is of the same order as the radius of the outer horizon of the Kerr black hole. So,

$$\frac{G\{M + \sqrt{M^2 - a^2}\}}{c^2} \sim \frac{\hbar}{m_p c}. \quad (26)$$

We choose as before $G = \hbar = c = 1$, so

$$m_p \sim \frac{1}{\{M + \sqrt{M^2 - a^2}\}}. \quad (27)$$

Similarly, the frequency of the incoming particle (or wave) should be of the same order as the inverse of the light crossing time of the radius of the black hole, i.e.,

$$\frac{c^3}{G\{M + \sqrt{M^2 - a^2}\}} \sim \sigma. \quad (28)$$

Using the same units as before, we can write,

$$m_p \sim \sigma \sim \{M + \sqrt{M^2 - a^2}\}^{-1}. \quad (29)$$

In principle, however, one can choose any values of σ and m_p for a particular black hole and the corresponding solution is possible.

One can easily check from Eq. (25) that for $r \rightarrow \infty$ (i.e., $\hat{r}_* \rightarrow \infty$) $V_{\pm} \rightarrow m_p^2$. So we expand the total parameter space in terms of the frequency of the particle (or wave), σ and the rest mass of the particle, m_p . It is clear that in half of the parameter space spanned

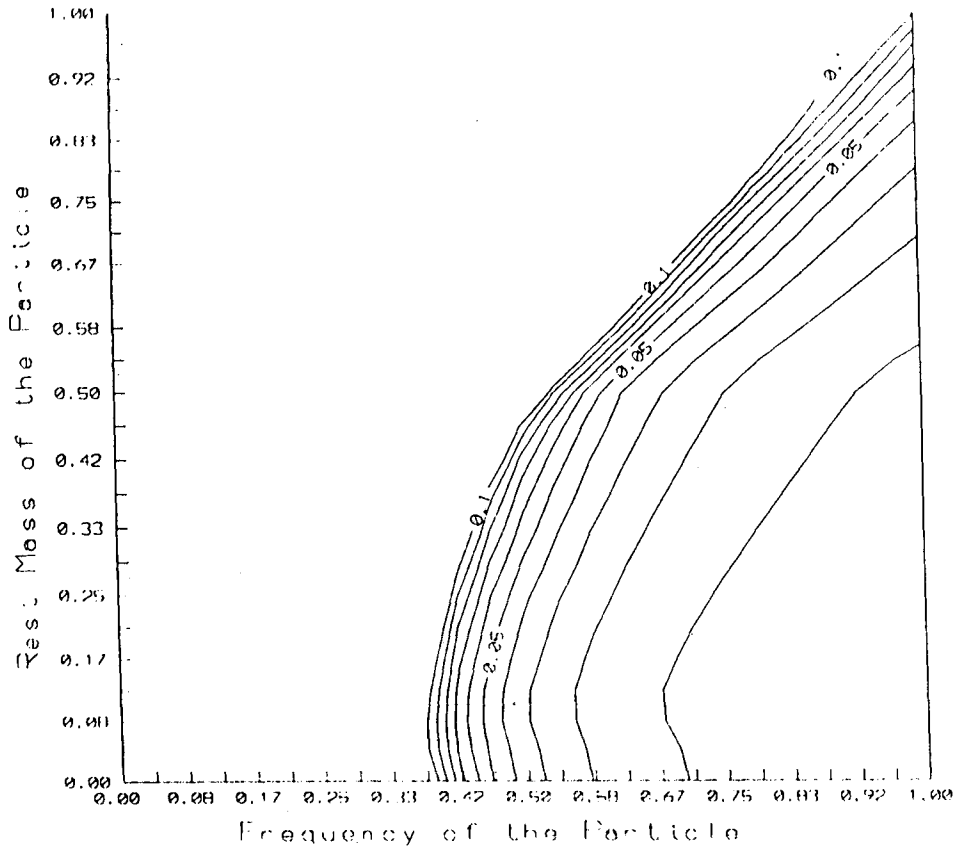


Fig. 1. Contours of constant $w_{\max} = \max(\frac{1}{k^2} \frac{dk}{d\hat{r}_*})$ are shown to indicate that generally $w \ll 1$ and therefore the WKB approximation is valid in most of the physical region. Labels indicate values of w_{\max} .

by $\sigma - m_p$ where, $\sigma < m_p$, particles are released at finite distance with so little energy that they cannot escape to infinity. In this case, the total energy $\sim \sigma^2$ of the incoming particle at a large distance is less than the potential energy of the system. We will not discuss solutions in this region. The rest of the parameter space ($\sigma \geq m_p$) is divided into two regions — I: $E > V_m$ and II: $E < V_m$, where E is the total energy of the incoming particle and V_m is the maximum of the potential. In region I, the wave is *locally* sinusoidal because the wave number k is real for the entire range of \hat{r}_* . In region II, on the other hand, the wave is decaying in some region when $E < V$, i.e., where the wave “hits” the potential barrier and in the rest of the region, the wave is propagating. We shall show solutions in these two regions separately. In region-I whatever be the physical parameters, the energy of the particle is always greater than the potential energy and the WKB approximation is generally valid in the whole range (i.e., $\frac{1}{k^2} \frac{dk}{d\hat{r}_*} \ll 1$). In cases of region-II, the energy of the particle is always less than the maximum height of potential barrier. Thus, at two points (where $k = 0$) the total energy matches the potential energy and in the neighbourhood of those two points the WKB approximate method is not valid. They have to be dealt with separately. In Fig. 1, we show contours of constant $w_{\max} = \max(\frac{1}{k^2} \frac{dk}{d\hat{r}_*})$ for a given set (σ, m_p) of parameters. The labels show the actual values of w_{\max} . Clearly, in most of the parameter regions the WKB approximation is safely valid for any value of \hat{r}_* . One has to

employ a different method (such as using Airy functions, see below) to find solutions in those regions where w_{\max} attains a large value which indicates the non-validity of WKB method.

3.1. Solutions of region I

We rewrite Eq. (24) as,

$$\frac{d^2 Z_+}{d\hat{r}_*^2} + (\sigma^2 - V_+)Z_+ = 0. \quad (30)$$

This is nothing but the Schrödinger equation with total energy of the wave σ^2 . This can be solved by regular WKB method.

Let

$$k(\hat{r}_*) = \sqrt{\sigma^2 - V_+}, \quad u(\hat{r}_*) = \int k(\hat{r}_*)d\hat{r}_* + \text{constant},$$

k is the wavenumber of the incoming wave and u as the *Eikonal*. The solution of the Eq. (30) is,

$$Z_+ = \frac{A_+}{\sqrt{k}} \exp(iu) + \frac{A_-}{\sqrt{k}} \exp(-iu) \quad (31)$$

with

$$A_+^2 + A_-^2 = k. \quad (32)$$

The motivation of Eq. (32) is to impose the WKB method at the each space point so that sum of the transmission and reflection coefficients are same at each location. In this case $\sigma^2 > V_+$ all along and also $\frac{1}{k} \frac{dk}{d\hat{r}_*} \ll k$, so the WKB approximation is valid in the whole region.

It is clear that a standard WKB solution where A_+ and A_- are kept constant throughout, can not be accurate in whole range of \hat{r}_* , since the physical inner boundary condition on the horizon must be that the reflected component is negligible there (since there the potential barrier height goes down to zero). Thus the WKB approximation requires a slight modification in which a spatial dependence of A_{\pm} is allowed. On the other hand, at a large distance, where the WKB is strictly valid, A_+ and A_- should tend to be constants, and hence their difference is also a constant:

$$A_+ - A_- = c. \quad (33)$$

Here, one can choose also the sum of A_+ and A_- are constant instead of difference as Eq. (33), but the final result will not be affected. Here, c is determined from the WKB solution at a large distance. For simplicity we choose A_{\pm} s are real. This along with Eq. (32) gives,

$$A_{\pm}(r) = \pm \frac{c}{2} + \frac{\sqrt{2k(r) - c^2}}{2}. \quad (34)$$

This spatial variation, strictly valid at large distances only, should not be extendable to the horizon without correcting for the inner boundary condition. These values are to be shifted

by, say, A_{+h} respectively, so that on the horizon one obtains the physical R and T . We first correct the reflection coefficient on the horizon as follows: Let A_{-h} be the value of A_- on the horizon (see Eq. (34)),

$$A_{-h} = -\frac{c}{2} + \frac{\sqrt{2k(r_+) - c^2}}{2}.$$

It is appropriate to use $\mathcal{A}_- = A_- - A_{-h}$ rather than A_- since \mathcal{A}_- vanishes at $r = r_+$.

Incorporating these conditions, the solution (31) becomes,

$$Z_+ = \frac{\mathcal{A}_+}{\sqrt{q}} \exp(iu) + \frac{\mathcal{A}_-}{\sqrt{q}} \exp(-iu) \tag{35}$$

with the usual normalization condition

$$\mathcal{A}_+^2 + \mathcal{A}_-^2 = q \tag{36}$$

where $\mathcal{A}_+ = A_+ - A_{+h}$.

Determination of A_{+h} is done by enforcing R obtained from Eq. (37a), which is shown below, is the same as that obtained by the actual WKB method. The q is used to compute the transmission coefficient T from Eq. (36). In this way, normalization of $R + T = 1$ is assured.

The normalization factor $q \rightarrow k$ as $\hat{r}_* \rightarrow \infty$ and the condition $\frac{1}{q} \frac{dq}{d\hat{r}_*} \ll q$ is found to be satisfied whenever $\frac{1}{k} \frac{dk}{d\hat{r}_*} \ll k$ is satisfied. This is the essence of our modification of the WKB. In a true WKB, A_{\pm} are constants and the normalization is with respect to a (almost) constant k . However, we are using it as if the WKB is instantaneously valid everywhere. Our method may therefore be called “Instantaneous” WKB approximation or IWKB for short. Using the new notations, the instantaneous values (i.e., local values) of the reflection and transmission coefficients are given by (see Eq. (35)),

$$R = \frac{\mathcal{A}_-^2}{q}, \tag{37a}$$

$$T = \frac{\mathcal{A}_+^2}{q}. \tag{37b}$$

Whatever may be the value of the physical parameters, $\frac{1}{k} \frac{dk}{d\hat{r}_*} \ll k$ is satisfied in whole range of \hat{r}_* for region I.

The variation of reflection and transmission coefficients would be well understood if we imagine the potential barrier consists of a large number of steps. From simple quantum mechanics, in between each two steps, we can calculate the reflection and transmission coefficients [9]. Clearly these reflection and transmission coefficients at different junctions will be different. This is discussed in detail below. To be concrete, we choose one set of parameters from region I. Here, the total energy of the incoming particle is greater than the potential barrier height for all values of \hat{r}_* . We use, Kerr parameter, $a = 0.5$; mass of the black hole, $M = 1$; Mass of the particle, $m_p = 0.8$; orbital angular momentum quantum number, $l = 1/2$; azimuthal quantum number, $m = -1/2$; frequency of the incoming wave, $\sigma = 0.8$. The derived parameters are, $r_+ = M + \sqrt{M^2 - a^2} \cong 1.86603$; $\sigma_r = 1$; $\sigma_s = 0.066987$; $\alpha^2 = -0.0625$. For these parameters, the eigenvalue is $\lambda = 0.92$ [7].

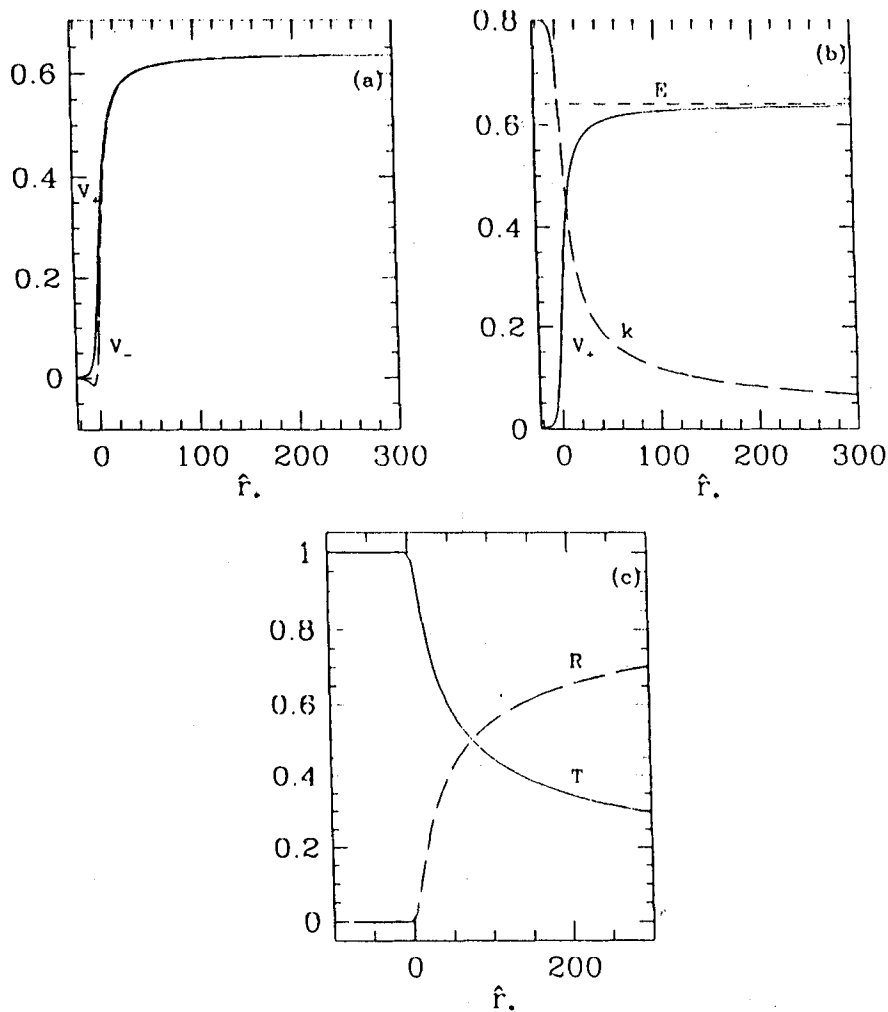


Fig. 2. Behaviour of (a) V_+ (solid curve) and V_- (dashed curve), (b) V_+ (solid curve), k (dashed curve), total energy E (short-dashed curve) and reflection (R , dashed curve) coefficients as functions of \hat{r}_* . The parameters are $a = 0.5$, $M = 1$, $m_p = 0.8$, $l = 1/2$, $m = -1/2$, $\sigma = 0.8$.

Here it is clear that σ is in between σ_c and σ_s and $\alpha^2 < 0$, $r_+ > |\alpha|$. So we are in a strictly non super-radiant regime since here, $\sigma > \sigma_s$ [4].

From Eq. (24) we observe that there are two wave equations for two potentials V_+ and V_- . The nature of the potentials is shown in Fig. 2(a). It is clear from the Fig. 2(a) that the potentials V_{\pm} are well behaved. They are monotonically decreasing as the particle approaches the black hole, and the total energy chosen in this case (σ^2) is always higher than V_+ . For concreteness, we study the equation with potential V_+ . A similar procedure (IWKB method) as explained above can be adopted using the potential V_- to compute Z_- and its form would be

$$Z_- = \frac{\Lambda'_+ - \Lambda'_{+h}}{\sqrt{q'}} \exp(iu') - \frac{\Lambda'_- - \Lambda'_{-h}}{\sqrt{q'}} \exp(-iu'). \quad (35')$$

Note the occurrence of the negative sign in front of the reflected wave. This is to satisfy the asymptotic property of the wave functions.

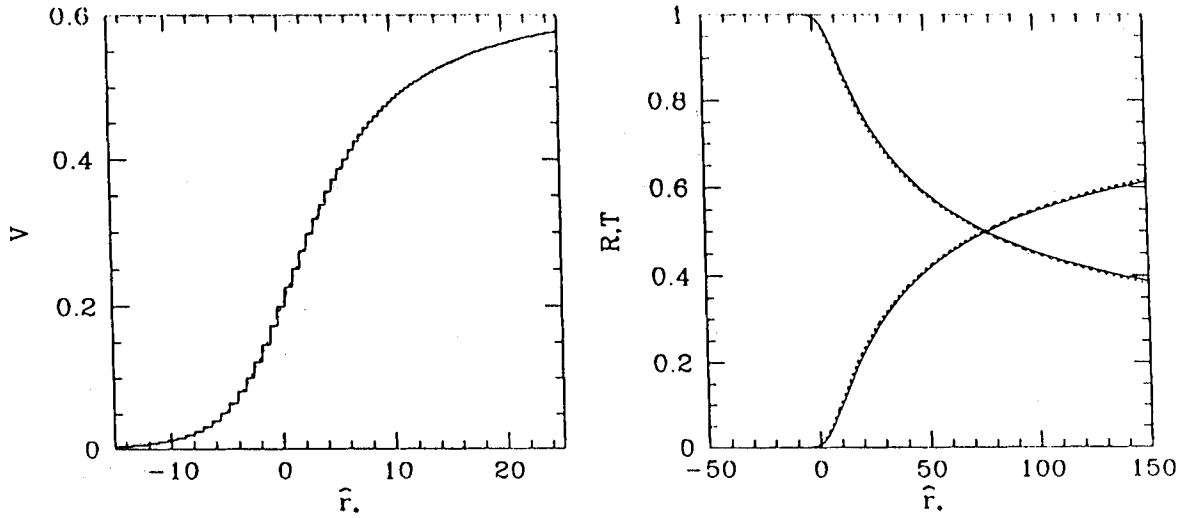


Fig. 3. (a) Steps (solid) approximating a potential (dotted), thus reducing the problem to that of a quantum mechanics. The parameters are same as in Fig. 2. (b) Comparison of variation of instantaneous reflection coefficient R and transmission coefficient T with the radial coordinate \hat{r}_* using analytical WKB method (solid) and step-potential method (dotted). The parameters are same as Fig. 2.

In Fig. 2(b), we show the nature of V_+ (solid curve), k (dashed curve) and $E (= \sigma^2)$ (short-dashed curve). In the solutions (Eqs. (35) and (35')) the first term corresponds to the incident wave and the second term corresponds to the reflected wave.

In Fig. 2(c), the variation of reflection and transmission coefficients are shown. It is seen that as matter comes close to the black hole, the barrier height goes down. As a result, the penetration probability increases, causing the rise of the transmission coefficient.

Local values of the reflection and transmission coefficients could also be calculated using the well known quantum mechanical approach. First one has to replace the potentials (as shown in Fig. 2(a)) by a collection of step functions as shown in Fig. 3(a). The standard junction conditions of the type

$$Z_{+,n} = Z_{+,n+1}, \tag{38a}$$

where

$$Z_{+,n} = A_n \exp[ik_n \hat{r}_{*,n}] + B_n \exp[-ik_n \hat{r}_{*,n}],$$

and

$$\left. \frac{dZ_+}{d\hat{r}_*} \right|_n = \left. \frac{dZ_+}{d\hat{r}_*} \right|_{n+1}, \tag{38b}$$

where

$$\left. \frac{dZ_+}{d\hat{r}_*} \right|_n = ik_n A_n \exp(ik_n \hat{r}_{*,n}) - ik_n B_n \exp(-ik_n \hat{r}_{*,n})$$

at each of the n steps were used to connect solutions at successive steps. From the simple quantum mechanical calculation we obtain the reflection and transmission coefficients at the each junctions. Clearly at different junctions; i.e., at different radii this reflection and

transmission coefficients will be different. As before, we use the inner boundary condition, to be $R \rightarrow 0$ at $\hat{r}_+ \rightarrow -\infty$. In reality we use as many steps as possible to follow accurately the shape of the potential. Smaller step sizes were used whenever k varies faster. Fig. 3(b) shows the comparison of the instantaneous reflection and transmission coefficients in both the methods. The agreement shows that the WKB can be used at each point quite successfully.

It is to be noted, that, strictly speaking, the terms “reflection” and “transmission” coefficients are traditionally defined with respect to the asymptotic values. The spatial dependence that we show are just the dependence of the instantaneous values. This is consistent with the spirit of IWKB approximation that we are using.

The radial wave functions $R_{+\frac{1}{2}}$ and $R_{-\frac{1}{2}}$ which are of spin up and spin down particles respectively of the original Dirac equation are given below,

$$\begin{aligned} \operatorname{Re}(R_{+\frac{1}{2}} \Delta^{1/2}) &= \frac{a_+ \cos(u - \theta) + a_- \cos(u + \theta)}{2\sqrt{k}} \\ &+ \frac{a'_+ \cos(u' - \theta) - a'_- \cos(u' + \theta)}{2\sqrt{k'}}. \end{aligned} \quad (39a)$$

$$\begin{aligned} \operatorname{Im}(R_{+\frac{1}{2}} \Delta^{1/2}) &= \frac{a_+ \sin(u - \theta) - a_- \sin(u + \theta)}{2\sqrt{k}} \\ &+ \frac{a'_+ \sin(u' - \theta) + a'_- \sin(u' + \theta)}{2\sqrt{k'}}. \end{aligned} \quad (39b)$$

$$\begin{aligned} \operatorname{Re}(R_{-\frac{1}{2}}) &= \frac{a_+ \cos(u + \theta) + a_- \cos(u - \theta)}{2\sqrt{k}} \\ &- \frac{a'_+ \cos(u' + \theta) - a'_- \cos(u' - \theta)}{2\sqrt{k'}}. \end{aligned} \quad (39c)$$

$$\begin{aligned} \operatorname{Im}(R_{-\frac{1}{2}}) &= \frac{a_+ \sin(u + \theta) - a_- \sin(u - \theta)}{2\sqrt{k}} \\ &- \frac{a'_+ \sin(u' + \theta) + a'_- \sin(u' - \theta)}{2\sqrt{k'}}. \end{aligned} \quad (39d)$$

Here, $a_+ = (\Lambda_+ - \Lambda_{+h})/\sqrt{q/k}$ and $a_- = (\Lambda_- - \Lambda_{-h})/\sqrt{q/k}$. $\frac{a'_+}{\sqrt{k'}}$ and $\frac{a'_-}{\sqrt{k'}}$ are the transmitted and reflected amplitudes, respectively, for the wave of corresponding potential V_- .

In Fig. 4(a)–(d) we show the nature of these wavefunctions. The eikonals used in plotting these functions (see Eqs. (39a)–(39d)) have been calculated by approximating V_+ in terms of a polynomial and using the definition $u(\hat{r}_+) = \int^{\hat{r}_+} \sqrt{\sigma^2 - V_+} d\hat{r}_+$. This was done since V_+ is not directly integrable. Note that the amplitude as well as wavelength remain constants in regions where k is also constant.

3.2. Solutions of region II

Here we study the solution of a region where for any set of physical parameters, the total energy of the incoming particle is less than the maximum height of the potential barrier. So the WKB approximation (more precisely, our IWKB approximation) is not valid in

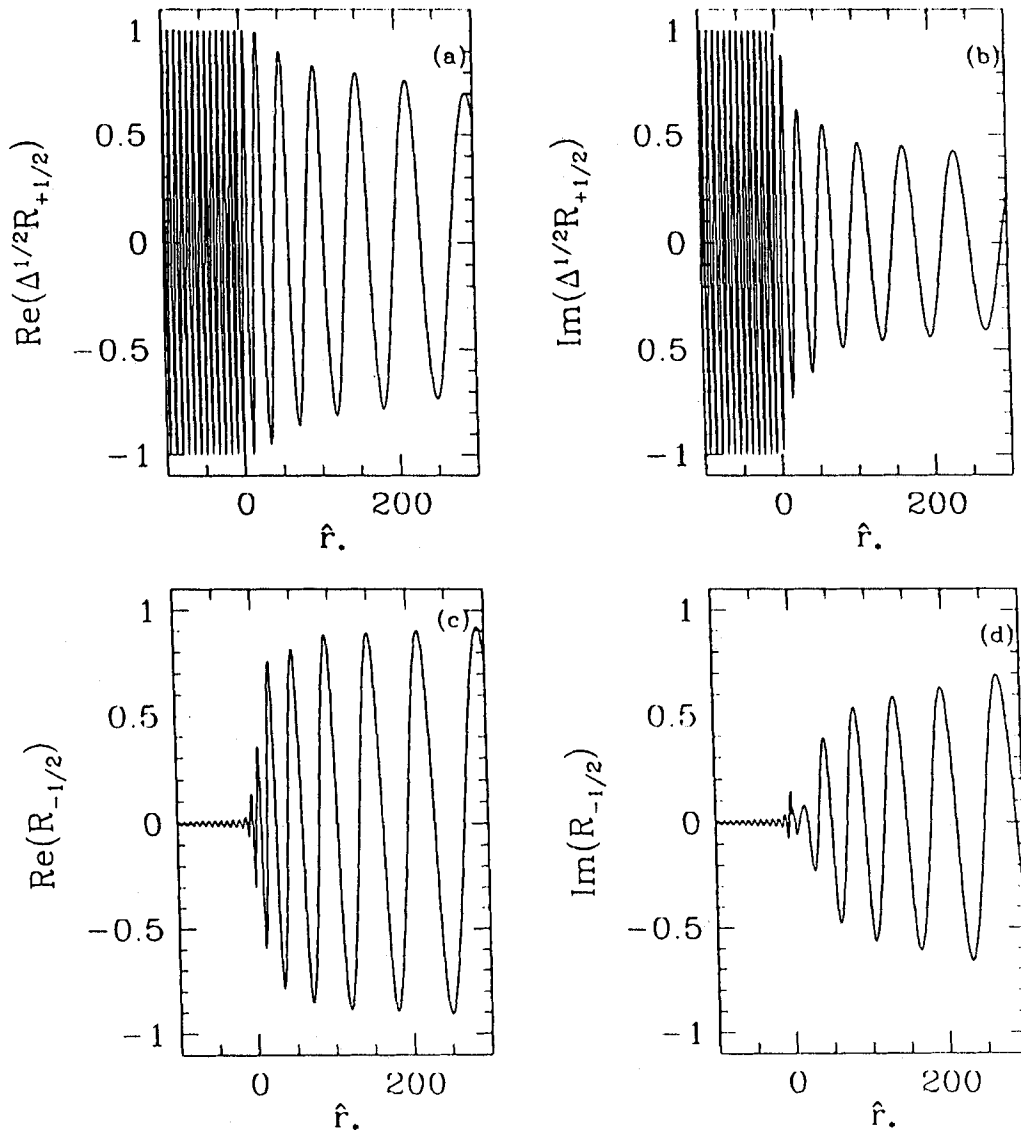


Fig. 4. Nature of real and imaginary parts of radial wave functions for Case 1.

the whole range of \hat{r}_* . In the regions where the WKB is not valid, the solutions will be the linear combination of Airy functions because the potential is a linear function of \hat{r}_* in those intervals. At the junctions one has to match the solutions including Airy functions with the solution obtained by WKB method.

In the region where the WKB approximation is valid, local values of reflection and transmission coefficients and the wave function can be calculated easily by following the same method described in previous sub-section (solutions of region I) and the solution will be same as Eqs. (35), (35'). In other regions, the equation reduces to

$$\frac{d^2 Z_+}{d\hat{r}_*^2} - x Z_+ = 0, \tag{40}$$

where $x = \beta^{1/3}(\hat{r}_* - p)$, β is chosen to be positive and p is the critical point where the total energy and potential energy are matching.

Let $Z_+(x) = x^{1/2}Y(x)$ and considering region $x > 0$ the equation (40) reduces to

$$x^2 \frac{d^2 Y}{dx^2} + x \frac{dY}{dx} - \left(x^3 + \frac{1}{4}\right) Y(x) = 0. \quad (41)$$

By making another transformation

$$\xi = \frac{2}{3}x^{3/2} \quad (42)$$

we obtain

$$\xi^2 \frac{d^2 Y}{d\xi^2} + \xi \frac{dY}{d\xi} - \left(\xi^2 + \frac{1}{9}\right) Y(\xi) = 0, \quad (43)$$

this is the modified Bessel equation. The solution of this equation is $I_{1/3}(\xi)$ and $I_{-1/3}(\xi)$. So the solution of Eq. (40) will be

$$Z_+(x) = x^{1/2} [C_1 I_{1/3}(\xi) + C_2 I_{-1/3}(\xi)]. \quad (44)$$

When $x < 0$ the corresponding equation is,

$$\xi^2 \frac{d^2 Y}{d\xi^2} + \xi \frac{dY}{d\xi} + \left(\xi^2 - \frac{1}{9}\right) Y(\xi) = 0, \quad (45)$$

which is the Bessel equation. The corresponding solution is

$$Z_+(x) = |x|^{1/2} [D_1 J_{1/3}(\xi) + D_2 J_{-1/3}(\xi)], \quad (46)$$

where $J_{\pm 1/3}$ and $I_{\pm 1/3}$ are the Bessel functions and the modified Bessel functions of order $1/3$, respectively.

The Airy functions are defined as

$$\text{Ai}(x) = \frac{1}{3}x^{1/2} [I_{-1/3}(\xi) - I_{1/3}(\xi)], \quad x > 0, \quad (47)$$

$$\text{Ai}(x) = \frac{1}{3}|x|^{1/2} [J_{-1/3}(\xi) + J_{1/3}(\xi)], \quad x < 0, \quad (48)$$

$$\text{Bi}(x) = \frac{1}{\sqrt{3}}x^{1/2} [I_{-1/3}(\xi) + I_{1/3}(\xi)], \quad x > 0, \quad (49)$$

$$\text{Bi}(x) = \frac{1}{\sqrt{3}}|x|^{1/2} [J_{-1/3}(\xi) - J_{1/3}(\xi)], \quad x < 0, \quad (50)$$

In terms of Airy functions, the solutions (44) and (46) can be written as

$$Z_+ = \frac{3}{2}(C_2 - C_1)\text{Ai}(x) + \frac{\sqrt{3}}{2}(C_2 + C_1)\text{Bi}(x) \quad \text{for } x > 0, \quad (51)$$

$$Z_+ = \frac{3}{2}(D_2 + D_1)\text{Ai}(x) + \frac{\sqrt{3}}{2}(D_2 - D_1)\text{Bi}(x) \quad \text{for } x < 0, \quad (52)$$

By matching boundary conditions it is easy to show that the solution corresponding $x > 0$ and that corresponding $x < 0$ are continuous when $C_1 = -D_1$ and $C_2 = D_2$.

As an example of solutions from this region, we choose: $a = 0.95$, $M = 1$, $m_p = 0.17$, $l = 1/2$, $m = -1/2$, and $\sigma = 0.21$. The black hole horizon is at $r_+ = M + \sqrt{M^2 - a^2} \cong$

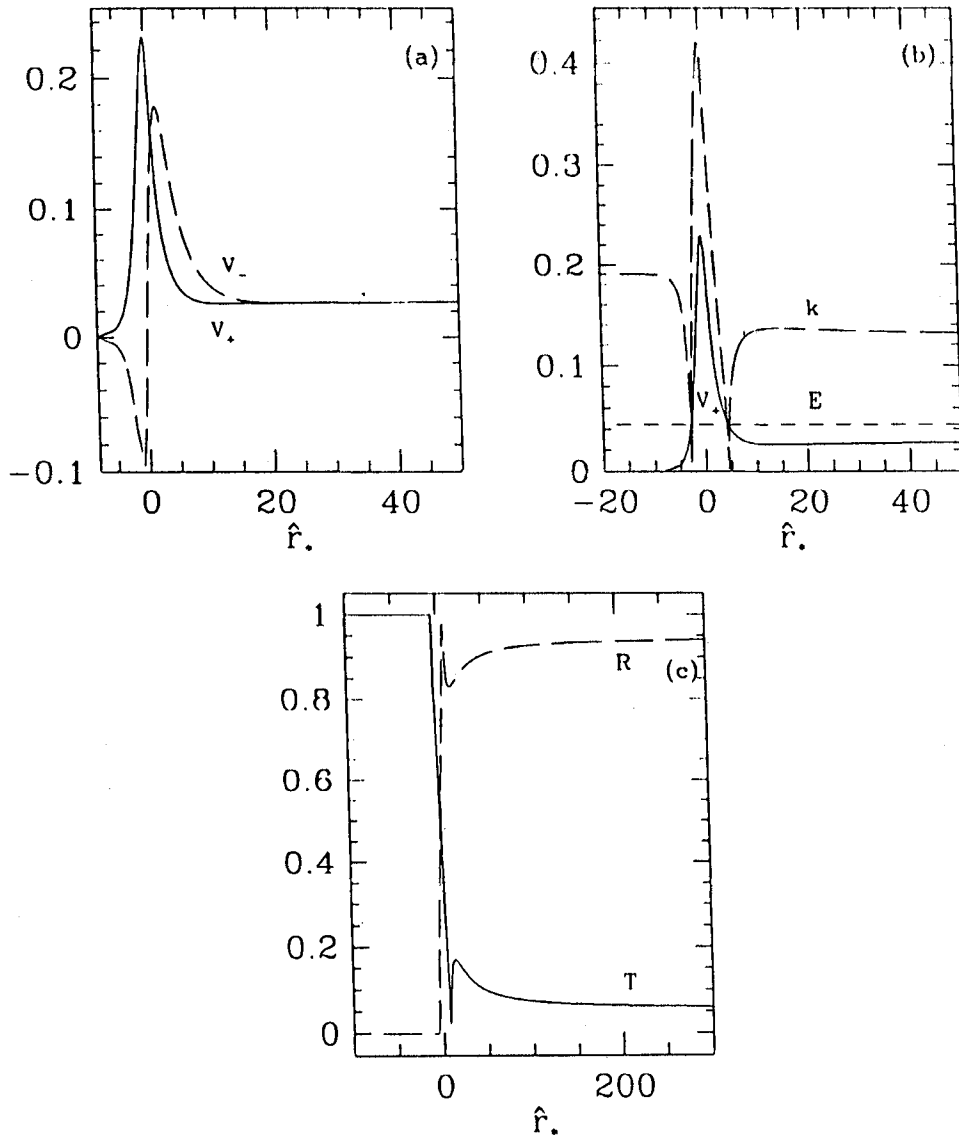


Fig. 5. Plots are same as in Fig. 2. The parameters are $a = 0.95$, $M = 1$, $m_p = 0.17$, $l = 1/2$, $m = -1/2$, $\sigma = 0.21$.

1.31225, $\sigma_r = 0.526316$, $\sigma_s = 0.180987$, $\alpha^2 = -1.356$ and $\lambda = 0.93$ [7]. It is clear that the values of σ_r , σ_s and α^2 indicate the region is non super-radiant. In Fig. 5(a), we show the nature of V_+ and V_- , however, while solving, we use the equation containing V_+ (Eq. (24)). Unlike the case in the previous subsection, here σ^2 is no longer greater than V_{\pm} at all radii. As a result, k^2 may attain negative values in some region. In Fig. 5(b), nature of V_+ (solid curve), parameter k (dashed curve) and energy E (short-dashed curve) are shown. Here, WKB approximation can be applied in regions other than $\hat{r}_* \sim -4$ to -1 and 1 to 7 where k is close to zero and the condition $\frac{1}{k} \frac{dk}{d\hat{r}_*} \ll k$ is not satisfied.

In the region $\hat{r}_* = 7$ to 1 around the turning point $\hat{r}_* = 4.45475$ the solutions turns out to be [10],

$$Z_+ = 1.087526 \text{Ai}(x) + 0.788968 \text{Bi}(x), \tag{53}$$

Similarly, the solution from \hat{r}_+ = 1 to -4 , i.e., around the turning point $\hat{r}_1 = -2.8053$ turns out to be [10],

$$Z_+ = -[1.328096 \text{Ai}(x) + 0.774426 \text{Bi}(x)]. \quad (54)$$

It is to be noted that in the region $\hat{r}_* \sim 1$ to -1 , even though the potential energy dominates over the total energy, WKB approximation method is still valid. Here the solution will take the form $\exp(-u)/\sqrt{k}$ and $\exp(+u)/\sqrt{k}$. Asymptotic values of the instantaneous reflection and the transmission coefficients (which are traditionally known as the “reflection” and “transmission” coefficients) are obtained from the WKB approximation. This yields the integral constant c as in previous case.

From Eqs. (37a), (37b) local reflection and transmission coefficients are calculated, behaviours of which are shown in Fig. 5(c). The constants Λ_{-h} and Λ_{+h} are calculated as before. Note the decaying nature of the reflection coefficient inside the potential barrier.

3.3. Solutions in the super-radiant region

In this region, the potential diverges at $r = |\alpha|$. Here, the barrier height goes up to infinity and then the potential changes sign so that its nature changes from repulsive to attractive and vice versa. This is because $\sigma \leq \sigma_s$ (which is the condition for super-radiance) and $r_+ < |\alpha|$ [see Eqs. (11) and (13)]. Unlike the previous two cases, the relation between r and \hat{r}_* is not single valued. Here, at both $r = r_+$ and $r = \infty$, the value of $\hat{r}_* = \infty$. With the decrement of r , \hat{r}_* is decreased initially up to $r = |\alpha|$. Subsequently, \hat{r}_* starts to rise and at the black hole horizon it diverges. Obviously, in this case particles hit the barrier and we can solve the equation following the same methods as explained in the previous cases, i.e., the solutions are the same as Eqs. (35) and (35') for the region where the WKB method is valid and Eqs. (51) and (52) where the WKB method is not valid.

For illustrative example, here, we choose: $a = 0.95$, $M = 1$, $m_p = 0.105$, $l = 1/2$, $m = -1/2$, and $\sigma = 0.105$. The black hole horizon is located at $r_+ = M + \sqrt{M^2 - a^2} \cong 1.31225$, and $\sigma_c = 0.526316$, $\sigma_s = 0.180987$, $\alpha^2 = -3.62$ and $\lambda = 0.97$ [7]. Chandrasekhar showed [4] that for integral spin particles this region exhibits super-radiance and conjectured that for half-integral spins the super-radiance may be absent. We investigate here if this conjecture is valid.

The behaviour of potentials V_+ and V_- are shown in Fig. 6(a). It is clear that at $r = |\alpha|$ the potential diverges and the nature of the potential is changed from repulsive to attractive (for V_-) and vice versa (for V_+). Here, we will treat the equation with V_- as the potential (it is equally easy to do the problem with V_+). We first divide our computations into two parts. In the repulsive part of the potential (i.e., when $V_- > 0$), particles come from infinity and most of them reflect back from the infinitely high barrier. In the attractive part of the potential (i.e., when $V_- < 0$), particle radiates outwards in the \hat{r}_* coordinate (actually, particle goes towards the horizon but due to multivaluedness of the radial coordinate \hat{r}_* (with respect to r) the horizon is mapped to infinity).

In Fig. 6(b), nature of V_- , k and E are shown. The WKB approximation (more precisely IWKB approximation) method is valid from infinity to $\hat{r}_* = 40$ since, otherwise, $\frac{1}{k} \frac{dk}{dr} \ll k$

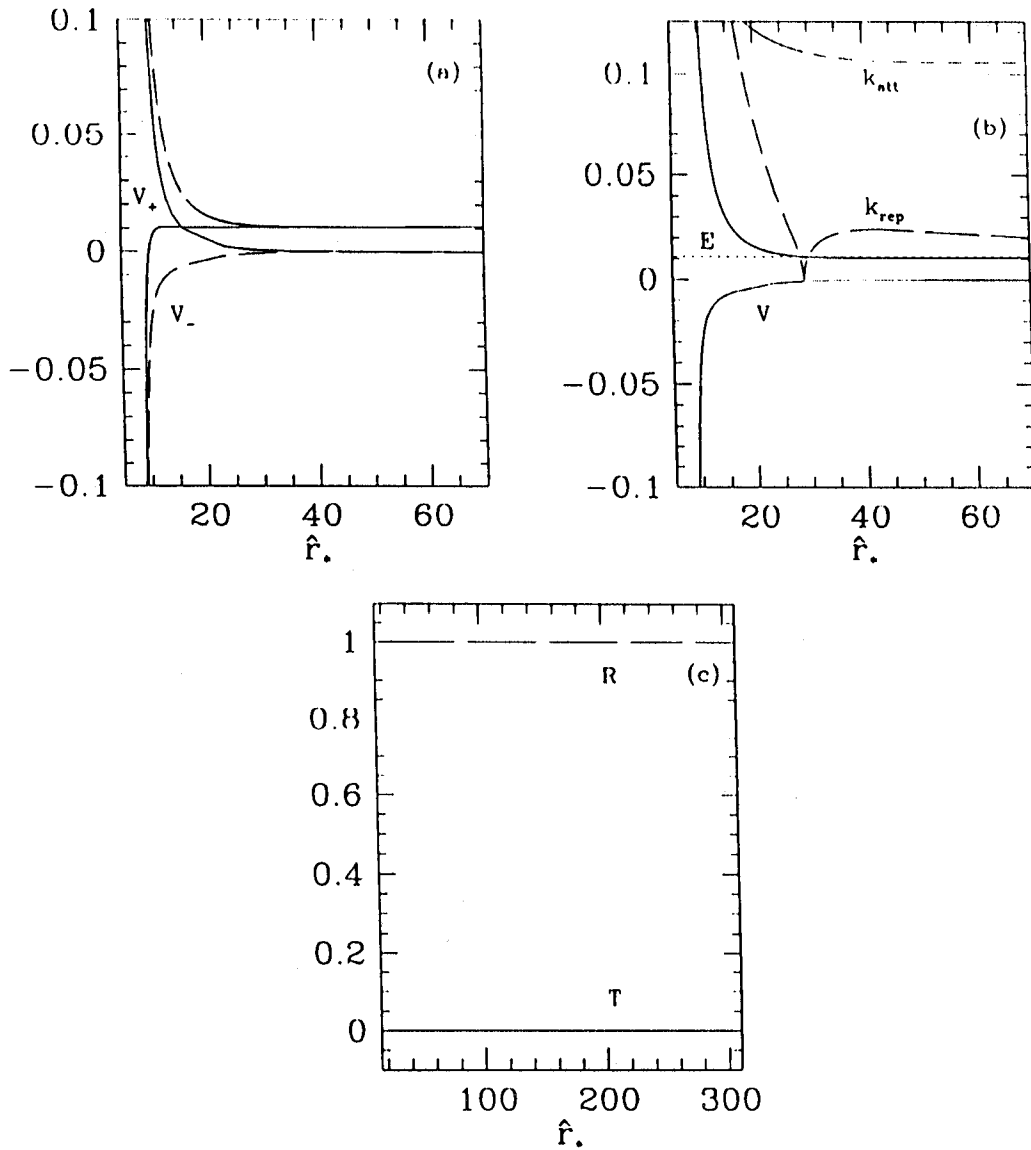


Fig. 6. Behaviour of (a) V_+ (solid curve) and V_- (dashed curve), (b) V (solid curve), k for region where potential is positive (k_{rep} , dashed curve), k for region where potential is negative (k_{att} , short-dashed curve), total energy E (dotted curve), (c) local transmission (T , solid curve) and reflection (R , dashed curve) coefficients as functions of \hat{r}_+ . The parameters are $a = 0.95$, $M = 1$, $m_p = 0.105$, $l = 1/2$, $m = -1/2$, $\sigma = 0.105$.

is not satisfied. In those other regions one has to apply a different method (which was also explained in last sub-section) to find solutions. The local values of the reflection and transmission coefficients and the wave function of the particle are calculated as in the previous cases. Since the matter which tunnels through the infinitely high barrier face infinitely strong attractive field, the possibility of extraction of energy would be zero. In Fig. 6(c), the variations of local transmission and reflection coefficients are shown. The net transmission of the wave through the horizon is non-negative all along and therefore super-radiation is absent, although σ is less than σ_c . We believe that the non-existence of super-radiation is due to $(r - |\alpha|)^{-3}$ variation of the potential near the singular point.

Because of the existence of attractive field, the extraction of energy is difficult, so the net transmission of the wave through the horizon from ∞ is always positive. This argument is valid for any set of parameters where $\sigma > \sigma_{\text{cr}}$.

4. Conclusion

In this paper, we studied scattering of massive, spin-half particles from a Kerr black hole, particularly the nature of the radial wave functions and the reflection and transmission coefficients. Our main motivation was to give a general analytical expression of the solution which can be useful for further study. We showed few illustrative cases as examples. We verified that these analytical solutions were indeed correct by explicitly solving the same set of equations using quantum mechanical step-potential approach as described in Section 3. We classified the entire parameter space in terms of the physical and unphysical regions and the physical region was further classified into two regions, depending on whether the particle “hits” the potential barrier or not. Again, the region where particle hits on the barrier, is divided into two parts, one is super-radiant region and other is non-super-radiant region. We chose one illustrative example in each of the regions. We emphasize that the most “interesting” region to study would be close to $m_p \sim \sigma$. However, we pointed out (Fig. 1) that for $m_p \leq 0.35$, the WKB solutions cannot be trusted, and other methods (such as those using Airy functions) must be employed.

We used the well known WKB approximation method as well as the step-potential method of quantum mechanics to obtain the spatial dependence of the coefficients of the wave function. This in turn, allowed us to determine the reflection and transmission coefficients and the nature of wave functions. The usual WKB method with constant coefficients and (almost) constant wave number k is successfully applied even when the coefficients and wave number are not constant everywhere. Solution from this “instantaneous” WKB (or IWKB) method agrees fully with that obtained from a purely quantum mechanical method where the potential is replaced by a collection of steps. Our method of obtaining solutions should be valid for any black hole geometry which are asymptotically flat so that radial waves could be used at a large distance. This way we ensure that the analytical solution is close to the exact solution. In region II, in some regions, the WKB method cannot be applied and hence Airy function approach or our step-potential approach could be used.

In the literature, reflection and transmission coefficients are defined at a single point. These definitions are meaningful only if the potential varies in a small region while studies are made from a large distance from it. In the present case, the potential changes over a large distance and we are studying in these regions as well. Although we used the words “reflection” and “transmission” coefficients, in this paper very loosely, our definitions are very rigorous and well defined. These quantities are simply the instantaneous values and in our belief more physical. The problem at hand is very similar to the problem of reflection and transmission of acoustic waves from a struck string of non-constant density where reflection and transmission occurs at each point.

Among other things, we verify Chandrasekhar's conjecture [4] based on the asymptotic solution, that for spin- $\frac{1}{2}$ particle the phenomenon of super-radiance is absent. We believe that this is due to the very way the potential develops the singularity at $r = |\alpha|$. Here $V_-(\hat{r}_*) \propto (r - |\alpha|)^{-3}$, which results an attractive potential in some region very close to the black hole. In contrast, $V_-(\hat{r}_*) \propto (r - |\alpha|)^{-4}$ when electromagnetic and gravitational waves are scattered off the black hole [4] does not create an attractive part in the potential and possibly exhibit the phenomenon of super-radiance. It is noted that all the cases where potential diverge at $r = \alpha$ (i.e., so called super-radiation cases) arise for $\sigma \leq \sigma_s$ with the negative values of azimuthal quantum number (here, $m = -1/2$) and the positive Kerr parameter, a . For positive values of m and positive values of a , potential does not diverge at any point for all values of σ . If we change the spin orientation of the black hole (negative values of a) and take positive m again divergence of the potential will arise. Thus, it seems that the cases with opposite sign of a and m are physically more interesting.

It is seen that for different physical parameters the solutions are different. The waves scattered off are distinctly different in different parameter regions. In a way, therefore, black holes can act as a mass spectrograph! Another interesting application of our method would be to study interactions of Hawking radiations in regions just outside the horizon.

References

- [1] S. Teukolsky, Phys. Rev. Lett. 29 (1972) 1114.
- [2] S. Teukolsky, Astrophys. J. 185 (1973) 635.
- [3] S. Chandrasekhar, Proc. R. Soc. London A 349 (1976) 571.
- [4] S. Chandrasekhar, The Mathematical Theory of Black Holes, Clarendon Press, London, 1983.
- [5] W.H. Press, S. Teukolsky, Astrophys. J. 185 (1973) 649.
- [6] S. Teukolsky, W.H. Press, Astrophys. J. 193 (1974) 443.
- [7] S.K. Chakrabarti, Proc. R. Soc. London A 391 (1984) 27.
- [8] J. Mathews, R.L. Walker, Mathematical Methods of Physics, 2nd edn., The Benjamin-Cummings Publishing Company, California, 1970.
- [9] A.S. Davydov, Quantum Mechanics, 2nd edn., Pergamon Press, Oxford, New York, 1976.
- [10] M. Abramowitz, I.A. Stegun (Eds.), Handbook of Mathematical Functions, National Bureau of Standards, Washington, 1972.

Scattering of Dirac waves off Kerr black holes

Sandip K. Chakrabarti^{*} and Banibrata Mukhopadhyay

S.N. Bose National Centre for Basic Sciences, JD-Block, Sector III, Salt Lake, Calcutta 700091, India

Accepted 2000 May 16. Received 2000 May 16; in original form 2000 January 4

ABSTRACT

Chandrasekhar separated the Dirac equation for spinning and massive particles in Kerr geometry into radial and angular parts. Here we solve the complete wave equation and find out how the Dirac wave scatters off Kerr black holes. The eigenfunctions, eigenvalues and reflection and transmission co-efficients are computed. We compare the solutions with several parameters to show how a spinning black hole recognizes the mass and energy of incoming waves. Very close to the horizon the solutions become independent of the particle parameters, indicating the universality of the behaviour.

Key words: black hole physic – waves – scattering.

1 INTRODUCTION

Chandrasekhar (1976) separated the Dirac equation in Kerr black hole geometry into radial (r) and angular (θ) parts. The radial equations governing the radial wavefunctions, $R_{\pm(1/2)}$ corresponding to spin $\pm 1/2$, are given by (with $\hbar = 1 = G = c$):

$$\Delta^{1/2} \mathcal{D}_0 R_{-1/2} = (\lambda + im_p r) \Delta^{1/2} R_{+1/2}; \quad \Delta^{1/2} \mathcal{D}_0^\dagger \Delta^{1/2} R_{+1/2} = (\lambda - im_p r) R_{-1/2}, \quad (1)$$

where the operators \mathcal{D}_n and \mathcal{D}_n^\dagger are given by

$$\mathcal{D}_n = \partial_r + \frac{iK}{\Delta} + 2n \frac{(r-M)}{\Delta}; \quad \mathcal{D}_n^\dagger = \partial_r - \frac{iK}{\Delta} + 2n \frac{(r-M)}{\Delta}, \quad (2)$$

and

$$\Delta = r^2 + a^2 - 2Mr; \quad K = (r^2 + a^2)\sigma + am. \quad (3)$$

Here, a is the Kerr parameter, n is an integer, σ is the frequency of the incident wave, M is the mass of the black hole, m_p is the rest mass of the Dirac particle, λ is the eigenvalue that is the separation constant of the complete Dirac equation and m is the azimuthal quantum number.

The equations governing the angular wave-functions $S_{\pm 1/2}$ corresponding to spin $\pm 1/2$ are given by:

$$\mathcal{L}_{1/2} S_{+1/2} = -(\lambda - am_p \cos \theta) S_{-1/2}; \quad \mathcal{L}_{1/2}^\dagger S_{-1/2} = +(\lambda + am_p \cos \theta) S_{+1/2} \quad (4)$$

where, the operators \mathcal{L}_n and \mathcal{L}_n^\dagger are given by,

$$\mathcal{L}_n = \partial_\theta + Q + n \cot \theta; \quad \mathcal{L}_n^\dagger = \partial_\theta - Q + n \cot \theta \quad (5)$$

and

$$Q = a\sigma \sin \theta + m \operatorname{cosec} \theta. \quad (6)$$

Combining equation (4), one obtains a second-order angular eigenvalue equation, which admits exact solutions for spin-half particles when $\rho = m_p/\sigma = 1$ (Chakrabarti 1984),

$$\lambda^2 = \left(l + \frac{1}{2}\right)^2 + a\sigma(p + 2m) + a^2\sigma^2 \left[1 - \frac{y^2}{2(l+1) + a\sigma x}\right] \quad (7)$$

and

$${}_{1/2} S_{lm} = {}_{1/2} Y_{lm} - \frac{a\sigma y}{2(l+1) + a\sigma x_{1/2}} Y_{l+1m} \quad (8)$$

^{*} E-mail: chakraba@boson.bose.res.in (SKC); bm@boson.bose.res.in (BM)

where

$$p = F(l, l); \quad x = F(l + 1, l + 1); \quad y = F(l, l + 1) \tag{9}$$

and

$$F(l_1, l_2) = [(2l_2 + 1)(2l_1 + 1)]^{1/2} \langle l_2 1 m 0 | l_1 m \rangle [\langle l_2 1 \frac{1}{2} 0 | l_1 \frac{1}{2} \rangle + (-1)^{l_2 - l_1} \langle l_2 1 m 0 | l_1 m \rangle] [\langle l_2 1 \frac{1}{2} 0 | l_1 \frac{1}{2} \rangle + (-1)^{l_2 - l_1} \rho \sqrt{2} \langle l_2 1 - \frac{1}{2} 1 | l_1 \frac{1}{2} \rangle].$$

Here, $\langle \dots \rangle$ are the usual Clebsh-Gordon coefficients and ${}_s Y_{lm}$ are the standard spin-weighted spherical harmonics (Chakrabarti 1984; see also, Goldberg et al. 1967, Breure et al. 1982) of spin s and usual quantum numbers l and m . When $\rho \neq m_p/\sigma = 1$, one obtains the solutions perturbatively with $a\sigma$ to be the perturbation parameter. The detailed procedure to obtain eigenfunctions and eigenvalues is in Chakrabarti (1984) and is not described here.

The radial equations in equation (1) are in coupled form. One can decouple them and express the equation either in terms of spin-up or spin-down wavefunctions $R_{\pm 1/2}$, but the expression loses its transparency. It is thus advisable to use the approach of Chandrasekhar (1983), changing the basis and independent variable r to,

$$r_* = r + \frac{2Mr_+ + am/\sigma}{r_+ - r_-} \log\left(\frac{r}{r_+} - 1\right) - \frac{2Mr_- + am/\sigma}{r_+ - r_-} \log\left(\frac{r}{r_-} - 1\right) \quad (r > r_+) \tag{10}$$

where

$$\frac{d}{dr_*} = \frac{\Delta}{\omega^2} \frac{d}{dr}; \quad \omega^2 = r^2 + \alpha^2; \quad \alpha^2 = a^2 + am/\sigma, \tag{11}$$

to transform the set of coupled equations (equation 1) into two independent one-dimensional wave equations given by:

$$\left(\frac{d}{dr_*} - i\sigma\right) P_{+1/2} = \frac{\Delta^{1/2}}{\omega^2} (\lambda - im_p r) P_{-1/2}; \quad \left(\frac{d}{dr_*} + i\sigma\right) P_{-1/2} = \frac{\Delta^{1/2}}{\omega^2} (\lambda + im_p r) P_{+1/2}. \tag{12}$$

Here, $\mathcal{D}_0 = \frac{d}{dr_*} \left(\frac{d}{dr_*} + i\sigma\right)$ and $\mathcal{D}_0^\dagger = \frac{d}{dr_*} \left(\frac{d}{dr_*} - i\sigma\right)$ were used and wavefunctions were redefined as $R_{-1/2} = P_{-1/2}$ and $\Delta^{1/2} R_{+1/2} = P_{+1/2}$.

2 SOLUTION PROCEDURE

We define a new variable, $\theta = \tan^{-1}(m_p r/\lambda)$, which gives

$$(\lambda \pm im_p r) = \exp(\pm i\theta) \sqrt{(\lambda^2 + m_p^2 r^2)}. \tag{13}$$

Also, define

$$P_{+1/2} = \psi_{+1/2} \exp\left[-\frac{1}{2} i \tan^{-1}\left(\frac{m_p r}{\lambda}\right)\right]; \quad P_{-1/2} = \psi_{-1/2} \exp\left[+\frac{1}{2} i \tan^{-1}\left(\frac{m_p r}{\lambda}\right)\right], \tag{14}$$

and choose $\hat{r}_* = r_* + 1/(2\sigma) \tan^{-1}((m_p r)/\lambda)$, so that $d\hat{r}_* = (1 + (\Delta/\omega^2)(\lambda m_p/2\sigma)(1/(\lambda^2 + m_p^2 r^2))) dr_*$, and $Z_{\pm} = \psi_{+1/2} \pm \psi_{-1/2}$. The above equations become

$$\left(\frac{d}{d\hat{r}_*} - W\right) Z_+ = i\sigma Z_-; \quad \left(\frac{d}{d\hat{r}_*} + W\right) Z_- = i\sigma Z_+, \tag{15}$$

where

$$W = \frac{\Delta^{1/2} (\lambda^2 + m_p^2 r^2)^{3/2}}{\omega^2 (\lambda^2 + m_p^2 r^2) + \lambda m_p \Delta / 2\sigma}. \tag{16}$$

From these equations, we readily obtain a pair of independent one-dimensional wave equations,

$$\left(\frac{d^2}{d\hat{r}_*^2} + \sigma^2\right) Z_{\pm} = V_{\pm} Z_{\pm}; \quad \text{where } V_{\pm} = W^2 \pm \frac{dW}{d\hat{r}_*}. \tag{17}$$

By transforming the variable from r to r_* (and \hat{r}_*), the horizon is shifted from $r = r_+$ to $\hat{r}_* = -\infty$ unless $\sigma \leq \sigma_s = -am/2Mr_+$ (equation 10). In this connection, it is customary to define σ_c where $\alpha^2 = 0$ (equation 11). Thus, $\sigma_c = -m/a$. If $\sigma \leq \sigma_s$, super-radiation is expected for particles with integral spins but not for those with half-integral spins (Chandrasekhar 1983). Thus, we concentrate on the region where, $\sigma > \sigma_s$.

The choice of parameters is generally made in such a way that there is significant interaction between the particle and the black hole, i.e. when the Compton wavelength of the incoming wave is of the same order as the outer horizon of the Kerr black hole. Similarly, the frequency of the incoming particle (or wave) should be of the same order as the inverse of the time taken for light to cross the radius of the black hole. These parameters yield the following equation:

$$m_p \sim \sigma \sim [M + \sqrt{M^2 - a^2}]^{-1}. \tag{18}$$

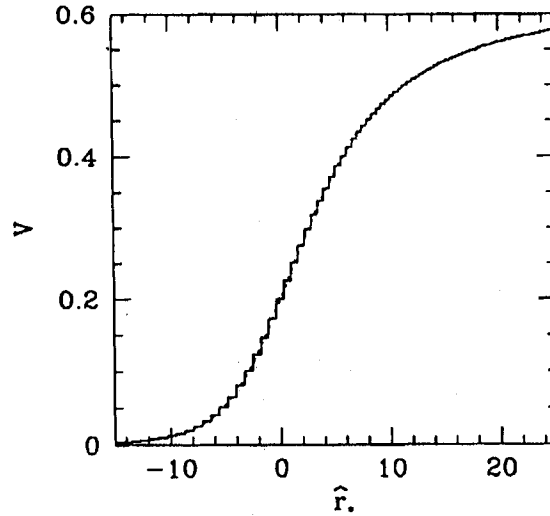


Figure 1. Behaviour of V_+ (smooth solid curve) for $a = 0.5$, $m_p = 0.8$ and $\sigma = 0.8$. This is approximated as a collection of steps. In reality, tens of thousand steps with varying size, which mimic the potential with arbitrary accuracy were used.

Thus, dealing with quantum black holes yields 'interesting' results. There are two cases of interest: (1) when the waves do not 'hit' the potential barrier, and (2) when the waves do hit the potential barrier. First, we replace the potential barrier by a large number of steps as in the step-barrier problem in quantum mechanics. Fig. 1 shows one such example of the potential barrier V_+ (equation 17), which is drawn for $a = 0.5$, $m_p = 0.8$ and $\sigma = 0.8$. In reality, we use tens of thousands of steps with suitably varying widths, so that the steps become indistinguishable from the actual function. The solution of equation (17) at the n th step can be written as (Davydov 1976)

$$Z_{+,n} = A_n \exp[ik_n \hat{r}_{*,n}] + B_n \exp[-ik_n \hat{r}_{*,n}], \quad (19)$$

when the energy of the wave is greater than the height of the potential barrier. The standard junction condition is given by (Davydov 1976), as

$$Z_{+,n} = Z_{+,n+1} \quad \text{and} \quad \frac{dZ_+}{d\hat{r}_*} \Big|_n = \frac{dZ_+}{d\hat{r}_*} \Big|_{n+1}. \quad (20)$$

The reflection and transmission co-efficients at the n th junction are given by:

$$R_n = \frac{A_{n+1}(k_{n+1} - k_n) + B_{n+1}(k_{n+1} + k_n)}{A_{n+1}(k_{n+1} + k_n) + B_{n+1}(k_{n+1} - k_n)}; \quad T_n = 1 - R_n \quad (21)$$

At each of the n steps, these conditions were used to connect solutions at successive steps. Here, k is the wave number ($k = \sqrt{\sigma^2 - V_{\pm}}$) of the wave and k_n is its value at the n th step. We use the 'no-reflection' inner boundary condition: $R \rightarrow 0$ at $\hat{r}_* \rightarrow -\infty$.

For the cases where waves hit the potential barrier, inside the barrier (where $\sigma^2 < V_+$) we use the wavefunction of the form

$$\mathfrak{Z}_{+,n} = A_n \exp[-\alpha_n \hat{r}_{*,n}] + B_n \exp[\alpha_n \hat{r}_{*,n}] \quad (22)$$

where, $\alpha_n = \sqrt{V_{\pm} - \sigma^2}$, as in ordinary quantum mechanics.

3 EXAMPLES OF SOLUTIONS

Fig. 2(a) shows three solutions [amplitudes of $\text{Re}(Z_+)$] for the following parameters: $a = 0.5$, $\sigma = 0.8$ and $m_p = 0.78, 0.79$ and 0.80 , solid, dotted and long-dashed curves respectively. The energy σ^2 is always higher than the height of the potential barrier (Fig. 1) and, therefore, the particles do not 'hit' the barrier. k increases and consequently, the wavelength decreases monotonically as the wave approaches a black hole. It is to be noted that though ours is apparently a 'crude' method, it is flexible and is capable of giving an insight into the problem, surpassing other methods such as ODE solver packages. This is because one can choose: (a) variable steps depending on the steepness of the potential to ensure uniform accuracy, and, at the same time, (b) a virtually infinite number of steps to follow the potential as closely as possible. For instance, in the inset, we show R in logarithmic scale, very close to the horizon. All the three curves merge, indicating that the solutions are independent of the mass of the particle. Closer inspection shows that here, the slope of the curve depends only on σ . The exponential dependence of R_n close to the horizon becomes obvious. Asymptotically, $V_{\pm} = m_p^2$ (equation 17), thus, as m_p decreases, the

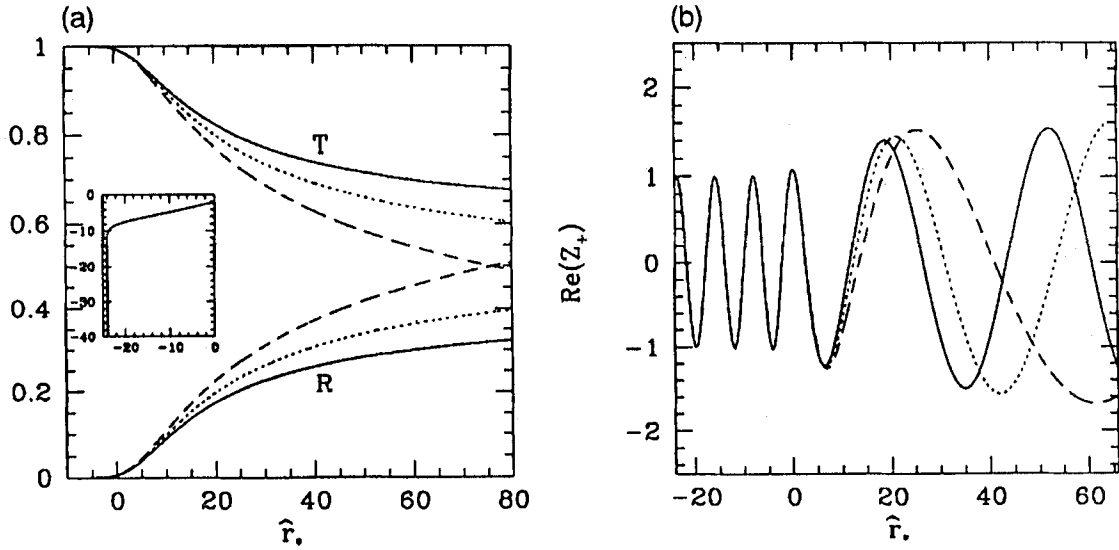


Figure 2. (a) Reflection (R) and transmission (T) coefficients of waves with varying mass as functions of \hat{r}_* . $m_p = 0.78$ (solid), $m_p = 0.79$ (dotted) and $m_p = 0.80$ (long-dashed) are used. Other parameters are $a = 0.5$ and $\sigma = 0.8$. The inset shows R in logarithmic scale, falling off exponentially just outside the horizon. (b) Amplitude of $\text{Re}(Z_+)$ of waves with varying mass as functions of \hat{r}_* . $m_p = 0.78$ (solid), $m_p = 0.79$ (dotted) and $m_p = 0.80$ (long-dashed) are used. Other parameters are $a = 0.5$ and $\sigma = 0.8$.

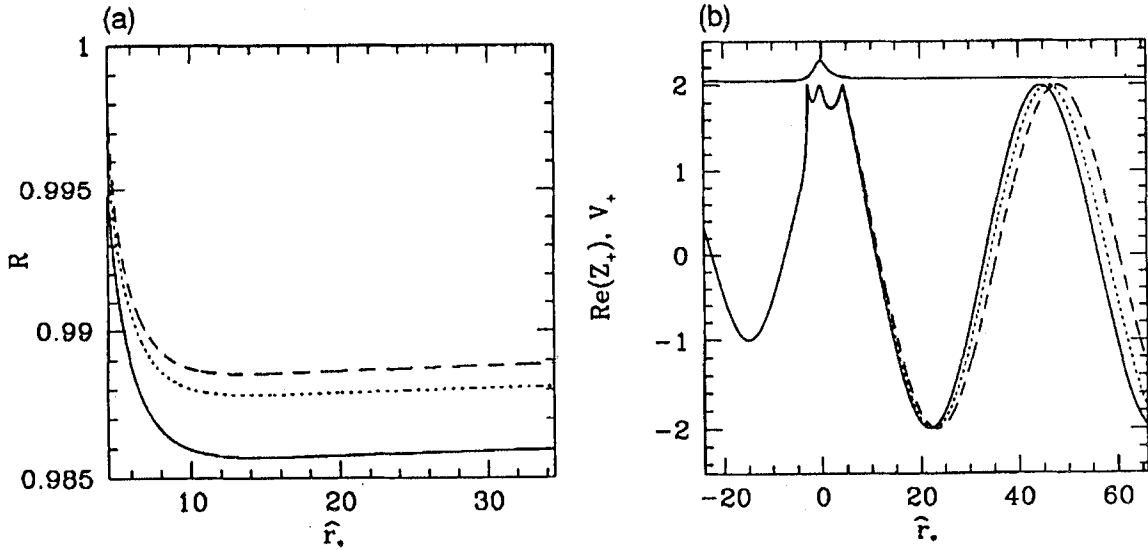


Figure 3. (a) Reflection (R) coefficient of waves with varying mass as functions of \hat{r}_* . $m_p = 0.16$ (solid), $m_p = 0.164$ (dotted) and $m_p = 0.168$ (long-dashed) are used. Other parameters are $a = 0.95$ and $\sigma = 0.168$. (b) Amplitude of $\text{Re}(Z_+)$ of waves with varying mass as functions of \hat{r}_* . $m_p = 0.16$ (solid), $m_p = 0.164$ (dotted) and $m_p = 0.168$ (long-dashed) are used. The nature of the potential with $m_p = 0.168$ is drawn shifted vertically by 2.05 units for clarity. Other parameters are $a = 0.95$ and $\sigma = 0.168$.

wavelength decreases. In Fig. 2b, we present the instantaneous values of the reflection R and transmission T coefficients (i.e., R_n and T_n of equation 21) for the same three cases. As the particle mass decreases, k increases and correspondingly R decreases, consistent with the limit that as $k \rightarrow \infty$, there should be no reflection at all as in a quantum mechanical problem.

Figs 3(a) and (b) compare a few solutions where the incoming particles 'hit' the potential barrier. We choose $a = 0.95$, $\sigma = 0.168$ and mass of the particle $m_p = 0.16$, 0.164 and 0.168, represented by solid, dotted and long-dashed curves, respectively. Inside the barrier, the wave decays and then returns to a sinusoidal behaviour, before entering into a black hole. In Fig. 3(b), we plotted the potential (shifted by

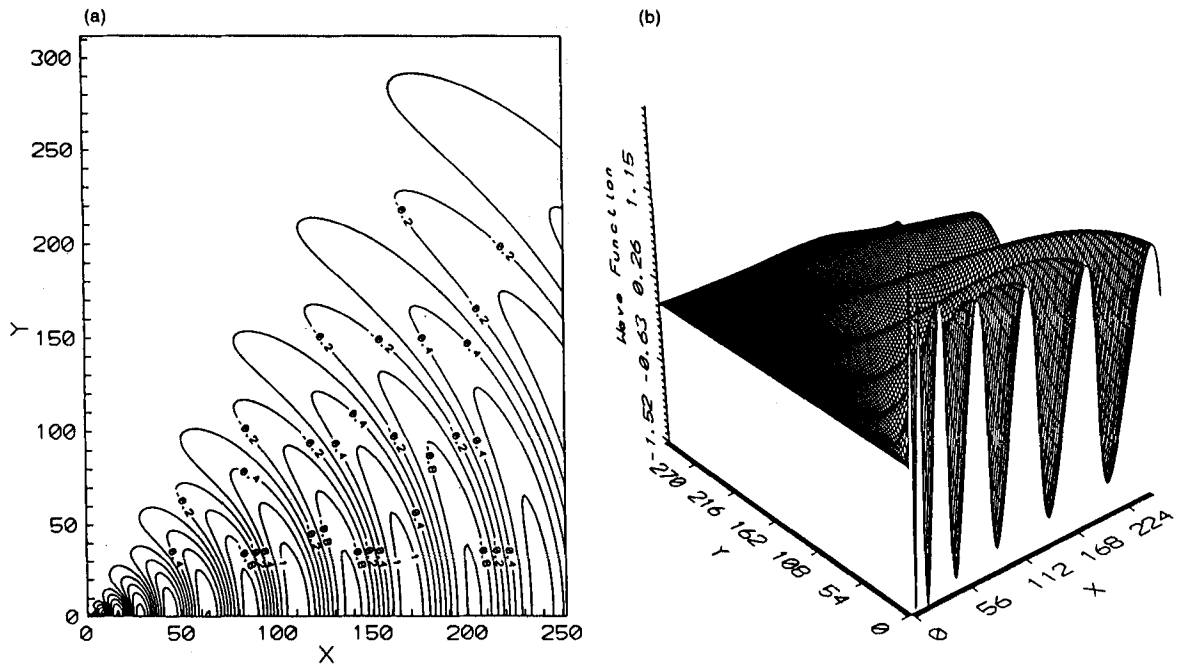


Figure 4. (a) Contours of constant amplitude are plotted in the meridional plane around a black hole. The radial direction on the equatorial plane is along the x -axis and the vertical direction is along the y -axis. Both radial and theta solutions have been combined. Parameters are $a = 0.5$, $m_p = 0.8$ and $\sigma = 0.8$. (b) Three-dimensional view of $R_{-1/2}S_{-1/2}$ are plotted in the meridional plane around a black hole. Both radial and theta solutions have been combined. Parameters are $a = 0.5$, $m_p = 0.8$ and $\sigma = 0.8$.

2.05 along the vertical axis for clarity). Here, too, the reflection coefficient decreases as k increases, consistent with the classical result that as the barrier height increases more and more, reflection is taking place strongly. Note, however, that the reflection is close to a hundred per cent. Tunneling causes only a small percentage to be lost into the black hole.

Figs 4(a) and (b) show the nature of the complete wavefunction when both the radial and the angular solutions (Chakrabarti 1984) are included. Fig. 4(a) shows the contours of constant amplitude of the wave ($R_{-1/2}S_{-1/2}$) in the meridional plane — X is along the radial direction in the equatorial plane and Y is along the vertical direction. The parameters are $a = 0.5$, $m_p = 0.8$ and $\sigma = 0.8$. Some levels are marked. Two successive contours have an amplitude difference of 0.1. In Fig. 4(b), the three-dimensional nature of the complete solution is given. Both these figures clearly show how the wavelength varies with distance. The amplitude of the spherical wave coming from a large distance away also gets weaker along the vertical axis and the wave is generally forced to fall along the equatorial plane, possibly due to the dragging of the inertial frame.

4 CONCLUSIONS

The scattering of massive, spin-half particles from a spinning black hole has been studied with particular emphasis on the nature of the radial wavefunctions and the reflection and transmission coefficients. The well-known quantum mechanical step-potential approach is applied successfully to a complex problem of barrier penetration in a space — time around a spinning black hole. One significant observation, was that the wavefunction and R , and T behave similarly close to the horizon independent of the initial parameter, such as the particle mass m_p . Particles of different mass scatter off to large distances, which are completely different, thus suggesting that a black hole could be treated as a mass spectrograph! When the energy of the particle becomes higher than the rest mass, the reflection coefficient diminishes as it should. Similar to a barrier penetration problem, the reflection coefficient becomes close to a hundred per cent when the wave hits the potential barrier. Another significant observation is that the reflection and transmission coefficients are functions of the radial coordinates. This is clear from the strongly space-dependent nature of the potential barrier, which we approximate as a collection of steps. Combined with the solution of the theta-equation, we find that the wave-amplitude vanishes close to the vertical axis, possibly because of frame-dragging effects.

REFERENCES

- Breure R. A., Ryan M. P., Jr Waller S., 1982, Proc. R. Soc. London, Ser. A, 358, 71

984 *S. K. Chakrabarti and Banibrata Mukhopadhyay*

Chakrabarti S. K., 1984, Proc. R. Soc. London, Ser. A, 391, 27

Chandrasekhar L., 1976, Proc. R. Soc. London, Ser. A, 349, 571

Chandrasekhar S., 1983, *The Mathematical Theory Of Black Holes*. Clarendon Press, London

Davydov A. S., 1976, *Quantum Mechanics*, 2nd edn. Pergamon Press, Oxford, New York

Goldberg J. N., Macfarlane A. J., Newman E. T., Rohrlich F., Sudarsan E. C. G., 1967, J. Math. Phys., 8, 2155

This paper has been typeset from a \TeX/L\AA\TeX file prepared by the author.

Dirac equation in Kerr geometry and its solution

SANDIP K. CHAKRABARTI⁽¹⁾ AND BANIBRATA MUKHOPADHYAY⁽¹⁾

⁽¹⁾ *S. N. Bose National Centre for Basic Sciences, JD-Block, Sector III, Salt Lake, Calcutta 700091, India emails: chakraba@boson.bose.res.in and bm@boson.bose.res.in*

Summary. —

Chandrasekhar separated the Dirac equation for spinning and massive particles in Kerr geometry into radial and angular parts. In the present review, we present solutions of the complete wave equation and discuss how the Dirac wave scatters off Kerr black holes. The eigenfunctions, eigenvalues and reflection and transmission coefficients are computed for different Kerr parameters. We compare the solutions with several parameters to show how a spinning black hole distinguishes mass and energy of incoming waves. Very close to the horizon, the solutions become independent of the particle parameters indicating an universality of the behaviour.

PACS 04.20.-q – Classical general relativity.

PACS 04.70.-s – Physics of black holes.

PACS 04.70.Dy – Quantum aspects of black holes.

PACS 95.30.Sf – Relativity and gravitation.

Il Nuovo Cimento (in press)

1. – Introduction

One of the most important solutions of Einstein's equation is that of the spacetime around and inside an isolated black hole. The spacetime at a large distance is flat and Minkowskian where usual quantum mechanics is applicable, while the spacetime closer to the singularity is so curved that no satisfactory quantum field theory could be developed as yet. An intermediate situation arises when a weak perturbation (due to, say, gravitational, electromagnetic or Dirac waves) originating from infinity interacts with a black hole. The resulting wave is partially transmitted into the black hole through the horizon and partially scatters off to infinity. In the linearized ('test field') approximation this problem has been attacked in the past by several authors [1, 2, 3, 4]. The master equations of Teukolsky [2] which govern these linear perturbations for integral spin (e.g., gravitational and electromagnetic) fields were solved numerically by Press & Teukolsky [5] and Teukolsky & Press [6]. While the equations governing the massive Dirac particles were separated in 1976 [3], the angular eigenfunction and eigenvalue (which happens to be the separation constant) have been obtained in 1984 [7] and radial solutions have

been obtained only recently [8, 9, 10, 11]. Particularly interesting is the fact that whereas gravitational and electromagnetic radiations were found to be amplified in some range of incoming frequencies, Chandrasekhar [4] predicted that no such amplifications should take place for Dirac waves because of the very nature of the potential experienced by the incoming fields. Although this later conclusion was drawn using an asymptotic equation, we show that this is indeed the case even when complete solutions are considered for the Dirac wave perturbations. Chandrasekhar also speculated that one needs to look into the problem for negative eigenvalues (λ) where one *might* come across super-radiance for Dirac waves.

In the present review, we discuss this important problem and its solutions. We show the nature of the radial wave functions as a function of the Kerr parameter, rest mass and frequency of incoming particle. We also verify that super-radiance is indeed absent for the Dirac field. Unlike earlier works [5, 6] where numerical (shooting) methods were used to solve the master equations governing gravitational and electromagnetic waves, we use a classical approach whereby we approximate the potential felt by the particle by a collection of small steps.

Below, we present the separated Dirac equations from Chandrasekhar [4] using the same choice of units: we choose $\hbar = 1 = G = c$, so that the unit of mass becomes $\sqrt{\frac{\hbar c}{G}}$, the unit of time becomes $\sqrt{\frac{\hbar G}{c^3}}$, and the unit of length becomes $\sqrt{\frac{\hbar G}{c^3}}$.

The equations governing the radial wave-functions $R_{\pm\frac{1}{2}}$ corresponding to spin $\pm\frac{1}{2}$ respectively are given by:

$$\Delta^{\frac{1}{2}} \mathcal{D}_0 R_{-\frac{1}{2}} = (\lambda + im_p r) \Delta^{\frac{1}{2}} R_{+\frac{1}{2}}, \quad (1a)$$

$$\Delta^{\frac{1}{2}} \mathcal{D}_0^\dagger \Delta^{\frac{1}{2}} R_{+\frac{1}{2}} = (\lambda - im_p r) R_{-\frac{1}{2}}, \quad (1b)$$

where, the operators \mathcal{D}_n and \mathcal{D}_n^\dagger are given by,

$$\mathcal{D}_n = \partial_r + \frac{iK}{\Delta} + 2n \frac{(r-M)}{\Delta}, \quad (2a)$$

$$\mathcal{D}_n^\dagger = \partial_r - \frac{iK}{\Delta} + 2n \frac{(r-M)}{\Delta}, \quad (2b)$$

and

$$\Delta = r^2 + a^2 - 2Mr, \quad (3a)$$

$$K = (r^2 + a^2)\sigma + am. \quad (3b)$$

Here, a is the Kerr parameter, n is an integer or half integer, σ is the frequency of incident wave, M is the mass of the black hole, m_p is the rest mass of the Dirac particle, λ is the eigenvalue of the Dirac equation and m is the azimuthal quantum number.

The equations governing the angular wave-functions $S_{\pm\frac{1}{2}}$ corresponding to spin $\pm\frac{1}{2}$ respectively are given by:

$$\mathcal{L}_{\frac{1}{2}}S_{+\frac{1}{2}} = -(\lambda - am_p \cos \theta)S_{-\frac{1}{2}} \quad (4a)$$

$$\mathcal{L}_{\frac{1}{2}}^\dagger S_{-\frac{1}{2}} = +(\lambda + am_p \cos \theta)S_{+\frac{1}{2}} \quad (4b)$$

where, the operators \mathcal{L}_n and \mathcal{L}_n^\dagger are given by,

$$\mathcal{L}_n = \partial_\theta + Q + n \cot \theta, \quad (5a)$$

$$\mathcal{L}_n^\dagger = \partial_\theta - Q + n \cot \theta \quad (5b)$$

and

$$Q = a\sigma \sin \theta + m \operatorname{cosec} \theta. \quad (6)$$

For massless particles these equations were solved using spin-weighted spheroidal harmonics [12, 13]. Note that both the radial and the angular sets of equations i.e., eqs. 1(a-b) and eqs. 4(a-b) are coupled equations. Combining eqs. 4(a-b), one obtains the angular eigenvalue equations for the spin- $\frac{1}{2}$ particles as [7]

$$\left[\mathcal{L}_{\frac{1}{2}} \mathcal{L}_{\frac{1}{2}}^\dagger + \frac{am_p \sin \theta}{\lambda + am_p \cos \theta} \mathcal{L}_{\frac{1}{2}}^\dagger + (\lambda^2 - a^2 m_p^2 \cos^2 \theta) \right] S_{-\frac{1}{2}} = 0. \quad (7)$$

There are exact solutions of this equation for the eigenvalues λ and the eigenfunctions $S_{-\frac{1}{2}}$ when $\rho = \frac{m_p}{\sigma} = 1$ in terms of the orbital quantum number l and azimuthal quantum number m . These solutions are [7]:

$$\lambda^2 = \left(l + \frac{1}{2}\right)^2 + a\sigma(p + 2m) + a^2\sigma^2 \left[1 - \frac{y^2}{2(l+1) + a\sigma x}\right], \quad (8)$$

and

$$\frac{1}{2}S_{lm} = \frac{1}{2}Y_{lm} - \frac{a\sigma y}{2(l+1) + a\sigma x} \frac{1}{2}Y_{l+1m} \quad (9)$$

where,

$$p = F(l, l); \quad x = F(l+1, l+1); \quad y = F(l, l+1)$$

and

$$F(l_1, l_2) = [(2l_2+1)(2l_1+1)]^{\frac{1}{2}} \langle l_2 1 m 0 | l_1 m \rangle \left[\langle l_2 1 \frac{1}{2} 0 | l_1 \frac{1}{2} \rangle + (-1)^{l_2-l} \rho \sqrt{2} \langle l_2 1 -\frac{1}{2} 1 | l_1 \frac{1}{2} \rangle \right]. \quad (10)$$

with $\langle \dots | \dots \rangle$ are the usual Clebsh-Gordon coefficients. For other values of ρ one has to use perturbation theories. Solutions upto sixth order using perturbation parameter $a\sigma$ are given in Chakrabarti [7] and are not described here. The eigenfunctions λ are required to solve the radial equations which we do now.

The radial equations 1(a-b) are in coupled form. One can decouple them and express the equation either in terms of spin up or spin down wave functions $R_{\pm\frac{1}{2}}$ but the expression loses its transparency. It is thus advisable to use the approach of Chandrasekhar [4] by changing the basis and independent variable r to,

$$r_* = r + \frac{2Mr_+ + am/\sigma}{r_+ - r_-} \log\left(\frac{r}{r_+} - 1\right) - \frac{2Mr_- + am/\sigma}{r_+ - r_-} \log\left(\frac{r}{r_-} - 1\right) \quad (r > r_+). \quad (11)$$

where,

$$\frac{d}{dr_*} = \frac{\Delta}{\omega^2} \frac{d}{dr}; \quad \omega^2 = r^2 + \alpha^2; \quad \alpha^2 = a^2 + am/\sigma, \quad (12)$$

to transform the set of coupled equations 1(a-b) into two independent one dimensional wave equations given by:

$$\left(\frac{d}{dr_*} - i\sigma\right) P_{+\frac{1}{2}} = \frac{\Delta^{\frac{1}{2}}}{\omega^2} (\lambda - im_p r) P_{-\frac{1}{2}}; \quad \left(\frac{d}{dr_*} + i\sigma\right) P_{-\frac{1}{2}} = \frac{\Delta^{\frac{1}{2}}}{\omega^2} (\lambda + im_p r) P_{+\frac{1}{2}}. \quad (13)$$

Here, $\mathcal{D}_0 = \frac{\omega^2}{\Delta} \left(\frac{d}{dr_*} + i\sigma\right)$ and $\mathcal{D}_0^\dagger = \frac{\omega^2}{\Delta} \left(\frac{d}{dr_*} - i\sigma\right)$ were used and wave functions were redefined as $R_{-\frac{1}{2}} = P_{-\frac{1}{2}}$ and $\Delta^{\frac{1}{2}} R_{+\frac{1}{2}} = P_{+\frac{1}{2}}$.

We are now defining a new variable,

$$\theta = \tan^{-1}(m_p r / \lambda) \quad (14)$$

which yields,

$$\cos \theta = \frac{\lambda}{\sqrt{(\lambda^2 + m_p^2 r^2)}}, \quad \text{and} \quad \sin \theta = \frac{m_p r}{\sqrt{(\lambda^2 + m_p^2 r^2)}}$$

and

$$(\lambda \pm im_p r) = \exp(\pm i\theta) \sqrt{(\lambda^2 + m_p^2 r^2)},$$

so the coupled equations take the form,

$$\left(\frac{d}{dr_*} - i\sigma\right) P_{+\frac{1}{2}} = \frac{\Delta^{\frac{1}{2}}}{\omega^2} (\lambda^2 + m_p^2 r^2)^{1/2} P_{-\frac{1}{2}} \exp\left[-i \tan^{-1}\left(\frac{m_p r}{\lambda}\right)\right], \quad (15a)$$

and

$$\left(\frac{d}{dr_*} + i\sigma\right) P_{-\frac{1}{2}} = \frac{\Delta^{\frac{1}{2}}}{\omega^2} (\lambda^2 + m_p^2 r^2)^{1/2} P_{+\frac{1}{2}} \exp\left[i \tan^{-1}\left(\frac{m_p r}{\lambda}\right)\right]. \quad (15b)$$

Then defining,

$$P_{+\frac{1}{2}} = \psi_{+\frac{1}{2}} \exp \left[-\frac{1}{2} i \tan^{-1} \left(\frac{m_p r}{\lambda} \right) \right] \quad (16a)$$

and

$$P_{-\frac{1}{2}} = \psi_{-\frac{1}{2}} \exp \left[+\frac{1}{2} i \tan^{-1} \left(\frac{m_p r}{\lambda} \right) \right], \quad (16b)$$

we obtain,

$$\frac{d\psi_{+\frac{1}{2}}}{dr_*} - i\sigma \left(1 + \frac{\Delta \lambda m_p}{\omega^2 2\sigma} \frac{1}{\lambda^2 + m_p^2 r^2} \right) \psi_{+\frac{1}{2}} = \frac{\Delta^{\frac{1}{2}}}{\omega^2} (\lambda^2 + m_p^2 r^2)^{1/2} \psi_{-\frac{1}{2}} \quad (17a)$$

and

$$\frac{d\psi_{-\frac{1}{2}}}{dr_*} + i\sigma \left(1 + \frac{\Delta \lambda m_p}{\omega^2 2\sigma} \frac{1}{\lambda^2 + m_p^2 r^2} \right) \psi_{-\frac{1}{2}} = \frac{\Delta^{\frac{1}{2}}}{\omega^2} (\lambda^2 + m_p^2 r^2)^{1/2} \psi_{+\frac{1}{2}}. \quad (17b)$$

Further choosing $\hat{r}_* = r_* + \frac{1}{2\sigma} \tan^{-1} \left(\frac{m_p r}{\lambda} \right)$ so that $d\hat{r}_* = \left(1 + \frac{\Delta \lambda m_p}{\omega^2 2\sigma} \frac{1}{\lambda^2 + m_p^2 r^2} \right) dr_*$, the above equations become,

$$\left(\frac{d}{d\hat{r}_*} - i\sigma \right) \psi_{+\frac{1}{2}} = W \psi_{-\frac{1}{2}}, \quad (18a)$$

and

$$\left(\frac{d}{d\hat{r}_*} + i\sigma \right) \psi_{-\frac{1}{2}} = W \psi_{+\frac{1}{2}}. \quad (18b)$$

where,

$$W = \frac{\Delta^{\frac{1}{2}} (\lambda^2 + m_p^2 r^2)^{3/2}}{\omega^2 (\lambda^2 + m_p^2 r^2) + \lambda m_p \Delta / 2\sigma}. \quad (19)$$

Now letting $Z_{\pm} = \psi_{+\frac{1}{2}} \pm \psi_{-\frac{1}{2}}$ we can combine the differential equations to give,

$$\left(\frac{d}{d\hat{r}_*} - W \right) Z_+ = i\sigma Z_-, \quad (20a)$$

and

$$\left(\frac{d}{d\hat{r}_*} + W \right) Z_- = i\sigma Z_+. \quad (20b)$$

From these equations, we readily obtain a pair of independent one-dimensional wave equations,

$$\left(\frac{d^2}{d\hat{r}_*^2} + \sigma^2\right) Z_{\pm} = V_{\pm} Z_{\pm}. \quad (21)$$

where, $V_{\pm} = W^2 \pm \frac{dW}{d\hat{r}_*}$,

$$\begin{aligned} &= \frac{\Delta^{\frac{1}{2}}(\lambda^2 + m_p^2 r^2)^{3/2}}{[\omega^2(\lambda^2 + m_p^2 r^2) + \lambda m_p \Delta / 2\sigma]^2} [\Delta^{\frac{1}{2}}(\lambda^2 + m_p^2 r^2)^{3/2} \pm ((r - M)(\lambda^2 + m_p^2 r^2) + 3m_p^2 r \Delta)] \\ &\mp \frac{\Delta^{\frac{3}{2}}(\lambda^2 + m_p^2 r^2)^{5/2}}{[\omega^2(\lambda^2 + m_p^2 r^2) + \lambda m_p \Delta / 2\sigma]^3} [2r(\lambda^2 + m_p^2 r^2) + 2m_p^2 \omega^2 r + \lambda m_p (r - M) / \sigma]. \quad (22) \end{aligned}$$

One important point to note: the transformation of spatial co-ordinate r to r_* (and \hat{r}_*) is taken not only for mathematical simplicity but also for a physical significance. When r is chosen as the radial co-ordinate, the decoupled equations for independent waves show diverging behaviour. However, by transforming those in terms of r_* (and \hat{r}_*) we obtain well behaved functions. The horizon is shifted from $r = r_+$ to $\hat{r}_* = -\infty$ unless $\sigma \leq \sigma_s = -am/2Mr_+$ (eq. 11). In this connection, it is customary to define σ_c where $\alpha^2 = 0$ (eq. 13). Thus, $\sigma_c = -m/a$. If $\sigma \leq \sigma_s$, the super-radiation is expected [4].

2. – Solution Procedure

The choice of parameters is generally made in such a way that there is a significant interaction between the particle and the black hole, i.e., when the Compton wavelength of the incoming wave is of the same order as the outer horizon of the Kerr black hole. Similarly, the frequency of the incoming particle (or wave) should be of the same order as inverse of light crossing time of the radius of the black hole. These yield [8],

$$m_p \sim \sigma \sim [M + \sqrt{(M^2 - a^2)}]^{-1}. \quad (23)$$

One can easily check from equation (22) that for $r \rightarrow \infty$ (i.e., $\hat{r}_* \rightarrow \infty$) $V_{\pm} \rightarrow m_p^2$. So the total energy of the physical particle should greater than square of its rest mass. So if we expand the total parameter space in terms of frequency of the particle (or wave), σ and rest mass of the particle, m_p , it is clear that 50% of total parameter space where $\sigma < m_p$ is unphysical (In this case, the energy is such that a particle released from a finite distance cannot go back to infinity after scattering.), and one need not study this region. Out of the total physical parameter space there are two cases of interest: (1) the waves do not ‘hit’ the potential barrier and (2) the waves do hit the potential barrier. To solve these potential problem first, we replace the potential barrier by a large number of steps as in the step-barrier problem in quantum mechanics. Fig. 1 shows one such example of the potential barrier [10] V_+ (Eq. 22) which is drawn for $a = 0.5$, $m_p = 0.8$ and $\sigma = 0.8$. In reality we use tens of thousands of steps with suitable variable widths so that the steps become indistinguishable from the actual function. The solution of Eq. 22 at n th step can be written as [14],

$$Z_{+,n} = A_n \exp[ik_n r_{*,n}] + B_n \exp[-ik_n r_{*,n}] \quad (24)$$

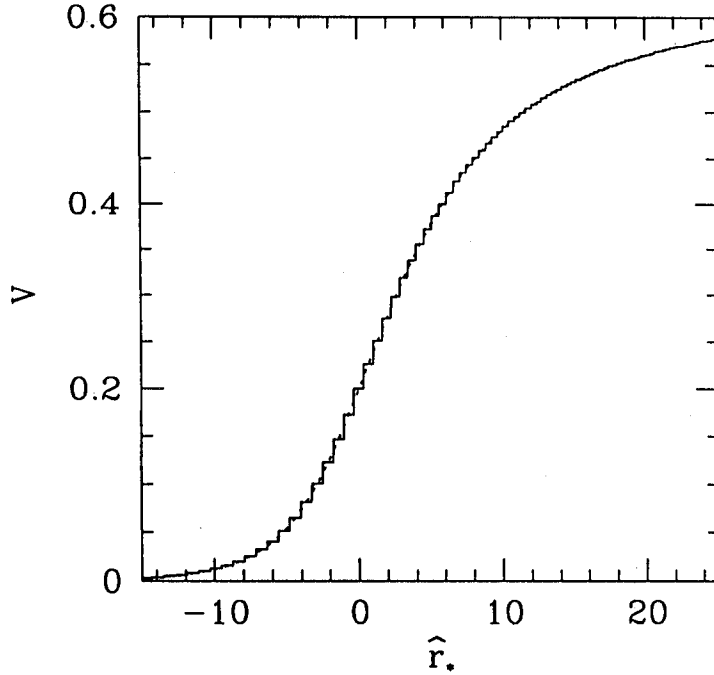


Fig. 1 : Behaviour of V_+ (smooth solid curve) for $a = 0.5$, $m_p = 0.8$, $\sigma = 0.8$. This is approximated as a collection of steps. In reality tens of thousand steps were used with varying step size which mimic the potential with arbitrary accuracy.

when energy of the wave is greater than the height of the potential barrier. The standard junction condition is given as [14],

$$Z_{+,n} = Z_{+,n+1} \quad \text{and} \quad \frac{dZ_+}{d\hat{r}_*}|_n = \frac{dZ_+}{d\hat{r}_*}|_{n+1}. \quad (25)$$

The reflection and transmission co-efficients at n th junction are given by:

$$R_n = \frac{A_{n+1}(k_{n+1} - k_n) + B_{n+1}(k_{n+1} + k_n)}{A_{n+1}(k_{n+1} + k_n) + B_{n+1}(k_{n+1} - k_n)}, \quad T_n = 1 - R_n \quad (26)$$

At each of the n steps these conditions were used to connect solutions at successive steps. Here, k is the wave number ($k = \sqrt{\sigma^2 - V_{\pm}}$) of the wave and k_n is its value at n th step. We use the 'no-reflection' inner boundary condition: $R \rightarrow 0$ at $\hat{r}_* \rightarrow -\infty$.

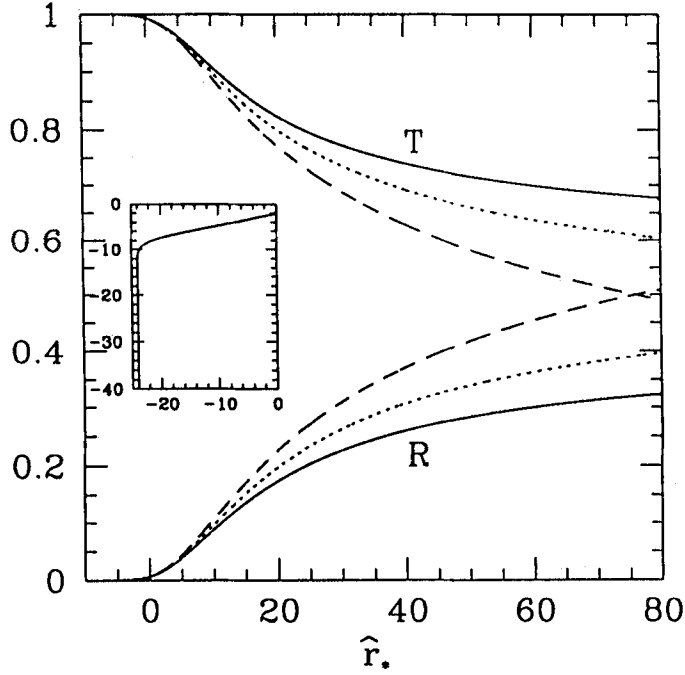


Fig. 2a: Reflection (R) and transmission (T) coefficients of waves with varying mass as functions of \hat{r}_* . $m_p = 0.78$ (solid), $m_p = 0.79$ (dotted) and $m_p = 0.80$ (long-dashed) are used. Other parameters are $a = 0.5$ and $\sigma = 0.8$. Inset shows R in logarithmic scale which falls off exponentially just outside the horizon.

For the cases where waves hit on the potential barrier, inside the barrier (where $\sigma^2 < V_+$) we use the wave function of the form

$$Z_{+,n} = A_n \exp[-\alpha_n \hat{r}_{*,n}] + B_n \exp[\alpha_n \hat{r}_{*,n}] \quad (27)$$

where, $\alpha_n = \sqrt{V_{\pm} - \sigma^2}$, as in usual quantum mechanics.

3. - Examples of Solutions

Fig. 2a shows three solutions [amplitudes of $\text{Re}(Z_+)$] for parameters: $a = 0.5$, $\sigma = 0.8$ and $m_p = 0.78$, 0.79 , and 0.80 respectively in solid, dotted and long-dashed curves. The energy σ^2 is always higher compared to the height of the potential barrier (Fig. 1) and

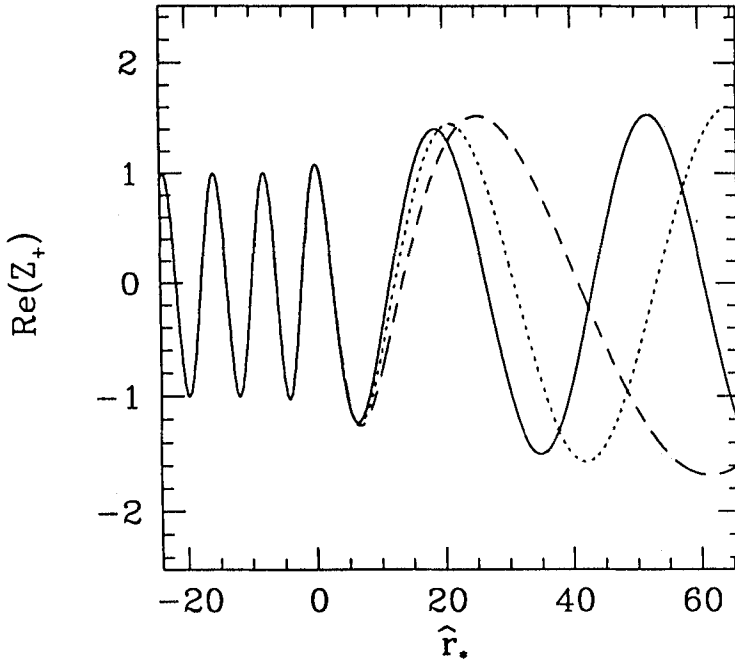


Fig. 2b: Amplitude of $\text{Re}(Z_+)$ of waves with varying mass as functions of \hat{r}_* . $m_p = 0.78$ (solid), $m_p = 0.79$ (dotted) and $m_p = 0.80$ (long-dashed) are used. Other parameters are $\alpha = 0.5$ and $\sigma = 0.8$.

therefore the particles do not ‘hit’ the barrier. k goes up and therefore the wavelength goes down monotonically as the wave approaches a black hole. It is to be noted that though ours is apparently a ‘crude’ method, it has flexibility and is capable of presenting insight into the problem, surpassing any other method such as ODE solver packages. This is because one can choose (a) variable steps depending on steepness of the potential to ensure uniform accuracy, and at the same time (b) virtually infinite number of steps to follow the potential as closely as possible. For instance, in the inset, we show R in logarithmic scale very close to the horizon. All the three curves merge, indicating that the solutions are independent of the mass of the particle and a closer inspection shows that here, the slope of the curve depends only on σ . The exponential dependence of R_n close to the horizon becomes obvious. Asymptotically, $V_{\pm} = m_p^2$ (eq. 22), thus, as m_p goes down, the wavelength goes down. In Fig. 2b, we present the instantaneous values of the reflection R and transmission T coefficients (i.e., R_n and T_n of Eq. 26) for the same three cases. As the particle mass is decreased, k goes up and corresponding R goes down consistent with the limit that as $k \rightarrow \infty$, there would be no reflection at all as in a quantum mechanical problem.

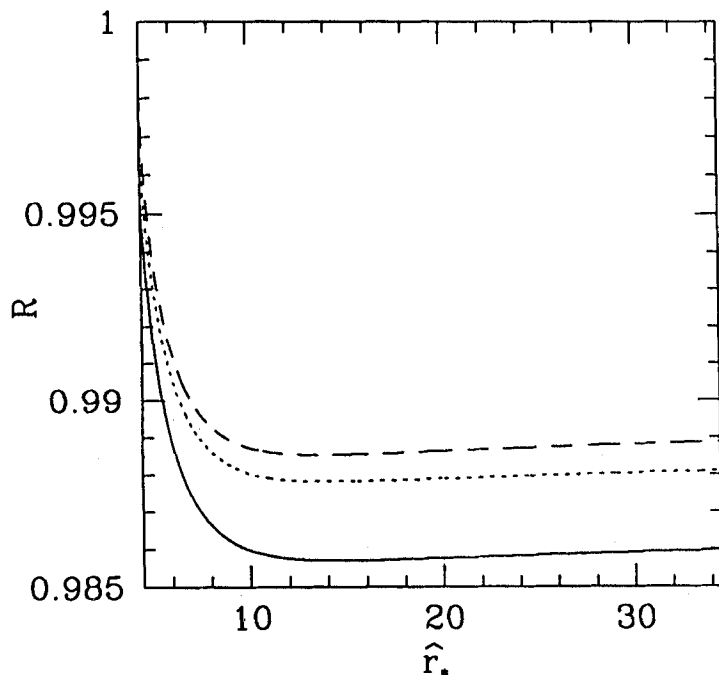


Fig. 3a: Reflection (R) coefficient of waves with varying mass as functions of \hat{r}_* . $m_p = 0.16$ (solid), $m_p = 0.164$ (dotted) and $m_p = 0.168$ (long-dashed) are used. Other parameters are $a = 0.95$ and $\sigma = 0.168$.

Figs. 3(a-b) compare a few solutions where the incoming particles 'hit' the potential barrier. We choose, $a = 0.95$, $\sigma = 0.168$ and mass of the particle $m_p = 0.16$, 0.164 , 0.168 respectively in solid, dotted and long-dashed curves. Inside the barrier, the wave decays before coming back to a sinusoidal behaviour, before entering into a black hole. In Fig. 3b, we plotted the potential (shifted by 2.05 along vertical axis for clarity). Here too, the reflection coefficient goes down as k goes up consistent with the classical result that as the barrier height goes up more and more, reflection is taking place strongly. Note however, that the reflection is close to a hundred percent. Tunneling causes only a few percent to be lost into the black hole.

Figs. 4(a-b) show the nature of the complete wave function when both the radial and the angular solutions [7] are included. Fig. 4a shows contours of constant amplitude of the wave ($R_{-1/2}S_{-1/2}$) in the meridional plane - X is along radial direction in the equatorial plane and Y is along the vertical direction. The parameters are $a = 0.5$,

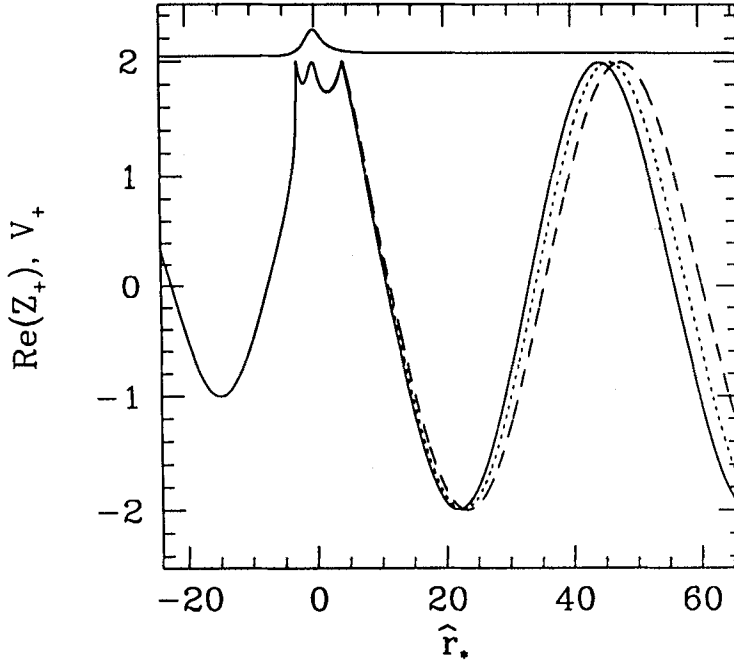


Fig. 3b: Amplitude of $\text{Re}(Z_+)$ of waves with varying mass as functions of \hat{r}_* . $m_p = 0.16$ (solid), $m_p = 0.164$ (dotted) and $m_p = 0.168$ (long-dashed) are used. Nature of potential with $m_p = 0.168$ is drawn shifting vertically by 2.05 unit for clarity. Other parameters are $a = 0.95$ and $\sigma = 0.168$.

$m_p = 0.8$ and $\sigma = 0.8$. Some levels are marked. Two successive contours have amplitude difference of 0.1. In Fig. 4b a three-dimensional nature of the complete solution is given. Both of these figures clearly show how the wavelength varies with distance. Amplitude of the spherical wave coming from a large distance also gets weaker along the vertical axis and the wave is forced to fall generally along the equatorial plane, possibly due to the dragging of the inertial frame.

4. – Conclusion

We review here the scattering of massive, spin-half particles from a spinning black hole with particular emphasis to the nature of the radial wave functions and reflection and transmission coefficients. Here we presented a well known quantum mechanical step-

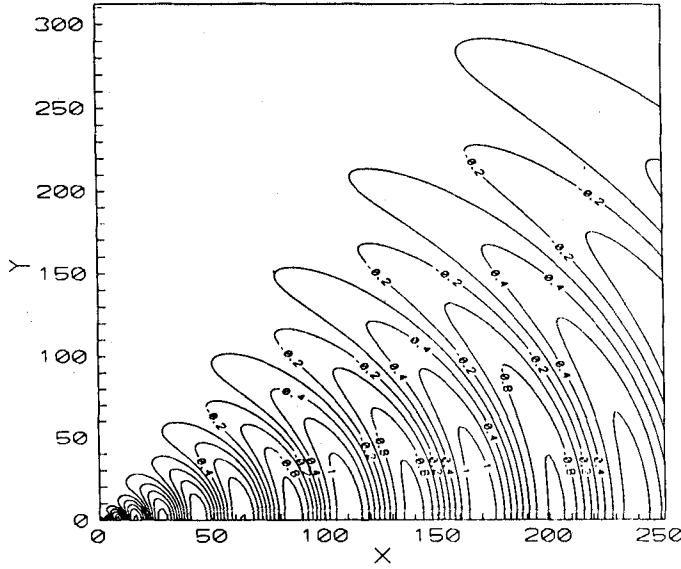


Fig. 4a: Contours of constant amplitude are plotted in the meridional plane around a black hole. Radial direction on equatorial plane is along X axis and the vertical direction and along Y . Both radial and theta solutions have been combined. Parameters are $a = 0.5$, $m_p = 0.8$ and $\sigma = 0.8$.

potential approach [10] but one can verify by any numerical technique that the solution would remain the same. A modified WKB approximation [8, 9, 11] also yields similar result in Kerr geometry [15]. The approach presented here (i.e., step potential approach) is very transparent since a complex problem of barrier penetration in a spacetime around a spinning black hole could be tackled very easily. We report a few significant observations of these papers that the wave function and R , and T behave similarly close to the horizon independent of the initial parameter, such as the particle mass m_p . Particles of different mass scatter off to a large distance completely differently, thus giving an impression that a black hole could be treated as a mass spectrograph! When the energy of the particle becomes higher compared to the rest mass, the reflection coefficient diminishes as it should it. Similar to a barrier penetration problem, the reflection coefficient becomes close to a hundred percent when the wave hits the potential barrier. Another significant observation is that the reflection and transmission coefficients are functions of the radial coordinates. This is understood easily because of the very nature of the potential barrier which is strongly space dependent which we approximate as a collection of steps. Combining with the solution of theta-equation, we find that the wave-amplitude

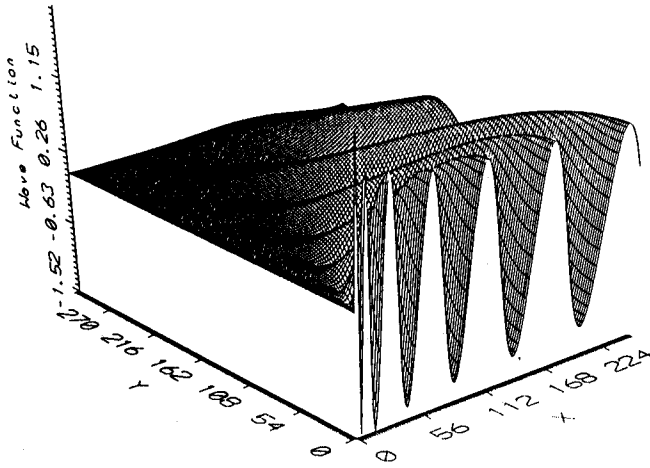


Fig. 4b: Three dimensional view of $R_{-1/2}S_{-1/2}$ are plotted in the meridional plane around a black hole. Both radial and theta solutions have been combined. Parameters are $a = 0.5$, $m_p = 0.8$ and $\sigma = 0.8$.

vanishes close to the vertical axis, possibly due to the frame-dragging effects.

REFERENCES

- [1] TEUKOLSKY S., *Phys. Rev. Lett.*, **29** (1972) 1114.
- [2] TEUKOLSKY S., *Astrophys. J.*, **185** (1973) 635.
- [3] CHANDRASEKHAR S., *Proc. R. Soc. Lond. A*, **349** (1976) 571.
- [4] CHANDRASEKHAR S., *The Mathematical Theory Of Black Holes*. John Wiley: New York (1984).
- [5] PRESS W. H. and TEUKOLSKY S., *Astrophys. J.*, **185** (1973) 649..
- [6] TEUKOLSKY S. and PRESS W. H., *Astrophys. J.*, **193** (1974) 443.
- [7] CHAKRABARTI S. K., *Proc. R. Soc. Lond. A*, **391** (1984) 27.
- [8] MUKHOPADHYAY B. and CHAKRABARTI S. K., *Proceedings of the Mini-Workshop on Applied Mathematics* edited by ISLAM J. N., HOSAIN M. A., REES D. A. S., ROY G. D. and GHOSH N. C. (Dept. of Mathematics, SUST) (1998) 251.
- [9] MUKHOPADHYAY B. and CHAKRABARTI S. K., *Class. Quant. Grav.*, **16** (1999) 3165.
- [10] CHAKRABARTI, S.K. and MUKHOPADHYAY, B., *Mon. Not. R. Astro. Soc.*, (2000) (submitted).
- [11] MUKHOPADHYAY, B., *Class Quant. Grav.*, (2000) (in press).
- [12] GOLDBERG J. N., MACFARLANE A. J., NEWMAN E. T., ROHRlich F. and SUDARSAN E. C. G., *J. Math. Phys.*, **8** (1967) 2155
- [13] BREURE R. A., RYAN M. P. JR. and WALLER S., *Proc. R. Soc. Lond. A*, **358** (1982) 71.
- [14] DAVYDOV A. S., *Quantum Mechanics* (New York: Pergamon Press) (1976).
- [15] MUKHOPADHYAY B. and CHAKRABARTI S. K., *Nuclear Physics B.*, (2000) (submitted).